Title	Molecular Design and Synthesis of Oligosaccharide-Based Block Copolymers for Functional Materials
Author(s)	勝原, 哲
Degree Grantor	北海道大学
Degree Name	博士(工学)
Dissertation Number	甲第15414号
Issue Date	2023-03-23
DOI	https://doi.org/10.14943/doctoral.k15414
Doc URL	https://hdl.handle.net/2115/91534
Type	doctoral thesis
File Information	KATSUHARA_Satoshi.pdf

Molecular Design and Synthesis of Oligosaccharide-Based Block Copolymers for Functional Materials

A Dissertation for the Degree of Doctor of Philosophy

Satoshi Katsuhara

Hokkaido University

March, 2023

Acknowledgements

The study presented in this dissertation has been performed under the direction of Professor Toshifumi Satoh, Division of Applied Chemistry, Faculty of Engineering, Hokkaido University, from 2018 to 2023. I wish to express my deepest appreciation to Professor Toshifumi Satoh, for his kind instruction, helpful advice, and unstinting encouragement during the course of this work as well as his kindness in everything in lab life.

I am deeply grateful to Associate Professor Takuya Isono and Associate Professor Kenji Tajima, Division of Applied Chemistry, Faculty of Engineering, Hokkaido University, for their helpful, valuable, and fruitful suggestions and discussion with continuous encouragement since my first day in the laboratory.

I also would like to express my sincere thanks to Associate Professor Takuya Yamamoto, Division of Applied Chemistry, Faculty of Engineering, Hokkaido University, whose kind understanding and generous supports have been indispensable throughout this work.

I have greatly benefitted from Professor Hajime Ito (Hokkaido University) for his assistance with the AFM experiments, Dr. Hiroaki Mamiya (National Institute for Materials Science) for his assistance with the SAXS experiments, Professor Ken’ichiro Matsumoto (Hokkaido University) for his assistance with tensile test, Associate Professor

Tasuku Nakajima (Hokkaido University) for his assistance with cycle tensile test, Mr. Kenji Ohkubo (Hokkaido University) and Mr. Tetsuya Konishi (Hokkaido University) for their assistance with the SEM experiments, Project Lecturer Naoki Sunagawa (The University of Tokyo), Professor Kiyohiko Igarashi (The University of Tokyo), and Professor Motomitsu Kitaoka (Niigata University) for kindly providing the pET-28a-CDP plasmid, and Professor Kenji Takahashi (Kanazawa University), Professor Yutaka Takeuchi (Kanazawa University), Mr. Hiroyuki Itaya (Kanazawa University), and Ms. Kaoru Kitani (Kanazawa University) for their assistance with biodegradation test.

Special thanks go to Yasuko Takagi and Yuki Tsuji. This dissertation would not have been possible without their enthusiastic hard work. It was my great honor to proceed the study with them. I am also grateful to other members of Professor Satoh's group for their good collaborations and for providing a good working atmosphere.

I would like to express my gratitude to Chemistry Personnel Cultivation Program.

Finally, I wish to give my thanks to my family and friends for their understanding, support, and continuous encouragement throughout my research and daily life.

March 2023

Satoshi Katsuhara

Contents

Chapter 1 General Introduction 1

1.1. Introduction to poly/oligosaccharides 2

1.2. Block copolymers (BCPs) 6

1.3. Poly/oligosaccharide-based BCP 12

1.4. Objective and Outline of the Dissertation 18

1.5. References 28

Chapter 2 Fabrication of Sub-10 nm Microphase-Separated Structures Using Metallopolymer-block-Oligosaccharide 35

2.1. Introduction 36

2.2. Experimental Section 41

2.2.1. Materials 41

2.2.2. Instruments 42

2.2.3. Synthetic details 45

2.3. Results and Discussion 50

2.3.1. Synthesis of PVFc-*b*-MT, PVFc-*b*-MH, and PVFc-*b*-$(MT)_2$ 50

2.3.2. Thermal properties and etching resistance 57

2.3.3. Microphase-separated structures 62

2.4. Conclusion 66

2.5. References 67

Chapter 3 Synthesis of Cellulose-Based Triblock Copolymers for Investigating Microphase Separation Behavior and Mechanical Properties: Comparisons with Amylose-Based Triblock Copolymers 73

3.1. Introduction 74

3.2. Experimental Section 79

3.2.1. Materials 79

3.2.2. Instruments 80

3.2.3. Synthetic details 85

3.3. Results and Discussion 104

3.3.1. Synthesis of propargyl-functionalized cellooligosaccharide triacetate and maltooligosaccharide triacetate 104

3.3.2. Triblock copolymer synthesis 113

3.3.3. Thermal properties 122

3.3.4. Microphase-separated structures 127

3.3.5. Mechanical properties 135

3.4. Conclusion 141

3.5. References 142

Chapter 4 Design of Cellulose-Based Block Copolymers: DS effects on Microphase Separation Behavior and Mechanical Properties 149
4.1. Introduction 150
4.2. Experimental Section 155
4.2.1. Materials 155
4.2.2. Instruments......156
4.2.3. Synthetic details......162
4.3. Results and Discussion......171
4.3.1. Synthesis of cellooligosaccharide......171
4.3.2. BCP synthesis 179
4.3.3. Thermal properties......187
4.3.4. Microphase-separated structures......191
4.3.5. Mechanical properties......199
4.3.6. Biodegradability potential......205
4.4. Conclusion......211
4.5. References 212
Chapter 5 Development of Cellulose-Based Compatibilizers for Toughening Cellulose Acetate 217
5.1. Introduction 218
5.2. Experimental Section 222
5.2.1. Materials 222
5.2.2. Instruments......223
5.2.3. Synthetic details......227
5.3. Results and Discussion......240
5.3.1. Synthesis of propargyl-functionalized cellooligosaccharide triacetate......240
5.3.2. BCP synthesis 244
5.3.3. Investigation of physical properties of CTA/PCL/BCP-blend film......253
5.4. Conclusion......260
5.5. References 261
Chapter 6 Conclusion 265

Chapter 1

General Introduction

1.1. Introduction to poly/oligosaccharides

Poly/oligosaccharides can be found in every living organism and are important biogenic substances, which are related with their biological activity, biocompatibility, and biodegradability (**Figure 1.1**).[1] Poly/oligosaccharides are the most abundant organic compounds on the earth and can be easily obtained as natural resources, so that they and their derivatives have been widely applied in food industry and biomedical fields, such as food additives, tissue scaffolds, drug delivery vehicles, biostimulants in agriculture, textiles, membranes, and films.[1–7] Furthermore, the representative biobased polymers such as polylactide, poly(3-hydroxybutyric acid), and poly(2,5-furandicarboxylic acid) are produced through chemical or fermentation processing of carbon sources obtained from poly/oligosaccharides, meaning that poly/oligosaccharides are been essential raw materials to produce bioplastics.[8–10] As describe above, poly/oligosaccharides are outstanding material in terms of both direct and indirect utilizations.

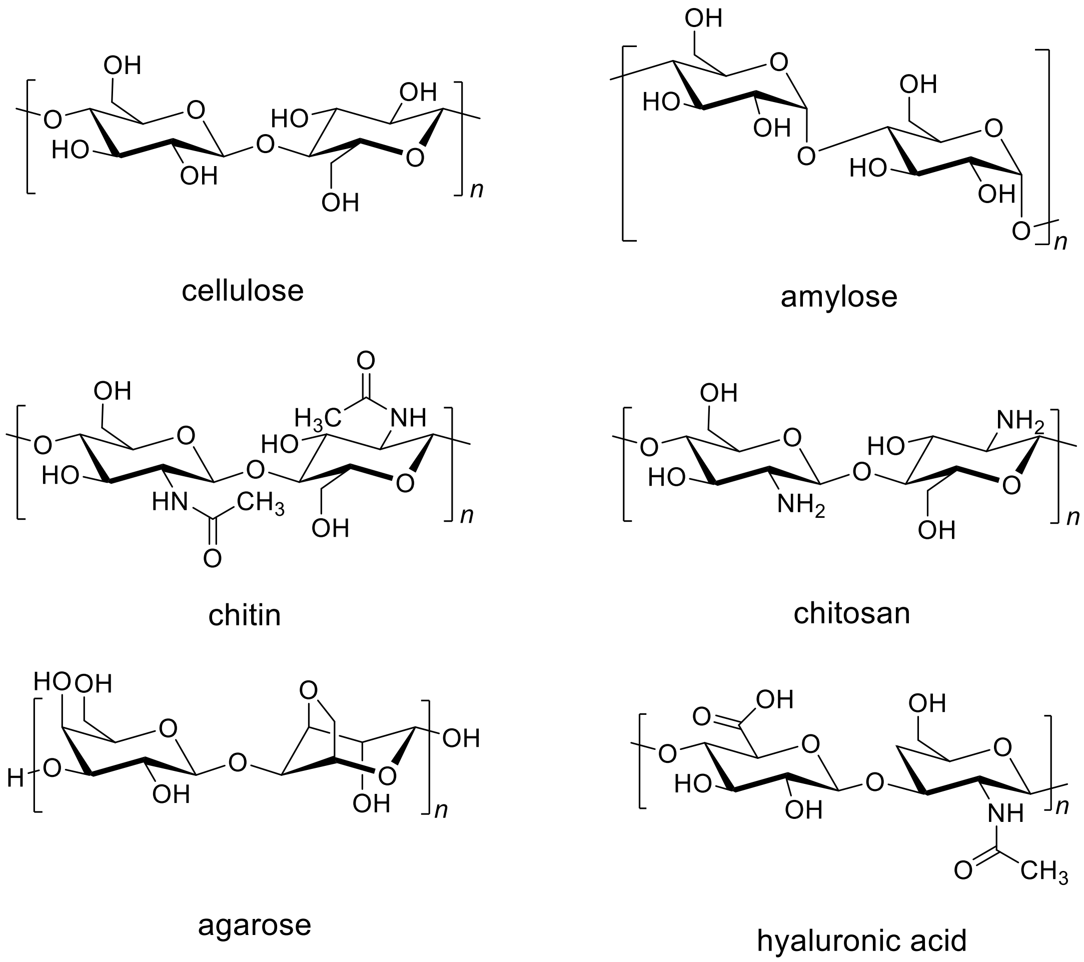

cellulose

amylose

chitin

chitosan

agarose

hyaluronic acid

Figure 1.1. Chemical structure of representative polysaccharide.

In addition to the above advantages e.g., high biodegradability and easiness to obtain from natural resources, poly/oligosaccharides have a wide variety of derivatives and exhibit diverse properties due to structural difference. For example, cellulose which is insoluble in common organic solvents and decomposes before melting with rising temperatures due to strong hydrogen bonding has many derivatives to give it thermoplastic property and solubility in organic solvents (**Figure 1.2**).[11] Indeed, derivatization is classically useful method to modify poly/oligosaccharides to expand their utilization. However, to develop the new application using the strong point of poly/oligosaccharide, another approach, molecular design, to expand the application of poly/oligosaccharide-based materials is needed.

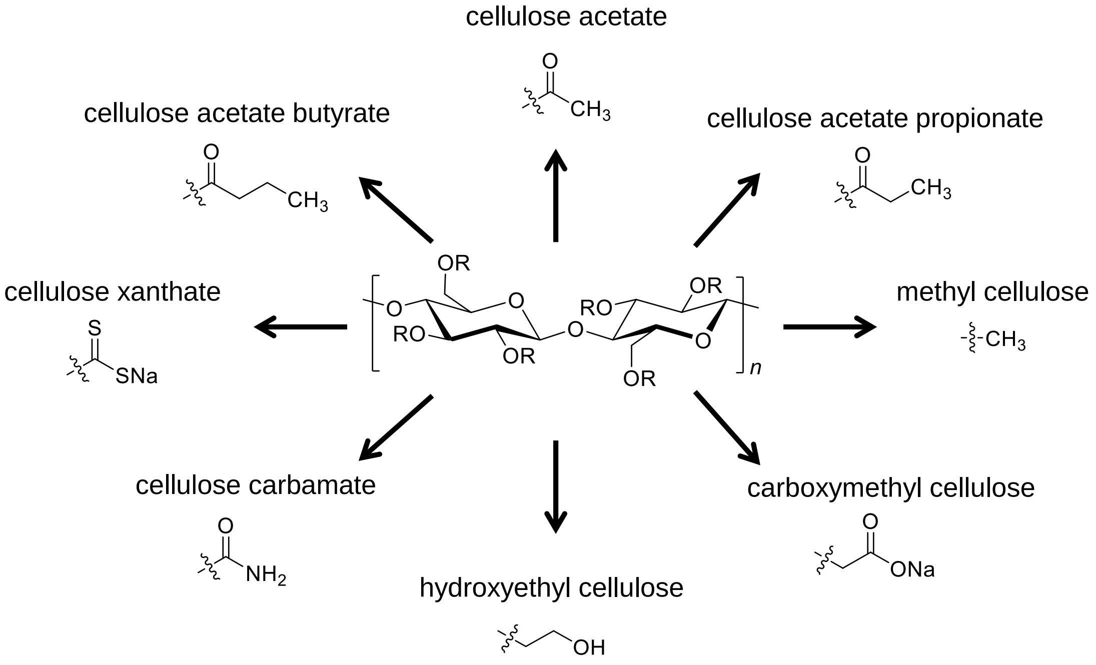

Figure 1.2. Chemical structure of representative cellulose derivatives.

Combining with synthetic polymers is the attractive choices to modify the physical properties of poly/oligosaccharides and to expand their possible applications. One of the means to combine synthetic polymer and poly/oligosaccharide is the synthesis of poly/oligosaccharide-based graft copolymers. The poly/oligosaccharide-based graft copolymers can be classified into two types: (1) main chain type which is consisted of poly/oligosaccharide main chain with synthetic polymer graft chains and (2) side chain type which is consisted of synthetic polymer main chain with poly/oligosaccharide graft chains (**Figure 1.3**).[12–18] Such poly/oligosaccharide-based graft copolymers have been applied in biomedical field as surfactants, carrier for controlled drug release system, and biomaterials due to their good biocompatibility and specific interaction with biological substances.[12] However, the grafting approach is not sufficient enough to expand the application range of poly/oligosaccharide.

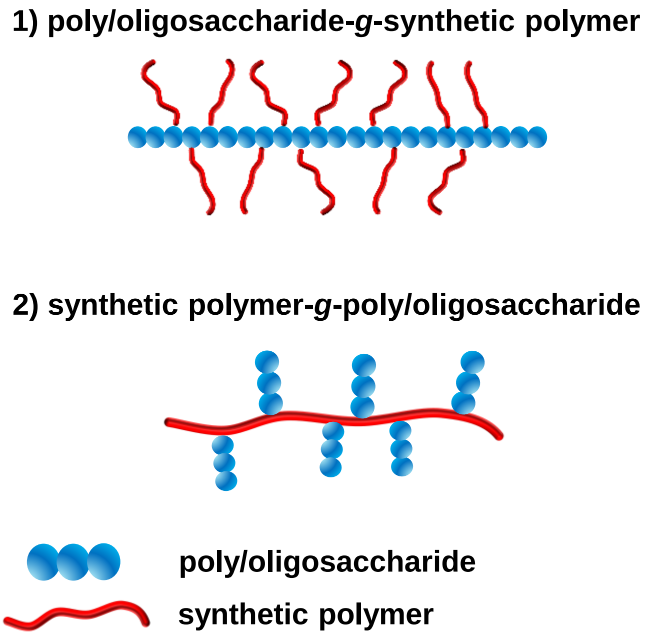

1) poly/oligosaccharide-*g*-synthetic polymer

2) synthetic polymer-*g*-poly/oligosaccharide

Figure 1.3. Schematic illustration of poly/oligosaccharide-based graft copolymers. (1) Main chain type which is consisted of poly/oligosaccharide main chain with synthetic polymer graft chains and (2) side chain type which is consisted of synthetic polymer main chain with poly/oligosaccharide graft chains.

1.2. Block copolymers (BCPs)

As the third choice to combine synthetic polymers and poly/oligosaccharide, end-to-end coupling to produce poly/oligosaccharide-based block copolymers is of great interest.[19–21] The poly/oligosaccharide-based block copolymers are expected to utilize properties of both poly/oligosaccharides and synthetic polymer due to preserve the integrity of each polymer chain. Block copolymers (BCPs) are distinct from the graft copolymers in terms of the self-assembly properties, and, in turn, application potential. Here, a general introduction to BCPs will be given. In general, BCPs consist of two or more chemically different polymers and exhibit interesting properties which are not observed in the related homopolymers and random copolymers. One of the most interesting properties of BCPs is the self-assembly behavior in the bulk and thin film states to form microphase-separated structures. AB diblock copolymer, the simplest BCP, is known to microphase separate into four types of periodic nanostructures, i.e., lamellar (LAM), bicontinuous double gyroid network (GYR), hexagonally close-packed cylinder (HEX), and body-centered-cubic (BCC) sphere, depending on the volume fraction (f) of the constituent blocks (**Figure 1.4**).[22,23]

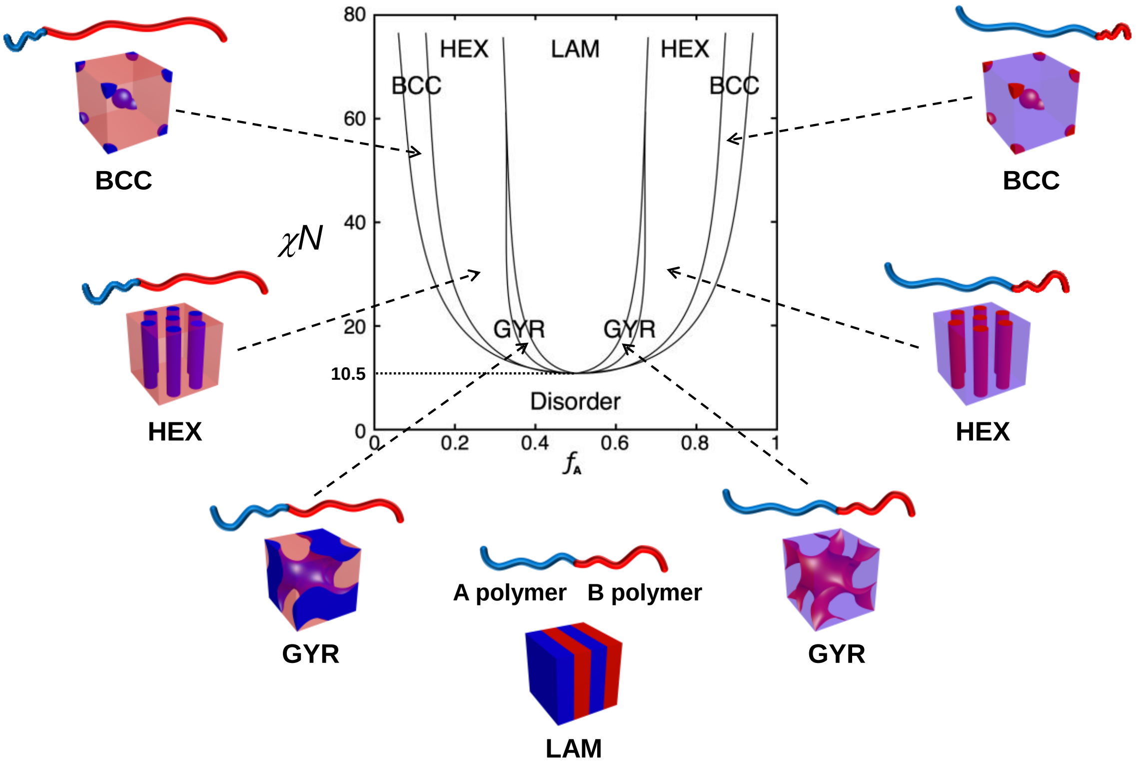

Figure 1.4. Theoretical phase diagram of AB diblock copolymer, exhibiting typical four types of morphologies (LAM, GYR, HEX, and BCC) with the BCPs chains possessing the corresponding volume fraction of A polymer (f_A).

The periodic length of the nanostructures, refer to as domain spacing (d), reflects the polymer radius of gyration (R_g) which is related with overall degree of polymerizations (N) of BCP. In the strong segregation limit, d is known to scales as follows:[24]

$d \propto N^{2/3}$ (1)

Considering this relation, the d can be easily controlled by adjusting the N; however, the product of χ and N must be higher than a critical value to induce microphase separation, where χ is the Flory-Huggins interaction parameter reflecting the incompatibility between the two blocks of the BCP. This is critical when considering the application of BCP microphase-separated structures in nanofablications, as discussed later.

The microphase-separated structures can be applied to next-generation nanotechnological materials such as memory devices,[25,26] optical materials,[27,28] nano-porous materials,[29] and nano-templates for lithography.[30–32] In particular, the lithographic application of BCPs, so-called "BCP-lithography", commits the improvement of microfabrication technology in microelectronics industry (**Figure 1.5**). The conventional semiconductor lithography has been achieved by photolithographic process using ArF excimer laser; however, such top-down lithographic technology is facing serious problems due to the limits of optical diffraction and light wavelength, which are directly related to the resolution limit. On the contrary, the d value of the microphase-separated structure is generally at 10–50 nm scale reflecting the R_g of polymer chain, which have high potential to break through the resolution limit of the conventional photolithography technology. In the next-generation lithography technique using self-assembled BCPs, the d value directly reflects to the resolution, so that decreasing the d value is highly significant for the sustainable development of BCP lithography technique. Indeed, the d value can be downsized by decreasing N based on eq. (1); however, the product of χ and N must exceed a critical value to microphase separation occur, as above mentioned. To overcome this dilemma, the high-χ BCPs which occur microphase separation even at low-

N region are attracting attention.

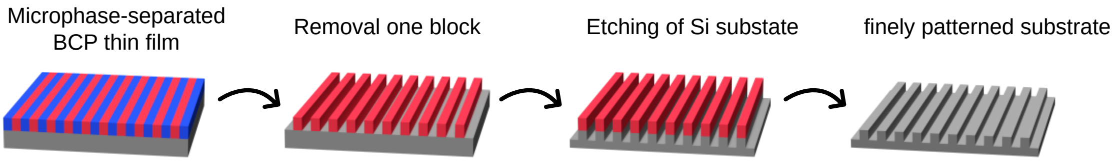

Figure 1.5. Schematic illustration of the BCP lithography process.

Importantly, the BCPs are also essential as industrial materials today as well as the next generation nanomaterial as above mentioned. This representative example is thermoplastic elastomers (TPEs). The typical TPEs are based on ABA-type triblock copolymer, where the A block is glassy polymer (high glass transition temperature or melting temperature) and the B block is rubbery polymer. Such ABA-type triblock copolymers with “hard-*b*-soft-*b*-hard” block sequence exhibit elastomeric property through microphase separation, in which the A block acts as strong physical cross-liked point (**Figure 1.6**). The most common TPEs in industrial area are the styrenic TPEs, such as polystyrene-*b*-polyisoprene-*b*-polystyrene, polystyrene-*b*-polybutadiene-*b*-polystyrene, and polystyrene-*b*-polyethylenepropylene-*b*-polystyrene.[33] Importantly, the material properties of the styrenic TPEs can be easily modified by controlling the molecular weight and choosing suitable soft segment polymer, so that they have been used for various application fields. However, these styrenic TPEs are petroleum origin and have no biodegradability. Thus, the environmentally benign TPEs are highly demanded with the increasing concern about environmental issues in recent years.

Furthermore, BCPs can be used as additives for polymer blends by acting like surfactants by judicious choice of the constitutional blocks.[34] This macromolecular surfactant is called as "compatibilizer", which compatibilize the immiscible two polymers. Polymer blend has been recognized as the simple and effective method to control and improve the physical properties of polymeric materials. However, basically, macrophase separation is occurred due to the small entropy gain when two different polymers are blended, which precludes improving the physical properties of the binary blend materials.[35,36] Compatibilizer consisting of two polymers segments each possessing miscibility with one of the polymer blend components enhances the compatibility of the two different polymers by localizing at the interface, which leads to materials with improved properties (**Figure 1.7**).[35,36]

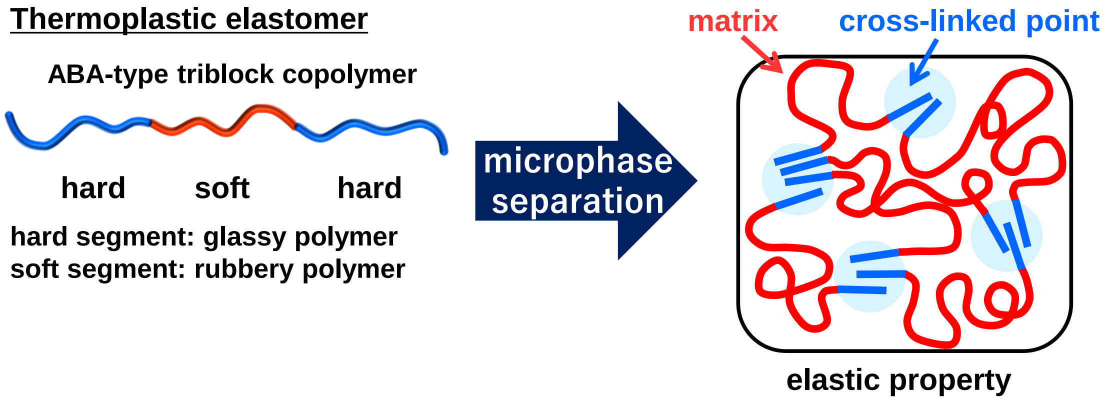

Figure 1.6. Schematic image of thermoplastic elastomer.

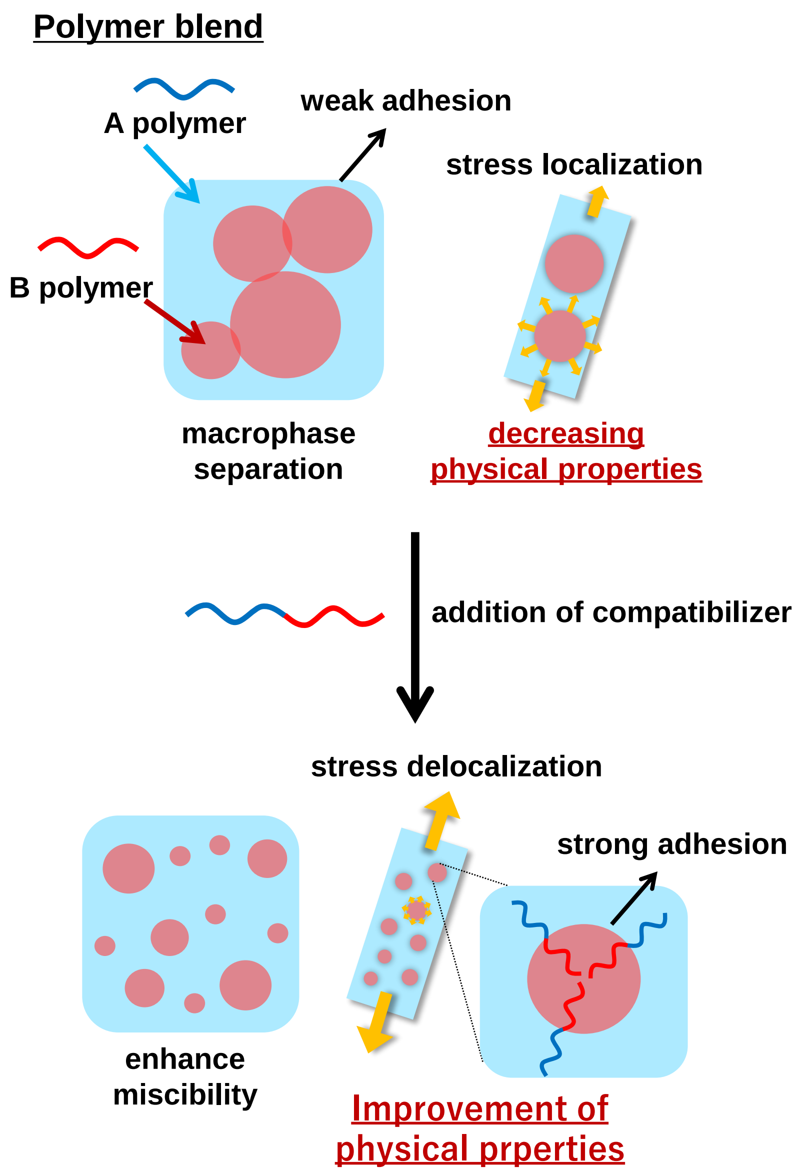

Figure 1.7. Schematic image of polymer blend and effect of compatibilizer.

1.3. Poly/oligosaccharide-based BCP

Considering the versatile applications of BCPs, the author thought that BCPs consisting of poly/oligosaccharide and synthetic polymer, i.e., poly/oligosaccharide-based BCPs, would expand the application of poly/oligosaccharide-based materials while retaining the unique characteristics of poly/oligosaccharide such as high hydrophilicity, rigidity, glass transition temperature, biocompatibility, and biodegradability.

The first synthesis of poly/oligosaccharide-based BCPs, i.e., cellulose-based BCP, was reported in the early 1960s.[12,37] As the polymerization technique has progressed, many kinds of poly/oligosaccharide-based BCPs have been synthesized, such as cellulose-*b*-polystyrene, dextran-*b*-polystyrene, maltoheptaose-*b*-poly(ε-caprolactone) etc.[1,12,38–40] These poly/oligosaccharide-based BCPs were synthesized by radical and ring-opening polymerization from a functionalized-reducing end of the poly/oligosaccharide segment. On the other hand, poly/oligosaccharides have many hydroxy groups which is incompatible with ionic polymerizations. This makes difficult to precisely synthesize poly/oligosaccharide-based BCPs.

As an alternative approach to obtain poly/oligosaccharide-based BCP, the end-to-end coupling of poly/oligosaccharide and synthetic polymer segments was reported.[41–43] The click reaction, such as azido-alkyne cycloaddition and thiol-ene reaction, was often adopted to perform the coupling reaction because it combines many merits such as mild experimental condition, functional group tolerance, high efficiency, and simplicity.[44–46]

As the application of poly/oligosaccharide-based BCPs, the nanoparticles of them have been utilized in biomedical field based on high hydrophilicity and biocompatibility of poly/oligosaccharide segment.[47,48] Importantly, the poly/oligosaccharide-based BCPs are highly fascinating as high-χ BCP to create ultrafine microphase-separated structures because of the high incompatibility between poly/oligosaccharide and hydrophobic synthetic polymer originating from the large polarity difference. The ultrafine microphase-separated structures hold great advantage for application to lithographic materials. In fact, Borsali, Isono, and Satoh et al. have synthesized many oligosaccharide-based BCPs consisting of maltooligosaccharide and hydrophobic synthetic polymers like polystyrene (PS),[49] poly(ε-caprolactone) (PCL),[19,50] poly(propylene oxide) (PPO),[51] oligodimethylsiloxane,[52] and oligoisoprene,[20,53] which achieved fine microphase-separated structures with a d of below 10 nm (**Figure 1.8**). Furthermore, interestingly, they have succeeded in forming unconventional morphologies (hexagonally perforated lamellar and *Fddd* bicontinuous structures) with ~ 7 nm scale from the BCPs containing maltooligosaccharide and oligoisoprene.[53] Sita et al. also reported the uncommon morphology that is Frank-Kasper A15 phase using cellobiose-*b*-polyolefin BCPs.[54] Therefore, the oligosaccharide-based BCPs with fine d value ($d < 10$ nm) are promising candidates for lithographic materials.

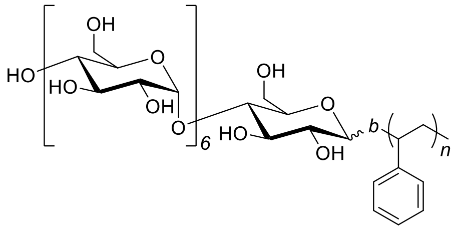

maltohexaose-*b*-PS

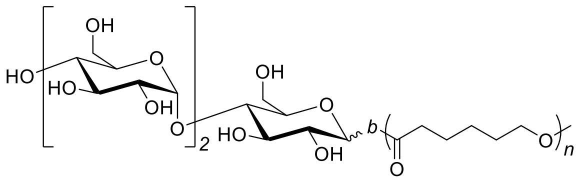

maltohexaose-*b*-PCL

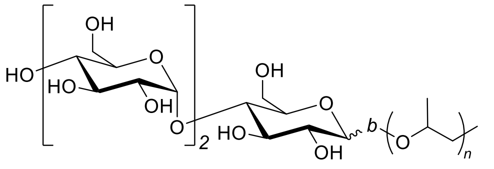

maltohexaose-*b*-PPO

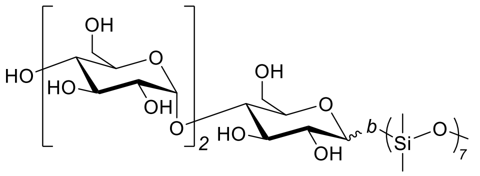

maltohexaose-*b*-oligodimethylsiloxane

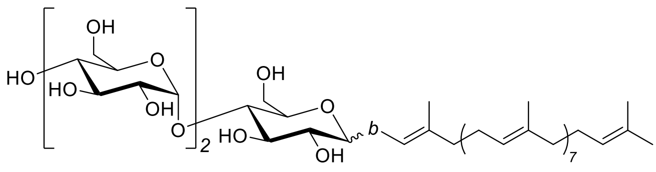

maltohexaose-*b*-oligoisoprene

Figure 1.8. Representative oligosaccharide-based high-χ BCPs forming sub-10 nm-scale microphase-separated structures.

In another fields, poly/oligosaccharides are expected to behave as outstanding hard segment of TPEs. They have high glass transition temperature ($T_g \geq 100$ °C) due to the strong hydrogen bonding resulting from many hydroxy groups.[55] Note that such T_g is comparable to that of polystyrene which is the most representative hard segment of TPE. By taking this advantage, Isono and Satoh et al. reported the BCPs consisting of maltooligosaccharide and poly(δ-decanolactone) (PDL), which showed elastomer-like behavior and mechanical properties comparable to styrenic TPEs (**Figure 1.9**).[56] This study is one of the good examples of utilizing both properties of poly/oligosaccharides and synthetic polymer as a form of BCP. More importantly, these maltooligosaccharide-based BCPs are fully bio-based, so that they also have high potential as novel sustainable TPEs to alternate with the existing styrenic TPEs.

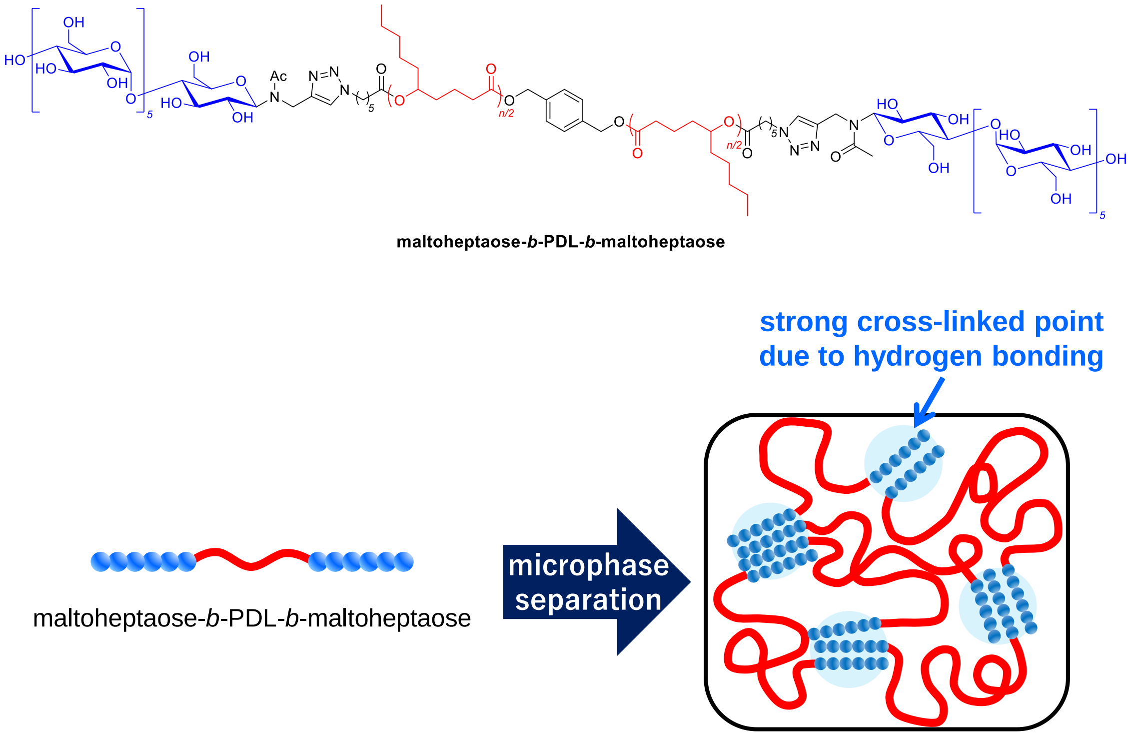

Figure 1.9. Chemical structure and schematic image of ABA-type BCPs consisting of maltooligosaccharide and PDL exhibiting elastomer-like behavior.

Matson et al tried to modify the mechanical properties of poly/oligosaccharides as another approach. They improved the brittle mechanical properties of cellulose triacetate (CTA) by blending with polybutadiene (PB) which is representative rubber polymer at room temperature. In the blend system, they added poly/oligosaccharide-based BCP, i.e., CTA-*b*-PB-*b*-CTA as a compatibilizer to enhance miscibility each other

(**Figure 1.10**).[57] As a result, they succeeded in toughening the cellulose acetate. Indeed, this research will expand the range of application of cellulose acetate. However, the PB has no biodegradability, so that this research does not utilize the merit of poly/oligosaccharide.

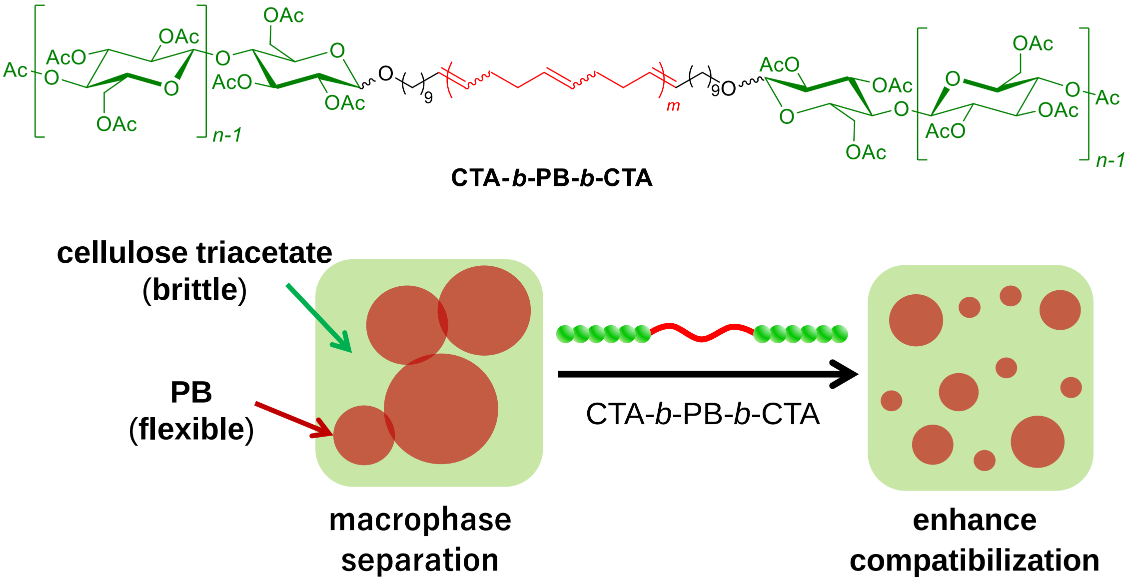

Figure 1.10. Chemical structure and schematic image of CTA-*b*-PB-*b*-CTA as compatibilizer.

Therefore, poly/oligosaccharides-based BCPs are very attracting polymers. However, perspective about poly/oligosaccharides-based BCPs towards practical applications has been lacking, though their synthesis and self-assembly behaviors have been actively studied. For example, the poly/oligosaccharides-based BCPs as lithographic materials have not been assessed in detail. In fact, there is unmet practical requirements, such as enhancement of the etching selectivity, reduction of structural defects, and variation in nanopatterning etc., in the BCP lithography.[32,58–60] In addition, most of the reported poly/oligosaccharides-based BCPs are consisting of amylose or its derivatives due to reasonable solubility and easy availability. On the other hand, amylose is important carbohydrate in food industry. Mass consumption of amylose for materials may compete with our food supply. Thus, the strategy to solve these problems related to poly/oligosaccharide-based BCPs should be established.

1.4. Objective and Outline of the Dissertation

As mentioned in Section 1.3, combining poly/oligosaccharide and synthetic polymer as a form of BCP is the effective method to expand the application potential of poly/oligosaccharide-based materials. Importantly, it is expected that the poly/oligosaccharide-based BCPs with various functions, such as etching selectivity, high elasticity, biocompatibility, and biodegradability, can be obtained by choosing appropriate synthetic polymer as the block partner. The type of poly/oligosaccharide should also influence on microphase separation behavior due to the difference in the intermolecular and intramolecular interactions, which would affect the physical properties of the poly/oligosaccharide-based BCPs.

In section 1.3, the author mentioned that it was important not only to achieve small *d* value but also to deal with other practical problems in BCP lithography process. In this dissertation, the author focused on enhancement of the etching selectivity for the poly/oligosaccharide-based BCPs. To satisfy high etching selectivity, the incorporation of inorganic segments into BCPs is one of the effective approaches. For instance, organic-inorganic BCPs, such as polydimethylsiloxane-*b*-poly(methyl methacrylate) (PDMS-*b*-PMMA),[61] poly(polyhedral oligomeric silsesquioxane methaecrylate)-*b*-poly(2,2,2-trifluoroethyl methacrylate) (PMAPOSS-*b*-PTEFMA),[62] polylactide-*b*-polydimethylsiloxane-*b*-polylactide (PLA-*b*-PDMS-*b*-PLA),[63] polyisoprene-*b*-

polyferrocenylsilane (PI-*b*-PFS)[64] etc.,[58] were designed to enhance etching selectivity (**Figure 1.11**). As mentioned in the section 1.3, the oligosaccharide-based BCPs are one of the promising candidates as high-χ BCP, so that the BCPs composed of oligosaccharide and inorganic polymer will succeed in achieving both small d value ($d < 10$ nm) and high etching selectivity, which supports the high potential as practical lithographic material.

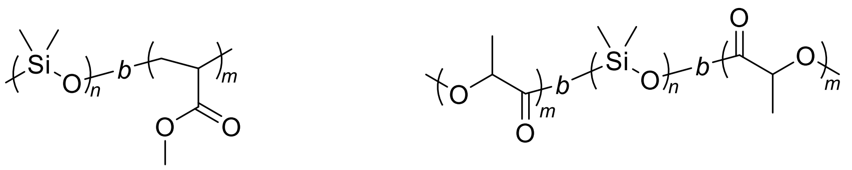

PDMS-*b*-PMMA **PLA-*b*-PDMS-*b*-PLA**

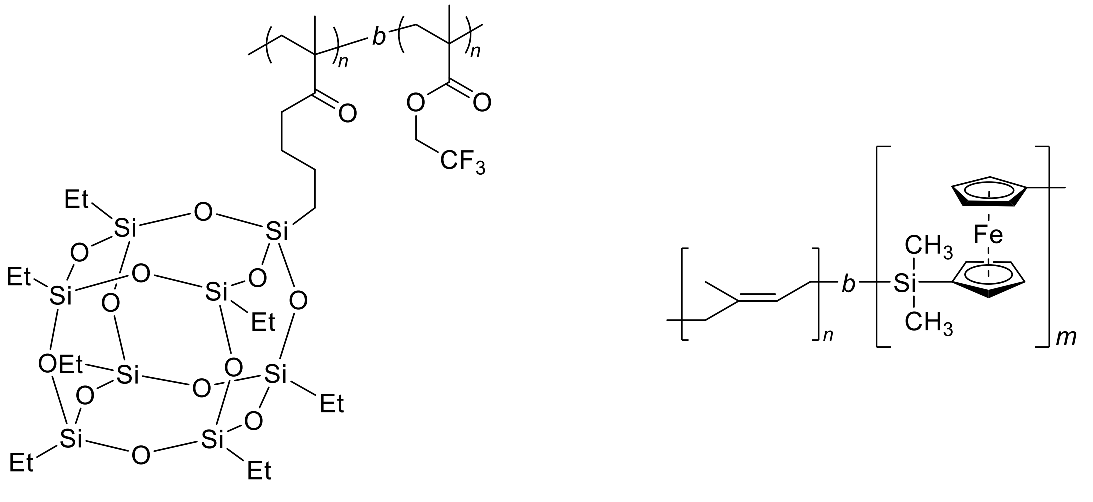

PMAPOSSS-*b*-PTFEMA **PI-*b*-PFS**

Figure 1.11. Representative organic-inorganic BCPs exhibiting high etching selectivity.

The poly/oligosaccharides are environmentally friendly material; however, they are important food resources for human, as mentioned in the section 1.3. Thus, the author focuses on cellulose (and its derivatives) because it can be obtained from inedible resources. Cellulose is insoluble in common organic solvents and cannot be subjected to melt processing due to strong intra- and intermolecular hydrogen bonding,[65] which limits the application and makes the precise synthesis of cellulose-based BCPs difficult. On the other hand, the cellulose-based BCPs are highly expected to exhibit interesting microphase separation behavior based on the strong intermolecular interactions of cellulose segment. Furthermore, cellulose is also the most abundant and renewable resources, so that it is significant to expand the application of cellulose-based materials.

The primary objective of this dissertation is designing and precisely synthesizing versatile poly/oligosaccharide-based BCPs for functional material applications. First, the author designed the novel BCP consisting of oligosaccharide and metallopolymer, i.e., maltooligosaccharide-*b*-poly(vinyl ferrocene) (PVFc) to achieve both small *d* value and improved etching selectivity for the next generation lithographic materials. The author next designed the cellulose-based BCPs. Above all, as next generation sustainable TPEs for alternating with conventional styrenic TPEs, the cellulose acetate-*b*-PDL-*b*-cellulose acetate was synthesized. Note that the author chose the PDL whose monomer, δ-decnolactone, is obtained from a plant as a middle segment to make fully bio-based TPEs. In addition, the author focused on the degree of substitution (DS) of cellulose acetate, which is the important factor governing the physical properties such as solubility and thermal properties.[66,67] Here, the author hypothesized that the cellulose-based TPEs could be more toughened by tuning the DS. Thus, the cellulose-based TPEs with various DS was synthesized and their physical properties were compared. Finally, the oligosaccharide-based BCPs consisting of cellulose acetate and poly(ε-caprolactone) (PCL) were synthesized for compatibilizer application. Cellulose acetate has biodegradability; however, it is too brittle, resulting in limits its application as mentioned in section 1.3. In this dissertation, the author aimed to improve the mechanical properties of cellulose acetate by blending PCL which is flexible and biodegradable polymer. To realize compatibilization, the BCPs consisting of cellulose acetate and PCL were added to this blend system. Four compatibilizers with different molecular weight and polymer structures were precisely synthesized and their compatibility ability was assessed.

An outline of this dissertation is as follows:

Chapter 2 describes novel high-χ BCPs comprising PVFc and an oligosaccharide (maltotriose and maltohexaose), which simultaneously accomplish small *d* values, sufficient thermal stability, and high etching selectivity (**Figure 1.12**). These novel BCPs, which displayed different architectures and oligosaccharide volume fractions, were synthesized by combining living anionic polymerization and the “click” reaction. Small angle X-ray scattering (SAXS) measurement revealed that PVFc-*b*-maltohexaose and PVFc-*b*-(maltotriose)$_2$ formed hexagonal cylinder morphology with *d* values of ~8 nm. Furthermore, lamellar morphology with *d* values of 9.3 nm was realized by mixing PVFc-*b*-(maltotriose)$_2$ and glucose. The thermal properties and etching resistance of PVFc and the oligosaccharides were also investigated. As expected, PVFc displayed a high thermal stability (PVFc: T_g, ~140 °C and decomposition temperature, ~350 °C) and higher etching resistance than the oligosaccharides.

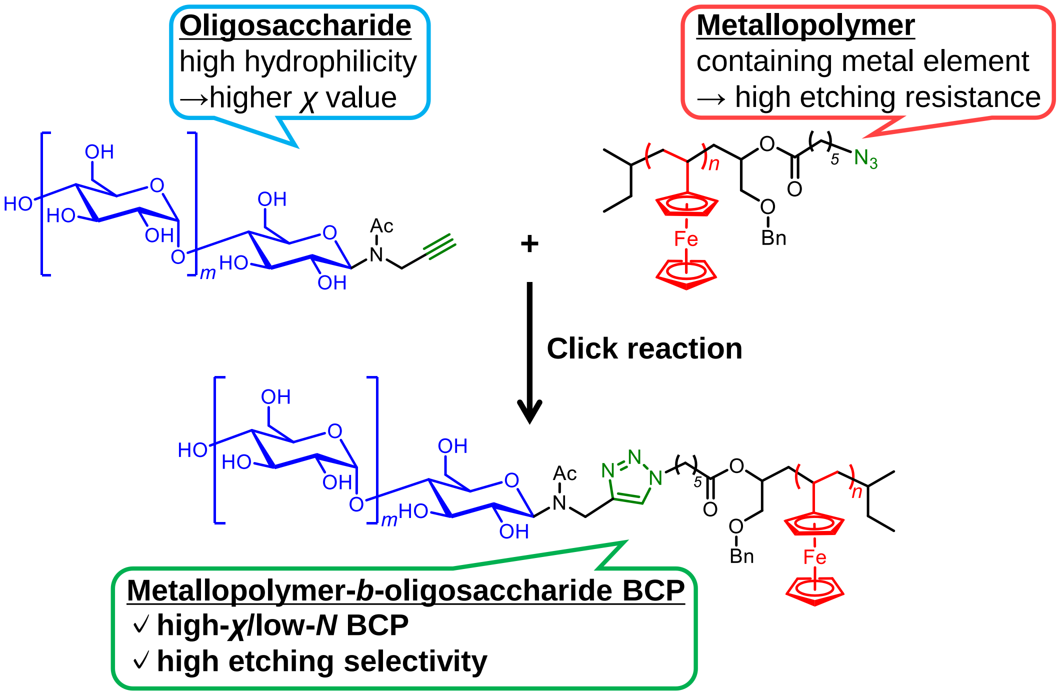

Figure 1.12. Schematic representation of high-χ BCPs comprising PVFc and oligosaccharide for accomplishing both small *d* values and high etching selectivity.

Chapter 3 describes the investigation of the microphase-separation behavior and mechanical properties of cellulose- and amylose-based BCPs (**Figure 1.13**). Various cellooligosaccharide triacetate-*b*-PDL-*b*-cellooligosaccharide triacetates (AcCel$_n$-*b*-PDL-*b*-AcCel$_n$s), which are cellulose-based ABA-type BCPs, with PDL molecular weights of approximately 5, 10, and 20 kg mol^{-1} and PDL volume fractions of 0.65, 0.77, and 0.87, were synthesized from *α*,*ω*-diazido-end-functionalized PDLs and propargyl-end-functionalized cellooligosaccharide triacetates via click chemistry. To synthesize the functional cellooligosaccharide segment precisely, the author adopted the cellodextrin-phosphorylase-mediated oligomerization of *α*-D-glucose-1-phosphase in the presence of a propargyl-end-functionalized cellobiose primer. The maltooligosaccharide triacetate-*b*-

PDL-*b*-maltooligosaccharide triacetate (AcMal$_n$-*b*-PDL-*b*-AcMal$_n$s) amylose counterparts were also synthesized in a similar manner. SAXS experiments and atomic force microscopy revealed that the AcCel$_n$-*b*-PDL-*b*-AcCel$_n$s are more likely to microphase-separate into ordered nanostructures compared to the AcMal$_n$-*b*-PDL-*b*-AcMal$_n$s, despite their comparable chemical compositions and molecular weights. Furthermore, the AcCel$_n$-*b*-PDL-*b*-AcCel$_n$s exhibited significantly superior mechanical performance compared to their amylose counterparts under tensile testing, with the Young's modulus and stress at break of AcCel$_n$-*b*-PDL$_{10k}$-*b*-AcCel$_n$ being 2.3- and 1.8-times higher, respectively, than those of AcMal$_n$-*b*-PDL$_{10k}$-*b*-AcMal$_n$. The enhanced microphase-separation and mechanical properties of the AcCel$_n$-*b*-PDL-*b*-AcCel$_n$s were found to be attributable to the stiffness and crystalline nature of the AcCel$_n$ segments. These results demonstrate the advantages of using cellulose derivatives to synthesize novel bio-functional materials.

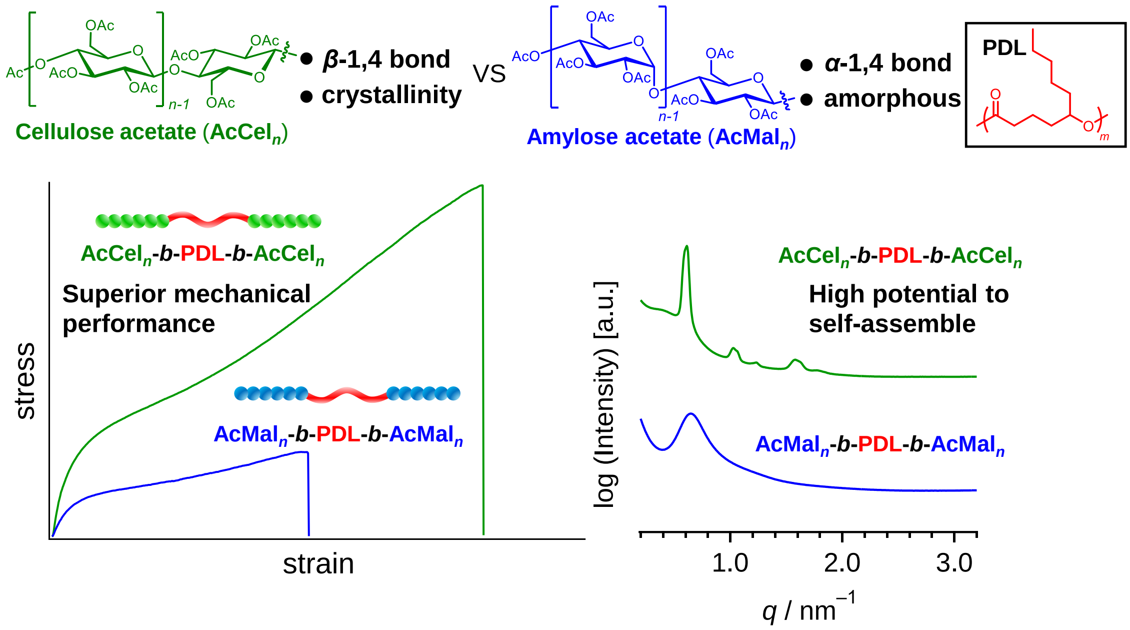

Figure 1.13. Schematic representation of comparisons of the microphase-separation behavior and mechanical properties of cellulose- and amylose-based BCPs.

Chapter 4 describes cellulose acetate-based ABA-type triblock copolymers (AcCel$_x$-*b*-PDL-*b*-AcCel$_x$) containing a celloologosaccharide acetate hard A segment (AcCel$_x$, where x is the DS; x = 3.0, 2.6, and 2.3) and PDL soft B segment (**Figure 1.14**). SAXS showed that decreasing the DS of AcCel$_x$-*b*-PDL-*b*-AcCel$_x$ resulted in a more ordered microphase-separated structure. Owing to the microphase separation of the hard cellulosic and soft PDL segments, all the AcCel$_x$-*b*-PDL-*b*-AcCel$_x$ samples exhibited elastomer-like properties. Moreover, the decrease in the DS was found to improve toughness and suppress the stress relaxation. Furthermore, preliminary, biodegradation tests in an aqueous environment revealed that the decrease in the DS endowed AcCel$_x$-*b*-PDL-*b*-AcCel$_x$ with higher biodegradability potential. This study demonstrates the usefulness of cellulose acetate-based TPEs as next generation sustainable materials.

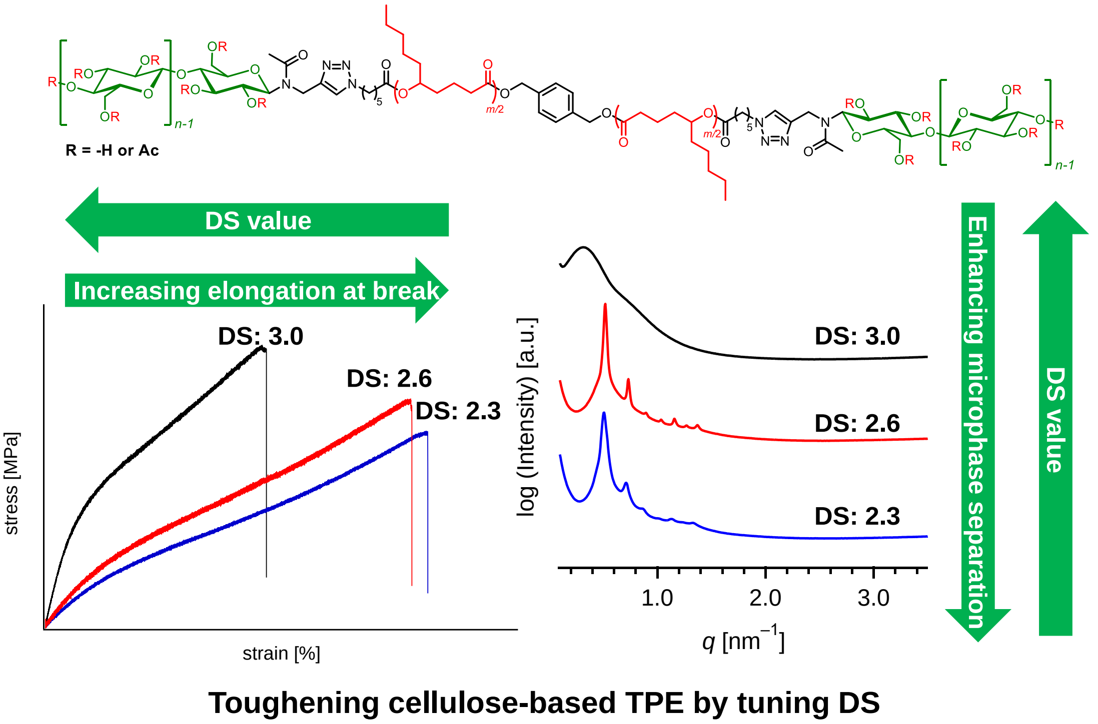

Figure 1.14. Schematic representation of investigation of cellulose-based BCPs for enhancing microphase separation and improving mechanical properties by tuning the DS.

Chapter 5 describes BCP consisting of cellulose acetate and PCL with various polymer architecture for application as a compatibilizer for cellulose acetate/PCL-blend (**Figure 1.15**). Tensile tests revealed that the cellulose acetate/PCL/BCP-blended films were superior to that of simple CTA/PCL-blended film, which indicates that the synthesized BCPs functioned as the compatibilizer. In particular, the toughness of cellulose acetate/PCL/BCP-blended film was improved in factor of up to 3.7 times when compared with the simple cellulose acetate/PCL-blended film. Interestingly, the author found that the mechanical properties of cellulose acetate/PCL/BCP-blended films depended on the polymer architecture of the added compatibilizer. The author successfully synthesized cellulose-based BCPs with versatile polymer architectures and modified effectively the physical properties of cellulose acetate, which expand the application of cellulose acetate as new sustainable materials.

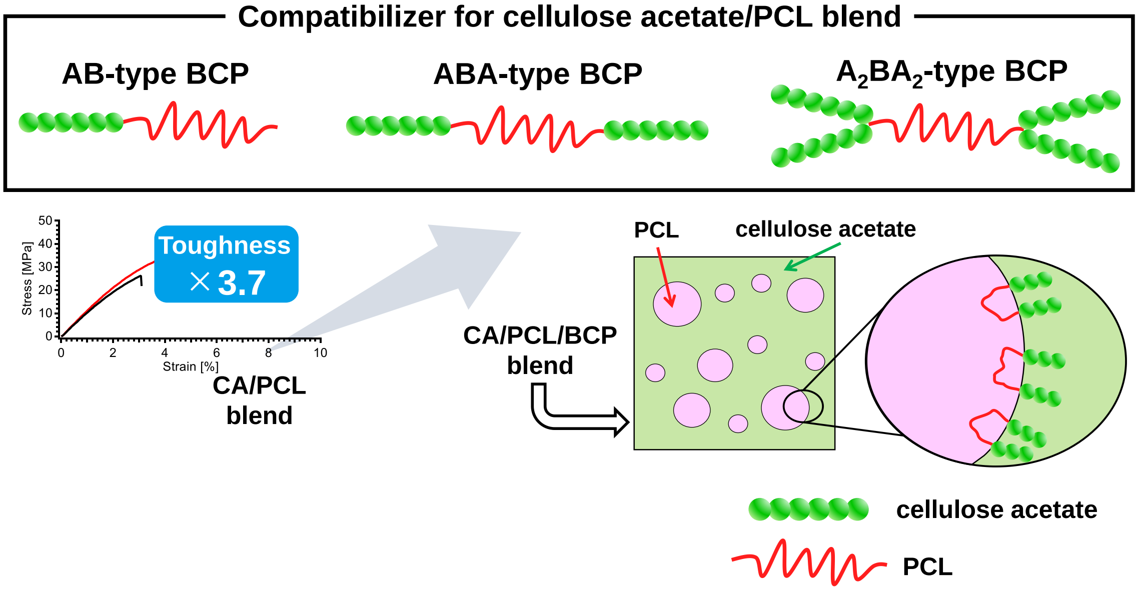

Figure 1.15. Schematic representation of investigation of BCPs consisting of cellulose acetate and PCL with various polymer architecture as a compatibilizer.

The concluding Chapter 6 summarizes the oligosaccharide-based BCPs for applying to versatile functional materials.

1.5. References

(1) Volokhova, A. S.; Edgar, K. J.; Matson, J. B. Polysaccharide-containing block copolymers: synthesis and applications. *Mater. Chem. Front.* **2020**, *4*, 99–112.

(2) Edgar, K. J.; Buchanan, C. M.; Debenham, J. S.; Rundquist, P. A.; Seiler, B. D.; Shelton, M. C.; Tindall, D. Advances in cellulose ester performance and applicaton. *Prog. Polym. Sci.* **2001**, *26*, 1605–1688.

(3) García-González, C. A.; Alnaief, M.; Smirnova, I. Polysaccharide-based aerogels-Promising biodegradable carriers for drug delivery systems. *Carbohydr. Polym.* **2011**, *86*, 1425–1438.

(4) Kobayashi, H.; Suzuki, Y.; Sagawa, T.; Saito, M.; Fukuoka, A. Selective Synthesis of Oligosaccharides by Mechanochemical Hydrolysis of Chitin over a Carbon-Based Catalyst. *Angew. Chem. Int. Ed.* **2023**, *62*, e202214229.

(5) Arca, H. C.; Mosquera-Giraldo, L. I.; Bi, V.; Xu, D.; Taylor, L. S.; Edgar, K. J. Pharmaceutical Applications of Cellulose Ethers and Cellulose Ether Esters. *Biomacromolecules* **2018**, *19*, 2351–2376.

(6) Edgar, K. J. Cellulose esters in drug delivery. *Cellulose* **2007**, *14*, 49–64.

(7) Roy, D.; Semsarilar, M.; Guthrie, J. T.; Perrier, S. Cellulose modification by polymer grafting: a review. *Chem. Soc. Rev.* **2009**, *38,* 2046–2064.

(8) Zhu, Y.; Romain, C.; Williams, C. K. Sustainable Polymers from Renewable Resources. *Nature* **2016**, *540,* 354–362.

(9) Bozell, J. J.; Petersen, G. R. Technology development for the production of biobased products from biorefinery carbohydrates—the US Department of Energy’s “Top 10” revisited. **2010**, *12*, 539–554.

(10) Esposito, D.; Antonietti, M. Redefining biorefinery: the search for unconventional building blocks for materials. *Chem. Soc. Rev.* **2015**, *44*, 5821–5835.

(11) Erdal, N. B.; Hakkarainen, M. Degradation of Cellulose Derivatives in Laboratory, Man-Made, and Natural Environments. *Biomacromolecules* **2022**, *23,* 2713–2729.

(12) Schatz, C.; Lecommandoux, S. Polysaccharide-Containing Block Copolymers: Synthesis, Properties and Applications of an Emerging Family of Glycoconjugates. *Macromol. Rapid Commun.* **2010**, *31*, 1664–1684.

(13) Nouvel, C.; Frochot, C.; Sadtler, V.; Dubois, P.; Dellacherie, E.; Six, J. L. Polylactide-Grafted Dextrans: Synthesis and Properties at Interfaces and in Solution. *Macromolecules* **2004**, *37*, 4981–4988.

(14) Palumbo, F. S.; Pitarresi, G.; Mandracchia, D.; Tripodo, G.; Giammona, G. New graft copolymers of hyaluronic acid and polylactic acid: Synthesis and characterization. *Carbohydr. Polym.* **2006**, *66*, 379–385.

(15) Colinet, I.; Dulong, V.; Hamaide, T.; Le Cerf, D.; Picton, L. New amphiphilic

modified polysaccharides with original solution behaviour in salt media. *Carbohydr. Polym.* **2009**, *75*, 454–462.

(16) Maruyama, A.; Ishihara, T.; Kim, J.-S.; Kim, S. W.; Akaike, T. Nanoparticle DNA Carrier with Poly(L-Lysine) Grafted Polysaccharide Copolymer and Poly(D,L-Lactic Acid). *Bioconjug. Chem.* **1997**, *8*, 735–742.

(17) Asayama, S.; Nogawa, M.; Takei, Y.; Akaike, T.; Maruyama, A. Synthesis of Novel Polyampholyte Comb-Type Copolymers Consisting of a Poly(L-Lysine) Backbone and Hyaluronic Acid Side Chains for a DNA Carrier. *Bioconjug. Chem.* **1998**, *9*, 476–481.

(18) Östmark, E.; Nyström, D.; Malmström, E. Unimolecular Nanocontainers Prepared by ROP and Subsequent ATRP from Hydroxypropylcellulose. *Macromolecules* **2008**, *41*, 4405–4415.

(19) Isono, T.; Kawakami, N.; Watanabe, K.; Yoshida, K.; Otsuka, I.; Mamiya, H.; Ito, H.; Yamamoto, T.; Tajima, K.; Borsali, R.; Satoh, T. Microphase separation of carbohydrate-based star-block copolymers with sub-10 nm periodicity. *Polym. Chem.* **2019**, *10*, 1119–1129.

(20) Isono, T.; Komaki, R.; Lee, C.; Kawakami, N.; Ree, B. J.; Watanabe, K.; Yoshida, K.; Mamiya, H.; Yamamoto, T.; Borsali, R.; Tajima, K.; Satoh, T. Rapid access to discrete and monodisperse block co-oligomers from sugar and terpenoid toward ultrasmall periodic nanostructures. *Commun. Chem.* **2020**, *3*, 1–9.

(21) Aissou, K.; Otsuka, I.; Rochas, C.; Fort, S.; Halila, S.; Borsali, R. Nano-Organization of Amylose-*b*-Polystyrene Block Copolymer Films Doped with Bipyridine. *Langmuir* **2011**, *27*, 4098–4103.

(22) Matsen, M. W.; Schick, M. Stable and Unstable Phases of a Diblock Copolymer Melt. *Phys. Rev. Lett.* **1994**, *72*, 2660–2663.

(23) Matsen, M. W. Effect of Architecture on the Phase Behavior of AB-Type Block Copolymer Melts. *Macromolecules* **2012**, *45*, 2161–2165.

(24) Ohta, T.; Kawasaki, K. Equilibrium Morphology of Block Copolymer Melts. *Macromolecules* **1990**, *23*, 4006–4019.

(25) Chuang, T.-H.; Chiang, Y.-C.; Hsieh, H.-C.; Isono, T.; Huang, C.-W.; Borsali, R.; Satoh, T.; Chen, W.-C. Nanostructure- and Orientation-Controlled Resistive Memory Behaviors of Carbohydrate-*block*-Polystyrene with Different Molecular Weights via Solvent Annealing. *ACS Appl. Mater. Interfaces* **2020**, *12*, 23217–23224.

(26) Hung, C.-C.; Nakahira, S.; Chiu, Y.-C.; Isono, T.; Wu, H.-C.; Watanabe, K.; Chiang, Y.-C.; Takashima, S.; Borsali, R.; Tung, S.-H.; Satoh, T.; Chen, W.-C. Control over Molecular Architectures of Carbohydrate-Based Block Copolymers for Stretchable Electrical Memory Devices. *Macromolecules* **2018**, *51*, 4966–4975.

(27) Yu, Y.-G.; Chae, C.-G.; Kim, M.-J.; Seo, H.-Bin; Grubbs, R. H.; Lee, J.-S. Precise Synthesis of Bottlebrush Block Copolymers from *ω*-End-Norbornyl Polystyrene and Poly(4-*tert*-butoxystyrene) via Living Anionic Polymerization and Ring-Opening Metathesis Polymerization. *Macromolecules* **2018**, *51*, 447–455.

(28) Stefik, M.; Guldin, S.; Vignolini, S.; Wiesner, U.; Steiner, U. Block copolymer self-assembly for nanophotonics. *Chem. Soc. Rev.* **2015**, *44*, 5076–5091.

(29) Dorin, R. M.; Sai, H.; Wiesner, U. Hierarchically Porous Materials from Block Copolymers. *Chem. Mater.* **2014**, *26*, 339–347.

(30) Cummins, C.; Ghoshal, T.; Holmes, J. D.; Morris, M. A. Strategies for Inorganic Incorporation using Neat Block Copolymer Thin Films for Etch Mask Function and Nanotechnological Application. *Adv. Mater.* **2016**, *28*, 5586–5618.

(31) Kim, B. H.; Kim, J. Y.; Kim, S. O. Directed self-assembly of block copolymers for universal nanopatterning. *Soft Matter* **2013**, *9*, 2780–2786.

(32) Bates, C. M.; Maher, M. J.; Janes, D. W.; Ellison, C. J.; Willson, C. G. Block Copolymer Lithography. *Macromolecules* **2014**, *47*, 2–12.

(33) Maji, P.; Naskar, K. Styrenic block copolymer-based thermoplastic elastomers in smart applications: Advances in synthesis, microstructure, and structure–property relationships—A review. *J. Appl. Polym. Sci.* **2022**, *139*, e52942.

(34) Schacher, F. H.; Rupar, P. A.; Manners, I. Functional Block Copolymers: Nanostructured Materials with Emerging Applications. *Angew. Chem. Int. Ed.* **2012**, *51*, 7898–7921.

(35) Koning, C.; Van Duin, M.; Pagnoulle, C.; Jerome, R. STRATEGIES FOR COMPATIBILIZATION OF POLYMER BLENDS. *Prog. Polym. Sci.* **1998**, *23*, 707–757.

(36) Self, J. L.; Zervoudakis, A. J.; Peng, X.; Lenart, W. R.; Macosko, C. W.; Ellison, C. J. Linear, Graft, and Beyond: Multiblock Copolymers as Next-Generation Compatibilizers. *JACS Au* **2022**, *2*, 310–321.

(37) Ceresa, R. J. The Synthesis of Block and Graft Copolymers of Cellulose and its Derivatives. *Polymer* **1961**, *2*, 213–219.

(38) Yagi, S.; Kasuya, N.; Fukuda, K. Synthesis and characterization of cellulose-*b*-polystyrene. *Polym. J.* **2010**, *42*, 342–348.

(39) Houga, C.; Meins, J.-F. Le; Borsali, R.; Taton, D.; Gnanou, Y. Synthesis of ATRP-induced dextran-*b*-polystyrene diblock copolymers and preliminary investigation of their self-assembly in water. *Chem. Commun.* **2007**, *29*, 3063–3065.

(40) Li, B.-G.; Zhang, L.-M. Synthesis and characterization of novel amphiphilic block copolymers based on maltoheptaose and poly(ε-caprolactone). *Carbohydr. Polym.* **2008**, *74*, 390–395.

(41) Otsuka, I.; Fuchise, K.; Halila, S.; Fort, S.; Aissou, K.; Pignot-Paintrand, I.; Chen,

Y.; Narumi, A.; Kakuchi, T.; Borsali, R. Thermoresponsive Vesicular Morphologies Obtained by Self-Assemblies of Hybrid Oligosaccharide-*block*-Poly(*N*-isopropylacrylamide) Copolymer Systems. *Langmuir* **2010**, *26*, 2325–2332.

(42) Schatz, C.; Louguet, S.; Meins, J. F. Le; Lecommandoux, S. Polysaccharide-*block*-polypeptide Copolymer Vesicles: Towards Synthetic Viral Capsids. *Angew. Chem. Int. Ed.* **2009**, *48*, 2572–2575.

(43) Halila, S.; Manguian, M.; Fort, S.; Cottaz, S.; Hamaide, T.; Fleury, E.; Driguez, H. Syntheses of Well-Defined Glyco-Polyorganosiloxanes by “Click” Chemistry and their Surfactant Properties. *Macromol. Chem. Phys.* **2008**, *209*, 1282–1290.

(44) Worrell, B. T.; Malik, J. A.; Fokin, V. V. Direct Evidence of a Dinuclear Copper Intermediate in Cu(I)-Catalyzed Azide-Alkyne Cycloadditions. **2010**, *340*, 457–461.

(45) Rostovtsev, V. V.; Green, L. G.; Fokin, V. V.; Sharpless, K. B. A Stepwise Huisgen Cycloaddition Process: Copper(I)-Catalyzed Regioselective “Ligation” of Azides and Terminal Alkynes. *Angew. Chem. Int. Ed.* **2002**, *41*, 2596–2599.

(46) Golas, P. L.; Matyjaszewski, K. Marrying click chemistry with polymerization: expanding the scope of polymeric materials. *Chem. Soc. Rev.* **2010**, *39*, 1338–1354.

(47) Zhang, N.; Wardwell, P. R.; Bader, R. A. Polysaccharide-Based Micelles for Drug Delivery. *Pharmaceutics* **2013**, *5*, 329–352.

(48) Zhao, Z.; Zhang, Z.; Chen, L.; Cao, Y.; He, C.; Chen, X. Biodegradable Stereocomplex Micelles Based on Dextran-*block*-Polylactide as Efficient Drug Deliveries. *Langmuir* **2013**, *29*, 13072–13080.

(49) Otsuka, I.; Zhang, Y.; Isono, T.; Rochas, C.; Kakuchi, T.; Satoh, T.; Borsali, R. Sub-10 nm Scale Nanostructures in Self-Organized Linear Di- and Triblock Copolymers and Miktoarm Star Copolymers Consisting of Maltoheptaose and Polystyrene. *Macromolecules* **2015**, *48*, 1509–1517.

(50) Otsuka, I.; Isono, T.; Rochas, C.; Halila, S.; Fort, S.; Satoh, T.; Kakuchi, T.; Borsali, R. 10 nm Scale Cylinder-Cubic Phase Transition Induced by Caramelization in Sugar-Based Block Copolymers. *ACS Macro Lett.* **2012**, *1*, 1379–1382.

(51) Mumtaz, M.; Takagi, Y.; Mamiya, H.; Tajima, K.; Bouilhac, C.; Isono, T.; Satoh, T.; Borsali, R. Sweet Pluronic poly(propylene oxide)-*b*-oligosaccharide block copolymer systems: Toward sub-4 nm thin-film nanopattern resolution. *Eur. Polym. J.* **2020**, *134*, 109831.

(52) Nishimura, T.; Katsuhara, S.; Lee, C.; Ree, B. J.; Borsali, R.; Yamamoto, T.; Tajima, K.; Satoh, T.; Isono, T. Fabrication of Ultrafine, Highly Ordered Nanostructures Using Carbohydrate-Inorganic Hybrid Block Copolymers.

Nanomaterials **2022**, *12*, 1–14.

(53) Isono, T.; Komaki, R.; Kawakami, N.; Chen, K.; Chen, H. L.; Lee, C.; Suzuki, K.; Ree, B. J.; Mamiya, H.; Yamamoto, T.; Borsali, R.; Tajima, K.; Satoh, T. Tailored Solid-State Carbohydrate Nanostructures Based on Star-Shaped Discrete Block Co-Oligomers. *Biomacromolecules* **2022**, *23*, 3978–3989.

(54) Lachmayr, K. K.; Wentz, C. M.; Sita, L. R. An Exceptionally Stable and Scalable Sugar–Polyolefin Frank–Kasper A15 Phase. *Angew. Chem. Int. Ed.* **2020**, *59*, 1521–1526.

(55) Imamura, K.; Sakaura, K.; Ohyama, K. I.; Fukushima, A.; Imanaka, H.; Sakiyama, T.; Nakanishi, K. Temperature Scanning FTIR Analysis of Hydrogen Bonding States of Various Saccharides in Amorphous Matrixes below and above Their Glass Transition Temperatures. *J. Phys. Chem. B* **2006**, *110*, 15094–15099.

(56) Isono, T.; Nakahira, S.; Hsieh, H.-C.; Katsuhara, S.; Mamiya, H.; Yamamoto, T.; Chen, W.-C.; Borsali, R.; Tajima, K.; Satoh, T. Carbohydrates as Hard Segments for Sustainable Elastomers: Carbohydrates Direct the Self-Assembly and Mechanical Properties of Fully Bio-Based Block Copolymers. *Macromolecules* **2020**, *53*, 5408–5417.

(57) Arrington, K. J.; Haag, J. V.; French, E. V.; Murayama, M.; Edgar, K. J.; Matson, J. B. Toughening Cellulose: Compatibilizing Polybutadiene and Cellulose Triacetate Blends. *ACS Macro Lett.* **2019**, *8*, 447–453.

(58) Nunns, A.; Gwyther, J.; Manners, I. Inorganic block copolymer lithography. *Polymer* **2013**, *54*, 1269–1284.

(59) Hur, S. M.; Thapar, V.; Ramírez-Hernández, A.; Nealey, P. F.; de Pablo, J. J. Defect Annihilation Pathways in Directed Assembly of Lamellar Block Copolymer Thin Films. *ACS Nano* **2018**, *12*, 9974–9981.

(60) Lee, K. S.; Lee, J.; Kwak, J.; Moon, H. C.; Kim, J. K. Reduction of Line Edge Roughness of Polystyrene-*block*-Poly(methyl methacrylate) Copolymer Nanopatterns By Introducing Hydrogen Bonding at the Junction Point of Two Block Chains. *ACS Appl. Mater. Interfaces* **2017**, *9*, 31245–31251.

(61) Luo, Y.; Montarnal, D.; Kim, S.; Shi, W.; Barteau, K. P.; Pester, C. W.; Hustad, P. D.; Christianson, M. D.; Fredrickson, G. H.; Kramer, E. J.; Hawker, C. J. Poly(dimethylsiloxane-*b*-methyl methacrylate): A Promising Candidate for Sub-10 nm Patterning. *Macromolecules* **2015**, *48*, 3422–3430.

(62) Nakatani, R.; Takano, H.; Chandra, A.; Yoshimura, Y.; Wang, L.; Suzuki, Y.; Tanaka, Y.; Maeda, R.; Kihara, N.; Minegishi, S.; Miyagi, K.; Kasahara, Y.; Sato, H.; Seino, Y.; Azuma, T.; Yokoyama, H.; Ober, C. K.; Hayakawa, T. Perpendicular Orientation Control without Interfacial Treatment of RAFT-Synthesized High-χ Block Copolymer Thin Films with Sub-10 nm Features

Prepared via Thermal Annealing. *ACS Appl. Mater. Interfaces* **2017**, *9*, 31266–31278.

(63) Rodwogin, M. D.; Spanjers, C. S.; Leighton, C.; Hillmyer, M. A. Polylactide-Poly(dimethylsiloxane)-Polylactide Triblock Copolymers as Multifunctional Materials for Nanolithographic Applications. *ACS Nano* **2010**, *4*, 725–732.

(64) Lammertink, R. G. H.; Hempenius, M. A.; Van Den Enk, J. E.; Chan, V. Z. H.; Thomas, E. L.; Vancso, G. J. Nanostructured Thin Films of Organic-Organometallic Block Copolymers: One-Step Lithography with Poly(ferrocenylsilanes) by Reactive Ion Etching. *Adv. Mater.* **2000**, *12*, 98–103.

(65) Hata, Y.; Serizawa, T. Self-assembly of cellulose for creating green materials with tailor-made nanostructures. *J. Mater. Chem. B* **2021**, *9*, 3944–3966.

(66) Kamide, K.; Saito, M. Thermal Analysis of Cellulose Acetate Solids with Tortal Degree of Substitution of 0.49, 1.75, 2.46, and 2.92. *Polym. J.* **1985**, *17*, 919–928.

(67) de Freitas, R. R. M.; Senna, A. M.; Botaro, V. R. Influence of degree of substitution on thermal dynamic mechanical and physicochemical properties of cellulose acetate. *Ind. Crops Prod.* **2017**, *109*, 452–458.

Chapter 2

Fabrication of Sub-10 nm Microphase-Separated Structures Using Metallopolymer-block-Oligosaccharide

2.1. Introduction

Block copolymers (BCPs) comprising two chemically distinct polymer segments undergo self-assembly into periodic lamellar, gyroid, cylindrical, and spherical structures with nanometer-scale periodicity in the bulk or thin film form, known as microphase-separated structures. Such nanostructures have attracted considerable attention for their potential applications in nanotechnological fields such as next-generation lithographic templates,[1–8] nanoporous material templates,[9] optical materials,[10–13] nanowire arrays,[14] and others.[15] Particularly, much research has focused on their application in lithography technology, where a microphase-separated BCP thin film on a semiconductor substrate is used as the resist material for fabricating electronic circuits. To improve the lithographic resolution, even down to the few-nanometer scale, the development of new BCPs that can achieve microphase-separated structures with extremely small domain spacings (d, <10 nm), has been an important subject in this research field. In general, d can be decreased by reducing the degree of polymerization (N) of the BCP. However, to promote phase separation, the product of χ and N must be sufficiently higher than the critical value (10.5 for a symmetric BCP), where χ is the Flory-Huggins interaction parameter and indicates the incompatibility of the two segments in the BCP.[16,17] Thus, much research has recently focused on the formation of high-χ BCPs that can microphase-separate, even with low N values, to attain d values < 10 nm.

The basic methodology to design high-χ BCPs is to combine the hydrophobic and hydrophilic polymer segments to increase incompatibility. Many reports of high-χ BCPs comprising vinyl polymer main chains, including poly(cyclohexylethylene)-*b*-poly(methyl methacrylate),[18] poly(dihydroxystyrene)-*b*-poly(styrene),[19] poly(*tert*-butylstyrene)-*b*-poly(2-vinylpyridine),[20] poly(3-hydroxystyrene)-*b*-poly(*tert*-butylstyrene),[21] poly(glycerol monomethactylate)-*b*-poly(styrene),[22] poly(hydroxyisobutylene)-*b*-poly(styrene),[22] and poly(hydroxypropylene)-*b*-poly(styrene),[23] have been published to date. In addition, Borsali and Satoh et al. have created a series of high-χ BCPs by combining hydrophobic synthetic polymers (e.g., poly(styrene), poly(*n*-butyl acrylate), poly(methyl methacrylate), poly(ε-caprolactone), and poly(δ-decanolactone)) and oligosaccharides (maltotriose and maltoheptaose), some of which successfully achieved microphase separation with d values of <10 nm.[24–29] Owing to the strong hydrophilicity and rigid chain nature of oligosaccharides, the oligosaccharide-containing BCPs easily achieve strong segregation with the combination of any type of hydrophobic polymer.

Another important challenge in the development of novel BCPs is to improve their etching selectivity and thermal stability. For application in an actual lithographic process, the etching selectivity of two blocks must be high enough to achieve pattern transfer to the underlying semiconductor substrate. To enhance the etching selectivity, high-χ BCPs comprising an inorganic segment, such as poly(dimethylsiloxane) (PDMS), polyhedral oligomeric silsesquioxane (POSS), and poly(trimethylsilylstyrene), have been developed, where the inorganic segments show higher resistance toward the etching process.[30–36] In addition, sufficient heat resistance is required for precise pattern transfer because the dry etching process is often implemented at high temperatures (~70 °C).[37] This is because a high glass transition temperature (T_g) is necessary to maintain the nanostructure of the resist material during the etching process. However, the molecular weights of high-χ BCPs for sub-10 nm microphase separation are in the range 2,200–7,000 g mol^{-1} and may lower the T_g. Thus, polymer pairs with sufficient etching selectivity and a high T_g should be employed to create new high-χ BCPs for high-resolution lithographic application.

To accommodate all these requirements in a high-χ BCP, the author envisaged a BCP system comprising a metal-containing polymer segment. Metal-containing polymers, so-called metallopolymers, are a class of inorganic polymers. Among them, ferrocene-containing polymers, such as poly(ferrocenylsilane) and poly(vinyl ferrocene) (PVFc), are the most widely studied from a synthetic and application view point. For example, Manners and Nuyken reported novel strategies to precisely synthesize ferrocene-containing polymers[38,39] and their properties have been revealed in detail.[30,40] Importantly, Vansco et al. disclosed that poly(ferrocenylsilane) presented high etching resistance due to complex oxide formation when exposed to oxygen plasma.[41] Furthermore, Nuyken, Higashihara, and Gallei reported high PVFc T_g values (~200 °C).[38,42,43] However, despite the suitable and promising properties for lithographic applications, ferrocene-containing polymers have never been applied in the design of high-χ BCPs for sub-10 nm microphase separation.

In this chapter, the author reports a novel high-χ/low-N BCP system comprising PVFc and maltooligosaccharide (maltotriose (MT) or maltohexaose (MH)) segments, which simultaneously accomplishes a small d value, sufficient thermal stability, and high etching selectivity. The author supposed that maltooligosaccharides would be the best counter block choice because of their strong hydrophilicity, high T_g, and weak etching resistance.[37] Three types of BCPs comprising PVFc and an oligosaccharide, namely the linear-type PVFc-*b*-MT and PVFc-*b*-MH and the miktoarm-type PVFc-*b*-(MT)$_2$, were synthesized *via* living anionic polymerization followed by the click reaction (**Scheme 2.1**). PVFc-*b*-MH and PVFc-*b*-(MT)$_2$ formed hexagonally close-packed cylinder structures with single nano-order *d*-spacing in the bulk and thin film states. To the best of my knowledge, this is the first to report on metallopolymer-containing BCPs with *d* values in the sub-10 nm range. In addition, sub-10 nm lamellar structures could be obtained by mixing PVFc-*b*-(MT)$_2$ and glucose. Thus, the author successfully obtained lithographically important morphologies from the novel BCP system.

Scheme 2.1. Synthesis of PVFc-*b*-MT, PVFc-*b*-MH, and PVFc-*b*-(MT)$_2$

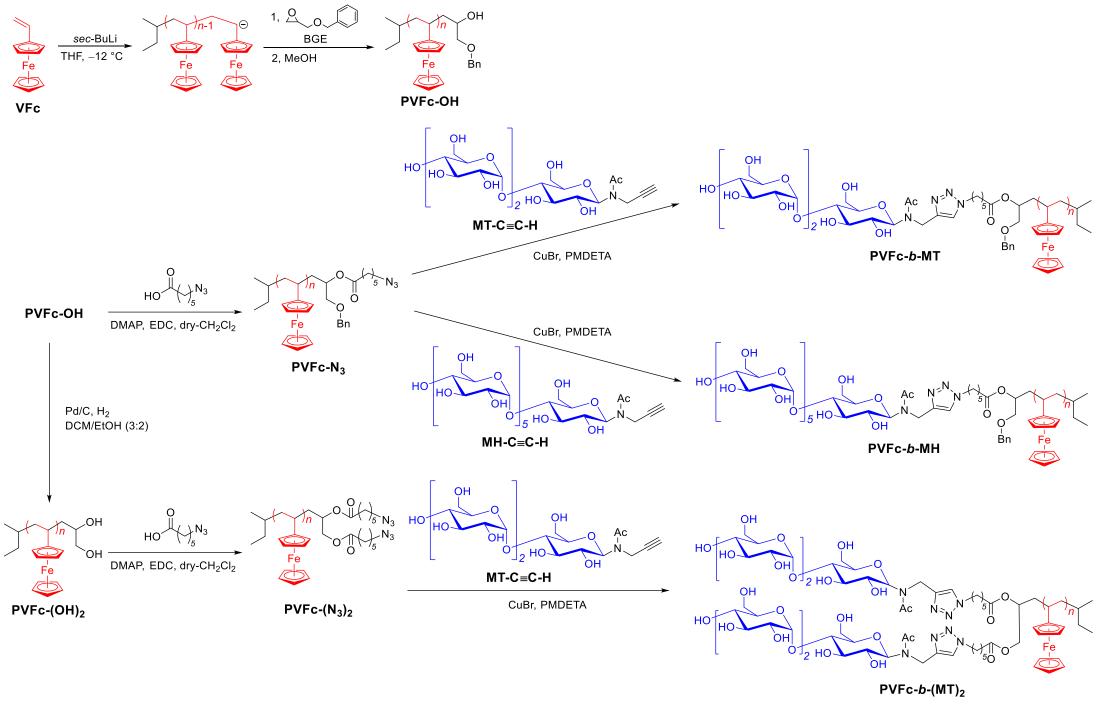

2.2. Experimental Section

2.2.1. Materials

sec-Butyllithium (*sec*-BuLi; Kanto Chemical Co., Inc. (Kanto), 1.00 mol L^{-1} in cyclohexane, *n*-hexane), CaH_2 (Kanto, >95.0%), dry MeOH (Kanto, >99.8), Palladium 10% on carbon (Pd/C; Tokyo Chemical Industry Co., Ltd (TCI), wetted with *ca*. 55% water), 4-dimethylaminopyridine (DMAP; TCI, >99.0%), 1-(3-dimethylaminopropyl)-3-ethylcarbodiimide hydrochloride (EDC · HCl; TCI, >98.0%), *N*,*N*,*N'*,*N''*,*N''*-pentamethyldiethylenetriamine, and copper(I) bromide (CuBr; Sigma-Aldrich Chemicals Co., 99.999% trace metals basis) were purchased from the commercial resources and used as received. Benzyl glycidyl ether (BGE; TCI, >97.0%) was purchased and purified by distillation over CaH_2 under vacuum. EtOH (Kanto, >99.5%) and dry DMF (Kanto, >99.5%, water content, <0.001%) were purchased and used as received. Dry CH_2Cl_2 (Kanto, >99.5%, water content, <0.001%), dry toluene (Kanto, >99.5%, water content, <0.001%) and dry THF (Kanto, >99.5%, water content, <0.001%) were further purified by an MBRAUN MB SPS Compact solvent purification system equipped with two MB-KOL-A columns (for dry CH_2Cl_2), a MB-KOL-C and a MB-KOL-A columns (for dry toluene) or a MB-KOL-A and a MB-KOL-M Type 1 columns (for dry THF), which were directly used for reactions. Vinylferrocene (VFc)[44] and 6-azidohexnoic acid[45] was synthesized according to reported methods.

2.2.2. Instruments

^{1}H NMR measurement

^{1}H NMR (400 MHz) spectra were obtained using a JEOL JNM-ESC 400 instrument at 25 °C.

Size exclusion chromatography (SEC)

The SEC measurements were performed at 40 °C in THF (flow rate, 1.0 mL min^{-1}) using a Jasco high-performance liquid chromatography system (PU-980 Intelligent HPLC Pump, CO-2065 Plus Intelligent Column Oven, RI-2031 Plus Intelligent RI Detector, and DG-2080-53 Degasser) equipped with a Shodex KF-G guard column (4.6 mm × 10 mm; particle size, 8 μm) and two Shodex KF-804L columns (linear; particle size 7 μm; 8.0 mm × 300 mm; exclusion limit, 4×10^{4}) or in DMF (flow rate, 0.6 mL min^{-1}; containing 0.01 mol L^{-1} LiCl) using a JASCO HPLC system (PU-980 Intelligent HPLC Pump, CO-965 Column Oven, RI-930 Intelligent RI Detector, and DG-2080-53 Degasser) equipped with a Shodex KD-G guard column (4.6 mm × 10 mm; particle size, 8 μm), a Shodex Asahipak GF-310 HQ column (linear; particle size, 5 μm; 7.5 mm × 300 mm; exclusion limit, 4×10^{4}) and a Shodex Asahipak GF-7 M HQ column (linear; particle size, 9 μm; 7.5 mm × 300 mm; exclusion limit, 1.0×10^{7}). The number-average molecular weight ($M_{\mathrm{n,SEC}}$) and dispersity ($Đ$) were calculated based on polystyrene standards.

Fourie transform infrared (FT-IR)

The FT-IR spectra were obtained using a PerkinElmer Frontier MIR spectrometer equipped with a single reflection diamond universal attenuated total reflection (ATR) accessory.

Differential scanning calorimetry (DSC)

DSC experiments were performed using a Hitachi DSC 7000X under nitrogen atmosphere. All the polymer samples were heated to 180 °C, cooled to 30 °C, and heated to 200 °C again at the heating and cooling rates of 10 °C min^{-1} and 20 °C min^{-1}, respectively.

Atomic force microscopy (AFM)

The AFM phase images were obtained using a Molecular Imaging PicoPlus atomic force microscope operating in the tapping mode with a silicon cantilever (Nanoworld AG, NANOSENSORS^{TM} PPP-NCH) having resonant frequency and spring constant of 190 kHz and 48 N m^{-1}, respectively. The thin films for the AFM observation were prepared by spin-coating (3,000 rpm for 60 s) the polymer solution in DMF (5 wt%) onto a Si substrate with a native oxide layer.

Small angle X-ray scattering (SAXS)

The morphology and domain-spacing (*d*) of the microphase-separated polymer samples were determined by SAXS analysis. The SAXS measurements were performed at the BL-6A beamline of the Photon Factory in the High Energy Accelerator Research

Organization (KEK, Tsukuba, Japan) using X-ray beams with λ = 0.15 nm at room temperature. The scattering data were collected by a 2D detector (a PILATUS3 1M detector (Dectris Ltd.)), where the samples-to-detector distance was set to be 1.5 m. The scattering angle (θ) was calibrated using silver behenate (Nagara Science Co., Ltd) as the standard and derived the scattering vector (q) from Bragg's equation ($q = (4\pi/\lambda)\sin(\theta/2)$). The d value was calculated by $d = 2\pi/q^*$ (q^* is principal scattering peak position.). Before the experiment, the powder samples of the block copolymers (BCPs) was placed in a glass capillary with an inner diameter of 1.5 mm and annealed under vacuum at 180 °C for 1 h, which were subjected to the SAXS measurement at room temperature.

Reactive ion etching (RIE)

Investigation of etching resistance of homopolymer thin films was performed using Samco RIE-10NRV. The thin film samples of PVFc were prepared by spin-coating (2,000 rpm for 60 s) the polymer solution in toluene (5 wt%) onto Si substrate with a native oxide layer. The thin film samples of maltotriose were prepared by spin-coating (3,000 rpm for 120 s) the DMF/MeOH (90/10 w/w) solution onto a Si substrate treated with air plasma. The samples of PVFc and MT were etched in O_2 plasma for 5, 10, 20, and 30 s with 80 W applied RF power at 10 Pa and 75 sccm. The film thickness of the samples before and after the etching were measured by ellipsometry (JASCO M-500S) to determine the etching depth.

2.2.3. Synthetic details

Synthesis of one ω-end hydroxy-functionalized poly(vinyl ferrocene) (PVFc–OH) [44,46,47]

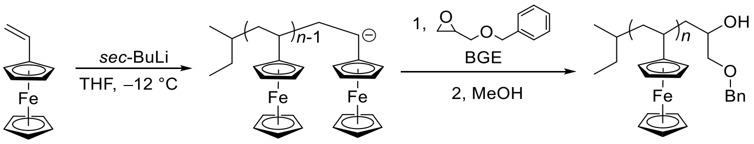

VFc was dissolved in dry toluene and stirred with CaH_2 overnight. After removing the solvent, the solid was purified by sublimation and the purified VFc was stored in the glovebox. In the glovebox, the purified VFc (2.78g, 13.1 mmol) and dry THF (73 mL) were placed in separate Schlenk flasks, then the flasks were sealed with a grease-less valve. After these Schlenk flasks were taken out from the glovebox, a little of *sec*-BuLi was added to the dry THF to completely remove impurities. Then, the dry THF was transferred to the VFc-containing Schlenk flask by trap-to-trap distillation. After cooling to −12 °C, *sec*-BuLi (728 μL, 0.728 mmol as a 1.00 mol L^{-1} stock solution in cyclohexane, *n*-hexane) was added to the monomer solution to initiate the polymerization under Ar atmosphere. After stirring for 50 min, benzyl glycidyl ether (BGE) was added to the solution. This mixture was stirred for 2 h at −12 °C and an additional overnight at room temperature. Then, a little of dry MeOH was added to the solution, then the mixture was stirred for 2 h. The reaction mixture was reprecipitated into cold MeOH to give PVFc–OH as a yellow powder. Yield: 1.83 g (65.8%)

^{1}H NMR (400 MHz, $CDCl_3$): δ (ppm) 7.47–7.22 (m, BGE aromatic), 4.66–3.44 (br, PVFc aromatic –C*H*), 2.86–0.50 (br, PVFc backbone –CH_2–C*H*–)

Synthesis of two *ω*-ends hydroxy-functionalized poly(vinyl ferrocene) (PVFc–(OH)$_2$) [46,47]

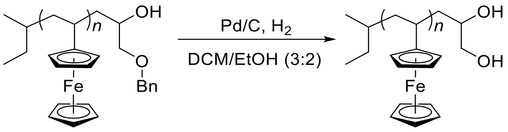

The obtained PVFc–OH (597.4 mg, 187 μmol), Pd/C (59.4 mg), dry CH_2Cl_2 (39 mL), and EtOH (26 mL) were placed in a flask. The flask was filled with H_2 gas and this mixture was stirred for 4 days at room temperature. This reaction mixture was filtered over celite to remove the catalyst, and the solvent was removed under reduced pressure. The resulting residue was dissolved in CH_2Cl_2 and reprecipitated to cold MeOH to give PVFc–(OH)$_2$ as a yellow powder. Yield: 420 mg (72.3%)

^{1}H NMR (400 MHz, $CDCl_3$): δ (ppm) 4.64–3.04 (br, PVFc aromatic –C*H*), 2.75–0.51 (br, PVFc backbone –C*H*$_2$–C*H*–)

Synthesis of one *ω*-end azido-functionalized poly(vinylferrocene) (PVFc–N$_3$)

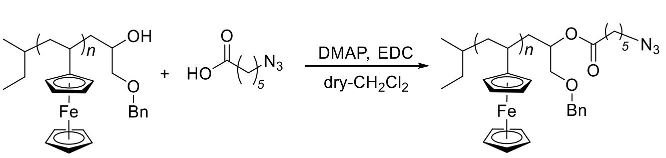

A typical procedure of the synthesis of PVFc–N$_3$ is as follows (method A): Prior to the reaction, the obtained PVFc–OH was subjected to coevaporation with dry toluene to remove any trace of MeOH. PVFc–OH (604.0 mg, 189 μmol), DMAP (115.8 mg, 948 μmol), EDC·HCl (256.9 mg, 1.34 mmol), 6-azidohexanoic acid (194.9 mg, 1.24 mmol), and dry CH_2Cl_2 (24 mL) were placed in a vial bottle. After stirring for 5 days at room temperature, the mixture was reprecipitated to cold MeOH, giving PVFc–N_3 as a yellow powder. Yield: 610 mg (96.7%)

^{1}H NMR (400 MHz, $CDCl_3$): δ (ppm) 7.43–7.20 (m, BGE aromatic), 4.62–3.12 (br, PVFc aromatic –C*H*), 3.29–3.12 (br, –C$H_2$$N_3$). 2.83–0.48 (br, PVFc backbone –CH_2–C*H*–)

Synthesis of two *ω*-ends azide-functionalized poly(vinyl ferrocene) (PVFc–(N_3)$_2$)

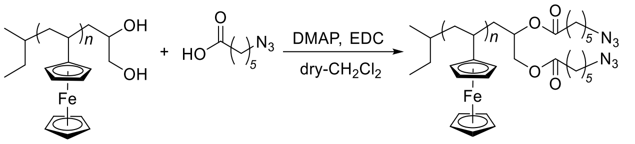

Method A was applied for PVFc–(OH)$_2$ (369.6 mg, 119 µmol), DMAP (128.8 mg, 1.05 mmol), EDC·HCl (261.9 mg, 1.37 mmol), 6-azidohexanoic acid (194.9 mg, 1.24 mmol), and dry CH_2Cl_2 (20 mL) at room temperature for 10 days to give PVFc–(N_3)$_2$ as a yellow powder. Yield: 340 mg (84.4%)

^{1}H NMR (400 MHz, $CDCl_3$): δ (ppm) 4.60–3.10 (br, PVFc aromatic –C*H*), 3.35–3.17 (br, –C$H_2$$N_3$). 2.75–0.51 (br, PVFc backbone –CH_2–C*H*–)

Synthesis of linear poly(vinyl ferrocene)-*block*-maltotriose (PVFc-*b*-MT)

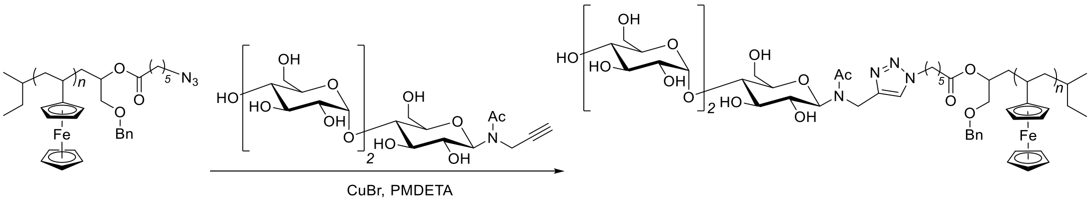

A typical procedure for the click reaction is as follows (Method B): PVFc–N_3

(421.8 mg, 127 μmol), *N*-maltotriosyl-3-acetamido-1-propyrene (MT–C≡CH; 96.8 mg, 166 μmol), and CuBr (24.8 mg, 173 μmol) were added in a Schlenk flask. A solution of *N*,*N*,*N*',*N*'',*N*''-pentamethyldiethylenetriamine (PMDETA; 34.2 μL, 164 μmol) in a mixed solvent of THF (8 mL) and DMF (8 mL) was transferred to the Schlenk flask under Ar atmosphere after degassing by Ar bubbling. After stirring at 60 °C for 3 days, Dowex® 50WX2 was added to remove the Cu catalyst. After removing the Dowex by filtration, the solution was reprecipitated to a mixed solvent of acetonitrile and water (acetonitrile/water = 7/3 (v/v)) to give PVFc-*b*-MT as an orange powder. Yield: 430 mg (86.8%)

^{1}H NMR (400 MHz, DMF-d_7): δ (ppm) 8.34–7.92, 7.75 (rotamers, triazole methine), 7.52–7.22 (br, m, BGE aromatic), 6.06, 5.92–5.52, 5.25–4.56 (sugar protons), 4.85–2.96 (br, PVFc aromatic –C*H*), 2.95–0.14 (br, PVFc backbone –C*H*$_2$–C*H*–)

Synthesis of linear poly(vinyl ferrocene)-*block*-maltohexaose (PVFc-*b*-MH)

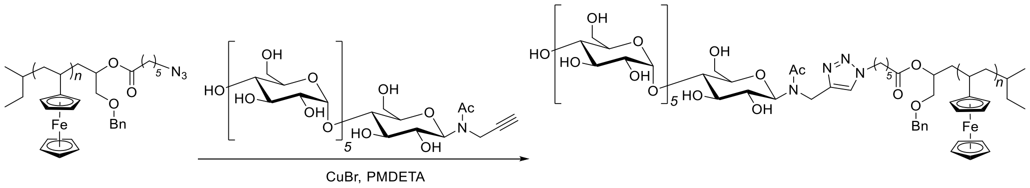

Method B was used applied for PVFc–(N$_3$)$_2$ (84.0 mg, 25.2 μmol), *N*-maltohexaosyl-3-acetamido-1-propyne (MH–C≡CH; 37.0 mg, 346 μmol), CuBr (4.8 mg, 33.5 μmol), *N*,*N*,*N*',*N*'',*N*''-pentamethyldiethylenetriamine (PMDETA; 6.8 μL, 32.8 μmol) in a mixed solvent of THF (5 mL) and DMF (5 mL) at 60 °C for 4 days to give PVFc-*b*-MH as a brown powder. Yield: 50 mg (41%)

^{1}H NMR (400 MHz, DMF-d_7) : δ (ppm) 8.34–8.10, 7.76, 7.71–7.64 (rotamers, triazole methine), 7.52–7.24 (br, m, BGE aromatic), 6.12–6.05, 6.01–5.54, 5.21–4.58 (sugar protons), 4.81–3.15 (br, PVFc aromatic –C*H*), 3.14–0.54 (br, PVFc backbone –CH_2–C*H*–)

Synthesis of miktoarm shape poly(vinyl ferrocene)-*block*-maltotriose (PVFc-*b*-(MT)$_2$)

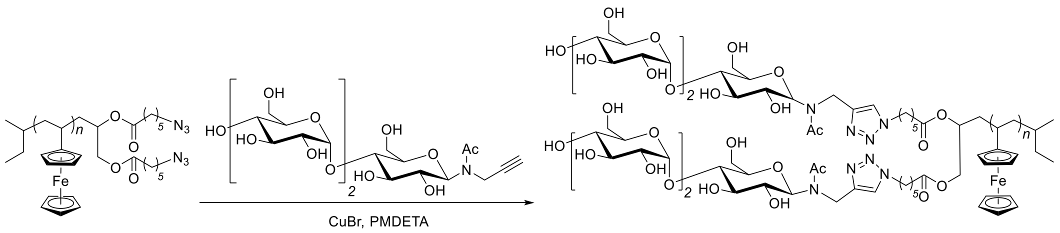

Method B was used applied for PVFc–(N_3)$_2$ (270 mg, 79.9 μmol), *N*-maltotriosyl-3-acetamido-1-propyrene (MT–C≡CH; 114.9 mg, 197 μmol), CuBr (28.0 mg, 195 μmol), *N*,*N*,*N*’,*N*”,*N*”-pentamethyldiethylenetriamine (PMDETA; 7 μL, 33.5 μmol) in a mixed solvent of THF (8.5 mL) and DMF (8.5 mL) at 60 °C for 4 days to give PVFc-*b*-(MT)$_2$ as a brown powder. Yield: 300 mg (82.5%)

^{1}H NMR (400 MHz, DMF-d_7) : δ (ppm) 8.34–7.92, 7.7 (rotamers, triazole methine), 7.52–7.22 (br, m, BGE aromatic), 6.07, 5.94–5.56, 5.25–4.57 (sugar protons), 4.85–3.18 (br, PVFc aromatic –C*H*), 3.16–0.51 (br, PVFc backbone –CH_2–C*H*–)

2.3. Results and Discussion

2.3.1. Synthesis of PVFc-*b*-MT, PVFc-*b*-MH, and PVFc-*b*-(MT)$_2$

The synthetic routes of PVFc-*b*-MT, PVFc-*b*-MH, and PVFc-*b*-(MT)$_2$ are illustrated in **Scheme 2.1**. First, PVFc possessing a hydroxyl group (PVFc–OH) at the ω-chain end was prepared by living anionic polymerization of vinylferrocene (VFc) followed by termination with benzyl glycidyl ether (BGE), according to previously reported methods.[46,47] To obtain PVFc–OH with a target number-average molecular weight (M_n) of ~3,000 g mol^{-1}, the polymerization of VFc was conducted at the $[\mathrm{VFc}]_0/[sec\text{-BuLi}]_0$ ratio of 18/1. BGE was added when the monomer conversion (conv.) reached 80%, so that the theoretical molecular weight ($M_{n,\mathrm{theo}}$) was calculated as 3,280 g mol^{-1}. The ^{1}H NMR spectra of the obtained PVFc–OH exhibited a signal assigned to the benzene ring of the ω-chain end group (*f* in **Figure 2.1**(ai)). End-group analysis by ^{1}H NMR revealed a molecular weight ($M_{n,\mathrm{NMR}}$) of 3,190 g mol^{-1} (degree of polymerization: ~14), which agreed well with the $M_{n,\mathrm{theo}}$ value. The size exclusion chromatography (SEC) trace of PVFc–OH presented a unimodal peak with the dispersity ($Đ$) value 1.24 (**Figure 2.1** (c)). The obtained PVFc–OH was then reacted with 6-azidohexanoic acid (N_3–COOH) to form PVFc possessing an azido group (PVFc–N_3) at the ω-chain end. The reaction was carried out with 4-dimethylaminopyridine (DMAP) and 1-(3-dimethylaminopropyl)-3-ethylcarbodiimide hydrochloride (EDC·HCl) as the catalyst and condensation reagent, respectively, at the $[\text{PVFc–OH}]_0/[\text{N}_3\text{–COOH}]_0/[\text{DMAP}]_0/[\text{EDC·HCl}]_0$ ratio 1/7/5/7, which afforded the desired PVFc–N_3 in high yield (97%). The ^{1}H NMR spectrum of PVFc–N_3 displayed a new signal in the range 3.12–3.29 ppm, assigned to the methylene proton adjacent to the azido group (*A* in **Figure 2.1** (aii)). In addition, the FT-IR spectra presented a new absorption band at 2095 cm^{-1}, assigned to the azido group (**Figure 2.1** (bii)). Finally, PVFc-*b*-MT was synthesized via the click reaction of PVFc–N_3 with *N*-maltotriosyl-3-acetamido-1-propyne (MT–C≡CH). The reaction was conducted using copper(I) bromide (CuBr) and *N*,*N*,*N'*,*N''*,*N''*-pentamethyldiethylenetriamine (PMDETA) as the catalyst and ligand, respectively, at the $[\text{PVFc–N}_3]_0/[\text{MT–C≡CH}]_0/[\text{CuBr}]_0/[\text{PMDETA}]_0$ ratio 1/1.3/1.4/1.3, which afforded PVFc-*b*-MT in 84% yield. The absence of the absorption band at 2095 cm^{-1} (**Figure 2.1** (biii)) in the FT-IR spectrum of the product suggested sufficient conversion from the azido group to the corresponding triazole ring. Moreover, the new strong absorption band at ~3,400 cm^{-1}, assigned to the hydroxyl group, indicated the successful installation of the MT block. The SEC data provided good evidence of BCP formation; the elution peak maximum shifted to the higher molecular weight region following the click reaction (**Figure 2.1** (c)). Although a small elution peak due to the PVFc homopolymer was observed, its fraction was calculated as ~18%. Nevertheless, the *Đ* value of PVFc-*b*-MT was estimated to be as narrow as 1.08. The ^{1}H NMR spectrum of PVFc-*b*-MT exhibited a characteristic signal in the range 7.92–8.34 ppm, ascribed to the triazole ring, along with a series of signals corresponding to both the PVFc and MT blocks (**Figure 2.1** (aiii)). The $M_{n,NMR}$ of the obtained PVFc-*b*-MT was calculated as 3,910 based on the ^{1}H NMR data. Beginning with the same PVFc–OH sample, PVFc-*b*-MH was synthesized in the same manner, using *N*-maltohexaosyl-3-acetamido-1-propyne (MH–C≡CH) instead of MT–C≡CH. The FT-IR, NMR, and SEC data revealed the successful synthesis of the desired PVFc-*b*-MH (**Figure 2.2**).

The miktoarm-type BCP, PVFc-*b*-$(MT)_2$, was synthesized in a similar manner with PVFc-*b*-MT and PVFc-*b*-MH (**Scheme 2.1**). Prior to esterification with 6-azidohexanoic acid, the benzyl group on PVFc–OH was deprotected by treatment with Pd-C/H_2 to afford PVFc possessing two hydroxyl groups at the ω-chain end (PVFc–$(OH)_2$) in 72% yield.[46,47] The deprotection reaction proceeded completely as evidenced by the disappearance of the signal, owing to the presence of the benzene ring without any side reactions (**Figures 2.3** and **2.4)**. Next, the obtained PVFc–$(OH)_2$ was reacted with N_3–COOH ([PVFc–$(OH)_2]_0$/[N_3–COOH$]_0$/[DMAP$]_0$/[EDC·HCl$]_0$ = 1/12/9/10) to afford PVFc possessing two azido groups (PVFc–$(N_3)_2$) in 87% yield. Finally, PVFc-*b*-$(MT)_2$ was afforded in 83% yield by the click reaction of PVFc–$(N_3)_2$ with MT–C≡CH ([PVFc–$(N_3)_2]_0$/[MT–C≡CH$]_0$/[CuBr$]_0$/[PMDETA$]_0$ = 1/2.5/2.4/2.3). The FT-IR, NMR, and SEC data revealed the successful formation of the desired PVFc-*b*-$(MT)_2$ (**Figure 2.3**).

Although SEC analysis revealed the presence of the PVFc homopolymer (~16%), the *Đ* value for the PVFc-*b*-(MT)$_2$ fraction was estimated to be quite narrow (1.08).

The PVFc volume fractions (f_{PVFc}) were calculated as 0.86, 0.75, and 0.74 for PVFc-*b*-MT, PVFc-*b*-MH, and PVFc-*b*-(MT)$_2$, respectively, based on the $M_{\mathrm{n,NMR}}$ and density values (**Table 2.1**). Here, the reported density value for PVFc (1.28 g cm^{-3}) was used for the calculation, while the reported density value for amylose (1.36 g cm^{-3}) was used instead of those of MT and MH. PVFc-*b*-MT, PVFc-*b*-MH, and PVFc-*b*-(MT)$_2$ were insoluble in protic solvents such as H_2O and MeOH, which are good solvents for MT. This occurred because the majority component (i.e., PVFc) dictated the overall solubility. Indeed, the PVFc homopolymer is insoluble in such solvents. Among the tested organic solvents, the BCPs were molecularly dissolved in DMF and dimethyl sulfoxide. The ^{1}H NMR spectra obtained in these D-solvents presented signals from both the PVFc and saccharidic blocks. On the other hand, the ^{1}H NMR spectra obtained in $CDCl_3$ only displayed signals corresponding to the PVFc block, probably due to micellar aggregate formation with the PVFc outer shell and the oligosaccharide core.

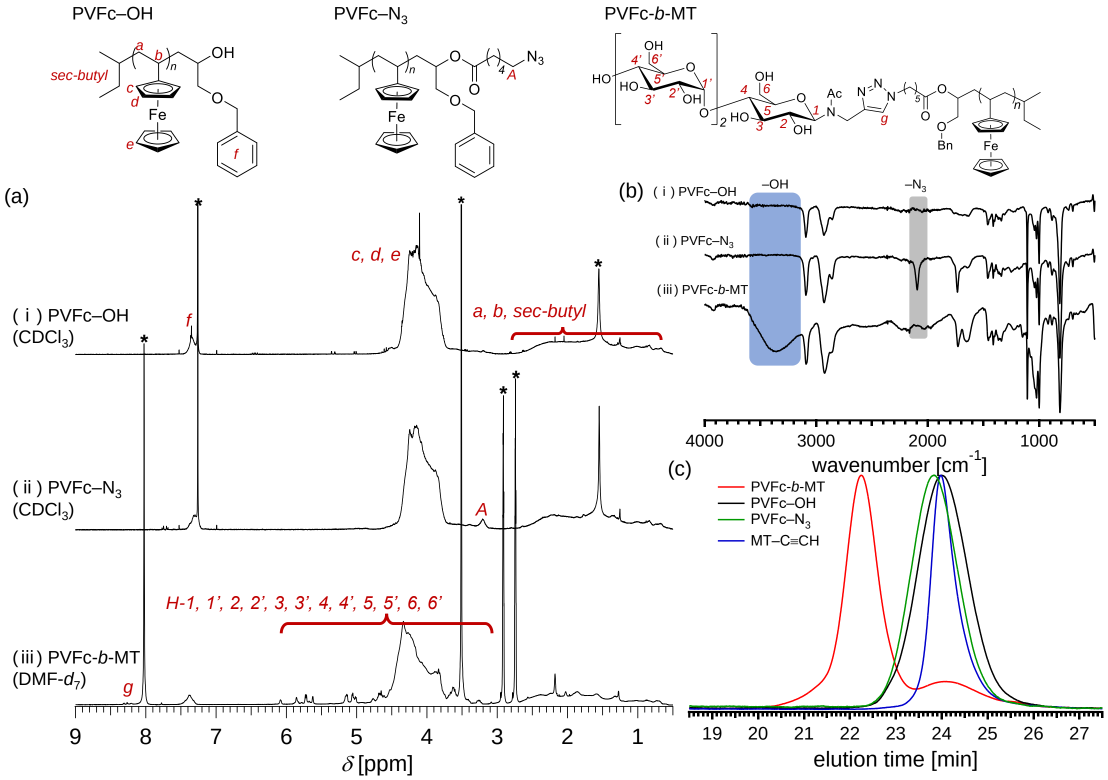

Figure 2.1. Characterization of PVFc-*b*-MT. (a) ^{1}H NMR spectra of PVFc–OH (i) and PVFc–N_3 (ii) in $CDCl_3$ and PVFc-*b*-MT (iii) in DMF-d_7 (400 MHz). (b) FT-IR spectra of PVFc–OH (i), PVFc–N_3 (ii), and PVFc-*b*-MT (iii). (c) SEC traces of PVFc-*b*-MT (red), PVFc–OH (black), PVFc–N_3 (green), and MT–C≡CH (blue) eluent, DMF containing 0.01 mol L^{-1} LiCl; flow rate, 0.60 mL min^{-1}).

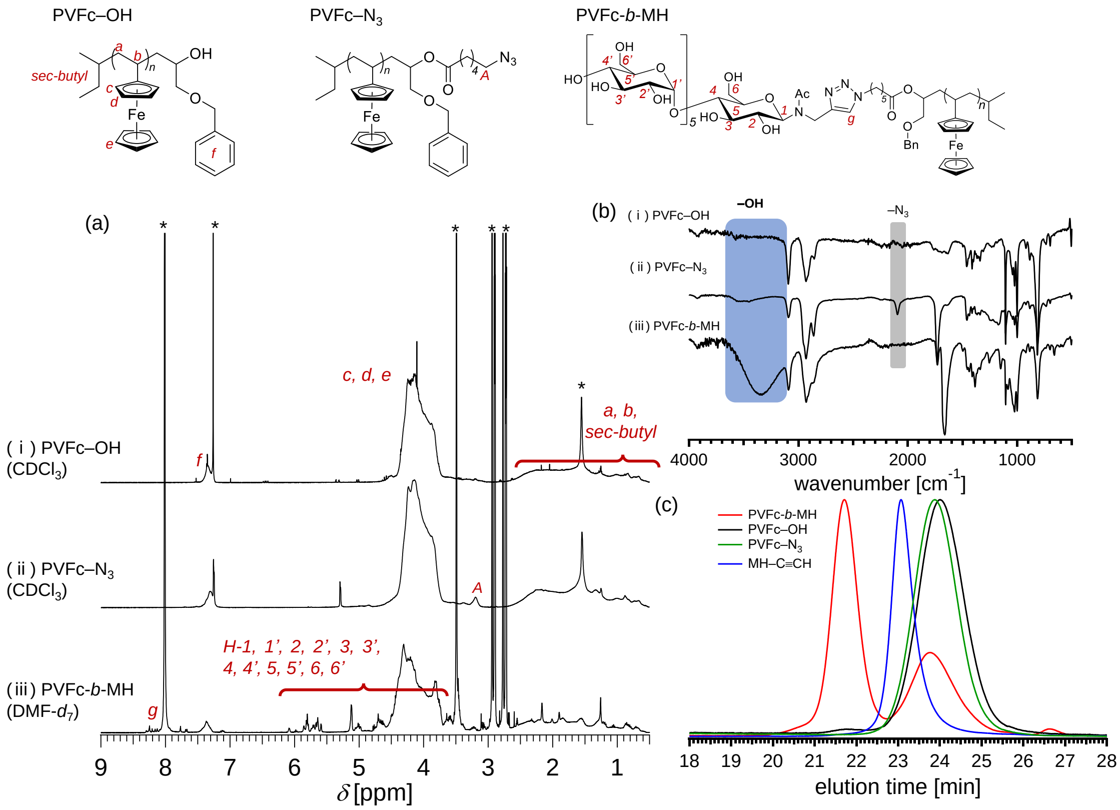

Figure 2.2. Characterization of PVFc-*b*-MH. (a) ^{1}H NMR spectra of PVFc–OH (i) and PVFc–N_3 (ii) in $CDCl_3$ and PVFc-*b*-MH (iii) in DMF-d_7 (400 MHz). (b) FT-IR spectra of PVFc–OH (i), PVFc–N_3 (ii), and PVFc-*b*-MH (iii). (c) SEC traces of PVFc-*b*-MH (red line), PVFc–OH (black line), PVFc–N_3 (green line), and MH–C≡CH (blue line) (eluent, DMF containing 0.01 mol L^{-1} LiCl; flow rate, 0.60 mL min^{-1}).

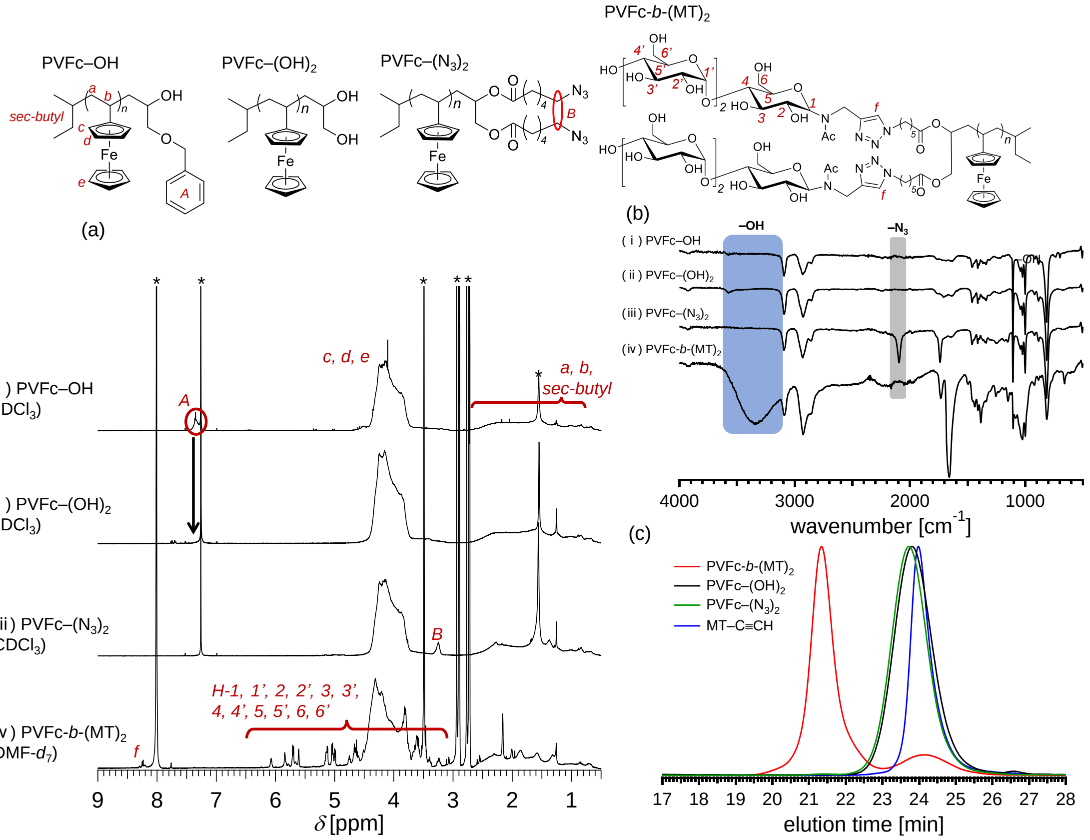

Figure 2.3. Characterization of PVFc-*b*-$(MT)_2$. (a) ^1H NMR spectra of PVFc–OH (i), PVFc–$(OH)_2$ (ii), PVFc–$(N_3)_2$ (iii) in $CDCl_3$, and PVFc-*b*-$(MT)_2$ (iv) in DMF-d_7 (400 MHz). (b) FT-IR spectra of PVFc–OH (i), PVFc–$(OH)_2$ (ii), PVFc–(N_3) (iii) and PVFc-*b*-$(MT)_2$ (iv). (c) SEC traces of PVFc-*b*-$(MT)_2$ (red line), PVFc–$(OH)_2$ (black line), PVFc–$(N_3)_2$ (green line), and MT–C≡CH (blue line) (eluent, DMF containing 0.01 mol L^{-1} LiCl; flow rate, 0.60 mL min^{-1}).

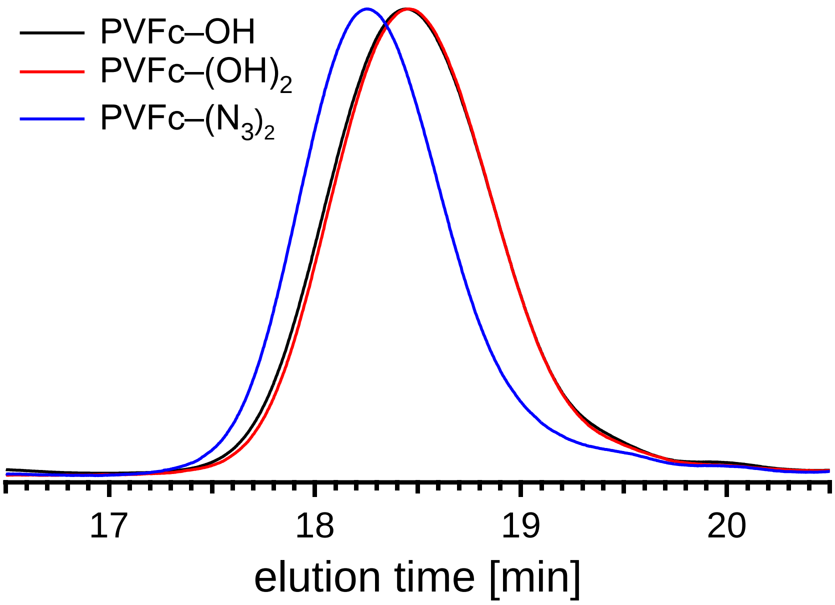

Figure 2.4. SEC traces of PVFc–OH (black line), PVFc–(OH)$_2$ (red line) and PVFc–(N$_3$)$_2$ (blue line) (eluent, THF; flow rate, 1.0 mL min^{-1}).

Table 2.1. Molecular characteristics of the block copolymers (BCPs) and their precursors

Polymer	$M_{n,NMR}$[a]	$M_{n,SEC}$	$Đ$	f_{PVFc}[d]	Yield / %
PVFc–OH	3,190	1,020[b]	1.24[b]	-	80
PVFc–N$_3$	3,330	1,180[b]	1.21[b]	-	97
PVFc-*b*-MT	3,910	4,180[c]	1.07[c]	0.86	84
PVFc-*b*-MH	3,980	6,370[c]	1.05[c]	0.74	41
PVFc–(OH)$_2$	3,100	1,020[b]	1.23[b]	-	72
PVFc–(N$_3$)$_2$	3,380	1,270[b]	1.37[b]	-	87
PVFc-*b*-(MT)$_2$	4,330	6,680[c]	1.08[c]	0.75	83

[a]Determined by ^{1}H NMR. [b]Determined by size exclusion chromatography (SEC) in THF using polystyrene standards. [c]Determined by SEC in DMF using polystyrene standards. [d]PVFc volume fractions (f_{PVFc}) were calculated using the known density values d_{PVFc} = 1.28 g cm^{-3} and $d_{amylose}$ = 1.36 g cm^{-3}.

2.3.2. Thermal properties and etching resistance

The thermal properties of PVFc-*b*-MT, PVFc-*b*-MH, and PVFc-*b*-(MT)$_2$ were investigated by thermogravimetric analysis (TGA) and differential scanning calorimetry

(DSC). The decomposition temperatures of PVFc–OH, MT–C≡CH, MH–C≡CH, and PVFc-*b*-MT were first investigated by TGA. The PVFc–OH, MT–C≡CH, and MH–C≡CH TGA profiles displayed decomposition temperatures at 360, 210, and 260 °C, respectively (**Figure 2.5**), confirming the high heat resistance of PVFc. The TGA profile of PVFc-*b*-MT displayed two decomposition points at 230 and 380 °C corresponding to the decomposition temperatures of maltotriose and PVFc, respectively.

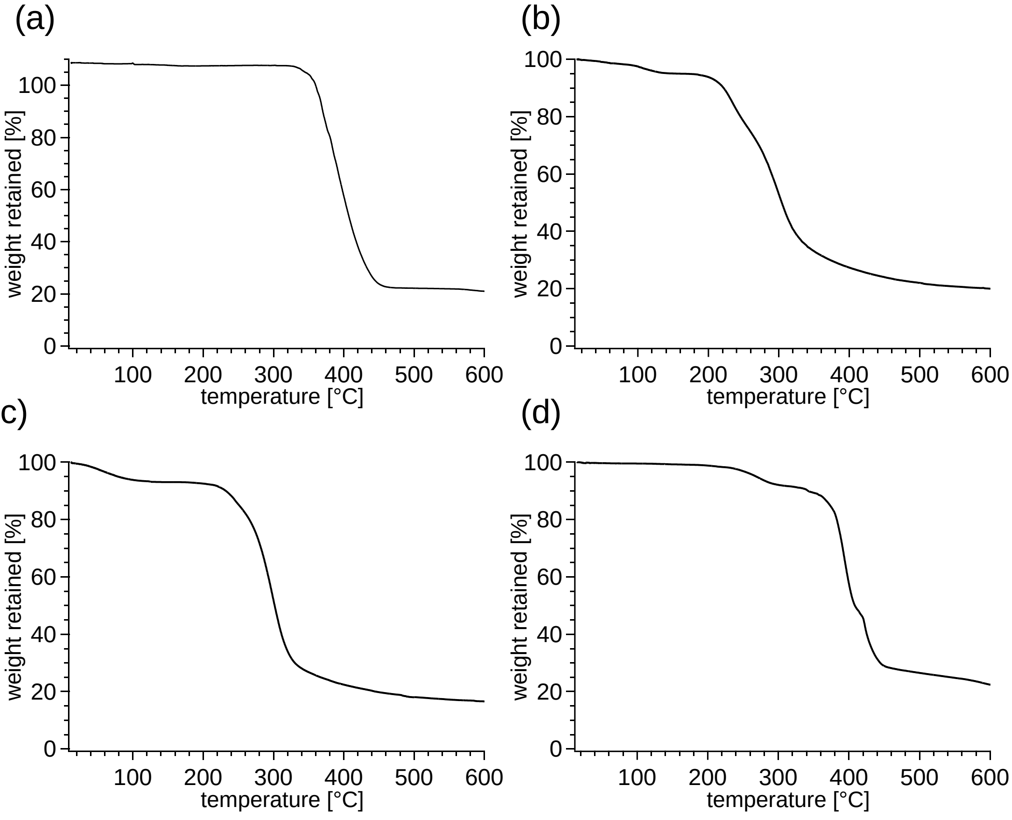

Figure 2.5. TGA profiles of (a) PVFc–OH, (b) MT–C≡CH, (c) MH–C≡CH, and (d) PVFc-*b*-MT obtained under a nitrogen atmosphere.

The DSC curve of the PVFc homopolymer presented only one base-line shift (136 °C) corresponding to the glass transition. The DSC curves of PVFc-*b*-MT and PVFc-*b*-(MT)$_2$ displayed a base-line shift corresponding to the glass transition of the PVFc segment during the second heating run. On the other hand, the PVFc-*b*-MH DSC curve only displayed a base line shift during the first heating run (**Figure 2.6**). Notably, no transitions due to melting and crystallization were observed in the DSC traces of PVFc-*b*-MT, PVFc-*b*-MH, PVFc-*b*-$(MT)_2$, and the PVFc homopolymer, demonstrating the absence of crystalline structures in these polymers. The glass transition temperatures of the PVFc segments ($T_{g,PVFc}$) in PVFc-*b*-MT, PVFc-*b*-MH, and PVFc-*b*-$(MT)_2$ were determined as 154, 143, and 143 °C, respectively, values that are higher than that of the PVFc homopolymer (136.1 °C). This was attributed to the decrease in the chain mobility of the PVFc segment because of the presence of the large oligosaccharide segment that can form strong intra- and intermolecular hydrogen-bonding.

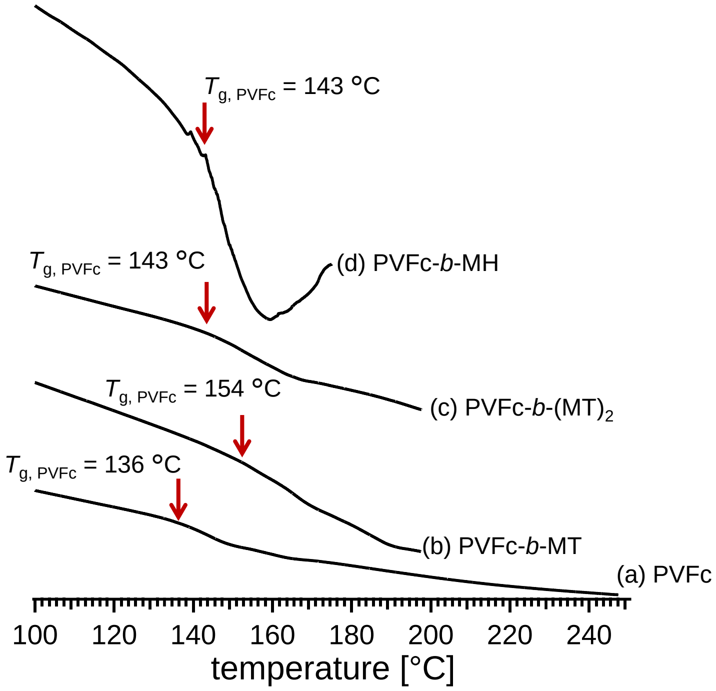

Figure 2.6. Differential scanning calorimetry (DSC) curves of (a) PVFc, (b) PVFc-*b*-MT, and (c) PVFc-*b*-(MT)$_2$ during the second heating run and (d) PVFc-*b*-MH during the first heating run.

The etching resistances of the PVFc and oligosaccharide were also investigated. Thus, thin films of PVFc (film thickness, ~230 nm) and maltotriose (film thickness, ~180 nm) on a Si substrate were prepared by spin-coating. The etching depth of these thin films was determined after they were subjected to oxygen reactive ion etching (RIE). As expected, PVFc exhibited higher etching resistance towards oxygen RIE than maltotriose (**Table 2.2** and **Figures 2.7** and **2.8**), and its etching selectivity (1.78) was superior to that of the well-known polystyrene-*b*-poly(methyl methacrylate).[48]

Table 2.2. Results of etching treatments on the PVFc and MT thin films[a]

etch time / s[b]	PVFc etch depth / nm	MT etch depth / nm[b]	PVFc etch rate / nm min^{-1c}	MT etch rate / nm min^{-1c}	PVFc to MT etch selectivity[d]
5	73	62	15	12	0.8
10	87	61	8.7	6.1	0.7
20	61	109	3.1	5.5	1.8
30	98	175	3.3	5.9	1.8

[a]Etching condition: pressure, 12 Pa; RF power, 80 W; gas flow, 75 sccm; etching gas, O_2

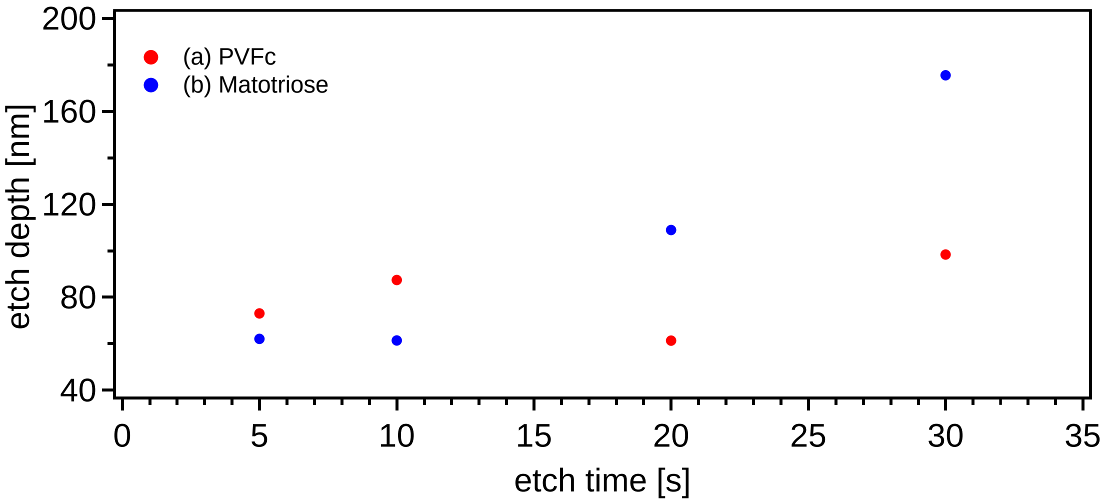

Figure 2.7. Etch profiles of (a) PVFc (red) and (b) MT (blue) thin films subjected to an oxygen RIE.

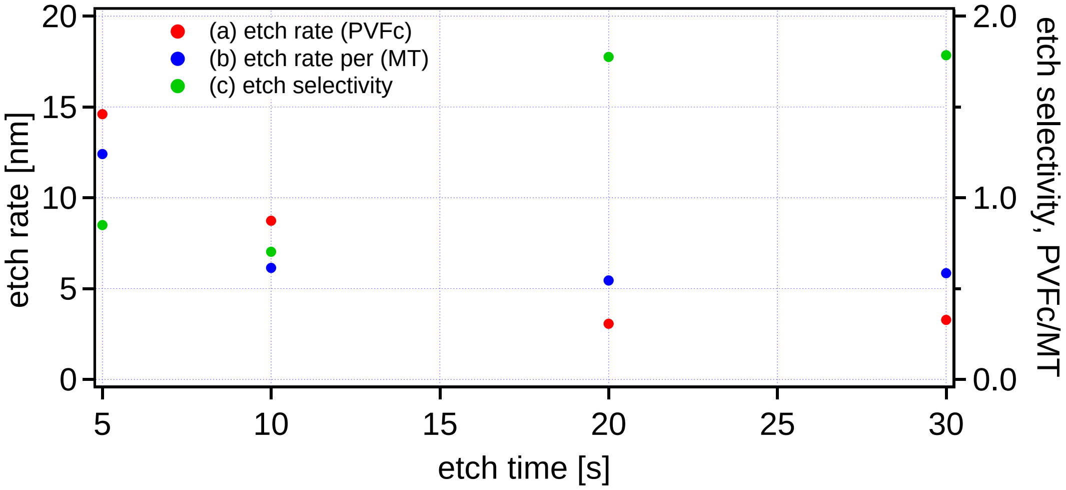

Figure 2.8. Etch rates for PVFc (black) and MT thin films (red) and etch selectivity between PVFc and MT (blue) as a function of etch time.

2.3.3. Microphase-separated structures

The microphase-separated structures of PVFc-*b*-MT, PVFc-*b*-MH, and PVFc-*b*-(MT)$_2$ in the bulk state were investigated using small angle X-ray scattering (SAXS). Prior to the SAXS experiment, the samples were thermally annealed at 180 °C that was higher than the T_g of the constitutional blocks.

The SAXS profile of PVFc-*b*-MT displayed an only weak primary scattering peak, suggesting that ill-ordered microphase separation occurred (**Figure 2.9** (a)). This was attributed to the N value of PVFc-*b*-MT, which was too small to gain enough segregation strength. On the other hand, PVFc-*b*-MH successfully self-assembled into a microphase-separated structure as evidenced by the SAXS profile, even though N was ~20. Specifically, the SAXS profile of PVFc-*b*-MH displayed a primary scattering peak at $q^* = 0.767$ nm^{-1} and higher-ordered scattering peaks at $\sqrt{3}q^*$ and $2q^*$, which corresponded to hexagonally close-packed cylinder (HEX) morphology (**Figure 2.9** (b)). Moreover, d, calculated based on the Bragg's equation ($d = 2\pi/q^*$), was extremely small (8.2 nm), while the center-to-center distance between the cylinders ($d_{\text{C-C,SAXS}} = 2d/\sqrt{3}$) was calculated as 9.5 nm. Thus, the addition of one more MT unit permitted the BCP to microphase-separate by overcoming the critical χN.

The SAXS profile of PVFc-*b*-(MT)$_2$ also displayed a scattering pattern corresponding to HEX morphology (**Figure 2.9** (c)). Notably, the d and $d_{\text{C-C,SAXS}}$ values were calculated as 7.8 and 9.0 nm, respectively, both <10 nm. This result strongly supported the above discussions that the χN exceeded the critical value to microphase-separate with the addition of one more MT unit. Notably, the scattering peaks for the PVFc-*b*-(MT)$_2$ sample were apparently sharper than those of PVFc-*b*-MH, suggesting the better long-range ordering in PVFc-*b*-(MT)$_2$. The lower T_g of maltotriose (110 °C) compared to that of maltohexaose (145 °C) suggested the superior chain mobility of PVFc-*b*-(MT)$_2$ during thermal annealing, which could facilitate grain coarsening in PVFc-*b*-(MT)$_2$.[49]

The microphase-separated structure in the thin film state was visualized by atomic force microscopy (AFM). The PVFc-*b*-(MT)$_2$ thin film was prepared by spin coating its 5 wt% DMF solution onto a silicon substrate followed by thermal annealing at 180 °C for 5 h under vacuum. The AFM phase image exhibited a finger-print-like pattern corresponding to the HEX structure parallel to the substrate (**Figure 2.10**). The center-to-center distance between the cylinders ($d_{\text{C-C,AFM}}$) was 8.3 nm, as estimated by the Fast Fourier transform (FFT) analysis of the phase image; this value roughly matched the $d_{\text{C-C,SAXS}}$ value. Such a parallel cylindrical structure could be applied to the fabrication of line-and-space patterns with the aid of directed self-assembly.[1,50]

It is quite important to obtain a variety of morphologies, such as spheres, cylinders, gyroids, and lamellars, to expand the possible nanofabrication applications. To diversify the available morphology from the present BCP system, the author investigated the microphase-separated structures of a series of blend samples of PVFc-*b*-MT and PVFc-*b*-$(MT)_2$ with glucose and PVFc homopolymers. The addition of an A homopolymer into an AB diblock copolymer has been reported to alter the microphase-separated structures by the selective swelling of the A block microdomain.[51,52] Thus, the author first attempted to induce and control microphase separation in PVFc-*b*-MT by adding glucose. However, no ordered microphase-separated structure was found in the PVFc-*b*-MT/glucose blend, regardless of the total volume fraction of the saccharide portion (f_{sac}). Next, the author prepared a PVFc-*b*-$(MT)_2$/Glc blend with an f_{sac} of 0.49, aiming at obtaining lamellar morphology (LAM). The SAXS profile of the thermally annealed PVFc-*b*-$(MT)_2$/Glc blend sample presented a primary peak at $q^* = 0.676\ \mathrm{nm}^{-1}$ and an additional higher-ordered peak at the $2q^*$ position (**Figure 2.9** (d)), which corresponded to LAM morphology. The d value was calculated as 9.3 nm, based on the Bragg's equation, which was significantly larger than that of pristine PVFc-*b*-$(MT)_2$. As expected, this result demonstrates the shift in the microphase-separated structure, from HEX to LAM, owing to the selective swelling of the saccharide domain as a result of the added glucose. On the other hand, the PVFc-*b*-$(MT)_2$/PVFc blend ($f_{\mathrm{sac}} = 0.21$), which was prepared aiming at achieving spherical morphology, only presented a broad primary peak. This suggested the absence of an ordered microphase-separated structure. Nevertheless, the author successfully constructed lithographically important lamellar and cylindrical morphologies from PVFc-*b*-(MT)$_2$.

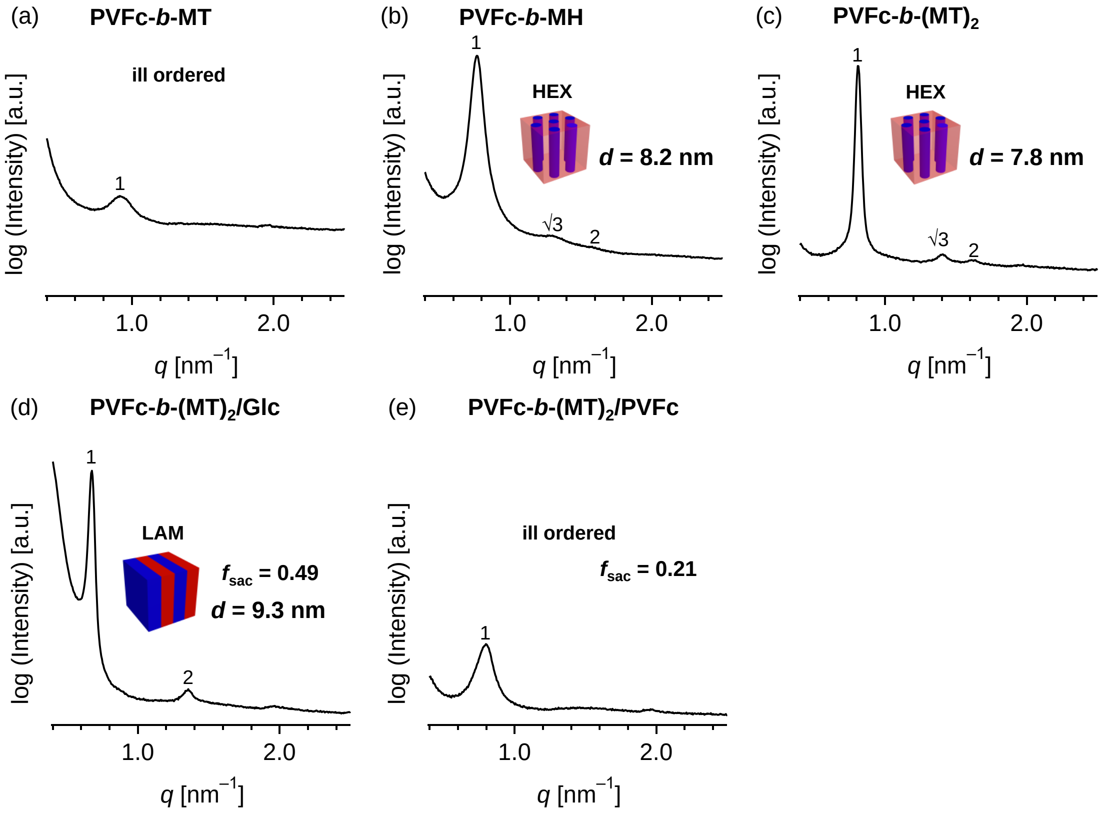

Figure 2.9. Small angle X-ray scattering (SAXS) profiles for the bulk samples of (a) PVFc-*b*-MT, (b) PVFc-*b*-MH, (c) PVFc-*b*-(MT)$_2$, (d) PVFc-*b*-(MT)$_2$/Glc, and (e) PVFc-*b*-(MT)$_2$/PVFc. All the samples were annealed at 180 °C for 1 h. The small peak at q = 1.95 nm^{-1} is artifact in the scattering data.

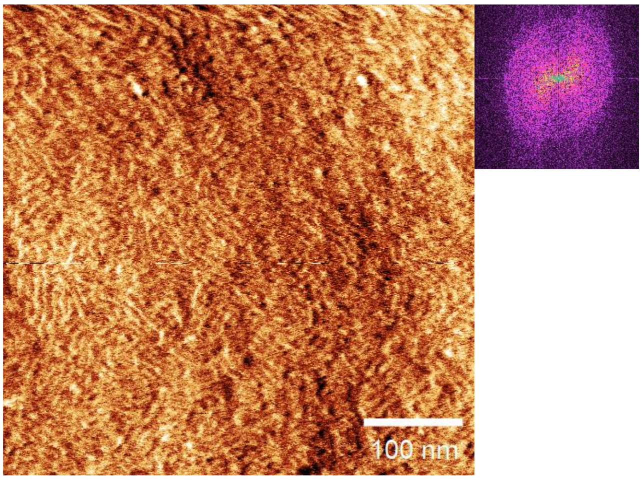

Figure 2.10. AFM phase image of PVFc-*b*-$(MT)_2$ thin film. The inset shows the FFT obtained from the phase image. Scale bar is 100 nm.

2.4. Conclusion

The author successfully synthesized three types of novel oligosaccharide-based BCPs (PVFc-*b*-MT, PVFc-*b*-MH, and PVFc-*b*-$(MT)_2$) using living anionic polymerization followed by the click reaction. PVFc-*b*-MH and PVFc-*b*-$(MT)_2$ formed HEX microphase-separated structures with sub-10 nm *d* values, which were affected by the polymer architecture. These results are the first experimental demonstration of metal-containing BCPs that formed microphase-separated structures with a domain spacing of <10 nm. Interestingly, the microphase-separated structure of the PVFc-*b*-$(MT)_2$/glucose mixtures was different from that of PVFc-*b*-$(MT)_2$. Thus, the morphology was shifted from HEX to LAM. Importantly, the author successfully obtained both LAM and HEX morphology, which are useful for the lithographic process. The author is currently optimizing the etching conditions to realize higher etching selectivity for directed self-assembly applications.[14] PVFc-*b*-oligosaccharide BCPs, featured by their small *d* value, sufficient thermal stability, and high etching selectivity, are highly promising lithographic materials and show great potential for use in other nanotechnological applications such as functional membranes[53,54] and polymer-based memory devices.[55,56]

2.5. References

(1) Bates, C. M.; Maher, M. J.; Janes, D. W.; Ellison, C. J.; Willson, C. G. Block Copolymer Lithography. *Macromolecules* **2014**, *47*, 2–12.

(2) Stoykovich, M. P.; Kang, H.; Daoulas, K. C.; Liu, G.; Liu, C.; de Pablo, J. J.; Müller, M.; Nealey, P. F. Directed Self-Assembly of Block Copolymers for Nanolithography: Fabrication of Isolated Features and Essential Integrated Circuit Geometries. *ACS Nano* **2007**, *1*, 168–175.

(3) Kim, B. H.; Kim, J. Y.; Kim, S. O. Directed self-assembly of block copolymers for universal nanopatterning. *Soft Matter* **2013**, *9*, 2780–2786.

(4) Bratton, D.; Yang, D.; Dai, J.; Ober, C. K. Recent Progress in High Resolution Lithography. *Polym. Adv. Technol.* **2006**, *17*, 94–103.

(5) Piunova, V. A.; Miyake, G. M.; Daeffler, C. S.; Weitekamp, R. A.; Grubbs, R. H. Highly Ordered Dielectric Mirrors via the Self-Assembly of Dendronized Block Copolymers. *J. Am. Chem. Soc.* **2013**, *135*, 15609–15616.

(6) Cushen, J.; Wan, L.; Blachut, G.; Maher, M. J.; Albrecht, T. R.; Ellison, C. J.; Willson, C. G.; Ruiz, R. Double-Patterned Sidewall Directed Self-Assembly and Pattern Transfer of Sub-10 nm PTMSS-*b*-PMOST. *ACS Appl. Mater. Interfaces* **2015**, *7*, 13476–13483.

(7) Ruiz, R.; Dobisz, E.; Albrecht, T. R. Rectangular Patterns Using Block Copolymer Directed Assembly for High Bit Aspect Ratio Patterned Media. *ACS Nano* **2011**, *5*, 79–84.

(8) Griffiths, R. A.; Williams, A.; Oakland, C.; Roberts, J.; Vijayaraghavan, A.; Thomson, T. Directed self-assembly of block copolymers for use in bit patterned media fabrication. *J. Phys. D. Appl. Phys.* **2013**, *46*, 503001.

(9) Olson, D. A.; Chen, L.; Hillmyer, M. A. Templating Nanoporous Polymers with Ordered Block Copolymers. *Chem. Mater.* **2008**, *20*, 869–890.

(10) Stefik, M.; Guldin, S.; Vignolini, S.; Wiesner, U.; Steiner, U. Block Copolymer Self-Assembly for Nanophotonics. *Chem. Soc. Rev.* **2015**, *44*, 5076–5091.

(11) Schacher, F. H.; Rupar, P. A.; Manners, I. Functional Block Copolymers: Nanostructured Materials with Emerging Applications. *Angew. Chem. Int. Ed.* **2012**, *51*, 7898–7921.

(12) Chae, C.-G.; Yu, Y.-G.; Seo, H.-Bin; Kim, M.-J.; Grubbs, R. H.; Lee, J.-S. Experimental Formulation of Photonic Crystal Properties for Hierarchically Self-Assembled POSS–Bottlebrush Block Copolymers. *Macromolecules* **2018**, *51*, 3458–3466.

(13) Yu, Y.-G.; Chae, C.-G.; Kim, M.-J.; Seo, H.-Bin; Grubbs, R. H.; Lee, J.-S. Precise Synthesis of Bottlebrush Block Copolymers from ω-End-Norbornyl Polystyrene and Poly(4-*tert*-butoxystyrene) via Living Anionic Polymerization and Ring-Opening Metathesis Polymerization. *Macromolecules* **2018**, *51*, 447–455.

(14) Hu, H.; Gopinadhan, M.; Osuji, C. O. Directed self-assembly of block copolymers: a tutorial review of strategies for enabling nanotechnology with soft matter. *Soft Matter* **2014**, *10*, 3867–3889.

(15) Fei, H. F.; Li, W.; Bhardwaj, A.; Nuguri, S.; Ribbe, A.; Watkins, J. J. Ordered Nanoporous Carbons with Broadly Tunable Pore Size Using Bottlebrush Block Copolymer Templates. *J. Am. Chem. Soc.* **2019**, *141*, 17006–17014.

(16) Leibler, L. Theory of Microphase Separation in Block Copolymers. *Macromolecules* **1980**, *13*, 1602–1617.

(17) Bates, F. S.; Fredrickson, G. H. BLOCK COPOLYMER THERMODYNAMICS: Theory And Experiment. *Annu. Rev. Phys. Chem.* **1990**, *41*, 525–557.

(18) Kennemur, J. G.; Yao, L.; Bates, F. S.; Hillmyer, M. A. Sub-5 nm Domains in Ordered Poly(cyclohexylethylene)-*block*-Poly(methyl methacrylate) Block Polymers for Lithography. *Macromolecules* **2014**, *47*, 1411–1418.

(19) Kwak, J.; Mishra, A. K.; Lee, J.; Lee, K. S.; Choi, C.; Maiti, S.; Kim, M.; Kim, J. K. Fabrication of Sub-3 nm Feature Size Based on Block Copolymer Self-Assembly for Next-Generation Nanolithography. *Macromolecules* **2017**, *50*, 6813–6818.

(20) Sweat, D. P.; Kim, M.; Larson, S. R.; Choi, J. W.; Choo, Y.; Osuji, C. O.; Gopalan, P. Rational Design of a Block Copolymer with a High Interaction Parameter. *Macromolecules* **2014**, *47*, 6687–6696.

(21) Kanimozhi, C.; Kim, M.; Larson, S. R.; Choi, J. W.; Choo, Y.; Sweat, D. P.; Osuji, C. O.; Gopalan, P. Isomeric Effect Enabled Thermally Driven Self-Assembly of Hydroxystyrene-Based Block Copolymers. *ACS Macro Lett.* **2016**, *5*, 833–838.

(22) Yu, D. M.; Smith, D. M.; Kim, H.; Mapas, J. K. D.; Rzayev, J.; Russell, T. P. Morphological Evolution of Poly(solketal methacrylate)-*block*-polystyrene Copolymers in Thin Films. *Macromolecules* **2019**, *52*, 3592–3600.

(23) Zhang, W.; Huang, M.; Abdullatif, S. Al; Chen, M.; Shao-Horn, Y.; Johnson, J. A.

Reduction of (Meth)acrylate-Based Block Copolymers Provides Access to Self-Assembled Materials with Ultrasmall Domains. *Macromolecules* **2018**, *51*, 6757–6763.

(24) Isono, T.; Otsuka, I.; Suemasa, D.; Rochas, C.; Satoh, T.; Borsali, R.; Kakuchi, T. Synthesis, Self-Assembly, and Thermal Caramelization of Maltoheptaose-Conjugated Polycaprolactones Leading to Spherical, Cylindrical, and Lamellar Morphologies. *Macromolecules* **2013**, *46*, 8932–8940.

(25) Isono, T.; Otsuka, I.; Kondo, Y.; Halila, S.; Fort, S.; Rochas, C.; Satoh, T.; Borsali, R.; Kakuchi, T. Sub-10 nm Nano-Organization in AB_2- and AB_3-Type Miktoarm Star Copolymers Consisting of Maltoheptaose and Polycaprolactone. *Macromolecules* **2013**, *46*, 1461–1469.

(26) Liao, Y.; Liu, K.; Chen, W.-C.; Wei, B.; Borsali, R. Robust Sub-10 nm Pattern of Standing Sugar Cylinders via Rapid "Microwave Cooking." *Macromolecules* **2019**, *52*, 8751–8758.

(27) Otsuka, I.; Zhang, Y.; Isono, T.; Rochas, C.; Kakuchi, T.; Satoh, T.; Borsali, R. Sub-10 nm Scale Nanostructures in Self-Organized Linear Di- and Triblock Copolymers and Miktoarm Star Copolymers Consisting of Maltoheptaose and Polystyrene. *Macromolecules* **2015**, *48*, 1509–1517.

(28) Isono, T.; Kawakami, N.; Watanabe, K.; Yoshida, K.; Otsuka, I.; Mamiya, H.; Ito, H.; Yamamoto, T.; Tajima, K.; Borsali, R.; et al. Microphase separation of carbohydrate-based star-block copolymers with sub-10 nm periodicity. *Polym. Chem.* **2019**, *10*, 1119–1129.

(29) Otsuka, I.; Nilsson, N.; Suyatin, D. B.; Maximov, I.; Borsali, R. Carbohydrate-based block copolymer systems: directed self-assembly for nanolithography applications. *Soft Matter* **2017**, *13*, 7406–7411.

(30) Nunns, A.; Gwyther, J.; Manners, I. Inorganic block copolymer lithography. *Polymer* **2013**, *54*, 1269–1284.

(31) Luo, Y.; Montarnal, D.; Kim, S.; Shi, W.; Barteau, K. P.; Pester, C. W.; Hustad, P. D.; Christianson, M. D.; Fredrickson, G. H.; Kramer, E. J.; Hawker, C. J. Poly(dimethylsiloxane-*b*-methyl methacrylate): A Promising Candidate for Sub-10 nm Patterning. *Macromolecules* **2015**, *48*, 3422–3430.

(32) Rodwogin, M. D.; Spanjers, C. S.; Leighton, C.; Hillmyer, M. A. Polylactide-Poly(dimethylsiloxane)-Polylactide Triblock Copolymers as Multifunctional Materials for Nanolithographic Applications. *ACS Nano* **2010**, *4*, 725–732.

(33) Kato, F.; Sugimoto, S.; Chandra, A.; Hayakawa, T. Morphology control and inducing a curvature on the domain interface by increasing the steric bulk of polymethacrylate in POSS-containing diblock copolymers s. *J. Polym. Sci. Part A Polym. Chem.* **2017**, *55*, 2234–2242.

(34) Nakatani, R.; Takano, H.; Chandra, A.; Yoshimura, Y.; Wang, L.; Suzuki, Y.; Tanaka, Y.; Maeda, R.; Kihara, N.; Minegishi, S.; Miyagi, K.; Kasahara, Y.; Sato, H.; Seino, Y.; Azuma, T.; Yokoyama, H.; Ober, C. K.; Hayakawa, T. Perpendicular Orientation Control without Interfacial Treatment of RAFT-Synthesized High-χ Block Copolymer Thin Films with Sub-10 nm Features Prepared via Thermal Annealing. *ACS Appl. Mater. Interfaces* **2017**, *9*, 31266–31278.

(35) Maher, M. J.; Rettner, C. T.; Bates, C. M.; Blachut, G.; Carlson, M. C.; Durand, W. J.; Ellison, C. J.; Sanders, D. P.; Cheng, J. Y.; Willson, C. G. Directed Self-Assembly of Silicon-Containing Block Copolymer Thin Films. *ACS Appl. Mater. Interfaces* **2015**, *7,* 3323–3328.

(36) Cushen, J. D.; Otsuka, I.; Bates, C. M.; Halila, S.; Fort, S.; Rochas, C.; Easley, J. A.; Rausch, E. L.; Thio, A.; Borsali, R.; Willson, C. G.; Ellison, C. J. Oligosaccharide/Silicon-Containing Block Copolymers with 5 nm Features for Lithographic Applications. *ACS Nano* **2012**, *6,* 3424–3433.

(37) Gokan, H.; Esho, S.; Ohnishi, Y. Dry Etch Resistance of Organic Materials. *J. Electrochem. Soc.* **1983**, *130,* 143–146.

(38) Nuyken, O.; Burkhardt, V.; Hübsch, C. Anionic homo- and block copolymerization of vinylferrocene. *Macromol. Chem. Phys.* **1997**, *198,* 3353–3363.

(39) Foucher, D. A.; Tang, B. Z.; Manners, I. Ring- opening polymerization of strained, ring-tilted ferrocenophanes: a route to high molecular weight poly (ferrocenylsilanes). *J. Am. Chem. Soc.* **1992**, *114*, 6246–6248.

(40) Hardy, C. G.; Zhang, J.; Yan, Y.; Ren, L.; Tang, C. Metallopolymers with transition metals in the side-chain by living and controlled polymerization techniques. *Prog. Polym. Sci.* **2014**, *39*, 1742–1796.

(41) Lammertink, R. G. H.; Hempenius, M. A.; Van Den Enk, J. E.; Chan, V. Z. H.; Thomas, E. L.; Vancso, G. J. Nanostructured Thin Films of Organic-Organometallic Block Copolymers: One-Step Lithography with Poly(ferrocenylsilanes) by Reactive Ion Etching. *Adv. Mater.* **2000**, *12,* 98–103.

(42) Gallei, M.; Tockner, S.; Klein, R.; Rehahn, M. Silacydobutane-Based Diblock Copolymers with Vinylferrocene, Ferrocenylmethyl Methacrylate, and [1]Dimethylsilaferrocenophane. *Macromol. Rapid Commun.* **2010**, *31,* 889–896.

(43) Higashihara, T.; Faust, R. Synthesis of Novel Block Copolymers Comprised of Polyisobutylene and Poly(vinylferrocene) Segments. *Macromolecules* **2007**, *40*, 7453–7463.

(44) Gallei, M.; Klein, R.; Rehahn, M. Silacyclobutane-Mediated Re-Activation of “Sleeping” Polyvinylferrocene Macro-Anions: A Powerful Access to Novel

Metalloblock Copolymers. *Macromolecules* **2010**, *43*, 1844–1854.

(45) Grandjean, C.; Boutonnier, A.; Guerreiro, C.; Fournier, J. M.; Mulard, L. A. On the Preparation of Carbohydrate-Protein Conjugates Using the Traceless Staudinger Ligation. *J. Org. Chem.* **2005**, *70*, 7123–7132.

(46) Tonhauser, C.; Mazurowski, M.; Rehahn, M.; Gallei, M.; Frey, H. Water-Soluble Poly(vinylferrocene)-*b*-Poly(ethylene oxide) Diblock and Miktoarm Star Polymers. *Macromolecules* **2012**, *45*, 3409–3418.

(47) Morsbach, J.; Natalello, A.; Elbert, J.; Winzen, S.; Kroeger, A.; Frey, H.; Gallei, M. Redox-Responsive Block Copolymers: Poly(vinylferrocene)-*b*-Poly(lactide) Diblock and Miktoarm Star Polymers and Their Behavior in Solution. *Organometallics* **2013**, *32*, 6033–6039.

(48) Farrell, R. A.; Petkov, N.; Shaw, M. T.; Djara, V.; Holmes, J. D.; Morris, M. A. Monitoring PMMA Elimination by Reactive Ion Etching from a Lamellar PS-*b*-PMMA Thin Film by Ex Situ TEM Methods. *Macromolecules* **2010**, *43*, 8651–8655.

(49) Imamura, K.; Sakaura, K.; Ohyama, K. I.; Fukushima, A.; Imanaka, H.; Sakiyama, T.; Nakanishi, K. Temperature Scanning FTIR Analysis of Hydrogen Bonding States of Various Saccharides in Amorphous Matrixes below and above Their Glass Transition Temperatures. *J. Phys. Chem. B* **2006**, *110*, 15094–15099.

(50) Jung, Y. S.; Chang, J. B.; Verploegen, E.; Berggren, K. K.; Ross, C. A. A Path to Ultranarrow Patterns Using Self-Assembled Lithography. *Nano Lett.* **2010**, *10*, 1000–1005.

(51) Tanaka, H.; Hascgawa, H.; Hashimoto, T. Ordered Structure in Mixtures of a Block Copolymer and Homopolymers. 1. Solubilization of Low Molecular Weight Homopolymers. *Macromolecules* **1991**, *24*, 240–251.

(52) Hashimoto, T.; Tanaka, H.; Hasegawa, H. Ordered Structure in Mixtures of a Block Copolymer and Homopolymers. 2. Effects of Molecular Weights of Homopolymers. *Macromolecules* **1990**, *23*, 4378–4386.

(53) Schöttner, S.; Hossain, R.; Rüttiger, C.; Gallei, M. Ferrocene-Modified Block Copolymers for the Preparation of Smart Porous Membranes. *Polymers* **2017**, *9*, 491.

(54) Gallei, M.; Rüttiger, C. Recent Trends in Metallopolymer Design: Redox-Controlled Surfaces, Porous Membranes, and Switchable Optical Materials Using Ferrocene-Containing Polymers. *Chem. Eur. J.* **2018**, *24*, 10006–10021.

(55) Hung, C.-C.; Nakahira, S.; Chiu, Y.-C.; Isono, T.; Wu, H.-C.; Watanabe, K.; Chiang, Y.-C.; Takashima, S.; Borsali, R.; Tung, S.-H.; Sato, T.; Chen, W.-C. Control over Molecular Architectures of Carbohydrate-Based Block Copolymers for Stretchable Electrical Memory Devices. *Macromolecules* **2018**, *51*, 4966–4975.

(56) Wang, J.-T.; Takshima, S.; Wu, H.-C.; Shih, C.-C.; Isono, T.; Kakuchi, T.; Satoh, T.; Chen, W.-C. Stretchable Conjugated Rod-Coil Poly(3-hexylthiophene)-*block*-Poly(butyl acrylate) Thin Films for Field Effect Transistor Applications. *Macromolecules* **2017**, *50*, 1442–1452.

Chapter 3

Synthesis of Cellulose-Based Triblock Copolymers for Investigating Microphase Separation Behavior and Mechanical Properties: Comparisons with Amylose-Based Triblock Copolymers

3.1. Introduction

The development of polymeric materials from natural and renewable resources has recently gained international momentum in order to mitigate the increasing environmental issues.[1–3] Poly/oligosaccharides are particularly interesting as renewable raw materials because they are readily available from a wide range of plant biomass resources, such as sugar corn, sugarcane, seaweed, waste wood, and agricultural waste.[1] Furthermore, the unique characteristics of poly/oligosaccharides, including their biocompatibilities, biodegradabilities, strong hydrophilicities, optical activities, and low toxicities, make them significantly attractive raw materials for creating novel sustainable polymers. Currently, the polymer industry employs carbohydrates mostly as carbon resources for producing bioplastics, such as polylactide, poly(3-hydroxybutyric acid), poly(ethylene furanoate), and poly(2,5-furandicarboxylic acid), through chemical or fermentation processes, despite the fact that cellulose and its derivatives have been used as precursors in their native states.[1–3] Using poly/oligosaccharides in their native or marginally modified forms may save the energy and time required to transform them to green and sustainable materials, while preserving their unique characteristics.

Directly combining poly/oligosahhcaride with synthetic polymers is an effective method for achieving the abovementioned goals; this combination can be achieved mainly through grafting synthetic polymer chains onto polysaccharide main chains,[4–7] grafting poly/oligosaccharide chains onto synthetic polymer main chains,[8,9] and tethering poly/oligosaccharides to synthetic polymers to form block copolymers (BCPs).[10–13] Among these, the approach that creates poly/oligosaccharide-based BCPs is particularly attractive because of the microphase-separation and micelle-forming abilities of these polymers, which are useful when designing elastomers,[14–16] lithographic materials,[17–19] electrical materials,[20–23] and drug-delivery nanocarriers.[24–26] Poly/oligosaccharide-based BCPs remain neglected compared to the other two poly/oligosaccharide-containing polymer types because of the difficulties associated with their syntheses. Recent progress in polymer chemistry has witnessed the evolution of strategies for the production of poly/oligosaccharide-based BCPs since the pioneering syntheses of poly/oligosaccharide-based BCPs were published in 1961.[13,27] For example, cellulose-*b*-polystyrene, dextran-*b*-polystyrene, and maltoheptaose-*b*-poly(*ε*-caprolactone) have been successfully synthesized by radical polymerization and ring-opening polymerization from the reducing end of the poly/oligosaccharide segment.[13,28–31] However, such a synthetic strategy is incompatible with ionic polymerization methods. An alternative pathway for producing poly/oligosaccharide-BCPs involves the end-to-end coupling of end-functionalized carbohydrates and synthetic polymer segments, to which various synthetic polymer segments can be joined.[11,12,17–19,26] In particular, the copper-catalyzed azido-alkyne cycloaddition (CuAAC) reaction has been widely employed for end-to-end coupling because of its high efficiency, simplicity, and functional group tolerance.[32–34]

Most poly/oligosaccharide-based BCPs comprise dextran and amylose. Surprisingly, there are a few reports on cellulose-containing BCPs, although cellulose and amylose comprise glucose and similar primary structures, with the only structural difference being the presence of α-1,4 linkages in amylose and β-1,4 linkages in cellulose. Consequently, little is known about the self-assembly behavior of cellulose-based BCPs in their solid and solution states, and their fundamental physical properties have not been studied in detail to date. Because cellulose can be obtained from inedible biomass, preventing the compete with food supply, it is highly attractive as a block partner for constructing poly/oligosaccharide-based BCPs. Moreover, it is probable that such cellulose-based BCPs will exhibit enhanced self-assembly properties as well as good mechanical performance because cellulose is highly rigid and crystalline.

However, directly using native cellulose to construct BCPs is significantly challenging because cellulose does not dissolve in common solvents or melt even at high temperatures because of strong inter- and intramolecular hydrogen bonding. This fundamental drawback has historically been overcome by chemically modifying the hydroxyl groups with other functional groups, such as cellulose ethers or esters. Cellulose acetate, one of the most common cellulose derivatives, is readily soluble in common organic solvents and melt-processable. Hence, it has been widely commercialized at different degrees of substitution for use as membranes, textiles, protecting films for polarizers, and cigarette filters. In addition, cellulose acetate has recently gained considerable attention because of its potential biodegradability.[35,36] Therefore, poly/oligosaccharide-based BCPs containing cellulose acetate segments are of significant interest in terms of their synthesis, self-assembly, and physical properties. Recently, the groups of Matson, Edgar, and Kamitakahara reported BCPs containing cellulose derivatives such as cellulose acetate-*b*-polybutadiene-*b*-cellulose acetate,[37] cellulose acetate-*b*-oligoamide,[38] and trimethyl cellulose-*b*-poly(ethylene glycol).[39] However, the microphase-separation behavior and mechanical properties of these BCPs have not been investigated. Furthermore, the advantages of using cellulose derivatives over other poly/oligosaccharides remain unclear.

Herein, the author reports a pioneering comparative study of cellulose-based BCPs and their amylose-based counterparts with the aim of unveiling the unique characteristics imparted by cellulose segments. To this end, the author designed and synthesized ABA-type cellooligosaccharide- and malooligosaccharide-based BCPs, namely, cellooligosaccharide triacetate-*b*-poly(δ-decanolactone)-*b*-cellooligosaccharide triacetates (AcCel$_n$-*b*-PDL-*b*-AcCel$_n$s) and maltooligosaccharide triacetate-*b*-poly(δ-decanolactone)-*b*-maltooligosaccharide triacetates (AcMal$_n$-*b*-PDL-*b*-AcMal$_n$s), as shown in **Scheme 3.1** Poly(δ-decanolactone) (PDL) is an amorphous, rubbery, aliphatic polyester that can be synthesized from plant-derived lactone monomers. The “hard moiety-*b*-soft moiety-*b*-hard moiety” ABA-type triblock architecture is important because it endows the BCPs with elastomer-like properties of the well-known styrene-based thermoplastic elastomers. In fact, Satoh and Isono et al. recently reported completely bio-based elastomers consisting of a maltooligosaccharide as the hard segment and PDL as the soft segment.[14] Importantly, X-ray scattering experiments and atomic force microscopy revealed that the AcCel$_n$-*b*-PDL-*b*-AcCel$_n$s are more likely to microphase-separate compared to their amylose counterparts. Furthermore, the author found that the AcCel$_n$-*b*-PDL-*b*-AcCel$_n$s had significantly superior mechanical properties compared to the AcMal$_n$-*b*-PDL-*b*-AcMal$_n$s, in terms of Young’s moduli, elongations at break, and toughnesses.

Scheme 3.1. Syntheses of AcCel$_n$-*b*-PDL-*b*-AcCel$_n$ and AcMal$_n$-*b*-PDL-*b*-AcMal$_n$

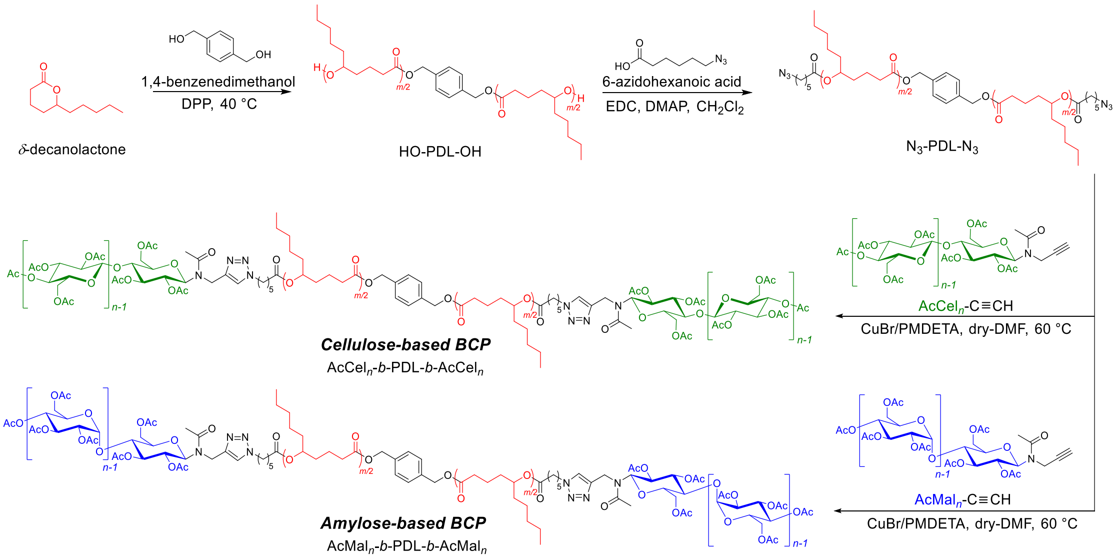

3.2. Experimental Section

3.2.1. Materials

α-D-Glucose 1-phosphate disodium salt hydrate (*α*G1P, ≥97%), 4-(2-hydroxyethyl)-1-piperazineethanesulfonic acid (HEPES, ≥99.5%, titration), copper(I) bromide (CuBr, 99.999%), and 2,5-dihydroxybenzonoic acid (98%) were purchased from Sigma Aldrich and used as received. D(+)-cellobiose (CB), sodium sulfate (Na_2SO_4, >99.0%), anhydrous magnesium sulfate ($MgSO_4$, >95%), propargylamine (>95%), acetic anhydride (>97%), hydrochloric acid (HCl, 35–37%), toluene (>99.0%), ethyl acetate (AcOEt, >99.3%), acetone (>99.0%), *N*,*N*-dimethylformamide (DMF, >99.0%), *N*,*N*-dimethylethanamide (DMAc, >99.0%), lithium chloride (LiCl, >99.0%), and dry CH_2Cl_2 (>99.5%; water content, <0.001%) were purchased from Kanto Chemical Co., Inc. and used as received. Dichloromethane (CH_2Cl_2, >99.0%) and methanol (MeOH, 99.6%)

were purchased from Junsei Chemical Co., Ltd., and used as received. *N*,*N*,*N'*,*N''*,*N''*-Pentamethyldiethlenetriamine (PMDETA, >98.0%), diphenyl phosphate (DPP, >98.0%), 1,4-benzenedimethanol (BDM, >99.0%), 1-(3-dimethylaminopropyl)-3-ethylcarbodiimide hydrochloride (EDC·HCl, >98.0%), and 4-dimethylaminopyridine (DMAP, >99.0%) were purchased from Tokyo Chemical Industry Co., Ltd. (TCI) and used as received. FujioligoG67 (Mal_n) was supplied from Nihon Shokuhin Kako Co., Ltd., and was co-evaporated with a mixed solvent of toluene and MeOH (9/1 (v/v)) and dried under vacuum to remove water for few days before use. δ-decanolactone (δ-DL) was purchased from TCI and purified by distillation over CaH_2 under reduced pressure. Dowex® 50WX2 hydrogen form was purchased from Sigma Aldrich and was washed with MeOH before use. Cellodextrin phosphorylase (CDP)[40] and 6-azidohexanoic acid[41] were prepared according to previous reported methods.

3.2.2. Instruments

^{1}H NMR measurement

^{1}H NMR (400 MHz) spectra were obtained using a JEOL JNM-ECS 400 instrument at 25 °C.

Size exclusion chromatography (SEC)

SEC measurements were performed at 40 °C in THF (flow rate, 1.0 mL min^{-1})

using a Jasco high-performance liquid chromatography system (PU-980 Intelligent HPLC Pump, CO-2065 Plus Intelligent Column Oven, RI-2031 Plus Intelligent RI Detector, and DG-2080-53 Degasser) equipped with a Shodex KF-G guard column (4.6 mm × 10 mm; particle size, 8 μm) and two Shodex KF-804L columns (linear; particle size 7 μm; 8.0 mm × 300 mm; exclusion limit, 4×10^4) or in DMF (flow rate, 0.6 mL min^{-1}; containing 0.01 mol L^{-1} LiCl) using a Jasco HPLC system (PU-980 Intelligent HPLC Pump, CO-965 Column Oven, RI-930 Intelligent RI Detector, and DG-2080-53 Degasser) equipped with a Shodex KD-G guard column (4.6 mm × 10 mm; particle size, 8 μm), a Shodex Asahipak GF-310 HQ column (linear; particle size, 5 μm; 7.5 mm × 300 mm; exclusion limit, 4×10^4) and a Shodex Asahipak GF-7 M HQ column (linear; particle size, 9 μm; 7.5 mm × 300 mm; exclusion limit, 1.0×10^7). The number-average molecular weight ($M_{\text{n,SEC}}$) and dispersity ($Đ$) were calculated based on polystyrene standards.

Preparative SEC

The preparative SEC purification was performed in $CHCl_3$ (3.5 mL min^{-1}) at room temperature using LC-9201 liquid chromatography system (Japan Analytical Industry Co. Ltd. (JAI)) equipped with a JAI JAIGEL-3H column (20 mm × 600 mm; exclusion limit, 7×10^4) and a JAI RI-50s refractive index detector.

Fourie transform infrared spectroscopy (FT-IR)

The FT-IR spectra were obtained using a PerkinElmer Frontier MIR spectrometer equipped with a single reflection diamond universal attenuated total reflection (ATR) accessory.

Differential scanning calorimetry (DSC) measurement

The DSC experiments were performed using a Hitachi DSC 7000X under nitrogen atmosphere. All polymer samples were heated to 200 °C, cooled to −100 °C, and heated again to 200 °C at the heating and cooling rate of 10 °C min^{-1}.

Thermogravimetric analysis (TGA)

The TGA analysis was performed using Hitachi STA200RV under nitrogen atmosphere. All polymer samples were heated up to 600 °C at the heating rate of 10 °C min^{-1}.

Matrix-assisted laser desorption ionization time-of-flight mass spectrometry (MALDI-TOF MS)

The MALDI-TOF MS of the obtained products was performed using an AB Sciex TOF/TOF 5800 system equipped with a 349-nm Nd:YAG laser. Five hundred shots were accumulated for the spectra and an acceleration voltage was adjusted between 10 and 30 kV depending on both the molecular weight and the nature of each analyzed compounds in the reflector mode. For the ethynyl-functionalized cellooligosaccharide, the sample was prepared by mixing an ultrapure water dispersion of the compound (1.0

mg mL^{-1}, 200 μL), acetonitrile solution of a matrix (2,5-dihydroxybenzoic acid, 10 mg mL^{-1}, 100 μL), and trifluoroacetic acid (0.2% (v/v), 300 μL). A 1 μL aliquot of this mixture was loaded on a sample plate. For ethynyl-functionalized cellooligosaccharide acetate, the ethynyl-functionalized maltooligosaccharide, and ethynyl-functionalized maltooligosaccharide acetate, the samples were prepared by mixing a THF solution of the compound (5 mg mL^{-1}, 100 μL) and a matrix (2,5-dihydroxybenzoic acid, 10 mg mL^{-1}, 500 μL). A 1 μL aliquot of this mixture was loaded on a sample plate, which was coated by an acetone solution of NaI (1 μL, 1 mmol L^{-1}) as the cationic agent.

Atomic force microscopy (AFM) observation

The AFM phase images were obtained using a Molecular Imaging PicoPlus atomic force microscope operating in the tapping mode with a silicon cantilever (Nanoworld AG, NANOSENSORS™ PPP-NCH) having resonant frequency and spring constant of 190 kHz and 48 N m^{-1}, respectively. The thin films for the AFM observation were prepared by spin-coating (2,000 rpm for 60 s) the polymer solution in toluene (1% (w/w)) onto a Si substrate with a native oxide layer.

Small-angle X-ray scattering (SAXS) and wide-angle X-ray diffraction (WAXD)

The SAXS and WAXD measurements of the obtained polymers were performed at the BL-6A beamline of the Photon Factory in the High Energy Accelerator Research Organization (KEK, Tsukuba, Japan) using X-ray beams with λ = 0.15 nm at room temperature. The scattering data were collected by a 2D detector (PILATUS3 1M (SAXS) (Dectris Ltd.)), where the samples-to-detector distance was set to be 1.5 m for SAXS measurement. The scattering angle (θ) was calibrated using silver behenate (Nagara Science Co., Ltd) as the standard and derived the scattering vector (q) from Bragg's equation ($|q| = (4\pi/\lambda)\sin(\theta/2)$). The domain-spacing ($d$) value was calculated by $d = 2\pi/q^*$ (q^* is principal scattering peak position). The polymer films or powders were sandwiched by two pieces of Kapton tapes with a spacer of a stainless washer, which were applied for the measurement.

Tensile testing

The tensile tests were performed with an EZ-SX (SHIMADZU CO.) tensile tester at the temperature of 23 °C and the humidity of 55%. The film samples for the tensile tests were prepared by casting the polymer solutions from the toluene solution (20% (w/w) for AcCel$_n$-*b*-PDL-*b*-AcCel$_n$ and 30% (w/w) for AcMal$_n$-*b*-PDL-*b*-AcMal$_n$) on a Teflon dish and drying at r.t. for 15 h followed by vacuum drying at room temperature for 1 day. After drying, the film samples were cut into a dog bone shape of 12 × 3 × 0.05–0.15 mm. For each polymer, five samples were tested and the average values of the elastic modulus, strain at break, stress at break, and toughness were calculated. The crosshead speed applied during the measurements was 10 mm min^{-1}. The strain at break was taken as the engineering strain where the stress drops suddenly.

3.2.3. Synthetic details

Synthesis of ethynyl-functionalized cellobiose (CB−C≡CH)[42]

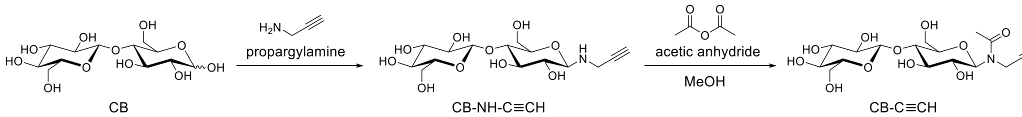

CB (10.00 g, 14.6 mmol) and propargylamine (20.7 mL, 323 mmol) were added to a round-bottom flask, and the mixture was stirred for 5 days under a nitrogen atmosphere. The mixture was co-evaporated with a mixed solvent of toluene and MeOH (9/1 (v/v)) to remove the excessive propargylamine. The obtained product was dissolved in MeOH and then precipitated in CH_2Cl_2. The precipitate was filtrated and washed with a mixture of MeOH and CH_2Cl_2 (1/4 (v/v), 100 mL). A solution of acetic anhydride in MeOH (1/20 (v/v), 480 mL) was added to the obtained precipitate and the whole mixture was stirred for 20 h at room temperature. After the reaction, the solvent was subjected to rotary evaporation, followed by co-evaporation of acetic anhydride with a mixed solvent of toluene and MeOH (1/1 (v/v)) to give CB−C≡CH as a white solid (11.1 g). Yield: 89.3%.

^{1}H NMR (400 MHz, D_2O): δ (ppm) 5.52, 5.07 (2x d, rotamers, −C*H*N(Ac)−), 4.50 (d, 1H, J = 7.6 Hz, *H*-1^{CB}), 4.31–3.25 (m, *H*-2, -3, -4, -5, -6^{CB}, O*H*^{CB},−N(Ac)CH_2−), 2.71, 2.55 (2x s, rotamers,−CC*H*), 2.29, 2.21 (2x s, rotamers, −N(C=O)CH_3).

Synthesis of ethynyl-functionalized cellooligosaccharide (Cel$_n$−C≡CH) using CDP

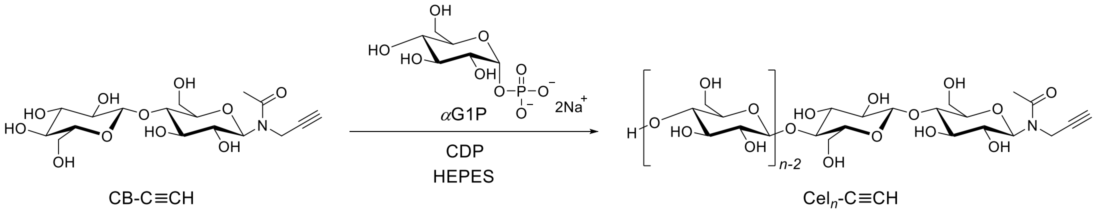

200 mM D-glucose 1-phosphate (*α*G1P) and 50 mM CB−C≡CH was incubated with 10 mg L^{-1} CDP in 500 mM 4-(2-hydroxyethyl)-1-piperazineethanesulfonic acid (HEPES) buffer solutions (pH 7.5, 300 mL, divided into 30 centrifuge tubes) at 60 °C. After incubating for 7 days, the reaction mixtures were centrifuged to isolate the insoluble product and the resulting pellet was washed with water purified by reverse osmosis filters (RO water) followed by centrifugation at 13,000 rpm for 10 min at 4 °C several times to give swollen Cel$_n$−C≡CH with water. The aliquot of the obtained product was dried by vacuum to calculate the yield (3.19 g). Yield: 23.0%.

$M_{\mathrm{n,NMR}}$ = 1,230 g mol^{-1}, $M_{\mathrm{n,MALDI}}$ = 1,190 g mol^{-1}.

^{1}H NMR (400 MHz, 10% (w/w) NaOD-D$_2$O): δ (ppm) 5.39, 4.88 (2x d, rotamers, 1H, −C*H*N(Ac)−), 4.48 (m, *H*-1$^{\mathrm{Cel}n}$), 4.31–3.21 (m, *H*-2, -3, -4, -5, -6$^{\mathrm{Cel}n}$, O*H*$^{\mathrm{Cel}n}$, −N(Ac)C*H*$_2$−), 2.54 (m, −CC*H*), 2.30, 2.23 (2x m, −N(C=O)C*H*$_3$).

Synthesis of ethynyl-functionalized cellooligosaccharide acetate (AcCel*n*−C≡CH)

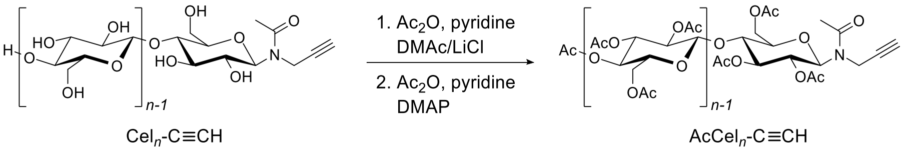

Wet Cel*n*−C≡CH (3.19 g, by dry weight) was dispersed in acetone (40 mL) and centrifuged twice (7,000 rpm/30 min/0 °C, 7,000 rpm/15 min/0 °C). The pellet was dispersed in acetone (100 mL) and stirred over night at room temperature. After the centrifugation (7,000 rpm/15 min/0 °C), the pellet was washed with DMAc (40 mL) followed by centrifugation (7,000 rpm/15 min/0 °C). The pellet was dispersed in DMAc (40 mL) and stirred at room temperature. After 3 h, LiCl (2.14 g, 50.5 mmol) was added to the mixture and kept stirring over-night. After adding a solution of acetic anhydride in pyridine (1/1 (v/v), 20 mL), the mixture was stirred 5 more days. The reaction mixture was diluted with CH_2Cl_2 and washed with dilute HCl (100 mL) three times. The organic layer was dried over $MgSO_4$ and concentrated to give a white solid. The obtained solid (3.02 g) and DMAP (76 mg, 0.62 mmol) was added to a solution of acetic anhydride in pyridine (1/2 (v/v), 60 mL) and stirred at room temperature for 70 h. After removing the solvent by evaporation, the residue was dissolved in ethyl acetate and washed with 1 M HCl and saturated $NaHCO_3$ solutions. The organic layer was dried over Na_2SO_4 and concentrated to give AcCel*n*−C≡CH as a pale yellow solid (3.03 g). Yield: 55.0%.

$M_{n,NMR}$ = 1,900 g mol^{-1}, $M_{n,MALDI}$ = 2,100 g mol^{-1}, $M_{n,SEC}$ = 2,080 g mol^{-1} (THF), $Đ$ =

1.06 (THF).

^{1}H NMR (400 MHz, CDCl$_3$): δ (ppm) 5.84, 5.65 (2x d, rotamers, −C*H*N(Ac)−), 5.30–4.76, 4.60–4.31, 4.25–3.47 (m, *H*-1, -2, -3, -4, -5, -6$^{\mathrm{AcCel}n}$, −N(Ac)C*H*$_2$−), 2.58, 2.56 (2x s, rotamers, –CC*H*), 2.40–1.76 (m, C*H*$_3$-Ac$^{\mathrm{AcCel}n}$, −N(C=O)C*H*$_3$).

Synthesis of ethynyl-functionalized maltooligosaccharide (Mal_n−C≡CH)

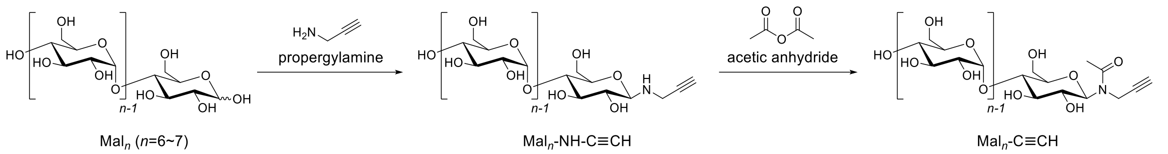

Mal_n (14.0 g) and propargylamine (15.6 mL, 243 mmol) were added to a round-bottom flask and the mixture was stirred for 5 days under the nitrogen atmosphere. The mixture was diluted with MeOH to remove the insoluble part with the high molecular weight, and the soluble part was then poured into CH_2Cl_2. The resulting precipitate was added to a solution of acetic anhydride in MeOH (1/20 (v/v), 1050 mL) and stirred for 45 h at room temperature. After the solvent removal, acetic anhydride was removed by co-evaporation with a mixed solvent of toluene and MeOH (1/1 (v/v)) followed by precipitation into CH_2Cl_2. The precipitate was then dissolved in MeOH and poured into EtOH to give Mal_n−C≡CH as a white solid (3.21 g). Yield: 21.2%.

$M_{\mathrm{n,NMR}}$ = 1,070 g mol^{-1}, $M_{\mathrm{n,MALDI}}$ = 1,080 g mol^{-1}, $M_{\mathrm{n,SEC}}$ = 2,650 g mol^{-1} (DMF), $Đ$ = 1.11 (DMF).

^{1}H NMR (400 MHz, D_2O): δ (ppm) 5.51, 5.06 (2x d, rotamers, −C*H*N(Ac)−), 5.43–5.30 (br, H-1$^{\mathrm{Mal}n}$), 4.31–3.30 (m, *H*-2, -3, -4, -5, -6$^{\mathrm{Mal}n}$, O*H*$^{\mathrm{Mal}n}$, −N(Ac)CH_2−), 2.39, 2.21 (2x s, rotamers, −N(C=O)CH_3).

Synthesis of ethynyl-functionalized maltooligosaccharide acetate (AcMal$_n$−C≡CH)

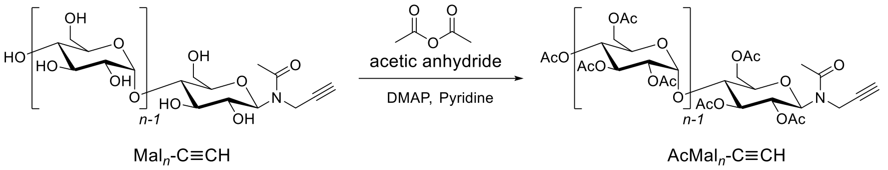

Mal$_n$−C≡CH (3.50 g, 3.27 mmol) and DMAP (76 mg, 0.62 mmol) were added to a solution of acetic anhydride in pyridine (1/2 (v/v), 105 mL) and stirred for 70 h at room temperature. After removing the solvent by evaporation, the residue was dissolved in ethyl acetate and washed with 1 M HCl, saturated $NaHCO_3$, and water. The organic layer was dried over Na_2SO_4 and concentrated by evaporation. The product was purified by preparative SEC in $CHCl_3$ to remove low molecular weight fraction, to afford AcMal$_n$−C≡CH as a pale yellow solid (2.22 g). Yield: 38.8%.

$M_{\text{n,NMR}}$ = 1,930 g mol^{-1}, $M_{\text{n,MALDI}}$ = 1,950 g mol^{-1}, $M_{\text{n,SEC}}$ = 1,490 g mol^{-1} (THF), $Đ$ = 1.09 (THF).

^{1}H NMR (400 MHz, $CDCl_3$): δ (ppm) 6.22, 5.91 (2x d, rotamers, −C*H*N(Ac)−), 5.65–3.64 (m, *H*-2, -3, -4, -5, -6$^{\text{AcMal}n}$, −N(Ac)C*H*$_2$−), 2.37–1.80 (m, C*H*$_3$-Ac$^{\text{AcMal}n}$, −N(C=O)C*H*$_3$).

Synthesis of dihydroxyl-functionalized poly(*δ*-decanolactone) (HO–PDL–OH)

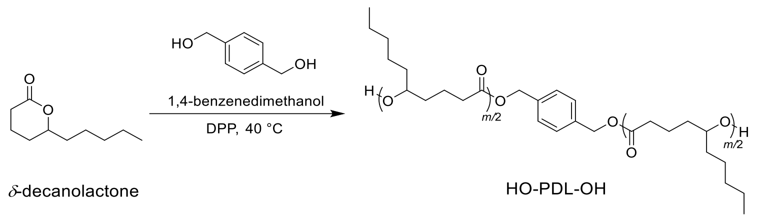

Synthesis of HO–PDL$_{6k}$–OH

Typical polymerization procedure is as follows (Method A). In an argon-filled glovebox, *δ*-DL (10.0 g, 58.7 mmol), 1,4-benzenedimethanol (199 mg, 1.44 mmol), and DPP (360 mg, 1.44 mmol) were placed in a Schlenk flask. The Schlenk flask was sealed with a septum and taken out from the glovebox. The whole mixture was stirred at 40 °C under an argon atmosphere in an oil bath. After stirring for 9 h, the monomer conversion was reached 73% as revealed by ^{1}H NMR analysis of the aliquot of the mixture. The polymerization mixture was poured into MeOH, and the precipitated product was washed with MeOH several times to remove the unreacted monomer and catalyst. Finally, HO−PDL$_{6k}$−OH was obtained as a colorless viscous liquid (7.80 g). Yield: 76.5%.

$M_{n,NMR}$ = 5,590 g mol^{-1}, $M_{n,SEC}$ = 8,770 g mol^{-1} (THF), $Đ$ = 1.07 (THF).

^{1}H-NMR (400 MHz, CDCl$_3$): *δ* (ppm) 7.28 (s, aromatic), 5.03 (s, $-\text{Ph}-\text{C}H_2\text{O}-$), 4.91−4.72 (m, main chain $-\text{CH}_2\text{C}H(\text{C}_5\text{H}_{11})\text{O}-$), 3.57−3.47 (br, *ω*-chain end $-\text{CH}_2\text{C}H(\text{C}_5\text{H}_{11})\text{OH}$), 2.34−2.14 (m, $-(\text{C=O})\text{C}H_2\text{CH}_2-$), 1.76–1.32 (m, $-(\text{C=O})\text{CH}_2\text{C}H_2\text{C}H_2\text{CH}(\text{C}H_2(\text{CH}_2)_3\text{CH}_3)\text{O}-$), 1.31–1.10 (br, $-\text{CH}(\text{CH}_2(\text{C}H_2)_3\text{CH}_3)\text{O}-$), 0.92−0.68 (m, $-\text{C}H_3$).

Synthesis of HO–PDL$_{10k}$–OH

The Method A was used for the polymerization of δ-DL (10.0 g, 58.7 mmol) with 1,4-benzenedimethanol (98 mg, 0.71 mmol) and DPP (178 mg, 0.710 mmol) to give HO–PDL$_{10k}$–OH as a colorless viscous liquid (6.29 g). Yield: 62.3%.

$M_{n,NMR}$ = 10,000 g mol^{-1}, $M_{n,SEC}$ = 12,800 g mol^{-1} (THF), $Đ$ = 1.06 (THF).

^{1}H-NMR (400 MHz, $CDCl_3$): δ (ppm) 7.34 (s, aromatic), 5.10 (s, −Ph−CH_2O−), 4.95−4.80 (m, main chain −CH_2CH(C_5H_{11})O−), 3.64−3.54 (m, ω-chain end −CH_2CH(C_5H_{11})OH), 2.40−2.17 (m, −(C=O)C$H_2$$CH_2$−), 1.72–1.41 (m, −(C=O)$CH_2CH_2CH_2$CH(C$H_2$($CH_2$)$_3$$CH_3$)O−), 1.38–1.14 (br, −CH(CH_2(CH_2)$_3$$CH_3$)O−), 0.95−0.79 (m, −C$H_3$).

Synthesis of HO–PDL$_{22k}$–OH

The Method A was used for the polymerization of δ-DL (10.0 g, 58.7 mmol) with 1,4-benzenedimethanol (49 mg, 0.35 mmol) and DPP (88 mg, 0.35 mmol) to give HO−PDL$_{22k}$−OH as a colorless viscous liquid (7.26 g). Yield: 72.2%.

$M_{\mathrm{n,NMR}}$ = 21,600 g mol^{-1}, $M_{\mathrm{n,SEC}}$ = 24,700 g mol^{-1} (THF), $Đ$ = 1.07 (THF).

^{1}H-NMR (400 MHz, $CDCl_3$): δ (ppm) 7.34 (s, aromatic), 5.10 (s, $-Ph-CH_2O-$), 4.93−4.81 (m, main chain $-CH_2CH(C_5H_{11})O-$), 3.66−3.55 (br, ω-chain end $-CH_2CH(C_5H_{11})OH$), 2.48–2.16 (m, $-(C{=}O)CH_2CH_2-$), 1.85–1.39 (m, $-(C{=}O)CH_2CH_2CH_2CH(CH_2(CH_2)_3CH_3)O-$), 1.37–1.14 (br, $-CH(CH_2(CH_2)_3CH_3)O-$), 0.95−0.78 (m, $-CH_3$).

Synthesis of diazido-functionalized poly(δ-decanolactone) (N_3−PDL−N_3)

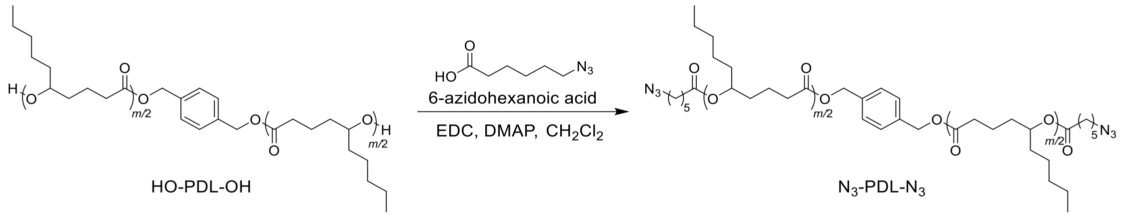

Synthesis of N_3−PDL_{6k}−N_3

A typical end azido-functionalization procedure is as follows (Method B). Prior to the reaction, a trace amount of MeOH in the HO−PDL_{6k}−OH was removed completely by coevaporation with dry toluene. HO−PDL_{6k}−OH (7.00 g, 1.25 mmol), 6-azidohexanoic acid (0.787 g, 5.01 mmol), EDC·HCl (1.20 g, 6.26 mmol), DMAP (0.765 g, 6.26 mmol), and dry CH_2Cl_2 (70 mL) were mixed in round-bottomed flask. After stirring for 96 h at room temperature, the mixture was purified in the same way as described in Method A to give N_3−PDL_{6k}−N_3 as a colorless viscous liquid (6.38 g). Yield: 86.3%.

$M_{n,NMR}$ = 5,900 g mol^{-1}, $M_{n,SEC}$ = 9,160 g mol^{-1} (THF), $Đ$ = 1.07 (THF).

^{1}H-NMR (400 MHz, $CDCl_3$): δ (ppm) 7.34 (s, aromatic), 5.10 (s, −Ph−CH_2O−), 4.94–4.80 (m, main chain −CH_2CH(C_5H_{11})O−), 3.27 (t, J = 6.9 Hz, −C$H_2$$N_3$), 2.39–2.22 (m, −(C=O)C$H_2$$CH_2$−), 1.73–1.38 (m, −(C=O)$CH_2CH_2CH_2$CH(C$H_2$($CH_2$)$_3$$CH_3$)O−, −C$H_2$$CH_2CH_2$$CH_2$−$N_3$), 1.38–1.16 (br, −CH($CH_2$(C$H_2$)$_3$$CH_3$)O−, −C$H_2$($CH_2$)$_2$−$N_3$), 0.95–0.78 (m, −C$H_3$).

Synthesis of N_3−PDL_{10k}−N_3

The Method B was used for the reaction of HO−PDL_{10k}−OH (6.00 g, 600 μmol) and 6-azidohexanoic acid (0.377 g, 2.40 mmol) in dry CH_2Cl_2 (60 mL) with EDC·HCl (0.575 g, 3.00 mmol) and DMAP (0.367 g, 3.00 mmol) to give N_3−PDL_{10k}−N_3 as a colorless viscous liquid (5.94 g). Yield: 96.0%.

$M_{\mathrm{n,NMR}}$ = 10,300 g mol^{-1}, $M_{\mathrm{n,SEC}}$ = 14,200 g mol^{-1} (THF), $Đ$ = 1.06 (THF).

^{1}H-NMR (400 MHz, $CDCl_3$): δ (ppm) 7.34 (s, aromatic), 5.10 (s, −Ph−CH_2O−), 4.94−4.81 (m, main chain, −CH_2CH(C_5H_{11})O−), 3.28 (t, J = 6.9 Hz, −C$H_2$$N_3$), 2.39–2.22 (m, −(C=O)C$H_2$$CH_2$−), 1.73–1.38 (m, −(C=O)$CH_2CH_2CH_2$CH(C$H_2$($CH_2$)$_3$$CH_3$)O−, −C$H_2$$CH_2CH_2$$CH_2$−$N_3$), 1.38–1.16 (br, −CH($CH_2$(C$H_2$)$_3$$CH_3$)O−, −C$H_2$($CH_2$)$_2$−$N_3$), 0.96−0.79 (m, −C$H_3$).

Synthesis of N_3−PDL_{22k}−N_3

The Method B was used for the reaction of HO−PDL_{22k}−OH (7.00 g, 324 μmol) and 6-azidohexanoic acid (0.204 g, 1.30 mmol) in dry CH_2Cl_2 (70 mL) with EDC·HCl (0.311 g, 1.62 mmol) and DMAP (198 mg, 1.62 mmol) to give N_3−PDL_{22k}−N_3 as a colorless viscous liquid (7.75 g). Yield: >99%.

$M_{n,NMR}$ = 21,900 g mol^{-1}, $M_{n,SEC}$ = 24,900 g mol^{-1} (THF), $Đ$ = 1.09 (THF).

^{1}H-NMR (400 MHz, $CDCl_3$): δ (ppm) 7.34 (s, aromatic), 5.10 (s, −Ph−CH_2O−), 4.83−4.80 (m , main chain, −CH_2CH(C_5H_{11})O−), 3.28 (t, J = 6.9 Hz, −CH_2N_3), 2.39–2.23 (m, −(C=O)CH_2CH_2−), 1.73–1.39 (m, −(C=O)CH_2CH_2CH_2CH(CH_2(CH_2)$_3CH_3$)O−, −CH_2CH_2CH_2CH_2−N_3), 1.39–1.16 (br, −CH(CH_2(CH_2)$_3CH_3$)O−, −CH_2(CH_2) $_2$−N_3), 0.95−0.79 (m, −CH_3).

Synthesis of ABA-type BCP consisting of cellooligosaccharide acetate and poly(*δ*-decanolactone) (AcCel*ₙ*-*b*-PDL-*b*-AcCel*ₙ*) via click reaction

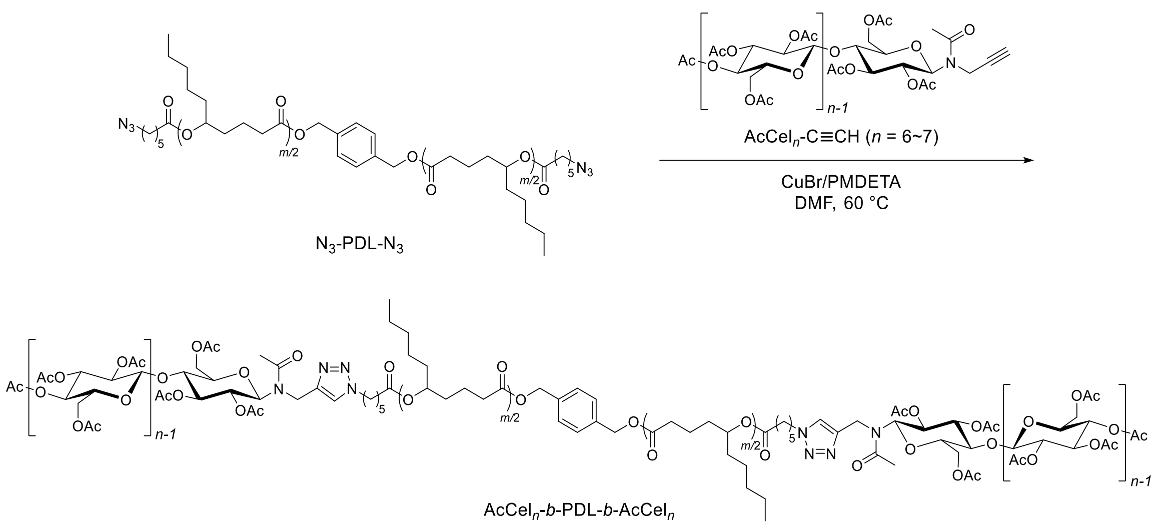

Synthesis of AcCel*ₙ*-*b*-PDL$_{6k}$-*b*-AcCel*ₙ*

A typical click reaction procedure is as follows (Method C). A degassed solution of N_3–PDL$_{6k}$–N_3 ($M_{n,NMR}$ = 5,900 g mol^{-1}, 1.00 g, 169 μmol) and PMDETA (124 μL, 593 μmol) in DMF (10 mL) was transferred to a Schlenk tube in which AcCel*ₙ*–C≡CH (925 mg, 441 μmol) and CuBr (85 mg, 0.59 mmol) were placed. The mixture was stirred for 55 h at 65 °C under an argon atmosphere. After cooling to room temperature, Dowex® 50WX2 and a few drops of water were added to remove Cu catalyst. The polymer was purified by the preparative SEC using $CHCl_3$ to remove unreacted AcCel*ₙ*–C≡CH, and the resulted solution was concentrated and dried under vacuum to give AcCel*ₙ*-*b*-PDL$_{6k}$-*b*-AcCel*ₙ* as a yellow elastic material (1.16 g). Yield: 66.2%.

$M_{n,SEC}$ = 14,100 g mol^{-1} (THF), $Đ$ = 1.04 (THF), $M_{n,total}$= 10,100 g mol^{-1}.

^{1}H NMR (400 MHz, $CDCl_3$): δ (ppm) 7.52, 7.41 (2x s, rotamers, triazole methine), 7.34

(s, aromatic), 5.97−5.90 (br, $-\mathrm{C}H(\mathrm{NAc})-$), 5.27−3.45 (m, $-\mathrm{Ph}-\mathrm{C}H_2\mathrm{O}-$, $-\mathrm{CH_2C}H(\mathrm{C_5H_{11}})\mathrm{O}-$, $-\mathrm{CH_2C}H_2-$triazole−, H-1, 2, -3, -4, -5, -6$^{\mathrm{AcCel}n}$, $-\mathrm{N(Ac)C}H_2-$), 2.45–1.83 (m, $-(\mathrm{C{=}O})\mathrm{C}H_2\mathrm{CH_2}-$, C$H_3$ in Ac$^{\mathrm{AcCel}n}$, $-\mathrm{N(C{=}O)C}H_3$), 1.77−1.42, (m, $-(\mathrm{C{=}O})\mathrm{CH_2(C}H_2)_2\mathrm{CH(C}H_2(\mathrm{CH_2})_3\mathrm{CH_3})\mathrm{O}-$, $-\mathrm{C}H_2\mathrm{CH_2C}H_2\mathrm{CH_2}-$triazole−), 1.42−0.99, (m, $-\mathrm{CH(CH_2(C}H_2)_3\mathrm{CH_3)O}-$, $-\mathrm{C}H_2(\mathrm{CH_2})_2-$triazole−), 0.88 (t, J = 6.6 Hz, $-\mathrm{C}H_3$)

Synthesis of AcCel$_n$-*b*-PDL$_{10k}$-*b*-AcCel$_n$

The Method C was used for the click reaction of N_3−PDL$_{10k}$−N_3 ($M_{n,NMR}$ = 10,300 g mol^{-1}, 1.00 g, 97.0 µmol) and AcCel$_n$−C≡CH (530 mg, 252 µmol) in DMF (10 mL) with CuBr (39 mg, 0.27 mmol) and PMDETA (57 µL, 0.27 mmol) to synthesize AcCel$_n$-*b*-PDL$_{10k}$-*b*-AcCel$_n$. The crude product was purified by preparative SEC to give AcMal$_n$-*b*-PDL$_{10k}$-*b*-AcMal$_n$ as a yellow elastic material (1.13 g). Yield: 80.3%.

$M_{n,SEC}$ = 19,200 g mol^{-1} (THF), $Đ$ = 1.04 (THF), $M_{n,total}$= 14,500 g mol^{-1}.

^{1}H NMR (400 MHz, $CDCl_3$): δ (ppm) 7.52, 7.41 (2x s, rotamers, triazole methine), 7.34 (s, aromatic), 5.96−5.90 (br, −CH(NAc)−), 5.23–3.47 (m, −Ph−CH_2O−, −CH_2CH(C_5H_{11})O−, −CH_2CH_2−triazole−, H-1, 2, -3, -4, -5, -6$^{\mathrm{AcCel}n}$, −N(Ac)CH_2−), 2.49–1.87 (m, −(C=O)C$H_2$$CH_2$−, C$H_3$ in Ac$^{\mathrm{AcCel}n}$, −N(C=O)CH_3), 1.76–1.41, (m, −(C=O)CH_2CH_2CH_2CH(CH_2(CH_2)$_3$$CH_3$)O−, −C$H_2$$CH_2CH_2$$CH_2$−triazole−), 1.38–1.15, (m, −CH(CH_2(CH_2)$_3$$CH_3$)O−, −C$H_2$($CH_2$)$_2$−triazole−), 0.88 (t, J = 6.8 Hz, −CH_3).

Synthesis of AcCel$_n$-*b*-PDL$_{22k}$-*b*-AcCel$_n$

The Method C was used for the click reaction of N_3−PDL$_{22k}$−N_3 ($M_{n,NMR}$ = 21,900 g mol^{-1}, 1.00 g, 46.0 µmol) and AcCel$_n$−C≡CH (252 mg, 120 µmol) in DMF (10 mL) with CuBr (23 mg, 0.16 mmol) and PMDETA (34 µL, 0.16 mmol). The crude product was purified by preparative SEC to give AcMal$_n$-*b*-PDL$_{22k}$-*b*-AcMal$_n$ as a yellow elastic material (537 mg). Yield: 45.0%.

$M_{n,SEC}$ = 30,800 g mol^{-1} (THF), $Đ$ = 1.06 (THF), $M_{n,total}$= 26,100 g mol^{-1}.

^{1}H NMR (400 MHz, $CDCl_3$): δ (ppm) 7.52, 7.41 (2x s, rotamers, triazole methine), 7.34 (s, aromatic), 5.97−5.90 (br, −C*H*(NAc)−), 5.28–3.47 (m, −Ph−CH_2O−, −CH_2C*H*(C_5H_{11})O−, −CH_2CH_2−triazole−, H-1, 2, -3, -4, -5, -6^{AcCeln}, −N(Ac)CH_2−), 2.49–1.86 (m, −(C=O)C$H_2$$CH_2$−, C$H_3$ in Ac^{AcCeln}, −N(C=O)CH_3), 1.83–1.39 (m, −(C=O)CH_2CH_2CH_2CH(CH_2(CH_2)$_3$$CH_3$)O−, −C$H_2$$CH_2CH_2$$CH_2$−triazole−), 1.39–0.96, (m, −CH(CH_2(CH_2)$_3$$CH_3$)O−, −C$H_2$($CH_2$)$_2$−triazole−), 0.88 (t, J = 6.6 Hz, −CH_3).

Synthesis of ABA-type BCP consisting of maltooligosaccharide acetate and poly(*δ*-decanolactone) (AcMal*ₙ*-*b*-PDL-*b*-AcMal*ₙ*) via click reaction

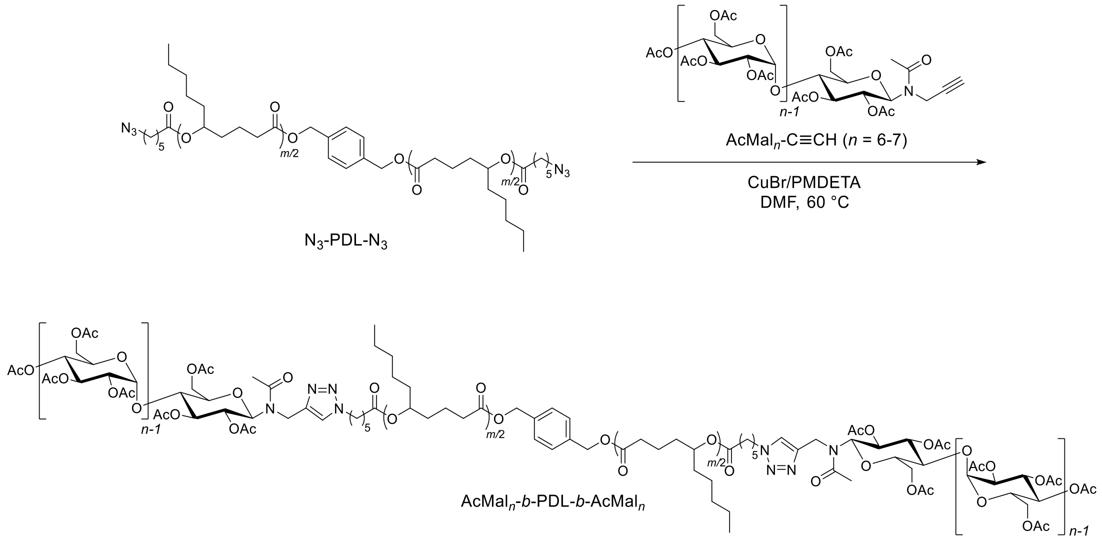

Synthesis of AcMal*ₙ*-*b*-PDL$_{6k}$-*b*-AcMal*ₙ*

The Method C was used for the click reaction of N_3−PDL$_{6k}$−N_3 ($M_{n,NMR}$ = 5,900 g mol^{-1}, 1.00 g, 169 μmol) and AcMal*ₙ*−C≡CH (859 mg, 441 μmol) in DMF (10 mL) with CuBr (85 mg, 593 μmol) and PMDETA (124 μL, 593 μmol). The crude product was purified by the preparative SEC to give AcMal*ₙ*-*b*-PDL$_{10k}$-*b*-AcMal*ₙ* as a yellow elastic material (1.02 g). Yield: 60.1%.

$M_{n,SEC}$ = 12,000 g mol^{-1} (THF), $Đ$ = 1.04 (THF), $M_{n,total}$= 9,800 g mol^{-1}.

^{1}H NMR (400 MHz, $CDCl_3$): δ (ppm) 7.52, 7.41 (2x s, rotamers, triazole methine), 7.34 (s, aromatic), 6.06–5.98 (br, –C*H*(NAc)–), 5.49–3.70 (m, −Ph−CH_2O−, −CH_2C*H*(C_5H_{11})O−, −CH_2CH_2−triazole−, H-1, 2, -3, -4, -5, -6$^{\text{AcMal}n}$, −N(Ac)CH_2−), 2.49–1.83 (m, −(C=O)C$H_2$$CH_2$−, C$H_3$ in Ac$^{\text{AcMal}n}$, −N(C=O)CH_3), 1.77–1.40, (m, main chain $-(CH_2)_2CH(CH_2(CH_2)_3CH_3)O-$, $-CH_2CH_2CH_2CH_2-$triazole), 1.38–0.98 (m, $-CH(CH_2(CH_2)_3CH_3)O-$, $-CH_2(CH_2)_2-$triazole), 0.88 (t, J = 6.6 Hz, $-CH_3$).

Synthesis of AcMal$_n$-*b*-PDL$_{10k}$-*b*-AcMal$_n$

The Method C was used for the click reaction of N_3−PDL$_{10k}$−N_3 ($M_{n,NMR}$ = 10,300 g mol^{-1}, 1.00 g, 97.0 μmol) and AcMal$_n$−C≡CH (492 mg, 252 μmol) in DMF (10 mL) with CuBr (39 mg, 0.27 mmol) and PMDETA (57 μL, 0.27 mmol) to synthesize AcMal$_n$-*b*-PDL$_{10k}$-*b*-AcMal$_n$. The crude product was purified by the preparative SEC to give AcMal$_n$-*b*-PDL$_{10k}$-*b*-AcMal$_n$ as a yellow elastic material (846 mg). Yield: 61.4%. $M_{n,SEC}$ = 17,000 g mol^{-1} (THF), $Đ$ = 1.04 (THF), $M_{n,total}$= 14,200 g mol^{-1}.

^{1}H NMR (400 MHz, $CDCl_3$): δ (ppm) 7.52, 7.41 (2x s, rotamers, triazole methine), 7.34 (s, aromatic), 6.04–5.99 (br, $-CH$(NAc)–), 5.48–3.77 (m, $-Ph-CH_2O-$, $-CH_2CH(C_5H_{11})O-$, $-CH_2CH_2-$triazole−, H-1, 2, -3, -4, -5, -6$^{AcMal n}$, $-N(Ac)CH_2-$), 2.41–1.80 (m, $-(C{=}O)CH_2CH_2-$, CH_3 in Ac$^{AcMal n}$, $-N(C{=}O)CH_3$), 1.75–1.41 (m, main chain $-(CH_2)_2CH(CH_2(CH_2)_3CH_3)O-$, $-CH_2CH_2CH_2CH_2-$triazole), 1.35–0.98 (m, $-CH(CH_2(CH_2)_3CH_3)O-$, $-CH_2(CH_2)_2-$triazole), 0.88 (t, J = 6.8 Hz, $-CH_3$).

Synthesis of AcMal$_n$-*b*-PDL$_{22k}$-*b*-AcMal$_n$

The Method C was used for the click reaction of N_3−PDL$_{22k}$−N_3 ($M_{n,NMR}$ = 21,900 g mol^{-1}, 1.00 g, 46.0 μmol) and AcMal$_n$−C≡CH (235 mg, 120 μmol) in DMF (10 mL) with CuBr (23 mg, 0.16 mmol) and PMDETA (34 μL, 0.16 mmol). The crude product was purified by the preparative SEC to give AcMal$_n$-*b*-PDL$_{22k}$-*b*-AcMal$_n$ as a yellow elastic material (309 mg). Yield: 26.2%.

$M_{n,SEC}$ = 28,300 g mol^{-1} (THF), $Đ$ = 1.04 (THF), $M_{n,total}$= 25,800 g mol^{-1}.

^{1}H NMR (400 MHz, $CDCl_3$): δ (ppm) 7.52, 7.41 (2x s, rotamers, triazole methine), 7.34 (s, aromatic), 6.04–5.99 (br, –C*H*(NAc)–), 5.45–3.55 (m, −Ph−CH_2O−, −CH_2C*H*(C_5H_{11})O−, −CH_2CH_2−triazole−, H-1, 2, -3, -4, -5, -6$^{\mathrm{AcMal}n}$, −N(Ac)CH_2−), 2.49–1.84 (m, −(C=O)C$H_2$$CH_2$−, C$H_3$ in Ac$^{\mathrm{AcMal}n}$, −N(C=O)CH_3), 1.84–1.40, (m, main chain −(CH_2)$_2$CH(CH_2(CH_2)$_3$$CH_3$)O−, −C$H_2$$CH_2CH_2$$CH_2$−triazole), 1.34–0.99 (m, −CH(CH_2(CH_2)$_3$$CH_3$)O−, −C$H_2$($CH_2$)$_2$−triazole), 0.88 (t, *J* = 6.6 Hz, −CH_3).

3.3. Results and Discussion

3.3.1. Synthesis of propargyl-functionalized cellooligosaccharide triacetate and maltooligosaccharide triacetate

The author initially synthesized propargyl-functionalized cellooligosaccharide triacetate (AcCel_n−C≡CH) and its maltooligosaccharide counterpart (AcMal_n−C≡CH). Some researchers reported the syntheses of cellooligosaccharides with different functional groups at the reducing end by the cellodextrin-phosphorylase-mediated (CDP-mediated) oligomerization of α-D-glucose-1-phosphase (αG1P) (glycosyl donor) in the presence of anomeric *O*-functionalized glucose (primer).[40,43–46] Inspired by this approach, the author envisaged the efficient CDP-mediated synthesis of propargyl-functionalized cellooligosaccharides (Cel_n−C≡CH) using propargyl-functionalized primers (**Scheme 3.2**, upper). In this Chapter, the author employed a CDP obtained from *Clostridium thermocellum*. Because His-tagged CDP expressed in *Escherichia coli* BL21(DE3) harbors the pET28a-CDP vector,[47] it was purified by nickel-nitrilotriacetic acid affinity chromatography.[40,47] CDP was obtained at a concentration of 7.7 mg mL^{-1} using the Bradford method. According to previous reports on CDP-mediated cellooligosaccharide syntheses, glucose and cellobiose are known to act as primers.[40,44] Therefore, to identify the optimal primer structure for the preparation of propargyl-functionalized cellooligosaccharides, the author examined cellooligosaccharide synthesis using glucose and cellobiose as primers (50 mM) in the presence of CDP (10 mg L^{-1}) and αG1P (200 mM) in 4-(2-hydroxyethyl)-1-piperazineethanesulfonic acid (HEPES) buffer solutions (pH = 7.5) at 60 °C for 7 d. Both reactions produced a cellooligosaccharide as a water-insoluble product; however, the yield was significantly higher when cellobiose (~23%) was used as the primer rather than glucose (~4%). Based on these results, the author employed *N*-acetyl-propargyl D-(+)-cellobiose (CB−C≡CH; **Figure 3.1** for ^{1}H NMR and FT-IR spectra) as the primer for the synthesis of Cel$_n$−C≡CH. The desired product was successfully synthesized in 23.0% yield under the aforementioned conditions using CB−C≡CH as the primer.

Scheme 3.2. Syntheses of propargyl-functionalized cellooligosaccharide triacetate and maltooligosaccharide triacetate

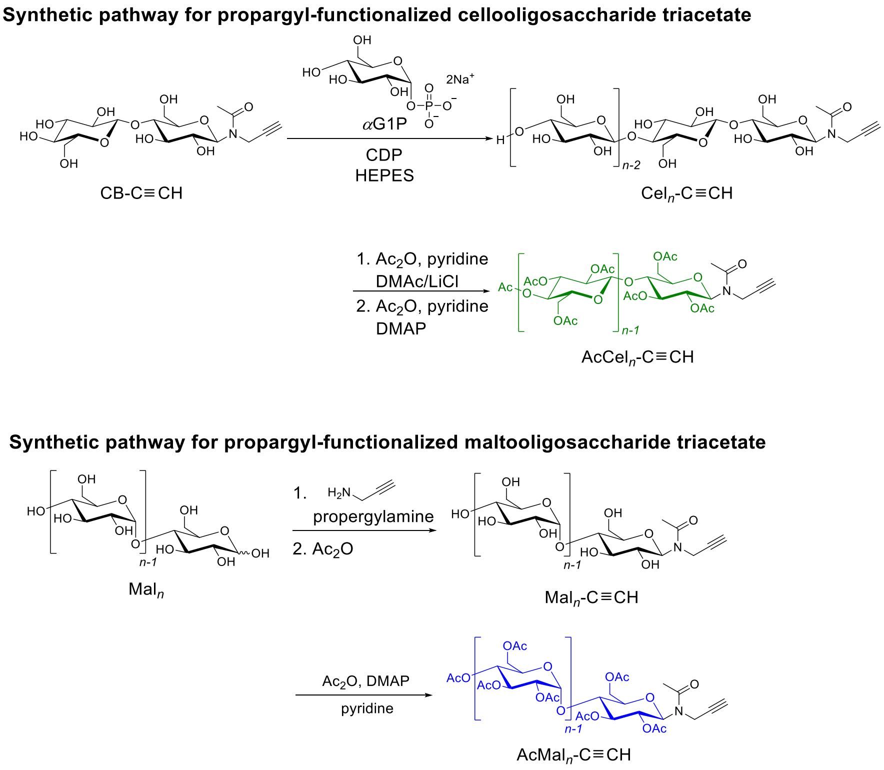

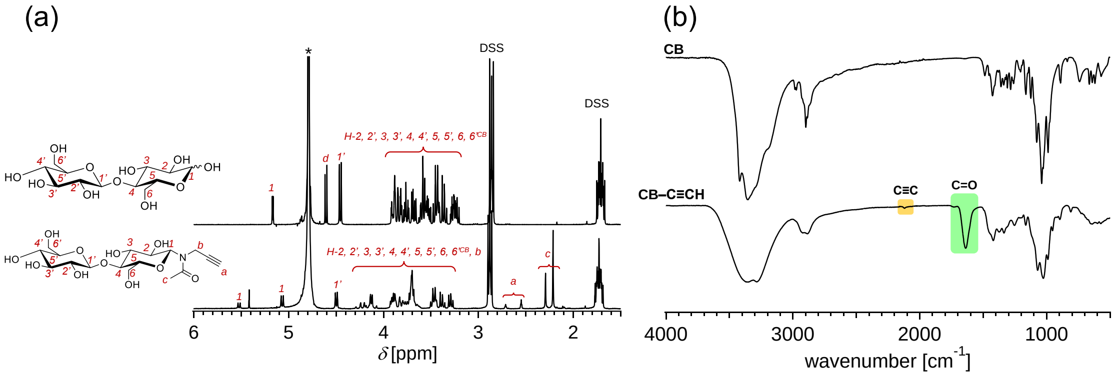

Figure 3.1. (a) ^{1}H NMR spectra (400 MHz, D_2O) and (b) FT-IR spectra of CB (upper) and CB–C≡CH (lower).

The ^{1}H NMR spectrum of the prepared Cel$_n$−C≡CH exhibited characteristic signals for the proton on the reducing terminal (*1*) at 5.39 and 4.88 ppm, the methine group (*a*) at 2.54 ppm, and the methyl groups (*b*) at 2.30 and 2.23 ppm; these signals were justifiably assigned to the expected structure (**Figure 3.2** (a), upper). The number-average degree of polymerization of the prepared Cel$_n$−C≡CH was calculated to be 7.19 by integrating and comparing the signals corresponding to the anomeric protons of the reducing terminal (*1*) and repeating units (*1*' and *1*"), which corresponds to a number-averaged molecular weight ($M_{\mathrm{n,NMR}}$) of 1,260. The FT-IR spectrum of the product shows a characteristic absorption band at 1,645 cm^{-1} that corresponds to the stretching of the amido C=O group on the anomeric functional group (**Figure 3.3** (a)). To investigate the structure in detail, the product was subjected to matrix-assisted laser desorption/ionization time-of-flight mass spectrometry (MALDI-TOF MS). The MALDI-TOF mass spectrum shows two series of repeating peaks separated by approximately 162 Da in the 900–1,600 Da range, among which one series is consistent with the Na^+ adducts, while the other with the K^+ adducts of $Cel_n{-}C{\equiv}CH$ (**Figure 3.2** (b)). For example, the peak at $m/z = 1254.4$ matches the theoretical molecular mass for the Na^+ adduct of the 7-mer in $Cel_n{-}C{\equiv}CH$ ($[M + Na]^+ = 1254.4$ Da). The synthesized $Cel_n{-}C{\equiv}CH$ mainly comprises 6- to 8-mers according to the MALDI-TOF mass spectrum. The number-average molecular weight was determined by MALDI-TOF MS ($M_{\mathrm{n,MALDI}}$) to be 1,190, which is in good agreement with the $M_{\mathrm{n,NMR}}$ value (1,230).

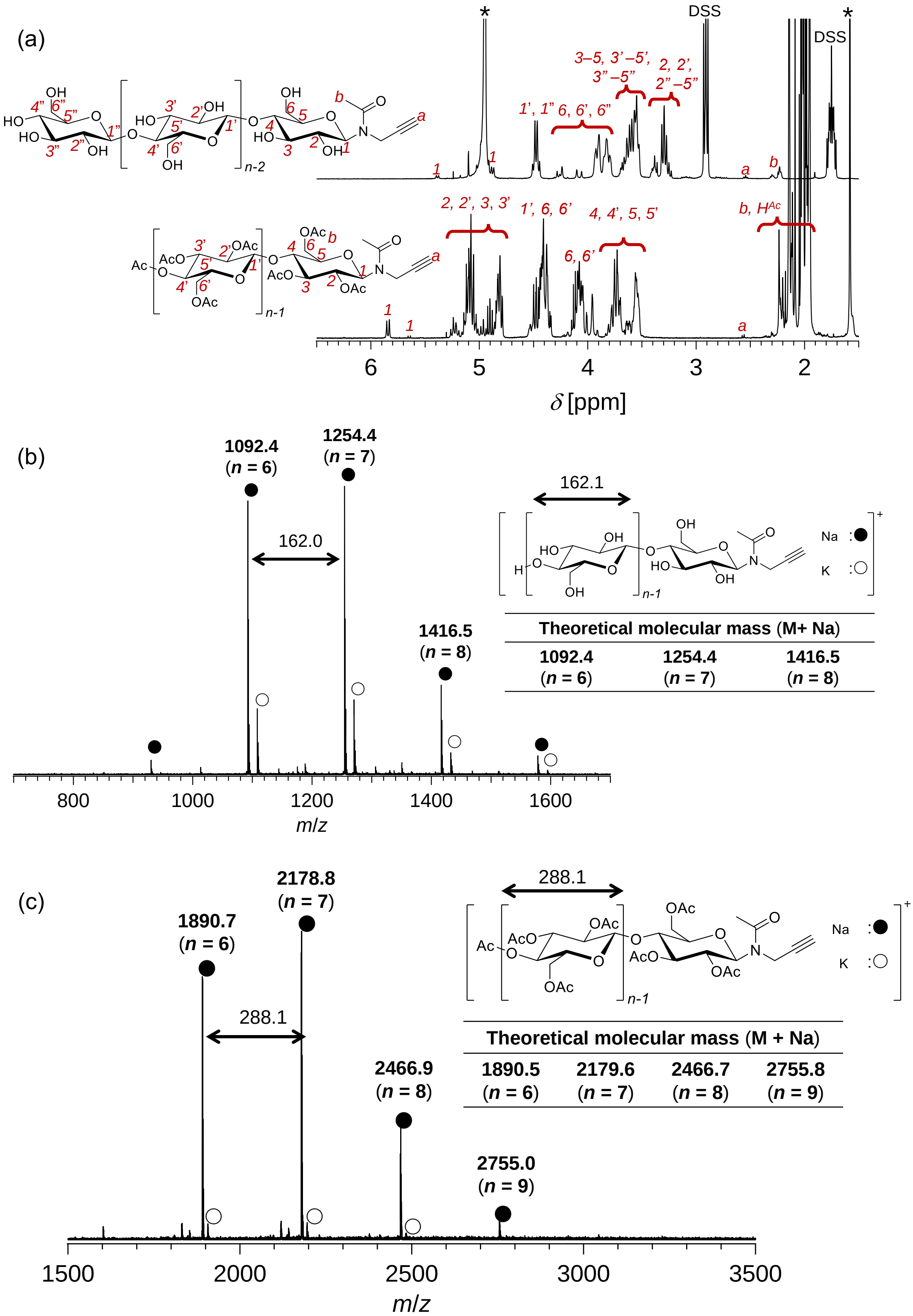

Theoretical molecular mass (M+ Na)		
1092.4 **(*n* = 6)**	**1254.4** **(*n* = 7)**	**1416.5** **(*n* = 8)**

Theoretical molecular mass (M + Na)			
1890.5 **(*n* = 6)**	**2179.6** **(*n* = 7)**	**2466.7** **(*n* = 8)**	**2755.8** **(*n* = 9)**

Figure 3.2. Characterization of Cel$_n$−C≡CH and AcCel$_n$−C≡CH. (a) ^{1}H NMR spectra of Cel$_n$−C≡CH (upper) in D_2O containing sodium trimethylsilylpropanesulfonate (DSS) and10% (w/w) NaOD and AcCel$_n$−C≡CH in $CDCl_3$ (lower) (400 MHz). (b) MALDI-TOF MS spectrum and theoretical molecular masses of AcCel$_n$−C≡CH.

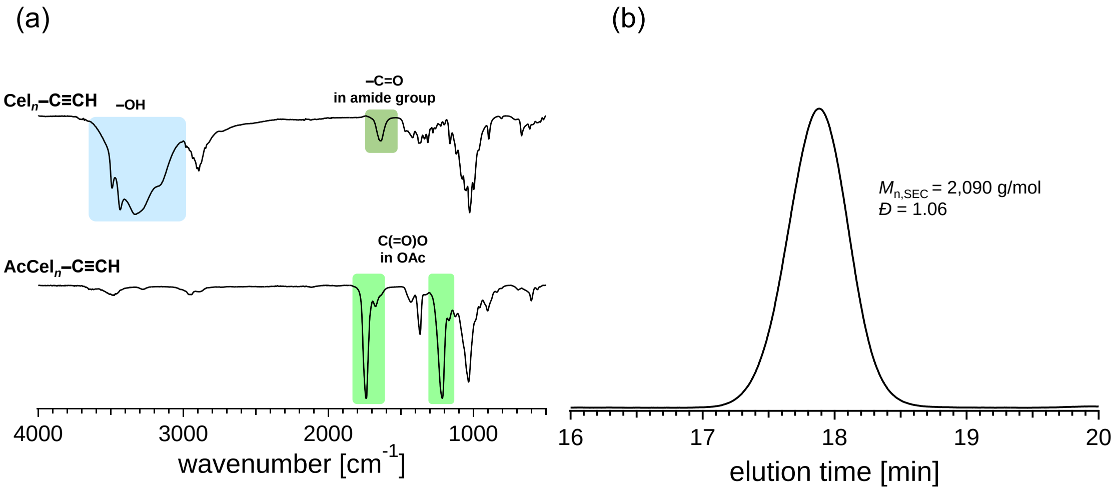

Figure 3.3. (a) FT-IR spectra of Cel$_n$−C≡CH (upper) and AcCel$_n$−C≡CH (lower) and (b) SEC trace of AcCel$_n$−C≡CH (eluent, THF; flow rate, 1.0 mL min^{-1}).

The prepared Cel$_n$−C≡CH was subsequently subjected to acetylation following solvent-exchange with H_2O, acetone, and *N*,*N*-dimethylacetamide (DMAc). Acetylation was carried out using Ac_2O and pyridine in LiCl/DMAc for 5 d.[48] However, ^{1}H NMR and FT-IR spectroscopy of the product revealed incomplete acetylation. Therefore, the partially acetylated product was further treated with Ac_2O and pyridine in the presence of 4-(dimethylamino)pyridine (DMAP) to ensure complete acetylation. The ^{1}H NMR spectrum of the final product exhibited the characteristic signals of the acetyl groups (**Figure 3.2** (a), lower). The number-average degree of polymerization of the prepared AcCel$_n$−C≡CH was calculated to be 6.10, which corresponds to a $M_{n,NMR}$ of 1,900. The FT-IR spectrum of the product lacks the absorption band attributable to the hydroxyl groups and exhibits new absorption bands attributable to ester bonds (**Figure 3.3** (a)). The MALDI-TOF mass spectrum exhibited two series of repeated peaks in the 1,800–

3,000 Da range separated by approximately 288 Da, which corresponds to the repeating unit of AcCel$_n$−C≡CH (**Figure 3.2** (c)). These spectroscopic results quantitatively confirmed that all hydroxyl groups of Cel$_n$−C≡CH had been acetylated. The size exclusion chromatography (SEC) trace of AcCel$_n$−C≡CH exhibited a monomodal peak and a narrow dispersity ($Đ$ = 1.06), and the SEC-based number-average molecular weight ($M_{\mathrm{n,SEC}}$) was calculated to be 2,080 when calibrated against a polystyrene standard (**Figure 3.3** (b)). In summary, the author successfully prepared a well-defined and perfectly acetylated AcCel$_n$−C≡CH with an average DP of 6.10.

AcMal$_n$−C≡CH, which is the amylose counterpart of AcCel$_n$−C≡CH, was successfully prepared in three steps (**Scheme 3.2**, lower). According to a previously reported procedure,[49] a commercially available maltooligosaccharide was treated with propargyl amine in the absence of a solvent followed by Ac_2O in MeOH, to produce propargyl-functionalized maltooligosaccharide (Mal$_n$−C≡CH). Subsequent *O*-acetylation with Ac_2O in the presence of DMAP in pyridine produced AcMal$_n$−C≡CH, which mainly comprises 6- to 8-mers according to MALDI-TOF MS. The $M_{\mathrm{n,NMR}}$ and $Đ$ values of the prepared AcMal$_n$−C≡CH were determined to be 1,930 (DP = 6.22) and 1.09, respectively, according to ^{1}H NMR spectroscopy and SEC (**Figures 3.4** and **3.5**).

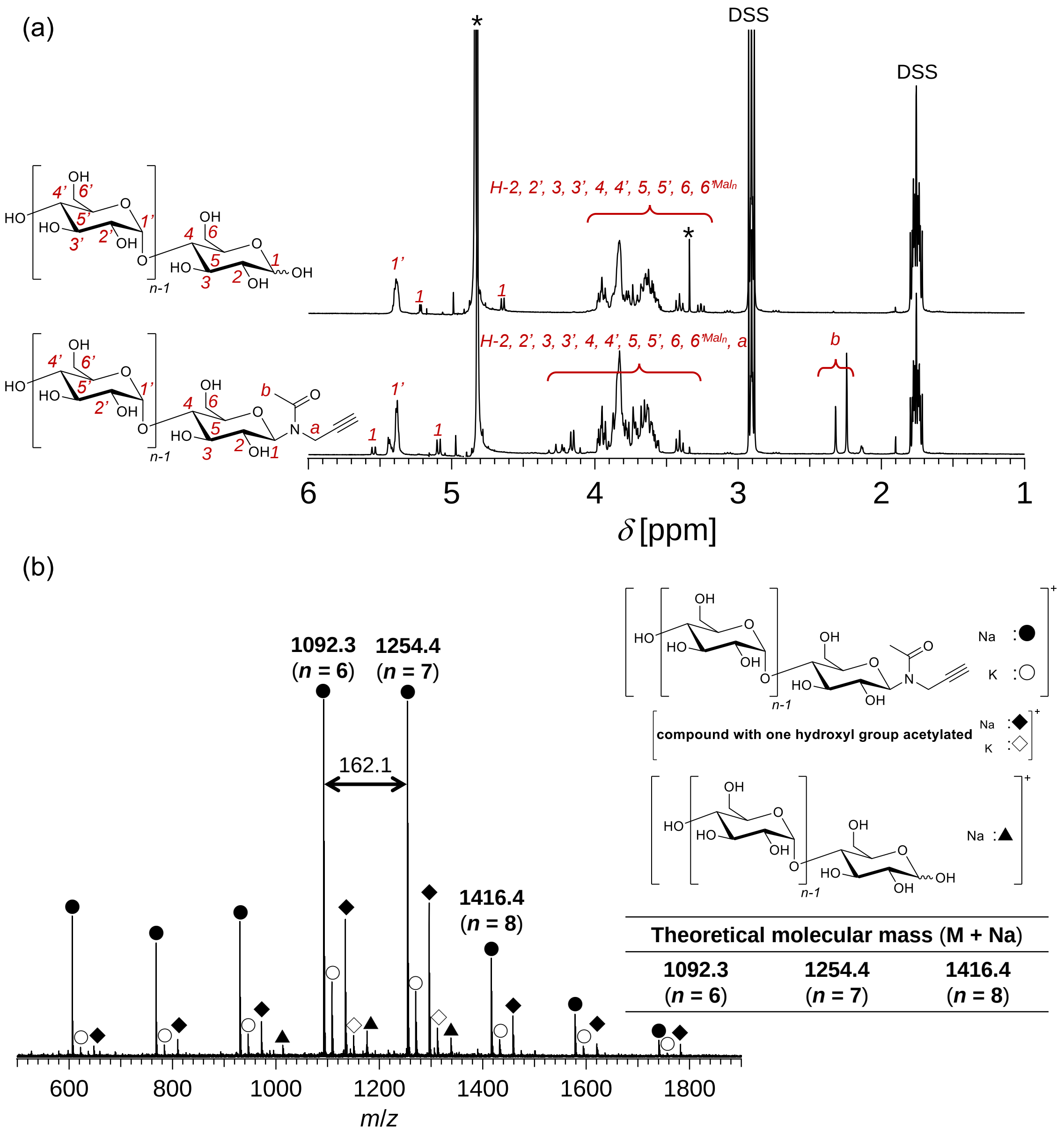

Figure 3.4. Characterization of Mal$_n$−C≡CH. (a) ^{1}H NMR spectra of Mal$_n$ (upper) and Mal$_n$−C≡CH (D_2O, 400 MHz). (b) MALDI-TOF MS spectrum and theoretical molecular mass.

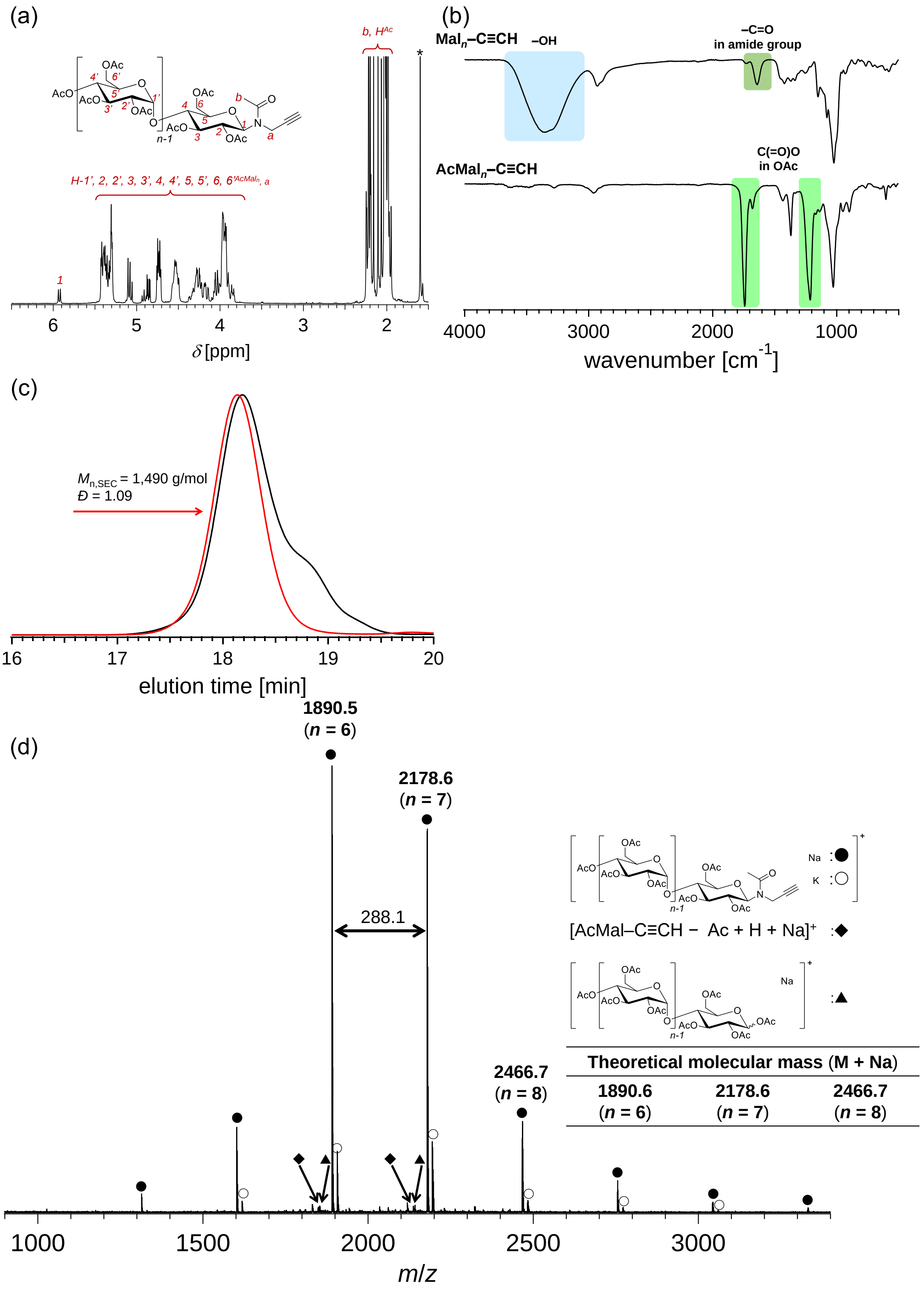

Figure 3.5. Characterization of AcMal$_n$–C≡CH. (a) ^{1}H NMR spectrum (CDCl$_3$, 400 MHz). (b) FT-IR spectra of Mal$_n$–C≡CH (upper) and AcMal$_n$–C≡CH (lower). (c) SEC trace of AcMal$_n$–C≡CH before (black) and after (red) preparative SEC purification (eluent, THF; flow rate, 1.0 mL min^{-1}. (d) MALDI-TOF MS spectrum and theoretical molecular mass.

3.3.2. Triblock copolymer synthesis

Ring-opening polymerization (ROP) of δ-decanolactone was carried at 40 °C using diphenyl phosphate (DPP) and 1,4-benzenedimethanol (BDM) as the catalyst and initiator, respectively, according the previously procedure, to produce poly(δ-decanolactone) diol (HO–PDL–OH) as the central soft segment of the target triblock copolymer.[14] In this Chapter, PDLs with three molecular weights were synthesized by varying the initial monomer-to-initiator ratio (HO–PDL$_{6k}$–OH, $M_{n,\,NMR}$ = 5,590, $Đ$ = 1.07; HO–PDL$_{10k}$–OH, $M_{n,\,NMR}$ = 10,000, $Đ$ = 1.06; HO–PDL$_{22k}$–OH, $M_{n,\,NMR}$ = 21,600, $Đ$ = 1.06). The HO–PDL–OH groups were thereafter treated with 6-azidohexanoic acid (N_3–COOH) to give the corresponding α,ω-diazido-functionalized PDLs (N_3–PDL$_{6k}$–N_3, $M_{n,NMR}$ = 5,900, $Đ$ = 1.07; N_3–PDL$_{10k}$–N_3, $M_{n,NMR}$ = 10,300, $Đ$ = 1.06; N_3–PDL$_{22k}$–N_3, $M_{n,NMR}$ = 21,900, $Đ$ = 1.09; **Figures 3.6–3.8** show the ^{1}H NMR spectra of the HO–PDL–OHs and N_3–PDL–N_3s).

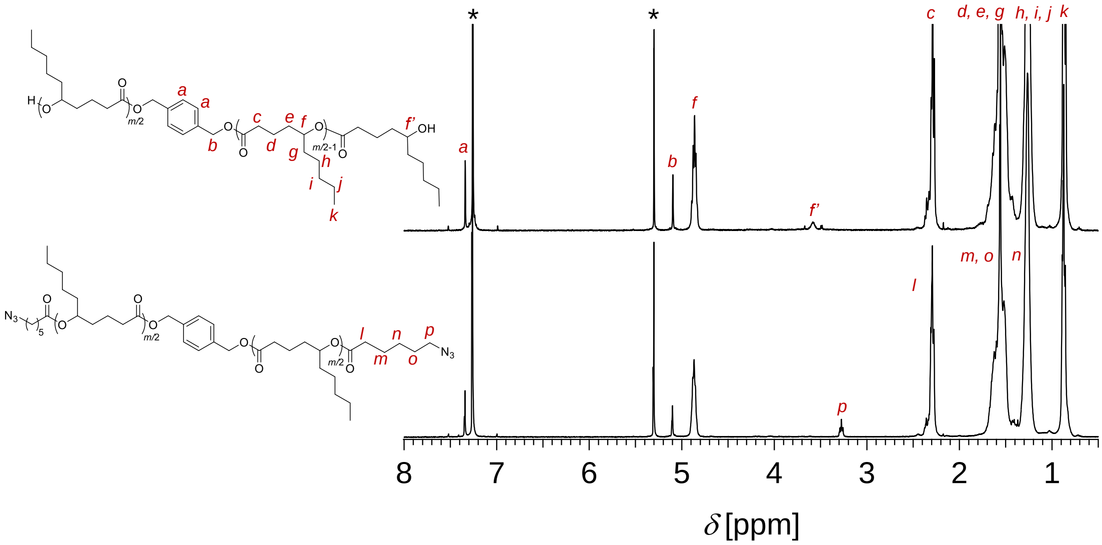

Figure 3.6. ^{1}H NMR spectra of HO−PDL$_{6k}$−OH (upper) and N$_3$−PDL$_{6k}$−N$_3$ (lower) (400 MHz, CDCl$_3$).

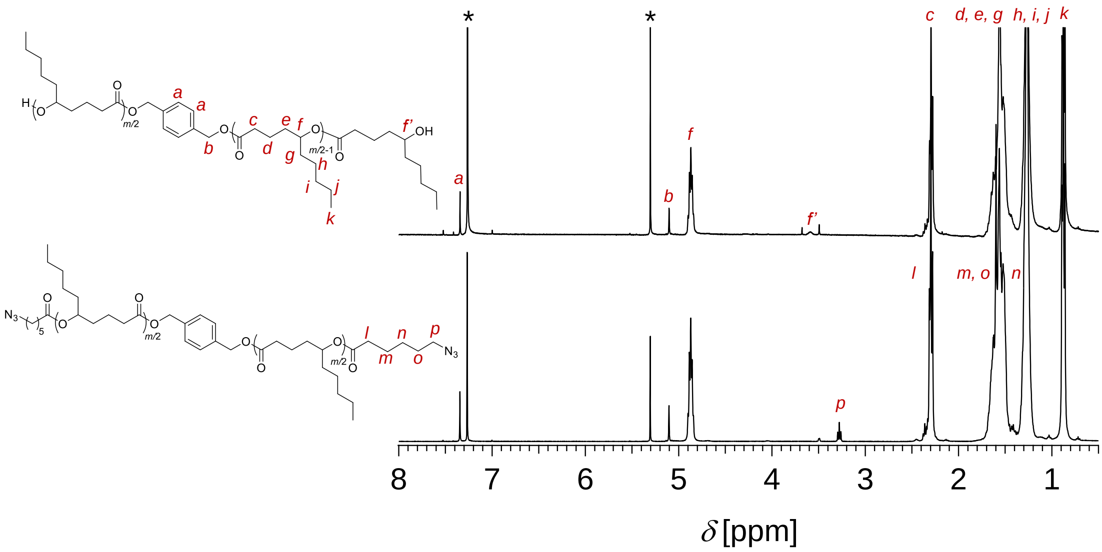

Figure 3.7. ^{1}H NMR spectra of HO−PDL$_{10k}$−OH (upper) and N$_3$−PDL$_{10k}$−N$_3$ (lower) (400 MHz, CDCl$_3$).

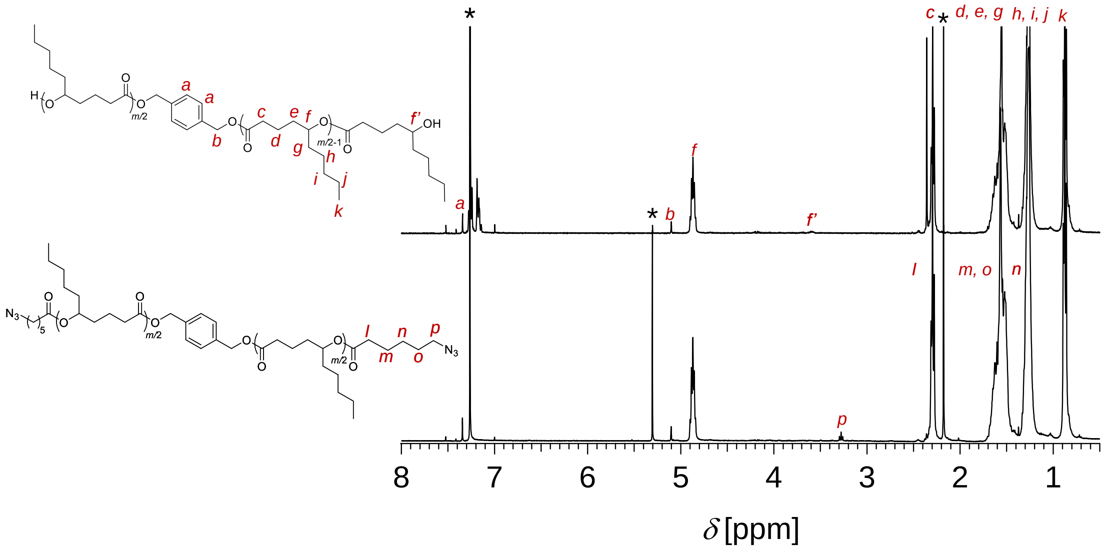

Figure 3.8. ^{1}H NMR spectra of HO–PDL$_{22k}$–OH (upper) and N_3–PDL$_{22k}$–N_3 (lower) (400 MHz, $CDCl_3$).

Finally, the CuAAC reactions between the prepared N_3–PDL–N_3s and AcCel$_n$–C≡CH or AcMal$_n$–C≡CH were carried out in DMF using CuBr/PMDETA as the catalyst to produce the target ABA-type triblock BCPs, namely, AcCel$_n$-*b*-PDL$_{6k}$-*b*-AcCel$_n$, AcCel$_n$-*b*-PDL$_{10k}$-*b*-AcCel$_n$, AcCel$_n$-*b*-PDL$_{22k}$-*b*-AcCel$_n$, AcMal$_n$-*b*-PDL$_{6k}$-*b*-AcMal$_n$, AcMal$_n$-*b*-PDL$_{10k}$-*b*-AcMal$_n$, and AcMal$_n$-*b*-PDL$_{22k}$-*b*-AcMal$_n$, in isolated yields of 26%–80%. The FT-IR spectra of the products confirmed the disappearance of the absorption band at approximately 2,100 cm^{-1} attributable to azido groups (**Figures 3.9–3.14** (a)), and each SEC elution peak appeared in a higher molecular weight region compared to the azido-functionalized PDL peak, which suggests that each click reaction proceeded quantitatively (**Figure 3.15**). Furthermore, the ^{1}H NMR spectra exhibit signals derived from the PDL and AcCel$_n$ or AcMal$_n$ segments that are assigned to the expected chemical structures, thereby confirming that the AcCel$_n$-*b*-PDL-*b*-AcCel$_n$s and AcMal$_n$-*b*-PDL-*b*-AcMal$_n$s had been successfully synthesized (**Figures 3.9−3.14** (b)). The molecular weights, *Đ* values, and volume fractions of the PDL segments (f_{PDL}) of the prepared AcCel$_n$-*b*-PDL-*b*-AcCel$_n$s and AcMal$_n$-*b*-PDL-*b*-AcMal$_n$s are summarized in **Table 3.1**.

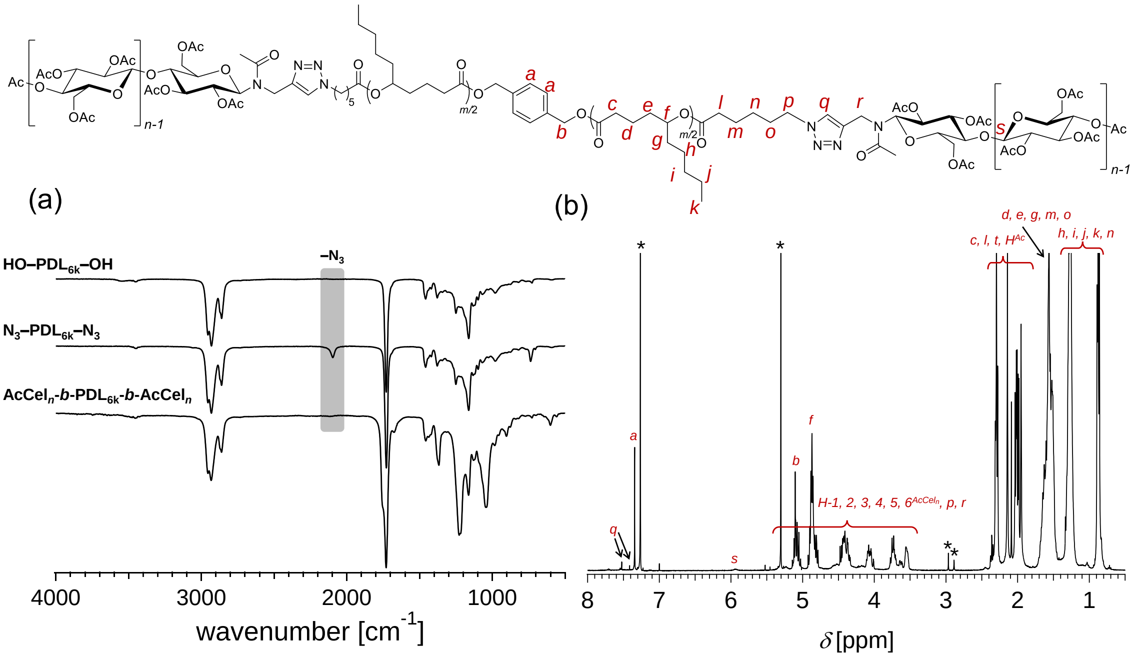

Figure 3.9. Characterization of AcCel$_n$-*b*-PDL$_{6k}$-*b*-AcCel$_n$. (a) ^{1}H NMR spectrum (CDCl$_3$, 400 MHz). (b) FT-IR spectra of HO−PDL$_{6k}$−OH (upper), N$_3$−PDL$_{6k}$−N$_3$ (middle), and AcCel$_n$-*b*-PDL$_{6k}$-*b*-AcCel$_n$ (lower).

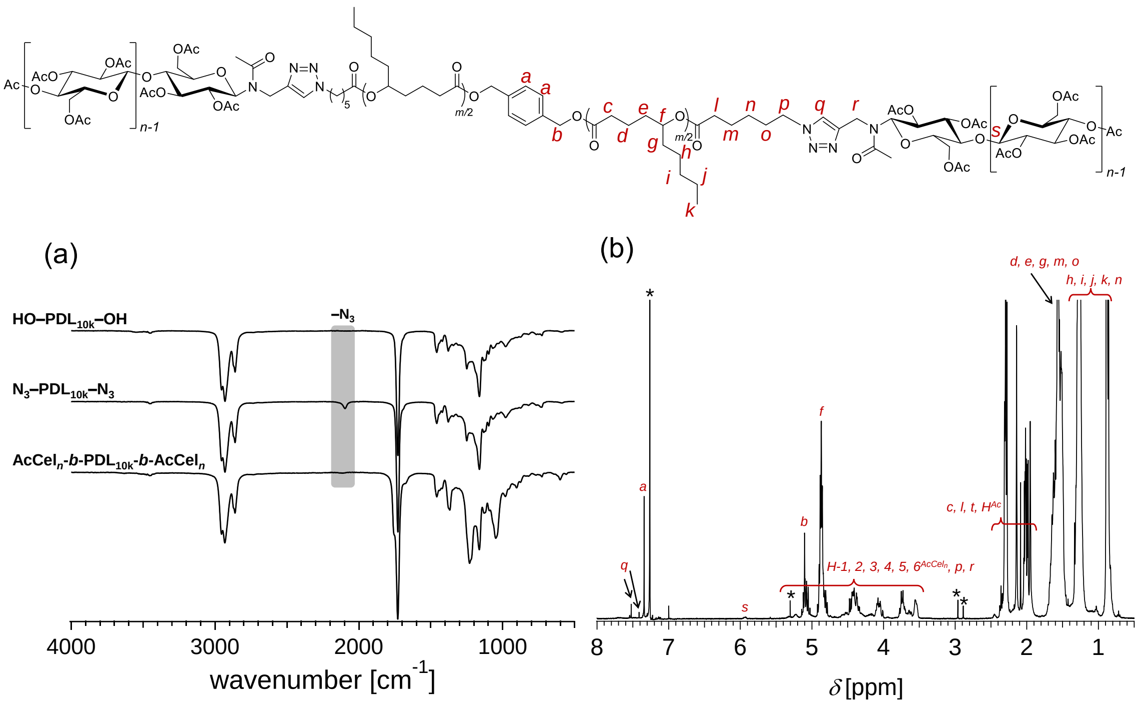

Figure 3.10. Characterization of AcCel$_n$-*b*-PDL$_{10k}$-*b*-AcCel$_n$. (a) ^{1}H NMR spectrum ($CDCl_3$, 400 MHz). (b) FT-IR spectra of HO−PDL$_{10k}$−OH (upper), N_3−PDL$_{10k}$−N_3 (middle), and AcCel$_n$-*b*-PDL$_{10k}$-*b*-AcCel$_n$ (lower).

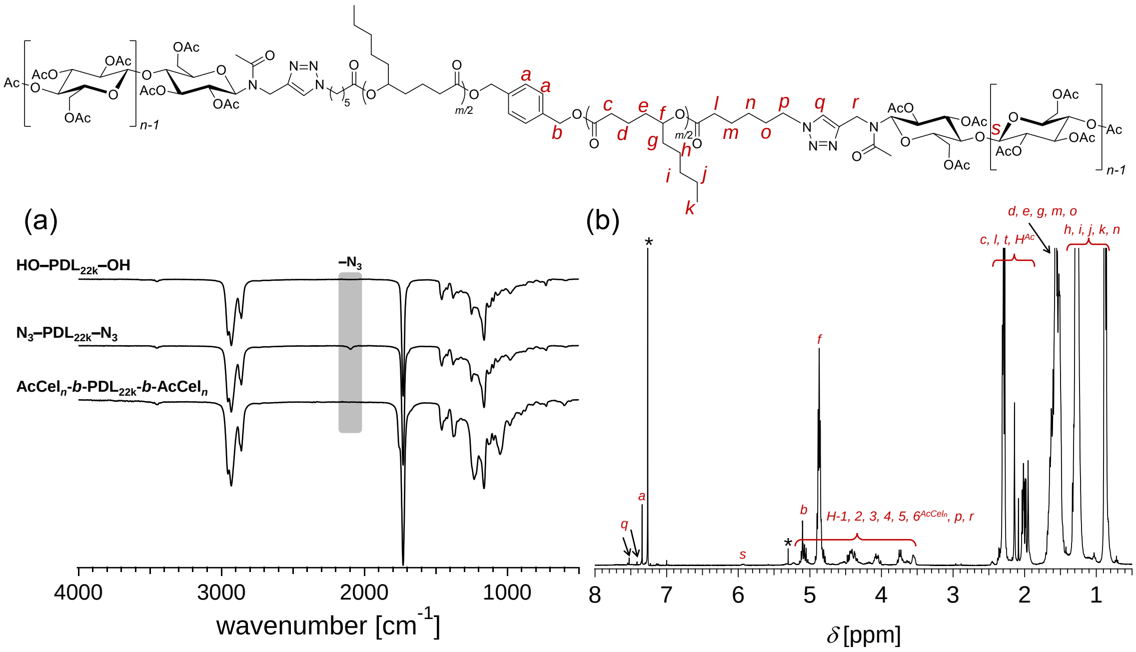

Figure 3.11. Characterization of AcCel$_n$-*b*-PDL$_{22k}$-*b*-AcCel$_n$. (a) ^{1}H NMR spectrum ($CDCl_3$, 400 MHz). (b) FT-IR spectra of HO−PDL$_{22k}$−OH (upper), N_3−PDL$_{22k}$−N_3 (middle), and AcCel$_n$-*b*-PDL$_{22k}$-*b*-AcCel$_n$ (lower).

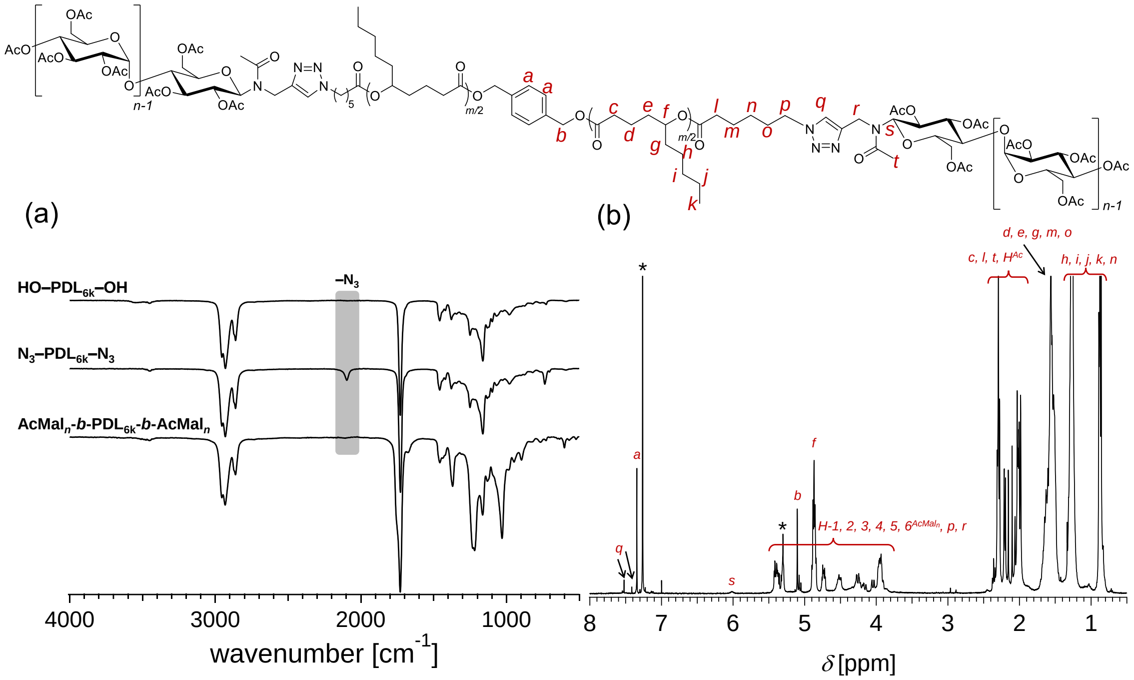

Figure 3.12. Characterization of AcMal$_n$- *b*-PDL$_{6k}$-*b*-AcMal$_n$. (a) ^{1}H NMR spectrum (CDCl$_3$, 400 MHz). (b) FT-IR spectra of HO−PDL$_{6k}$−OH (upper), N$_3$−PDL$_{6k}$−N$_3$ (middle) and AcMal$_n$-*b*-PDL$_{6k}$-*b*-AcMal$_n$ (lower).

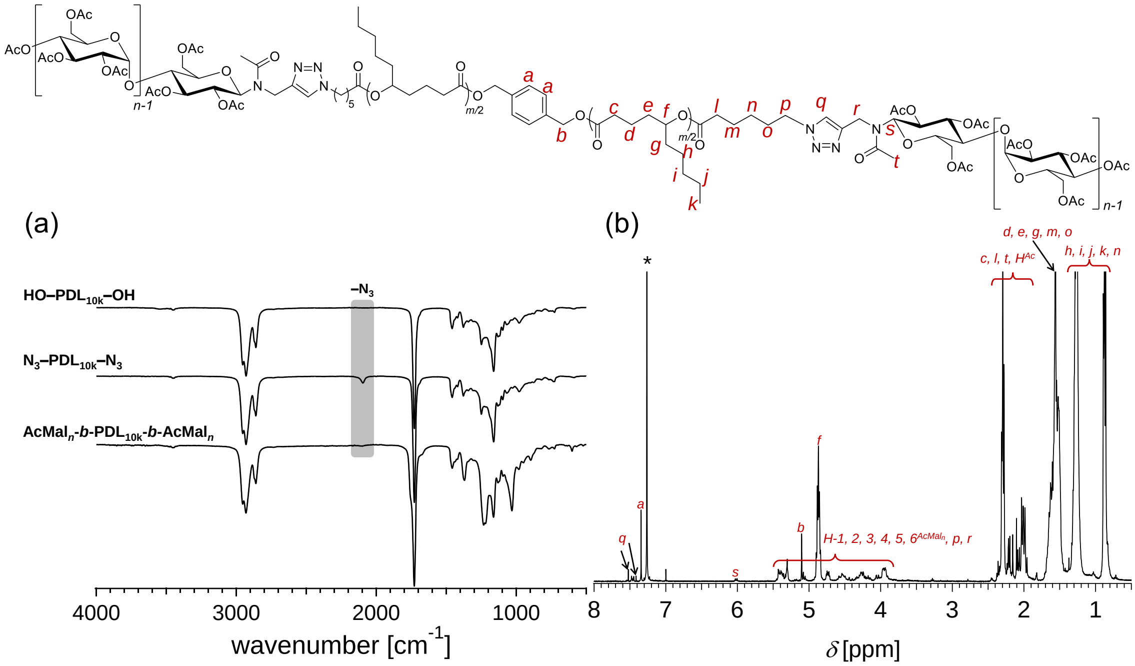

Figure 3.13. Characterization of AcMal$_n$-*b*-PDL$_{10k}$-*b*-AcMal$_n$. (a) ^{1}H NMR spectrum (CDCl$_3$, 400 MHz). (b) FT-IR spectra of HO−PDL$_{10k}$−OH (upper), N$_3$−PDL$_{10k}$−N$_3$ (middle), and AcMal$_n$-*b*-PDL$_{10k}$-*b*-AcMal$_n$ (lower).

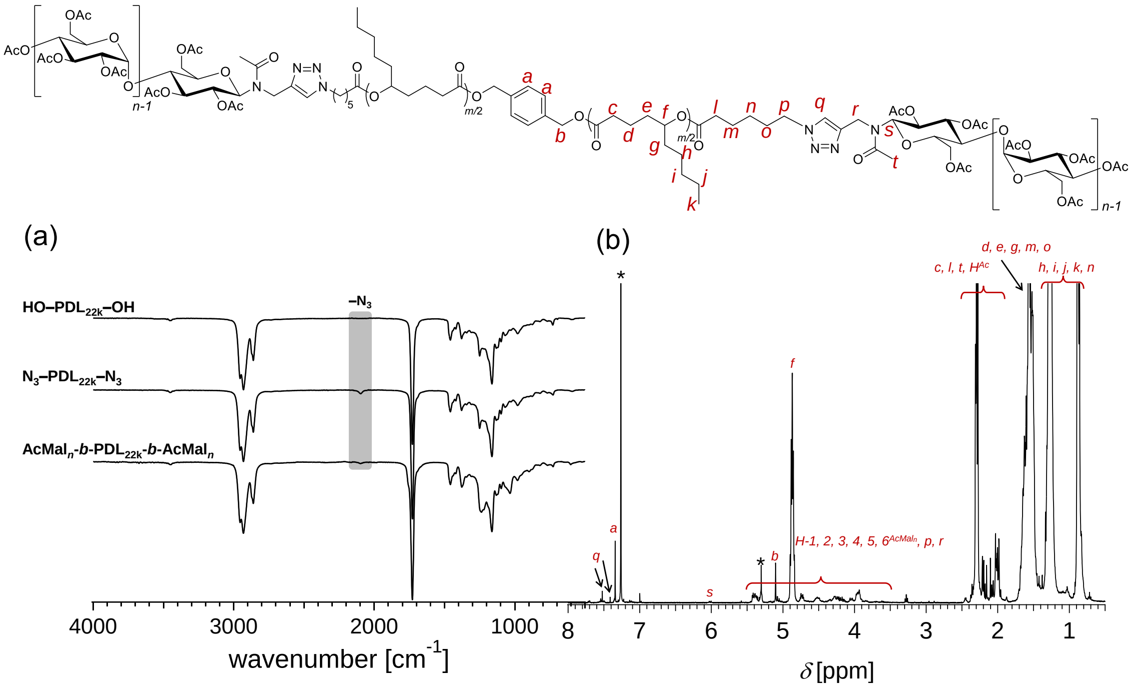

Figure 3.14. Characterization of AcMal$_n$-*b*-PDL$_{22k}$-*b*-AcMal$_n$. (a) ^{1}H NMR spectrum (CDCl$_3$, 400 MHz). (b) FT-IR spectra of HO−PDL$_{22k}$−OH (upper), N$_3$−PDL$_{22k}$−N$_3$ (middle) and AcMal$_n$-*b*-PDL$_{22k}$-*b*-AcMal$_n$ (lower).

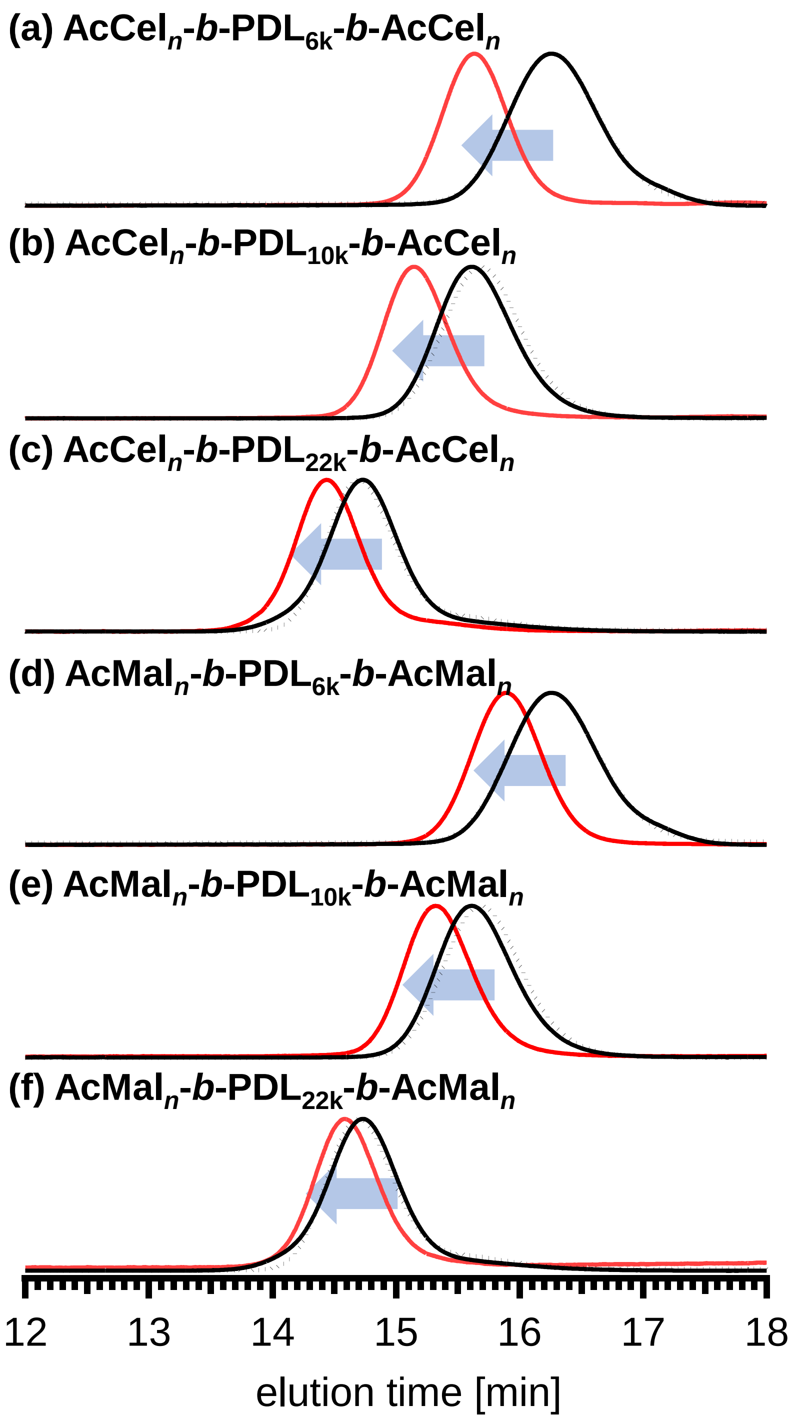

Figure 3.15. SEC traces of (a) AcCel$_n$-b-PDL$_{6k}$-b-AcCel$_n$, (b) AcCel$_n$-b-PDL$_{10k}$-b-AcCel$_n$, (c) AcCel$_n$-b-PDL$_{22k}$-b-AcCel$_n$, (d) AcMal$_n$-b-PDL$_{6k}$-b-AcMal$_n$, (e) AcMal$_n$-b-PDL$_{10k}$-b-AcMal$_n$, and (f) AcMal$_n$-b-PDL$_{22k}$-b-AcMal$_n$ (eluent, THF; flow rate, 1.0 mL min^{-1}). The solid red, solid black, and dotted black lines represent the BCPs and their corresponding N_3–PDL–N_3 and HO–PDL–OH units, respectively.

Table 3.1. Molecular characteristics of AcCel$_n$-*b*-PDL-*b*-AcCel$_n$s and AcMal$_n$-*b*-PDL-*b*-AcMal$_n$s

Polymer	M_n	$Đ^c$	$T_{\mathrm{g,PDL}}{}^d$ [°C]	$T_{\mathrm{g,Cel}}{}^d$ [°C]	$T_{\mathrm{m,Cel}}{}^d$ [°C]	$T_{\mathrm{g,Mal}}{}^d$ [°C]	$f_{\mathrm{PDL}}{}^e$
AcCel$_n$−C≡CH	2,100^a	1.06	-	110	167	-	-
AcMal$_n$−C≡CH	1,950^a	1.09	-	-	-	101	-
AcCel$_n$-*b*-PDL$_{6k}$-*b*-AcCel$_n$	9,790^b	1.04	−52	86	-	-	0.64
AcCel$_n$-*b*-PDL$_{10k}$-*b*-AcCel$_n$	14,200^b	1.04	−52	97	162	-	0.76
AcCel$_n$-*b*-PDL$_{22k}$-*b*-AcCel$_n$	25,800^b	1.06	−53	106	-	-	0.87
AcMal$_n$-*b*-PDL$_{6k}$-*b*-AcMal$_n$	9,490^b	1.04	−52	-	-	60	0.64
AcMal$_n$-*b*-PDL$_{10k}$-*b*-AcMal$_n$	13,900^b	1.04	−51	-	-	60	0.76
AcMal$_n$-*b*-PDL$_{22k}$-*b*-AcMal$_n$	25,500^b	1.04	−54	-	-	55	0.87

^{a}Determined by MALDI-TOF MS. ^{b}Calculated from the molecular weight of AcCel$_n$−C≡CH or AcMal$_n$−C≡CH determined by MALDI-TOF MS and the molecular weight of the corresponding N_3–PDL–N_3 determined by ^{1}H NMR spectroscopy in $CDCl_3$. ^{c}Determined by SEC in THF using polystyrene standards. ^{d}Determined by DSC at a heating rate of 10 °C min^{-1}. ^{e}Calculated using the density of each block: 1.29 g cm^{-3} for AcCel$_n$−C≡CH,[50] 1.20 g cm^{-3} for AcMal$_n$−C≡CH,[51] and 0.97 g cm^{-3} for PDL.[52]

3.3.3. Thermal properties

To gain fundamental insight into the differences in the physical properties originating from the oligosaccharide blocks, the author initially evaluated the thermal properties of the AcCel$_n$-*b*-PDL-*b*-AcCel$_n$s and AcMal$_n$-*b*-PDL-*b*-AcMal$_n$s by thermogravimetric analysis (TGA) and differential scanning calorimetry (DSC) in a nitrogen atmosphere. According to the TGA data, all of the studied BCP samples were thermally stable up to approximately 280 °C and exhibited 5% weight-loss temperatures ($T_{\mathrm{d5\%}}$) in the 290–320 °C range (**Figures 3.16** and **3.17**). Visual inspection during TGA revealed that all BCP samples changed their appearance; they transformed from a solid to a melt state close to the glass transition temperature of the AcCel$_n$ or AcMal$_n$ segment, consistent with thermoplastic behavior. The DSC curves of the AcCel$_n$-*b*-PDL-*b*-AcCel$_n$s and AcMal$_n$-*b*-PDL-*b*-AcMal$_n$s acquired during the second heating process exhibited two baseline shifts derived from the glass transitions of the PDL and AcCel$_n$ or AcMal$_n$ segments (**Figure 3.18**). The glass transition temperatures of the PDL ($T_{\mathrm{g,PDL}}$), AcCel$_n$ ($T_{\mathrm{g,Cel}}$), and AcMal$_n$ segments ($T_{\mathrm{g,Mal}}$) are approximately −50, 95, and 60 °C, respectively (**Figures 3.18** and **3.19**). The fact that $T_{\mathrm{g,PDL}}$ and $T_{\mathrm{g,Cel}}$ (or $T_{\mathrm{g,Mal}}$) were observed separately indicates phase separation between the PDL and AcCel$_n$ (or AcMal$_n$) segments. The $T_{\mathrm{g,Mal}}$ values of the AcMal$_n$-*b*-PDL-*b*-AcMal$_n$s were considerably lower than that of AcMal$_n$–C≡CH, which indicates partial mixing of the AcMal$_n$ and PDL domains. Similarly, partial mixing of the AcCel$_n$ and PDL domains resulted in lower $T_{g,Cel}$ values for the AcCel$_n$-*b*-PDL-*b*-AcCel$_n$s than AcCel$_n$–C≡CH. Interestingly, $T_{g,Cel}$ was observed to increase with increasing f_{PDL}, which is attributable to increasing segregation strength associated with increasing AcCel$_n$-*b*-PDL-*b*-AcCel$_n$ total molecular weight. Notably, the DSC curve of AcCel$_n$-*b*-PDL$_{10k}$-*b*-AcCel$_n$ exhibited a small endothermic peak at 163 °C due to the melting of the AcCel$_n$ segment ($T_{m,Cel}$), which indicates that the BCP is semi-crystalline in nature. The DSC trace of AcCel$_n$−C≡CH clearly exhibits a $T_{m,Cel}$ at 167 °C; however, the traces for AcCel$_n$-*b*-PDL$_{6k}$-*b*-AcCel$_n$ and AcCel$_n$-*b*-PDL$_{22k}$-*b*-AcCel$_n$ did not exhibit any melting peaks. Given the small area of the melting transition of the AcCel$_n$ segment in AcCel$_n$-*b*-PDL$_{10k}$-*b*-AcCel$_n$, crystallization tends to occur slowly. In contrast, the AcMal$_n$-*b*-PDL-*b*-AcMal$_n$s and AcMal$_n$−C≡CH did not exhibit any melting transition, which confirms the amorphous nature of the AcMal$_n$ segment.

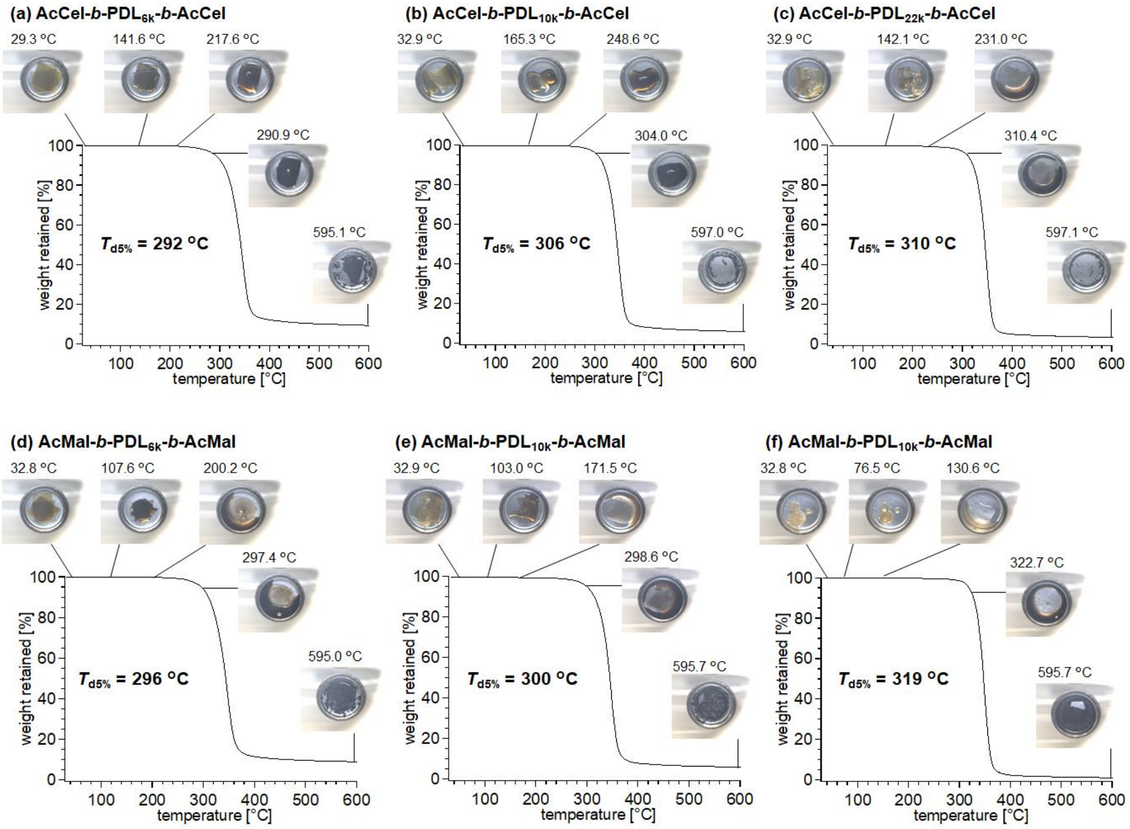

Figure 3.16. TGA curves of (a) AcCel$_n$-PDL$_{6k}$-AcCel$_n$, (b) AcCel$_n$-PDL$_{10k}$-AcCel$_n$, (c) AcCel$_n$-PDL$_{22k}$-AcCel$_n$, (d) AcMal$_n$-PDL$_{6k}$-AcMal$_n$, (e) AcMal$_n$-PDL$_{10k}$-AcMal$_n$, and (f) AcMal$_n$-PDL$_{22k}$-AcMal$_n$ (under nitrogen atmosphere; heating rate, 10 °C min^{-1}). Inset photographs show the sample appearance at the indicated temperature. $T_{d5\%}$ means 5% weight loss temperature.

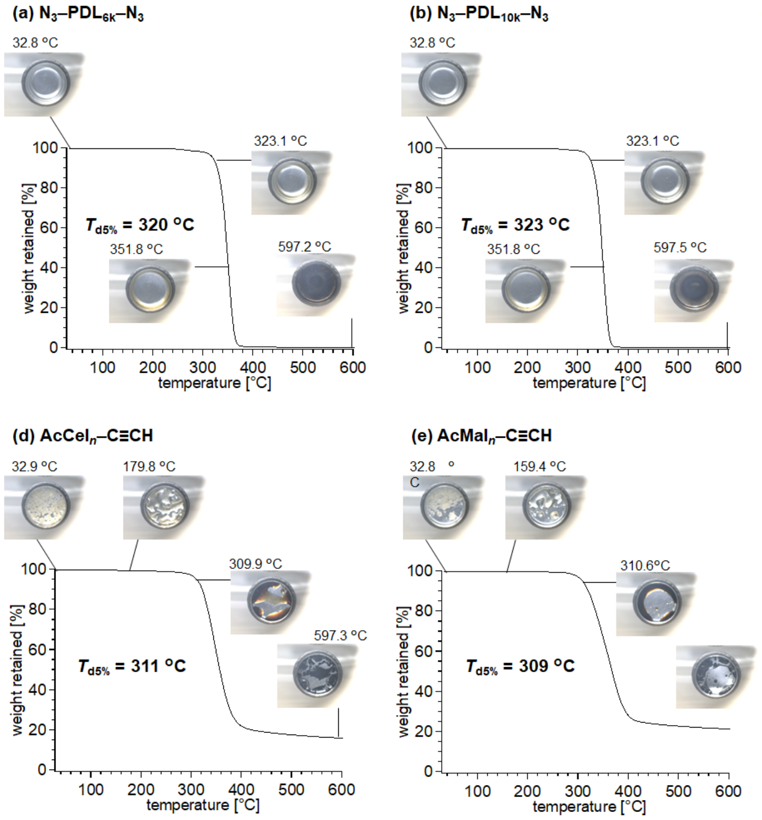

Figure 3.17. TGA curves of (a) N$_3$–PDL$_{6k}$–N$_3$, (b) N$_3$–PDL$_{10k}$–N$_3$, (c) N$_3$–PDL$_{22k}$–N$_3$, (d) AcCel$_n$–C≡CH, and (e) AcMal$_n$–C≡CH (under nitrogen atmosphere; heating rate, 10 °C min^{-1}). Inset photographs show the sample appearance at the indicated temperature. $T_{d5\%}$ means 5% weight loss temperature.

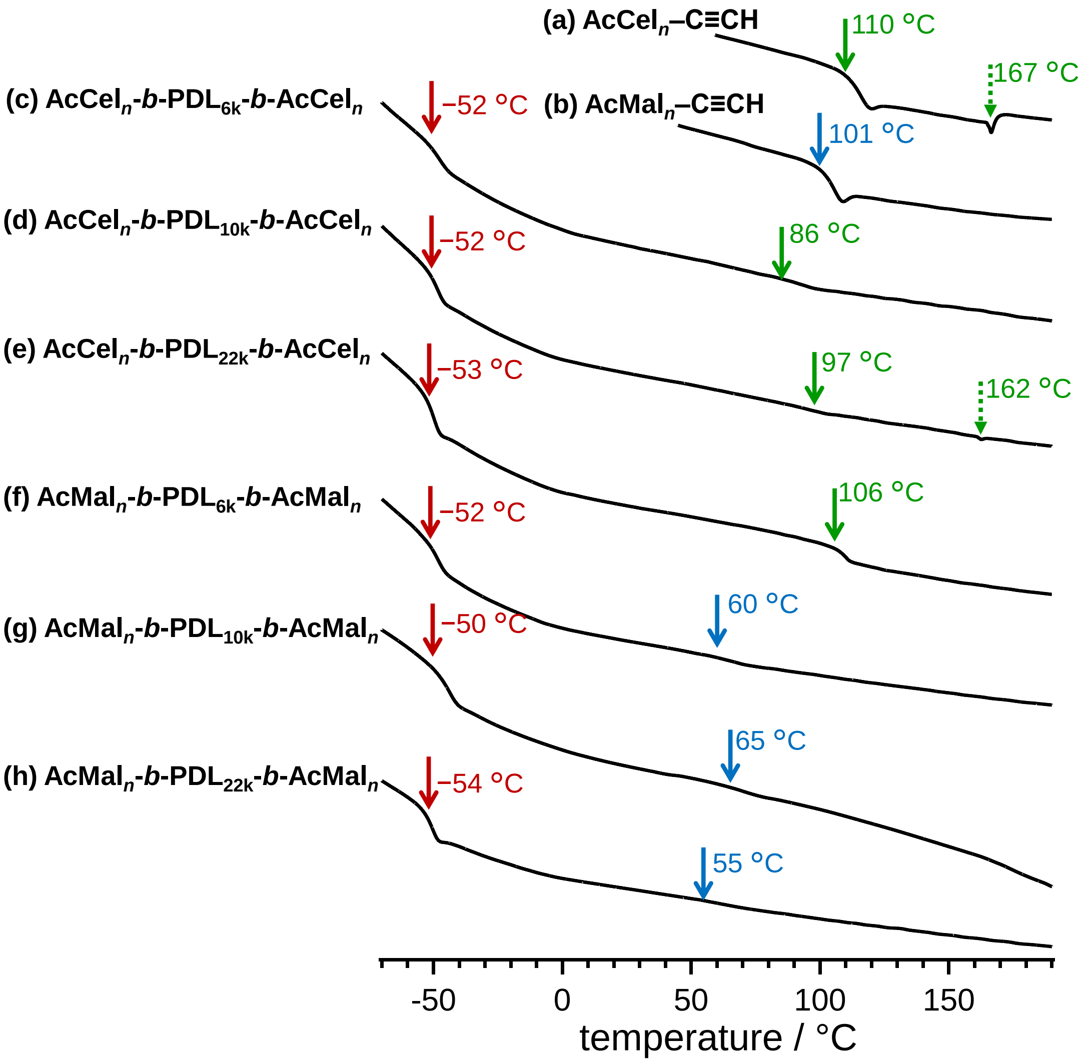

Figure 3.18. DSC curves of (a) AcCel$_n$–C≡CH, (b) AcMal$_n$–C≡CH, (c) AcCel$_n$-*b*-PDL$_{6k}$-*b*-AcCel$_n$, (d) AcCel$_n$-*b*-PDL$_{10k}$-*b*-AcCel$_n$, (e) AcCel$_n$-*b*-PDL$_{22k}$-*b*-AcCel$_n$, (f) AcMal$_n$-*b*-PDL$_{6k}$-*b*-AcMal$_n$, (g) AcMal$_n$-*b*-PDL$_{10k}$-*b*-AcMal$_n$, and (h) AcMal$_n$-*b*-PDL$_{22k}$-*b*-AcMal$_n$ during the second heating run (heating rate: 10 °C min^{-1}).

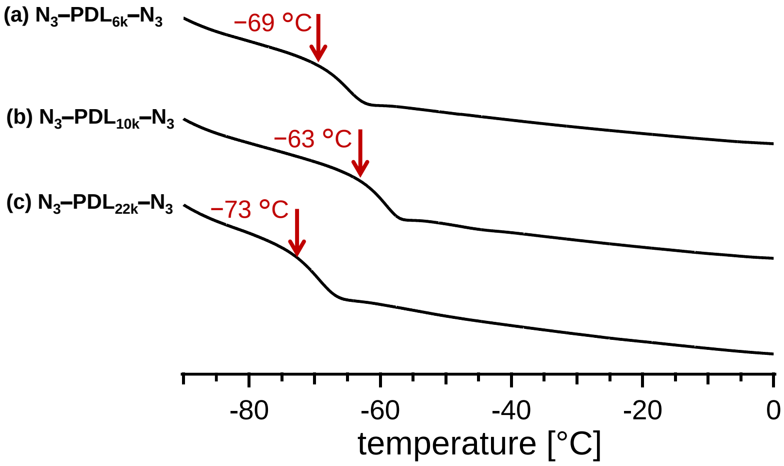

Figure 3.19. DSC curves traces of (a) N_3–PDL_{6k}–N_3, (b) N_3–PDL_{10k}–N_3, and (c) N_3–PDL_{22k}–N_3 during 2nd heating run (heating rate: 10 °C min^{-1}).

3.3.4. Microphase-separated structures

To investigate the impact of the oligosaccharide segments on the BCP self-assembly behavior, the microphase-separated structures of the AcCel$_n$-*b*-PDL-*b*-AcCel$_n$s and AcMal$_n$-*b*-PDL-*b*-AcMal$_n$s were investigated through small-angle X-ray scattering (SAXS) experiments on film samples, which were prepared by casting toluene solutions of the BCPs, followed by drying for 15 h at atmospheric pressure and for 1 d under vacuum at room temperature. The prepared films were subsequently thermally annealed under vacuum at 130 °C for 6 or 24 h.

The SAXS profiles of the non-annealed AcCel$_n$-*b*-PDL-*b*-AcCel$_n$s and AcMal$_n$-*b*-PDL-*b*-AcMal$_n$s exhibited only primary peaks indicative of weak segregation between the PDL and acetyl oligosaccharide segments with no periodically ordered structures (**Figure 3.20**). The mean distance between the phase-separated microdomains was calculated to be approximately 10 nm based on the Bragg equation using the position of the primary peak (q^*). In contrast, dramatic differences were observed in the microphase-separated structures of the AcCel$_n$-*b*-PDL-*b*-AcCel$_n$s and AcMal$_n$-*b*-PDL-*b*-AcMal$_n$s upon thermal annealing. The SAXS profiles of the AcMal$_n$-*b*-PDL-*b*-AcMal$_n$s exhibited only primary peaks, regardless of the annealing conditions, which implies that these BCPs do not meet the requirements for ordered microphase-separation. In contrast, the SAXS profiles of the AcCel$_n$-*b*-PDL-*b*-AcCel$_n$s exhibited primary peaks and additional higher-order scattering peaks upon thermal annealing at 130 °C for appropriate durations. The SAXS profile of AcCel$_n$-*b*-PDL$_{6k}$-*b*-AcCel$_n$ exhibited a higher-order scattering peak at $3q^*$ in addition to q^*, indicative of a lamellar (LAM) structure (**Figure 3.20** (a)); no even-ordered peak appeared in this SAXS profile, which indicates that the volumes of the AcCel$_n$ and PDL microdomains are nearly equal.[53] The SAXS profiles of AcCel$_n$-*b*-PDL$_{10k}$-*b*-AcCel$_n$ and AcCel$_n$-*b*-PDL$_{22k}$-*b*-AcCel$_n$ also exhibited higher-order scattering peaks at $\sqrt{3}q^*$, $2q^*$, $\sqrt{7}q^*$, and $3q^*$, and $\sqrt{2}q^*$, $\sqrt{3}q^*$, $\sqrt{5}q^*$, and $\sqrt{7}q^*$, indicative of hexagonal cylindrical (HEX) and body-centered cubic (BCC) spherical structures, respectively (**Figure 3.20** (c) and (e), respectively). The domain-spacing (*d*) of the thermally annealed AcCel$_n$-*b*-PDL$_{6k}$-*b*-AcCel$_n$, AcCel$_n$-*b*-PDL$_{10k}$-*b*-AcCel$_n$, and AcCel$_n$-*b*-PDL$_{22k}$-*b*-AcCel$_n$ were determined to be 9.6, 10.3, and 12.1 nm, respectively; the *d* value increases with increasing molecular weight. Overall, the AcCel$_n$-*b*-PDL-*b*-AcCel$_n$s are more likely to undergo ordered microphase-separation than the AcMal$_n$-*b*-PDL-*b*-AcMal$_n$s, despite being composed of the same monomeric units and possessing comparable chemical compositions. This is partly attributable to the rigidity granted to the AcCel$_n$ segments by their β-1,4-linked cellulose backbone. The longer Kuhn and persistence lengths of cellulose compared to those of amylose[13,54,55] induce microphase-separation in the AcCel$_n$-*b*-PDL-*b*-AcCel$_n$s. The fact that AcCel$_n$–C≡CH has a larger $M_{\mathrm{n,SEC}}$ than AcMal$_n$–C≡CH, despite their comparable $M_{\mathrm{n,MALDI}}$ and $M_{\mathrm{n,NMR}}$ values, implies that the AcCel$_n$ segment is more rigid than AcMal$_n$. In addition, the AcCel$_n$ segment exhibited the potential to crystallize, as revealed by DSC, which indicates its stronger tendency to self-aggregate. The wide-angle X-ray diffraction (WAXD) data also confirmed that the AcCel$_n$ segment is crystalline in nature (**Figures 3.21** and **3.22**). While the WAXD profile of AcMal$_n$–C≡CH and the AcMal$_n$-*b*-PDL-*b*-AcMal$_n$s showed only amorphous halos, AcCel$_n$–C≡CH and the AcCel$_n$-*b*-PDL-*b*-AcCel$_n$s showed diffraction peaks assignable to cellulose triacetate I crystals.[56,57] This may further enhance microphase-separation in the AcCel$_n$-*b*-PDL-*b*-AcCel$_n$s and significantly alter the self-assembly properties of the AcCel$_n$-*b*-PDL-*b*-AcCel$_n$s and AcMal$_n$-*b*-PDL-*b*-AcMal$_n$s.

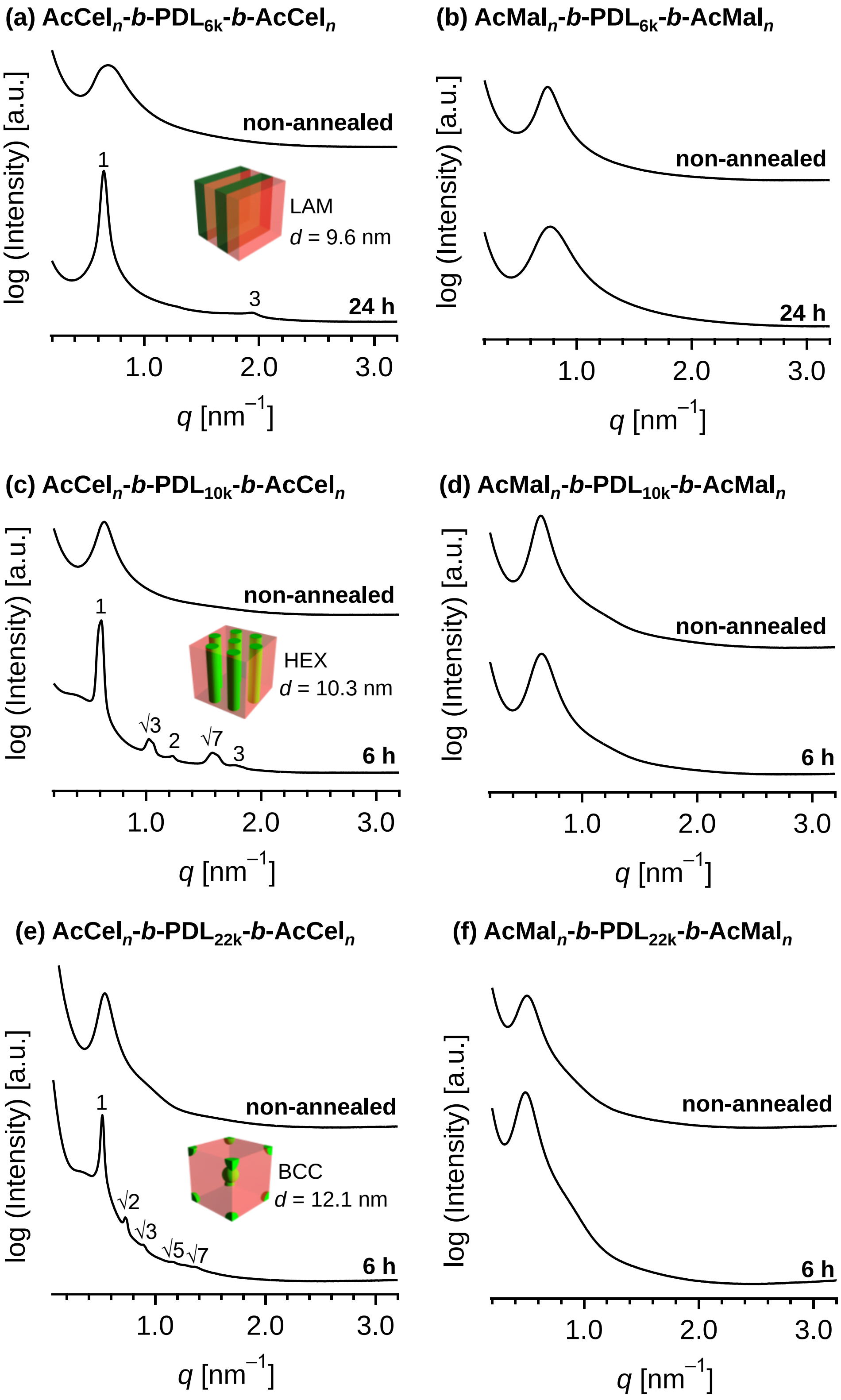

Figure 3.20. SAXS profiles of (a) AcCel$_n$-b-PDL$_{6k}$-b-AcCel$_n$, (b) AcMal$_n$-b-PDL$_{6k}$-b-AcMal$_n$, (c) AcCel$_n$-b-PDL$_{10k}$-b-AcCel$_n$, (d) AcMal$_n$-b-PDL$_{10k}$-b-AcMal$_n$, (e) AcCel$_n$-b-PDL$_{22k}$-b-AcCel$_n$, and (f) AcMal$_n$-b-PDL$_{22k}$-b-AcMal$_n$ without thermal annealing (upper) and after annealing (lower) at 130 °C for 6 or 24 h.

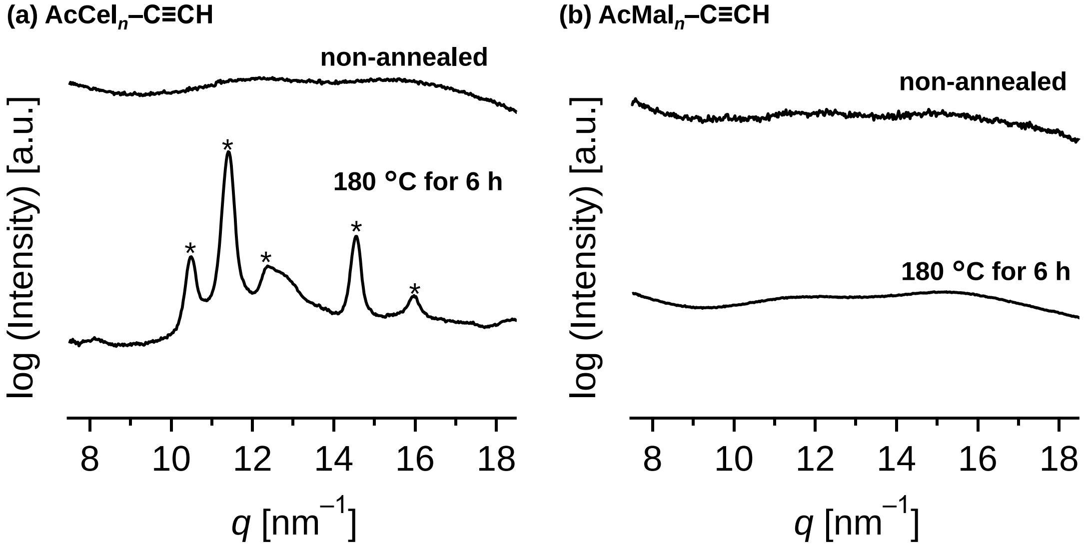

Figure 3.21. WAXD profiles of (a) AcCel$_n$–C≡CH and (b) AcMal$_n$–C≡CH without thermal annealing (upper) and after thermal annealing (lower) at 180 °C for 6 h. The asterisks denote the diffraction peak from cellulose triacetate I crystal.

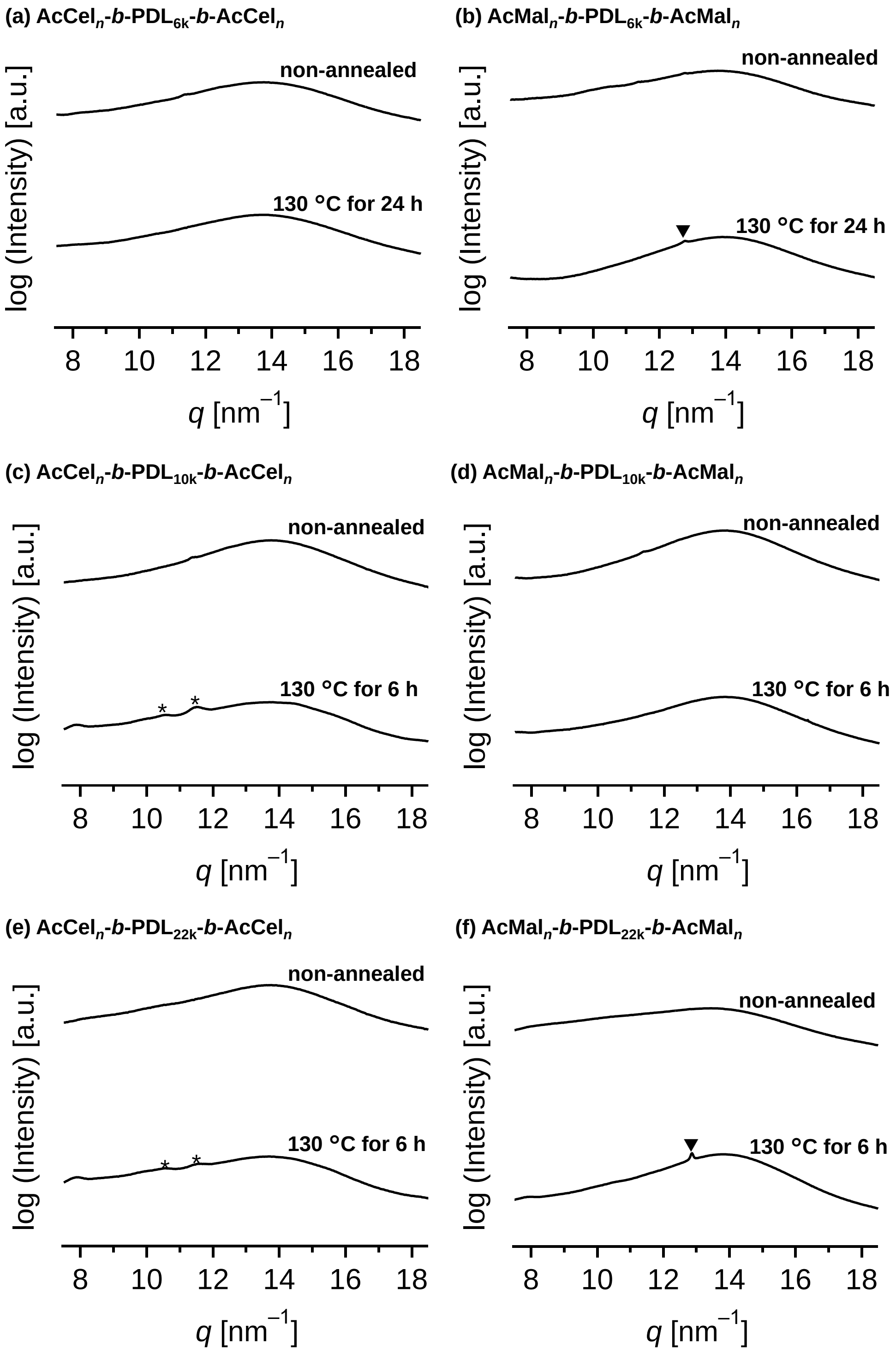

Figure 3.22. WAXD profiles of (a) AcCel$_n$-*b*-PDL$_{6k}$-*b*-AcCel$_n$, (b) AcMal$_n$-*b*-PDL$_{6k}$-*b*-AcMal$_n$, (c) AcCel$_n$-*b*-PDL$_{10k}$-*b*-AcCel$_n$, (d) AcMal$_n$-*b*-PDL$_{10k}$-*b*-AcMal$_n$, (e) AcCel$_n$-*b*-PDL$_{22k}$-*b*-AcCel$_n$, and (f) AcMal$_n$-*b*-PDL$_{22k}$-*b*-AcMal$_n$ without thermal annealing (upper) and after thermal annealing (lower) at 130 °C for 6 or 24 h. The asterisks denote the diffraction peak from cellulose triacetate I crystal and inverted triangles denote artifact peak.

To further investigate the microphase-separation behavior, the author subjected BCP thin films to atomic force microscopy (AFM) (**Figure 3.23**); the thin-film samples were prepared by spin-coating 1% (w/w) solutions of AcCel$_n$-*b*-PDL-*b*-AcCel$_n$s and AcMal$_n$-*b*-PDL-*b*-AcMal$_n$s in toluene onto bare Si substrates. The AFM phase images of the non-annealed AcCel$_n$-*b*-PDL$_{6k}$-*b*-AcCel$_n$, AcCel$_n$-*b*-PDL$_{10k}$-*b*-AcCel$_n$, AcMal$_n$-*b*-PDL$_{6k}$-*b*-AcMal$_n$, and AcMal$_n$-*b*-PDL$_{10k}$-*b*-AcMal$_n$ thin films show less-ordered fingerprint patterns. In contrast, the non-annealed AcCel$_n$-*b*-PDL$_{22k}$-*b*-AcCel$_n$ and AcMal$_n$-*b*-PDL$_{22k}$-*b*-AcMal$_n$ thin films show less-ordered spheres. These results are consistent with the fact that featureless SAXS profiles were observed for the non-annealed samples in the bulk. The morphologies of the AcCel$_n$-*b*-PDL-*b*-AcCel$_n$s were significantly altered by thermal annealing in the thin-film and bulk states. The AFM phase image of the AcCel$_n$-*b*-PDL$_{6k}$-*b*-AcCel$_n$ thin film showed a peculiar morphology consisting of rectangular units, which are related to the crystallization of the AcCel$_n$ segment.[58] A highly ordered fingerprint-like pattern was observed in the thermally annealed AcCel$_n$-*b*-PDL$_{10k}$-*b*-AcCel$_n$ thin film, which is attributable to the horizontally orientated HEX structure, considering the SAXS result. The spherical structures observed in the thermally annealed AcCel$_n$-*b*-PDL$_{22k}$-*b*-AcCel$_n$ are attributable to the BCC spherical structure. The AFM images of AcCel$_n$-*b*-PDL$_{10k}$-*b*-AcCel$_n$ and AcCel$_n$-*b*-PDL$_{22k}$-*b*-AcCel$_n$ revealed the *d* values of 10.8 and 12.0 nm, respectively, which were in good agreement with the values derived from the SAXS results. As expected from the SAXS results, the AcMal$_n$-*b*-PDL-*b*-AcMal$_n$ thin films did not exhibit any ordered patterns following thermal annealing, which verifies that the cellulose-based BCPs are more likely to microphase-separate than their amylose counterparts.

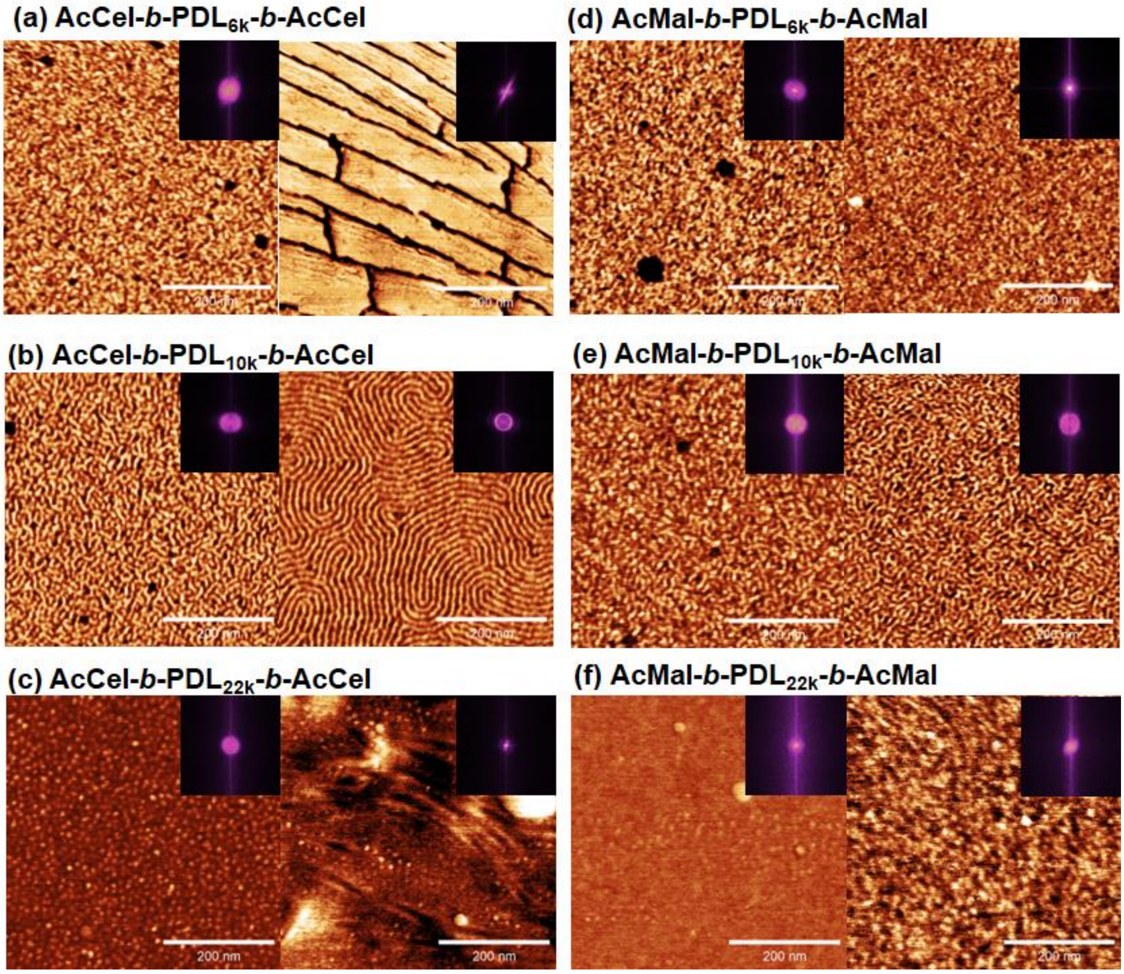

Figure 3.23. AFM phase images of (a) AcCel$_n$-*b*-PDL$_{6k}$-*b*-AcCel$_n$, (b) AcCel$_n$-*b*-PDL$_{10k}$-*b*-AcCel$_n$, (c) AcCel$_n$-*b*-PDL$_{22k}$-*b*-AcCel$_n$, (d) AcMal$_n$-*b*-PDL$_{6k}$-*b*-AcMal$_n$, (e) AcMal$_n$-*b*-PDL$_{10k}$-*b*-AcMal$_n$, and (f) AcMal$_n$-*b*-PDL$_{22k}$-*b*-AcMal$_n$ thin film before (left) and after (right) thermal annealing at 130 °C. The insets show the corresponding FFT profiles. Scale bars are 200 nm.

3.3.5. Mechanical properties

Finally, to investigate the impact of the hard oligosaccharide segment on mechanical properties, dog-bone-shaped specimens of solvent-cast BCPs were subjected to tensile testing. Note that it was difficult to subject AcMal$_n$-*b*-PDL$_{22k}$-*b*-AcMal$_n$ to tensile testing because it is a sticky material. The other BCPs exhibited elastic properties, which confirms that the hard microphase-separated oligosaccharide domains act as physical crosslinks between the rubbery PDL chains. The stress–strain curves and key mechanical properties (Young's modulus (E), strain at break (ε_b), stress at break (σ_b), and toughness, and their average values and standard deviations) of the BCP specimens are shown in **Table 3.2** and **Figure 3.24**, respectively.

Table 3.2. Tensile properties of the BCP specimens[a]

BCP	E[a] [MPa]	ε_b[a] [%]	σ_b[a] [MPa]	Toughness[a] [MJ m^{-3}]
AcCel$_n$-*b*-PDL$_{6k}$-*b*-AcCel$_n$	69±5.1	209±17.6	5.8±0.082	8.9±0.90
AcCel$_n$-*b*-PDL$_{10k}$-*b*-AcCel$_n$	13±1.7	356±8.99	7.1±0.47	15±1.2
AcCel$_n$-*b*-PDL$_{22k}$-*b*-AcCel$_n$	1.3±0.062	385±16.0	1.7±0.047	3.8±0.17
AcMal$_n$-*b*-PDL$_{6k}$-*b*-AcMal$_n$	61±6.8	150±14.6	2.8±0.12	4.2±0.48
AcMal$_n$-*b*-PDL$_{10k}$-*b*-AcMal$_n$	5.6±0.68	198±13.6	1.6±0.14	2.2±0.29

[a]Tensile properties are shown as average values (with standard deviations) for three specimens.

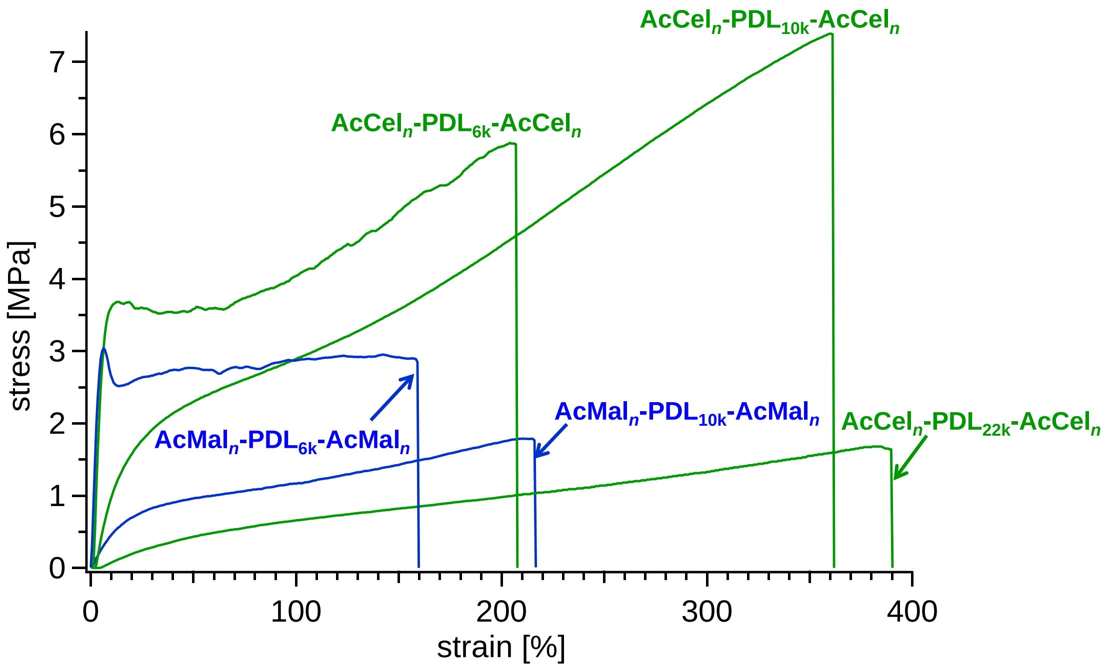

Figure 3.24. Typical stress–strain curves of the AcCel$_n$-b-PDL$_{6k}$-b-AcCel$_n$, AcCel$_n$-b-PDL$_{10k}$-b-AcCel$_n$, AcCel$_n$-b-PDL$_{22k}$-b-AcCel$_n$, AcMal$_n$-b-PDL$_{6k}$-b-AcMal$_n$, and AcMal$_n$-b-PDL$_{10k}$-b-AcMal$_n$ specimens (crosshead speed: 10 mm min^{-1}).

The stress–strain curves show that AcCel$_n$-b-PDL$_{6k}$-b-AcCel$_n$ and AcMal$_n$-b-PDL$_{6k}$-b-AcMal$_n$, which possess the lowest f_{PDL} values, exhibit yield points, suggestive of plastic-like behavior irrespective of the type of hard segment. In contrast, AcCel$_n$-b-PDL$_{10k}$-b-AcCel$_n$, AcCel$_n$-b-PDL$_{22k}$-b-AcCel$_n$, and AcMal$_n$-b-PDL$_{10k}$-b-AcMal$_n$ did not exhibit clear yield points, suggesting that BCPs with longer PDL segments exhibit elastomer-like behavior, which is supported by the results of cyclic tensile testing (**Figure 3.25**), which suggest that the areas enclosed by hysteresis loops, which correlate with the level of plastic deformation, diminish with increasing f_{PDL}. No obvious residual strain was observed following five loading/unloading cycles for AcCel$_n$-b-PDL$_{22k}$-b-AcCel$_n$, confirming its high level of elastic recovery. A general trend in which ε_b increases and *E* decreases with increasing f_{PDL} was observed; for example, the ε_b value of AcCel$_n$-*b*-PDL$_{22k}$-*b*-AcCel$_n$ was 1.8-times higher than that of AcCel$_n$-*b*-PDL$_{6k}$-*b*-AcCel$_n$, and the *E* value of AcCel$_n$-*b*-PDL$_{6k}$-*b*-AcCel$_n$ was 53-times higher than that of AcCel$_n$-*b*-PDL$_{22k}$-*b*-AcCel$_n$. This trend was observed when the ε_b and *E* values for AcMal$_n$-*b*-PDL$_{6k}$-*b*-AcMal$_n$ and AcMal$_n$-*b*-PDL$_{10k}$-*b*-AcMal$_n$ were compared.

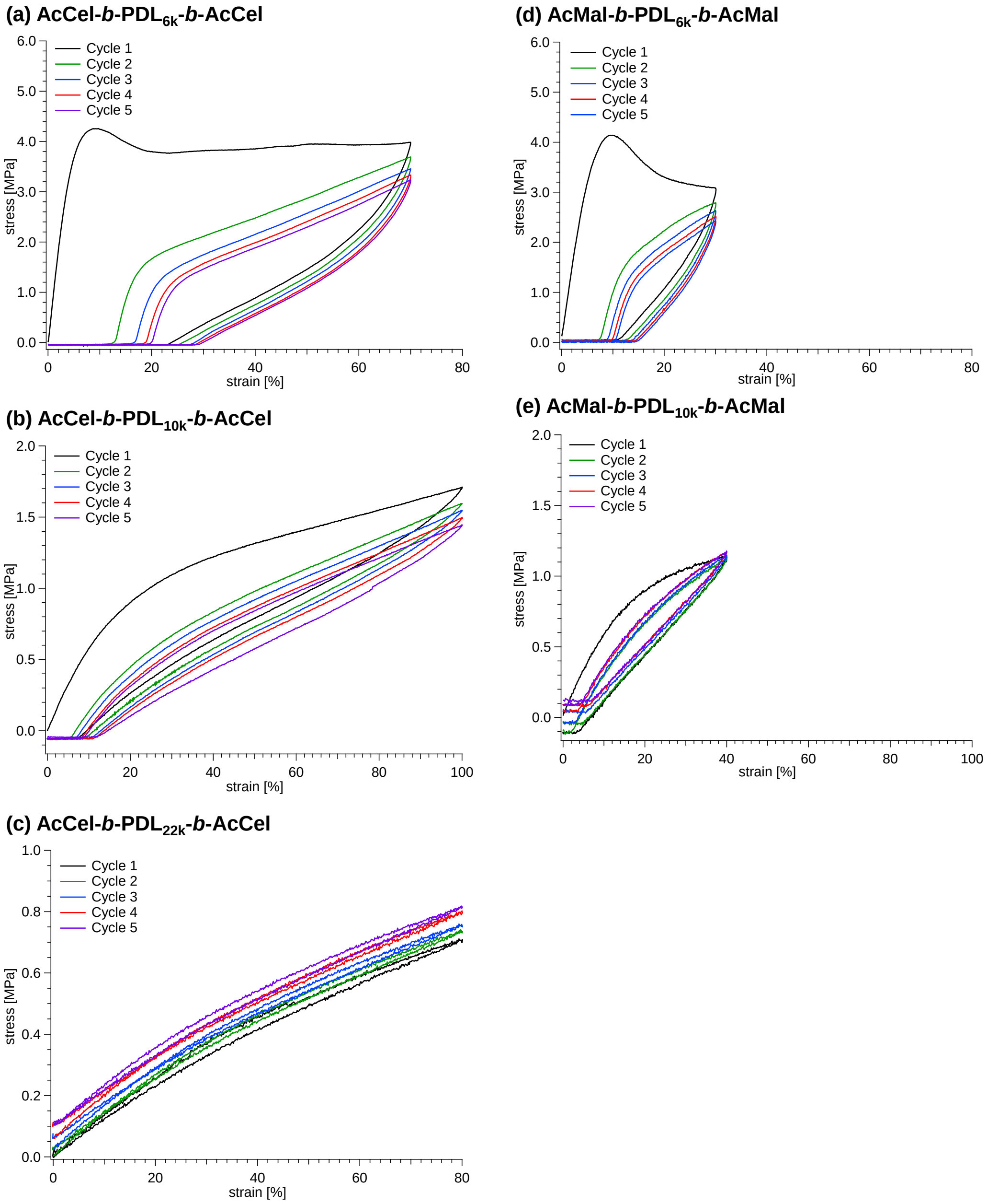

Figure 3.25. Cycle tensile testing (crosshead speed, 10 mm min^{-1}) for (a) AcCel$_n$-*b*-PDL$_{6k}$-*b*-AcCel$_n$, (b) AcCel$_n$-*b*-PDL$_{10k}$-*b*-AcCel$_n$, (c) AcCel$_n$-*b*-PDL$_{22k}$-*b*-AcCel$_n$, (d) AcMal$_n$-*b*-PDL$_{6k}$-*b*-AcMal$_n$, and (e) AcMal$_n$-*b*-PDL$_{10k}$-*b*-AcMal$_n$.

The BCPs containing AcCel$_n$ segments possess significantly superior mechanical properties to those containing AcMal$_n$ segments, despite their comparable molecular weights and chemical compositions. Specifically, the E, ε_b, σ_b, and toughness values of AcCel$_n$-*b*-PDL$_{10\mathrm{k}}$-*b*-AcCel$_n$ were 2.3-, 1.8-, 4.4-, and 6.8-times greater than those of AcMal$_n$-*b*-PDL$_{10\mathrm{k}}$-*b*-AcMal$_n$, respectively. Furthermore, stress on the AcCel$_n$-*b*-PDL$_{6\mathrm{k}}$-*b*-AcCel$_n$ specimen gradually increased beyond the yield point, while AcMal$_n$-*b*-PDL$_{6\mathrm{k}}$-*b*-AcMal$_n$ maintained constant stress beyond the yield point until rupture. AcCel$_n$-*b*-PDL-*b*-AcCel$_n$ strain hardening reveals that cellulosic hard-segment pull-out was more effectively hindered in these polymers compared to that in their amylose counterparts.[59] The stronger crosslinking ability of the AcCel$_n$ segment is partly attributable to its crystalline nature, in contrast to the amorphous nature of AcMal$_n$. X-ray crystallography previously revealed that cellulose triacetate and amylose triacetate adopt sheet and helix conformations, respectively.[50,51,60,61] Evidently, the sheet-like conformation is preferred for creating larger interchain attractive forces, which may be responsible for the stronger crosslinking of the AcCel$_n$ segment. In addition, the higher potential to form ordered microphase-separated structures seems to be another important factor that contributes to the superior mechanical performance of the AcCel$_n$-*b*-PDL-*b*-AcCel$_n$s.

Figure 3.26 compares σ_b and E of AcCel$_n$-*b*-PDL$_{6\mathrm{k}}$-*b*-AcCel$_n$, AcCel$_n$-*b*-PDL$_{10\mathrm{k}}$-*b*-AcCel$_n$, AcCel$_n$-*b*-PDL$_{22\mathrm{k}}$-*b*-AcCel$_n$, AcMal$_n$-*b*-PDL$_{6\mathrm{k}}$-*b*-AcMal$_n$, and AcMal$_n$-*b*-

PDL$_{10k}$-*b*-AcMal$_n$ with those of commercial thermoplastic elastomers (TPEs). Notably, the *E* value of AcCel$_n$-*b*-PDL$_{10k}$-*b*-AcCel$_n$ was comparable to or even higher than those of commercial TPEs, such as melt-processable rubber and TPEs containing polyamide hard blocks. The σ_b of AcCel$_n$-PDL$_{10k}$-*b*-AcCel$_n$ was also comparable to those of commercial TPEs, such as melt-processable rubber and silicone TPEs. This comparison highlights the potential of the AcCel$_n$-*b*-PDL-*b*-AcCel$_n$s as fully bio-based high-performance elastomers.

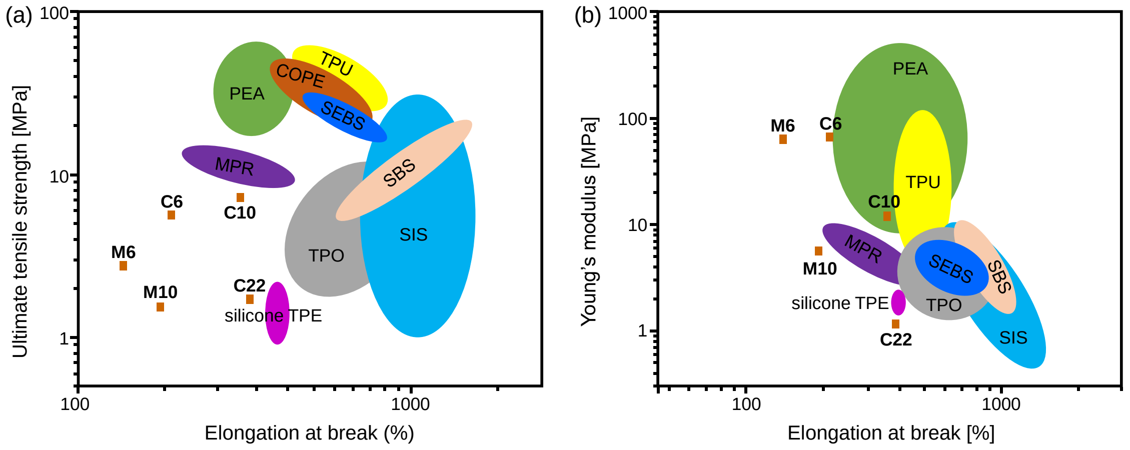

Figure 3.26. Comparison of (a) σ_b and (b) *E* value of AcCel$_n$-*b*-PDL$_{6k}$-*b*-AcCel$_n$ (C6), AcCel$_n$-*b*-PDL$_{10k}$-*b*-AcCel$_n$ (C10), AcCel$_n$-*b*-PDL$_{22k}$-*b*-AcCel$_n$ (C22), AcMal$_n$-*b*-PDL$_{6k}$-*b*-AcMal$_n$ (M6), and AcMal$_n$-*b*-PDL$_{10k}$-*b*-AcMal$_n$ (M10) with commercial TPEs. SBS, poly(styrene)-*b*-poly(butadiene)-*b*-poly(styrene); SIS, poly(styrene)-*b*-poly(isoprene)-*b*-poly(styrene); SEBS, poly(styrene)-*b*-poly(ethylene-*co*-butylene)-*b*-poly(styrene); PEA, TPEs with polyamide hard blocks; TPO, thermoplastic olefins; COPE, copolyester TPEs; MPR, melt processable rubber; TPU, thermoplastic polyurethanes.[62]

3.4. Conclusion

In this work, novel cellulose-based BCPs (AcCel$_n$-*b*-PDL-*b*-AcCel$_n$s) and their amylose counterparts (AcMal$_n$-*b*-PDL-*b*-AcMal$_n$s) were precisely synthesized. The AcCel$_n$-*b*-PDL-*b*-AcCel$_n$s were found to be more likely to self-assemble than the AcMal$_n$-*b*-PDL-*b*-AcMal$_n$s in their bulk and thin-film states. Because these BCPs have comparable chemical compositions and molecular weights, the dramatic difference in their self-assembly behavior stems from the differences in the types of bonding (i.e., β-1,4 or α-1,4 linkages) in their oligosaccharide segments. More interestingly, the AcCel$_n$-*b*-PDL-*b*-AcCel$_n$s exhibit superior mechanical properties than the AcMal$_n$-*b*-PDL-*b*-AcMal$_n$s, which indicates that stronger physical crosslinking was achieved in the AcCel$_n$ segments. In addition, the Young's modulus (~69 MPa) and elongation at break (~5.8 MPa) of the AcCel$_n$-*b*-PDL-*b*-AcCel$_n$s were comparable to or higher than those of commercially available TPEs. To the best of my knowledge, this is the first report that investigates in detail how small differences in the primary structures of oligosaccharide segments (i.e., α-1,4 or β-1,4 linkages) affect the microphase-separation and mechanical properties of poly/oligosaccharide-based BCPs. Overall, the author verified the applicability of cellulose-based BCPs exhibit as bio-based and sustainable polymeric materials. Encouraged by these promising results, the author hypothesized that the cellulose-based materials could be more toughened by optimizing the degree of substitution. This study is mentioned in next Chapter 4.

3.5. References

(1) Zhu, Y.; Romain, C.; Williams, C. K. Sustainable polymers from renewable resources. *Nature* **2016**, *540*, 354–362.

(2) Esposito, D.; Antonietti, M. Redefining biorefinery: the search for unconventional building blocks for materials. *Chem. Soc. Rev.* **2015**, *44*, 5821–5835.

(3) Bozell, J. J.; Petersen, G. R. Technologu development for the production of biobased products from biorefinery carbohydrates—the US Department of Energy's "Top 10" revisited. *Green Chem*. **2010**, *12*, 539–554.

(4) Östmark, E.; Nyström, D.; Malmström, E. Unimolecular Nanocontainers Prepared by ROP and Subsequent ATRP from Hydroxypropylcellulose. *Macromolecules* **2008**, *41*, 4405–4415.

(5) Nouvel, C.; Frochot, C.; Sadtler, V.; Dubois, P.; Dellacherie, E.; Six, J.-L. Polylactide-Grafted Dextrans: Synthesis and Properties at Interfaces and in Solution. *Macromolecules* **2004**, *37*, 4981–4988.

(6) Palumbo, F. S.; Pitarresi, G.; Mandracchia, D.; Tripodo, G.; Giammona, G. New graft copolymers of hyaluronic acid and polylactic acid: Synthesis and characterization. *Carbohydr. Polym.* **2006**, *66*, 379–385.

(7) Colinet, I.; Dulong, V.; Hamaide, T.; Le Cerf, D.; Picton, L. New amphiphilic modified polysaccharides with original solution behaviour in salt media. *Carbohydr. Polym.* **2009**, *75*, 454–462.

(8) Maruyama, A.; Ishihara, T.; Kim, J.- S.; Kim, S. W.; Akaike, T. Nanoparticle DNA Carrier with Poly(L-Lysine) Grafted Polysaccharide Copolymer and Poly(D,L-Lactic Acid). *Bioconjug. Chem.* **1997**, *8*, 735–742.

(9) Asayama, S.; Nogawa, M.; Takei, Y.; Akaike, T.; Maruyama, A. Synthesis of Novel Polyampholyte Comb-Type Copolymers Consisting of a Poly(L-Lysine) Backbone and Hyaluronic Acid Side Chains for a DNA Carrier. *Bioconjug. Chem.* **1998**, *9*, 476–481.

(10) Aissou, K.; Otsuka, I.; Rochas, C.; Fort, S.; Halila, S.; Borsali, R. Nano-Organization of Amylose-*b*-Polystyrene Block Copolymer Films Doped with Bipyridine. *Langmuir* **2011**, *27*, 4098–4103.

(11) Isono, T.; Kawakami, N.; Watanabe, K.; Yoshida, K.; Otsuka, I.; Mamiya, H.; Ito, H.; Yamamoto, T.; Tajima, K.; Borsali, R.; Satoh, T. Microphase separation of

carbohydrate-based star-block copolymers with sub-10 nm periodicity. *Polym. Chem.* **2019**, *10*, 1119–1129.

(12) Isono, T.; Komaki, R.; Lee, C.; Kawakami, N.; Ree, B. J.; Watanabe, K.; Yoshida, K.; Mamiya, H.; Yamamoto, T.; Borsali, R.; Tajima, K.; Satoh, T. Rapid access to discrete and monodisperse block co-oligomers from sugar and terpenoid toward ultrasmall periodic nanostructures. *Commun. Chem.* **2020**, *3*, 1–9.

(13) Schatz, C.; Lecommandoux, S. Polysaccharide-Containing Block Copolymers: Synthesis, Properties and Applications of an Emerging Family of Glycoconjugates. *Macromol. Rapid Commun.* **2010**, *31*, 1664–1684.

(14) Isono, T.; Nakahira, S.; Hsieh, H. -C.; Katsuhara, S.; Mamiya, H.; Yamamoto, T.; Chen, W.- C.; Borsali, R.; Tajima, K.; Satoh, T. Carbohydrates as Hard Segments for Sustainable Elastomers: Carbohydrates Direct the Self-Assembly and Mechanical Properties of Fully Bio-Based Block Copolymers. *Macromolecules* **2020**, *53*, 5408–5417.

(15) Ikeda, Y.; Nakamura, Y.; Kajiwara, K.; Kohjiya, S. Chemical Modification of Butyl Rubber. III. Butyl Rubber with D-maltose Derivative as Pendant Groups. *J. Polym. Sci. Part A Polym. Chem.* **1995**, *33*, 2657–2665.

(16) Nasiri, M.; Reineke, T. M. Sustainable glucose-based block copolymers exhibit elastomeric and adhesive behavior. *Polym. Chem.* **2016**, *7*, 5233–5240.

(17) Katsuhara, S.; Mamiya, H.; Yamamoto, T.; Tajima, K.; Isono, T.; Satoh, T. Metallopolymer-*block*-oligosaccharide for sub-10 nm microphase separation. *Polym. Chem.* **2020**, *11*, 2995–3002.

(18) Otsuka, I.; Nilsson, N.; Suyatin, D. B.; Maximov, I.; Borsali, R. Carbohydrate-based block copolymer systems: directed self-assembly for nanolithography applications. *Soft Matter* **2017**, *13*, 7406–7411.

(19) Cushen, J. D.; Otsuka, I.; Bates, C. M.; Halila, S.; Fort, S.; Rochas, C.; Easley, J. A.; Rausch, E. L.; Thio, A.; Borsali, R.; Willson, C. G.; Ellison, C, J. Oligosaccharide/Silicon-Containing Block Copolymers with 5 nm Features for Lithographic Applications. *ACS Nano* **2012**, *6*, 3424–3433.

(20) Hung, C. -C.; Nakahira, S.; Chiu, Y. -C.; Isono, T.; Wu, H. -C.; Watanabe, K.; Chiang, Y. -C.; Takashima, S.; Borsali, R.; Tung, S. -H.; Satoh, T.; Chen, W. -C. Control over Molecular Architectures of Carbohydrate-Based Block Copolymers for Stretchable Electrical Memory Devices. *Macromolecules* **2018**, *51*, 4966–4975.

(21) Chuang, T. -H.; Chiang, Y. -C.; Hsieh, H. -C.; Isono, T.; Huang, C. -W.; Borsali, R.; Satoh, T.; Chen, W. -C. Nanostructure- and Orientation-Controlled Resistive Memory Behaviors of Carbohydrate-*block*-Polystyrene with Different Molecular Weights via Solvent Annealing. *ACS Appl. Mater. Interfaces* **2020**, *12*, 23217–23224.

(22) Sun, H. -S.; Chen, Y.; Lee, W. -Y.; Chiu, Y. -C.; Isono, T.; Satoh, T.; Kakuchi, T.; Chen, W. -C. Synthesis, morphology, and electrical memory application of oligosaccharide-based block copolymers with π-conjugated pyrene moieties and their supramolecules. *Polym. Chem.* **2016**, *7*, 1249–1263.

(23) Sun, H. -S.; Chiu, Y. -C.; Lee, W. -Y.; Chen, Y.; Hirao, A.; Satoh, T.; Kakuchi, T.; Chen, W. -C. Synthesis of Oligosaccharide-Based Block Copolymers with Pendent Conjugated Oligofluorene Moieties and Their Electrical Device Applications. *Macromolecules* **2015**, *48*, 3907–3917.

(24) Breitenbach, B. B.; Schmid, I.; Wich, P. R. Amphiphilic Polysaccharide Block Copolymers for pH-Responsive Micellar Nanoparticles. *Biomacromolecules* **2017**, *18*, 2839–2848.

(25) Zhang, N.; Wardwell, P. R.; Bader, R. A. Polysaccharide-Based Micelles for Drug Delivery. *Pharmaceutics* **2013**, *5*, 329–352.

(26) Zhao, Z.; Zhang, Z.; Chen, L.; Cao, Y.; He, C.; Chen, X. Biodegradable Stereocomplex Micelles Based on Dextran-*block*-Polylactide as Efficient Drug Deliveries. *Langmuir* **2013**, *29*, 13072–13080.

(27) Ceresa, R. J. The Synthesis of Block and Graft Copolymers of Cellulose and its Derivatives. *Polymer.* **1961**, *2*, 213–219.

(28) Yagi, S.; Kasuya, N.; Fukuda, K. Synthesis and characterization of cellulose-*b*-polystyrene. *Polym. J.* **2010**, *42*, 342–348.

(29) Houga, C.; Meins, J. -F. Le; Borsali, R.; Taton, D.; Gnanou, Y. Synthesis of ATRP-induced dextran-*b*-polystyrene diblock copolymers and preliminary investigation of their self-assembly in water. *Chem. Commun.* **2007**, 3063–3065.

(30) Li, B.- G.; Zhang, L. -M. Synthesis and characterization of novel amphiphilic block copolymers based on maltoheptaose and Poly(ε-caprolactone). *Carbohydr. Polym.* **2008**, *74*, 390–395.

(31) Volokhova, A. S.; Edgar, K. J.; Matson, J. B. Polysaccharide-containing block copolymers: synthesis and applications. *Mater. Chem. Front.* **2020**, *4*, 99–112.

(32) Golas, P. L.; Matyjaszewski, K. Marrying click chemistry with polymerization: expanding the scope of polymeric materials. *Chem. Soc. Rev.* **2010**, *39*, 1338–1354.

(33) Rostovtsev, V. V.; Green, L. G.; Fokin, V. V.; Sharpless, K. B. A Stepwise Huisgen Cycloaddition Process: Copper(I)-Catalyzed Regioselective “Ligation” of Azides and Terminal Alkynes. *Angew. Chem. Int. Ed.* **2002**, *41*, 2596–2599.

(34) Worrell, B. T.; Malik, J. A.; Fokin, V. V. Direct Evidence of a Dinuclear Copper Intermeiate in Cu(I)-Catalyzed Azide-Alkyne Cycloadditions. *Science* **2010**, *340*, 457–461.

(35) Puls, J.; Wilson, S. A.; Hölter, D. Degradation of Cellulose Acetate-Based Materials: A Review. *J. Polym. Environ.* **2011**, *19*, 152–165.

(36) Edgar, K. J.; Buchanan, C. M.; Debenham, J. S.; Rundquist, P. A.; Seiler, B. D.; Shelton, M. C.; Tindall, D. Advances in cellulose ester performance and applicaton. *Prog. Polym. Sci.* **2001**, *26*, 1605–1688.

(37) Arrington, K. J.; Haag, J. V.; French, E. V.; Murayama, M.; Edgar, K. J.; Matson, J. B. Toughening Cellulose: Compatibilizing Polybutadiene and Cellulose Triacetate Blends. *ACS Macro Lett.* **2019**, *8*, 447–453.

(38) Kamitakahara, H.; Enomoto, Y.; Hasegawa, C.; Nakatsubo, F. Synthesis of diblock copolymers with cellulose derivatives. 2. Characterization and thermal properties of cellulose triacetate-block-oligoamide-15. *Cellulose* **2005**, *12*, 527–541.

(39) Chen, J.; Kamitakahara, H.; Edgar, K. J. Synthesis of polysaccharide-based block copolymers via olefin cross-metathesis. *Carbohydr. Polym.* **2020**, *229*, No. 115530.

(40) Hiraishi, M.; Igarashi, K.; Kimura, S.; Wada, M.; Kitaoka, M.; Samejima, M. Synthesis of highly ordered cellulose II in vitro using cellodextrin phosphorylase. *Carbohydr. Res.* **2009**, *344*, 2468–2473.

(41) Grandjean, C.; Boutonnier, A.; Guerreiro, C.; Fournier, J. M.; Mulard, L. A. On the Preparation of Carbohydrate-Protein Conjugates Using the Traceless Staudinger Ligation. *J. Org. Chem.* **2005**, *70*, 7123–7132.

(42) Halila, S.; Manguian, M.; Fort, S.; Cottaz, S.; Hamaide, T.; Fleury, E.; Driguez, H. Syntheses of Well-Defined Glyco-Polyorganosiloxanes by “Click” Chemistry and Their Surfactant Properties. *Macromol. Chem. Phys.* **2008**, *209*, 1282–1290.

(43) Nohara, T.; Sawada, T.; Tanaka, H.; Serizawa, T. Enzymatic Synthesis of Oligo(ethylene glycol)-Bearing Cellulose Oligomers for in Situ Formation of Hydrogels with Crystalline Nanoribbon Network Structures. *Langmuir* **2016**, *32,* 12520–12526.

(44) Pylkkänen, R.; Mohammadi, P.; Arola, S.; De Ruijter, J. C.; Sunagawa, N.; Igarashi, K.; Penttilä, M. *In Vitro* Synthesis and Self-Assembly of Cellulose II Nanofibrils Catalyzed by the Reverse Reaction of Clostridium Thermocellum Cellodextrin Phosphorylase. *Biomacromolecules* **2020**, *21*, 4355–4364.

(45) Serizawa, T.; Kato, M.; Okura, H.; Sawada, T.; Wada, M. Hydrolytic activities of artificial nanocellulose synthesized via phosphorylase-catalyzed enzymatic reactions. *Polym. J.* **2016**, *48*, 539–544.

(46) Yataka, Y.; Sawada, T.; Serizawa, T. Enzymatic synthesis and post-functionalization of two-dimensional crystalline cellulose oligomers with surface-reactive Groups. *Chem. Commun.* **2015**, *51*, 12525–12528.

(47) Krishnareddy, M.; Kim, Y.-K.; Kitaoka, M.; Mori, Y.; Hayashi, K. Cellodextrin Phosphorylase from *Clostridium thermocellum* YM4 Strain Expressed in

Escherichia Coli. *J. Appl. Glycosci.* **2002**, *49*, 1–8.

(48) Kamitakahara, H.; Enomoto, Y.; Hasegawa, C. Synthesis of diblock copolymers with cellulose derivatives . 2 . Characterization and thermal properties of cellulose triacetate-block-Oligoamide-15. **2005**, *12*, 527–541.

(49) Sakai-otsuka, Y.; Zaioncz, S.; Otsuka, I.; Halila, S.; Rannou, P.; Borsali, R. Self-Assembly of Carbohydrate-*block*-Poly(3-hexylthiophene) Diblock Copolymers into Sub-10 nm Scale Lamellar Structures. *Macromolecules* **2017**, *50*, 3365–3376.

(50) Roche, E.; Chanzy, H.; Boudeulle, M.; Marchessault, R. H.; Sundararajan, P. Three-Dimensional Crystalline Structure of Cellulose Triacetate II. *Macromolecules* **1978**, *11*, 86–94.

(51) Takahashi, Y.; Nishikawa, S. Crystal Structure of Amylose Triacetate I. *Macromolecules* **2003**, *36*, 8656–8661.

(52) Martello, M. T.; Burns, A.; Hillmyer, M. Bulk Ring-Opening Transesterification Polymerization of the Renewable δ-Decalactone Using an Organocatalyst. *ACS Macro Lett.* **2012**, *1*, 131–135.

(53) Hamley, I. W.; Castelletto, V. Small-angle scattering of block copolymers in the melt, solution and crsystal states. *Prog. Polym. Sci.* **2004**, *29*, 909–948.

(54) Jiang, X.; Kitamura, S.; Sato, T.; Terao, K. Chain Dimensions and Stiffness of Cellulosic and Amylosic Chains in an Ionic Liquid: Cellulose, Amylose, and an Amylose Carbamate in BmimCl. *Macromolecules* **2017**, *50*, 3979–3984.

(55) Seger, B.; Aberle, T.; Burchard, W. Solution behaviour of cellulose and amylose in iron-sodiumtartrate (FeTNa). *Carbohydr. Polym.* **1996**, *31*, 105–112.

(56) Watanabe, S. Takai, M.; Hayashi, J. An X-Ray Study of Cellulose Triacetate. *J. Polym. Sci., Part C: Polym. Symp.* **1968**, *23*, 825–835.

(57) Braun, J. L.; Kadla, J. F. CTA III: A Third Polymorph of Cellulose Triacetate. *J. Carbohydr. Chem.* **2013**, *32*, 120–138.

(58) Liang, G. D.; Xu, J. -T.; Fan, Z. -Q.; Mai, S. -M.; Ryan, A. J. Thin Film Morphology of Symmetric Semicrystalline Oxyethylene/Oxybutylene Diblock Copolymers on Silicon. *Macromolecules* **2006**, *39*, 5471–5478.

(59) Wang, W.; Schlegel, R.; White, B. T.; Williams, K.; Voyloy, D.; Steren, C. A.; Goodwin, A.; Coughlin, E. B.; Gido, S.; Beiner, M.; et al. High Temperature Thermoplastic Elastomers Synthesized by Living Anionic Polymerization in Hydrocarbon Solvent at Room Temperature. *Macromolecules* **2016**, *49*, 2646–2655.

(60) Sikorski, P.; Wada, M.; Heux, L.; Shintani, H.; Stokke, B. T. Crystal Structure of Cellulose Triacetate I. *Macromolecules* **2004**, *37*, 4547–4553.

(61) Zugenmaier, P.; Steinmeier, H. Conformation of Some Amylose Triesters: The Influence of Side Groups. *Polymer.* **1986**, *27*, 1601–1608.

(62) Gregory, G. L.; Sulley, G. S.; Carrodeguas, L. P.; Chen, T. T. D.; Santmarti, A.; Terrill, N. J.; Lee, K. Y.; Williams, C. K. Triblock polyester thermoplastic Elastomers with semi-aromatic polymer end blocks by ring-opening Copolymerization. *Chem. Sci.* **2020**, *11*, 6567–6581.

Chapter 4

Design of Cellulose-Based Block Copolymers: DS effects on Microphase Separation Behavior and Mechanical Properties

4.1. Introduction

Thermoplastic elastomers (TPEs) are essential materials in daily life and have been used in various fields. The hot-melt processability and reusability of TPEs are major advantages over conventional vulcanized rubbers, the thermoset nature of which prevents recycling. Most TPEs are ABA-type triblock copolymers, where the A block is an amorphous or semicrystalline polymer with a high glass transition temperature (T_g) and the B block is an amorphous rubbery polymer with a low T_g. Microphase separation into the "hard" A domain and the "soft" B matrix plays a key role in the elastic properties, with the hard A segments serving as physical crosslinks for the rubbery B chains. Commonly, TPEs utilize polystyrene (PS) as the hard segment, and various PS-based TPEs have been commercialized, as exemplified by PS-*b*-polyisoprene-*b*-PS, PS-*b*-polybutadiene-*b*-PS, and PS-*b*-polyethylenepropylene-*b*-PS.[1] TPEs with other combinations of soft and hard segments, such as thermoplastic polyurethane and polyolefin elastomers, have also been widely commercialized. However, these TPEs are derived from petroleum and lack biodegradability. Considering the recent demand for bio-based and biodegradable plastics, it is necessary to develop new environmentally benign TPEs. Various research groups have investigated bio-based and biodegradable alternatives to PS-based TPEs. For instance, TPEs with polylactide (PLA) hard segments combined with amorphous and low-T_g aliphatic polyesters such as poly(γ-methyl-ε-

caprolactone), poly(ε-decalactone), and poly(menthide) as soft segments have been fabricated.[2–7]

Most bio-based TPEs utilize PLA as the hard segment, but poly/oligosaccharides have potential as novel biodegradable hard segments. From a physiochemical point of view, oligosaccharides are highly attractive hard domains because of their reasonable solubility, high T_g (>100 °C), rigidity, and strong intermolecular interactions via hydrogen bonding or crystallization. Advantageously, oligosaccharides are also strongly incompatible with hydrophobic polymers, which leads to the formation of microphase-separated structures. Borsali, Kakuchi, and Satoh et al. revealed that block copolymers (BCPs) consisting of maltooligosaccharide with a wide variety of hydrophobic polymers such as PS, poly(ε-caprolactone), poly(propylene oxide), polydimethylsiloxane, and oligoisoprene self-assembled into highly ordered microphase-separated structures with domain spacings (d) of less than 10 nm.[8–14] Surprisingly, oligosaccharide-based BCPs with low molecular weights (<2,000 g mol^{-1}) also formed microphase-separated structures, which indicates an unusually high potential for microphase separation.[11–13] In fact, fully bio-based ABA-type triblock copolymers containing maltooligosaccharide as the A block and bio-based poly(δ-decalactone) (PDL; $T_g \approx -60$ °C) as the B block had highly ordered microphase-separated structures and exhibited elastomeric properties, with a stress at break of ~700% and a Young's modulus comparable to that of conventional PS-based TPEs.[15] In Chapter 3, the author replaced unprotected maltooligosaccharide with cellulose triacetate to endow the BCPs with enhanced thermoplasticity. Compared with their amylose triacetate-based counterparts, the cellulose triacetate-based TPEs exhibited a greater self-assembly tendency and superior mechanical performance, likely due to stronger intermolecular interactions.[16] In addition, because cellulose can be obtained from inedible resources, the use of cellulose (and its derivatives) can avoid competition with the food supply such as amylose. Although cellulose-based TPEs have potential as next-generation sustainable TPEs, challenges still exist in controlling and improving the material properties, such as microphase-separated structures, mechanical properties, thermal properties, and biodegradability, for practical applications.

An important factor in determining the physical properties of cellulose derivatives is the degree of substitution (DS). For example, good solvents for cellulose acetates depend on the DS. Cellulose triacetate (DS $\approx$ 3) is soluble in dichloromethane and chloroform ($CHCl_3$) but not in acetone and tetrahydrofuran (THF), whereas cellulose diacetate (DS $\approx$ 2) is soluble in acetone and THF.[17] The DS also critically affects the hydrogen bonding profile. Native cellulose (DS = 0) is insoluble in common solvents because of its highly crystalline nature originating from strong inter- and intramolecular hydrogen bonds.[18] Free hydroxy groups provide hydrogen bonding sites and increase polarity, which could positively affect the microphase separation and mechanical strength of cellulose acetate-based TPEs. The DS of cellulose acetate is also known to influence biodegradability. Cellulose triacetate does not biodegrade, but cellulose acetates with lower DSs (~2) biodegrade quickly, even in natural environments.[19–22]

Thus, the material properties of cellulose-based TPEs can be improved and optimized by controlling the DS of the cellulose acetate block. In this study, the author synthesized cellulose acetate-*b*-PDL-*b*-cellulose acetate ($\mathrm{AcCel_x}$-*b*-PDL-*b*-$\mathrm{AcCel_x}$, where x is the DS; x = 3.0, 2.6, and 2.3) triblock copolymers (**Scheme 4.1**). Cellulose acetate blocks with three different DSs were used to investigate the influence of the DS on the microphase separation behavior and mechanical properties. Small-angle X-ray scattering (SAXS) and atomic force microscopy (AFM) revealed that $\mathrm{AcCel_x}$-*b*-PDL-*b*-$\mathrm{AcCel_x}$ tends form more ordered microphase-separated structures as the DS decreases. Notably, $\mathrm{AcCel_{2.6}}$-*b*-PDL-*b*-$\mathrm{AcCel_{2.6}}$ and $\mathrm{AcCel_{2.3}}$-*b*-PDL-*b*-$\mathrm{AcCel_{2.3}}$ exhibited superior mechanical properties to $\mathrm{AcCel_{3.0}}$-*b*-PDL-*b*-$\mathrm{AcCel_{3.0}}$. In addition, the biodegradability of $\mathrm{AcCel_x}$-*b*-PDL-*b*-$\mathrm{AcCel_x}$ in an aqueous environment was enhanced by decreasing the DS of the $\mathrm{AcCel_x}$ segment. The findings of this study reveal that DS is an important factor for governing the properties of cellulose-based BCPs and demonstrate the potential of cellulose-derived TPEs as new sustainable materials.

Scheme 4.1. Synthesis of AcCel$_x$-*b*-PDL-*b*-AcCel$_x$

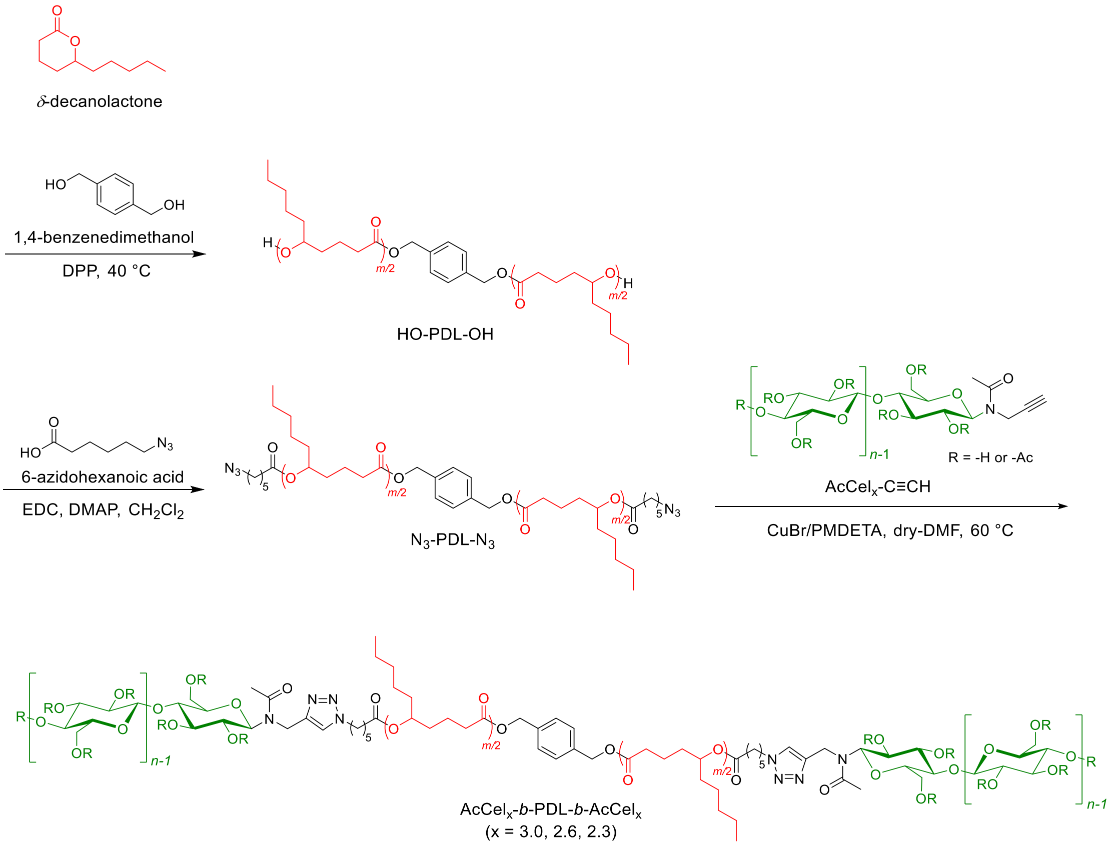

4.2. Experimental Section

4.2.1. Materials

α-D-Glucose 1-phosphate disodium salt hydrate (*α*G1P, ≥97%), 4-(2-hydroxyethyl)-1-piperazineethanesulfonic acid (HEPES, ≥99.5%, titration), copper(I) bromide (CuBr, 99.999%), and 2,5-dihydroxybenzonoic acid (98%) were purchased from Sigma Aldrich and used as received. D(+)-cellobiose, sodium sulfate (Na_2SO_4, >99.0%), anhydrous magnesium sulfate ($MgSO_4$, >95%), propargylamine (>95%), acetic anhydride (>97%), hydrochloric acid (HCl, 35–37%), sulfuric acid (>96.0%), ethyl acetate (AcOEt, >99.3%), acetone (>99.0%), *N*,*N*-dimethylformamide (DMF, >99.0%), *N*,*N*-dimethylethanamide (DMAc, >99.0%), lithium chloride (LiCl, >99.0%), dry DMF (>99.5%; water content, <0.001%), dry toluene (>99.5%; water content, <0.001%), and dry CH_2Cl_2 (>99.5%; water content, <0.001%) were purchased from Kanto Chemical Co., Inc. and used as received. Dichloromethane (CH_2Cl_2, >99.0%), chloroform ($CHCl_3$, >99.0%), and methanol (MeOH, 99.6%) were purchased from Junsei Chemical Co., Ltd., and used as received. *N*,*N*,*N'*,*N''*,*N''*-Pentamethyldiethlenetriamine (PMDETA, >98.0%), diphenyl phosphate (DPP, >98.0%), 1,4-benzenedimethanol (BDM, >99.0%), 1-(3-dimethylaminopropyl)-3-ethylcarbodiimide hydrochloride (EDC·HCl, >98.0%), and 4-dimethylaminopyridine (DMAP, >99.0%) were purchased from Tokyo Chemical Industry Co., Ltd. (TCI) and used as received. *δ*-Decanolactone (*δ*-DL) was purchased from TCI and purified by distillation over CaH_2 under reduced pressure (6 Pa/112 °C). Dowex® 50WX2 hydrogen form was purchased from Sigma Aldrich and was washed with MeOH before use. Sucrose phosphorylase (SP) was purchased from Oriental Yeast Co., Ltd., and kept in a freezer after dissolved in Lysis buffer which composed of 20 mM tris(hydroxymethyl)aminomethane-HCl and 10 mM imidazole. Cellodextrin phosphorylase (CDP)[23], 6-azidohexanoic acid[24], and ethynyl-functionalized cellobiose (CB−C≡CH)[25] were prepared according to previous reported methods.

4.2.2. Instruments

^{1}H NMR measurement.

^{1}H NMR (400 MHz) spectra were obtained using a JEOL JNM-ECS 400 instrument at 25 °C. Note that ^{1}H NMR measurement of ethynyl-functionalized cellooligosaccharide (Cel−C≡CH) was performed at 55 °C.

Size exclusion chromatography (SEC).

SEC measurements were performed at 40 °C in THF (flow rate, 1.0 mL min^{-1}) using a Jasco high-performance liquid chromatography system (PU-980 Intelligent HPLC Pump, CO-2065 Plus Intelligent Column Oven, RI-2031 Plus Intelligent RI Detector, and DG-2080-53 Degasser) equipped with a Shodex KF-G guard column (4.6 mm × 10 mm; particle size, 8 μm) and two Shodex KF-804L columns (linear; particle size 7 μm; 8.0 mm × 300 mm; exclusion limit, 4×10^4). The number-average molecular weight ($M_{\mathrm{n,SEC}}$) and dispersity ($Đ$) were calculated based on polystyrene standards.

Fourie transform infrared spectroscopy (FT-IR).

The FT-IR spectra were obtained using a PerkinElmer Frontier MIR spectrometer equipped with a single reflection diamond universal attenuated total reflection (ATR) accessory.

Differential scanning calorimetry (DSC) measurement.

The DSC experiments were performed using a Hitachi DSC 7000X under nitrogen atmosphere. All polymer samples were heated to 240 °C, cooled to −100 or 30 °C, and heated again to 250 °C at the heating and cooling rate of 10 °C min^{-1}.

Thermogravimetric analysis (TGA).

The TGA analysis was performed using Hitachi STA200RV under nitrogen atmosphere. All polymer samples were heated up to 550 °C at the heating rate of 10 °C min^{-1}.

Matrix-assisted laser desorption ionization time-of-flight mass spectrometry (MALDI-TOF MS).

The MALDI-TOF MS of the obtained products was performed using a Bruker Daltonick GmbsH Co., Inc. in the reflector mode controlled by the Flexcontrol 3.0 software package. For the Cel−C≡CH, the sample was prepared by mixing an ultrapure water dispersion of the compound (1.0 mg mL^{-1}, 200 μL), acetonitrile solution of a matrix (2,5-dihydroxybenzoic acid, 10 mg mL^{-1}, 100 μL), and trifluoroacetic acid (0.2% (v/v), 300 μL). A 1 μL aliquot of this mixture was loaded on a sample plate. For ethynyl-functionalized cellooligosaccharide acetate, the ethynyl-functionalized maltooligosaccharide, and ethynyl-functionalized maltooligosaccharide acetate, the samples were prepared by mixing a THF solution of the compound (5 mg mL^{-1}, 100 μL) and a matrix (2,5-dihydroxybenzoic acid, 10 mg mL^{-1}, 500 μL). A 1 μL aliquot of this mixture was loaded was loaded on a sample plate, which was coated by an acetone solution of NaI (1 μL, 1 mmol L^{-1}) as the cationic agent.

Atomic force microscopy (AFM) observation.

The AFM phase images were obtained using a Molecular Imaging PicoPlus atomic force microscope operating in the tapping mode with a silicon cantilever (Nanoworld AG, NANOSENSORS^{TM} PPP-NCH) having resonant frequency and spring constant of 190 kHz and 48 N m^{-1}, respectively. The thin film samples for the AFM observation were prepared by spin-coating (1,500 rpm for 60 s) the polymer solution in $CHCl_3$ (1 wt%) onto a Si substrate with a native oxide layer.

Scanning electron microscope (SEM).

The samples were mounted on a brass stub put conductive carbon tape and coated gold particle by ion sputtering for 1 min at 15 mA using a Hitachi E-1010. The sample observations were conducted using a JEOL JSM-7001FA scanning electron microscope at an accelerating voltage of 5kV.

Small-angle X-ray scattering (SAXS) and wide-angle X-ray diffraction (WAXD).

The SAXS and WAXD measurements of the obtained polymers were performed at the BL-6A or BL-10C beamline of the Photon Factory in the High Energy Accelerator Research Organization (KEK, Tsukuba, Japan) using X-ray beams with λ = 0.15 nm at room temperature. The scattering data were collected by a 2D detector (PILATUS3 1M or 2M (SAXS) (Dectris Ltd.); PILATUS3 100K or 200K (WAXD) (Dectris Ltd.)), where the samples-to-detector distance was set to be 1.5 m and 0.2 m for SAXS and WAXD measurement, respectively. The scattering angle (θ) was calibrated using silver behenate (Nagara Science Co., Ltd) as the standard and derived the scattering vector (q) from Bragg's equation ($|q| = (4\pi/\lambda)\sin(\theta/2)$). The domain-spacing ($d$) value was calculated by $d = 2\pi/|q^*|$ ($|q^*|$ is principal scattering peak position). The polymer films or powders were sandwiched by two pieces of Kapton tapes with a spacer of a stain less washer, which were applied for the measurement.

Tensile testing.

The tensile tests were performed with an 34SC-1 (INSTRON) tensile tester at the temperature of 20 °C and the humidity of 45%. The film samples for the tensile tests were prepared by casting the polymer solutions from the $CHCl_3$ (15 mL) on a Teflon dish and drying at r.t. for 2 d followed by vacuum drying at r.t. for 2 d. The obtained elastic films were cut into a dog bone shape of 12 × 2 × ca. 0.13 mm (Japanese Industrial Standards (JIS) K6251). For each film, three samples were tested and the average values of the elastic modulus, strain at break, stress at break, and toughness were calculated. The crosshead speed applied during the measurements was 10 mm min^{-1}. The strain at break was taken as the engineering strain where the stress drops suddenly.

Biodegradation test.

Biodegradation test was conducted in freshwater closed recirculating aquaculture system (RAS) rearing the Nile tilapia *Oreochromis niloticus* where samples cut into 1 cm squares were put in polyethylene net (**Figure 4.1**). The temperature of 200-L fish tank was controlled at 26 °C by heater. Dissolved oxygen level was maintained at saturation （~8 mg/L） by aeration. To maintain the water quality for rearing fish healthy, a 45-L down hanging sponge (DHS) reactor with the flow rate of 600 L/h by water pump was equipped for nitrification of ammonia nitrogen. Fish density of RAS in this study was approximately 4 kg fish/kL. The 900 CFU/mL bacteria in the water of RAS was detected using culture medium for determining a total viable cell count, Compact dry (Nissui Pharmaceutical Co., Ltd.). Pictures of samples were taken with a digital camera (Floyd 4K, Wraymer, Japan) installed on a stereo microscope (SZX10, Olympus, Japan) in once a week. After the biodegradation test, the samples were washed pure water and lyophilized for 1 day.

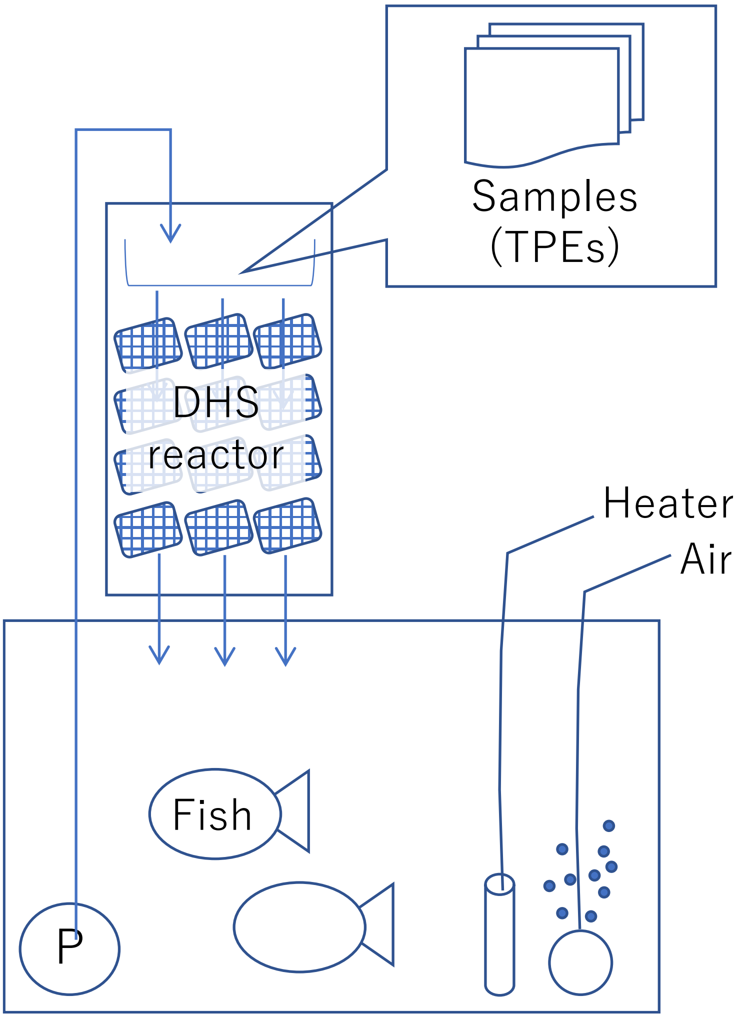

Figure 4.1. Schematic images of the RAS used in this study.

4.2.3. Synthetic details

Synthesis of ethynyl-functionalized cellooligosaccharide (Cel−C≡CH) using CDP and SP

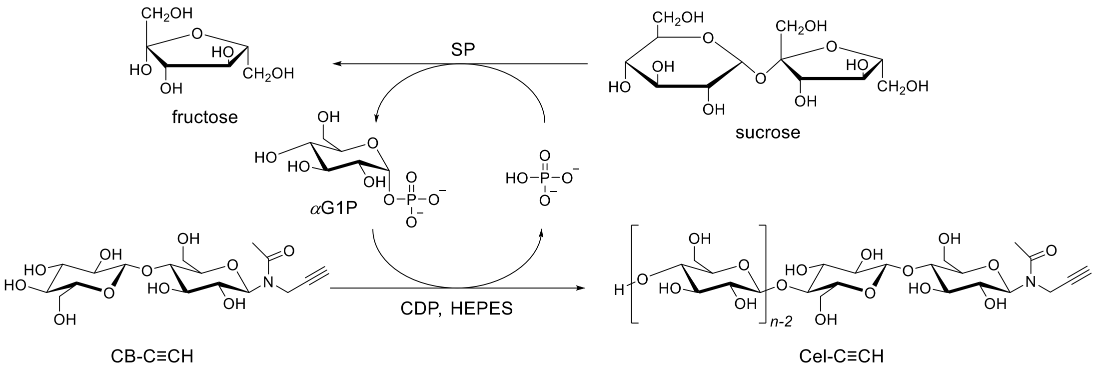

10 mM αG1P, 50 mM CB−C≡CH, and 500 mM sucrose were incubated with 50 μg mL^{-1} CDP and 5 U mL^{-1} SP in 50 mM HEPES buffer solutions (pH 7.5, 104 mL, divided into 11 centrifuge tubes) at 40 °C. After incubating for 7 days, the reaction mixtures were centrifuged to isolate the insoluble product and the resulting pellet was washed with water followed by centrifugation at 14,000 rpm for 20 min at 4 °C several times to give swollen Cel−C≡CH. The aliquot of the obtained product was freeze-dried in vacuo for 2 d to give white powder (6.68 g). Yield: 58.4%.

$M_{\mathrm{n,NMR}}$ = 1,170 g mol^{-1}, $M_{\mathrm{n,MALDI}}$ = 1,210 g mol^{-1}.

^{1}H NMR (400 MHz, 10% (w/w) NaOD-D$_2$O): δ (ppm) 5.59–5.42, 4.55–4.32 (2x m, rotamers, −C*H*N(Ac)−), 4.15 (d, *J* = 8.0 Hz, *H*-1$^{\mathrm{Cel}}$), 4.06–2.67 (m, *H*-2, -3, -4, -5, -6$^{\mathrm{Cel}n}$, O*H*$^{\mathrm{Cel}n}$, −N(Ac)C*H*$_2$−), 2.53–2.45, 2.32–2.17 (m, rotamers, −CC*H*), 1.67–1.55 (m, −N(C=O)C*H*$_3$).

Synthesis of ethynyl-functionalized cellooligosaccharide triacetate ($AcCel_{3.0}$−C≡CH)

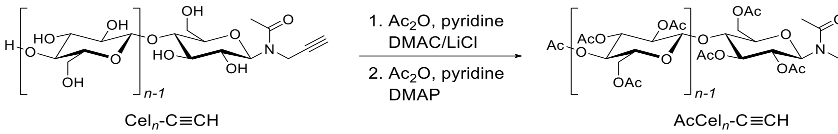

Wet Cel_n−C≡CH (6.28 g, by dry weight) was dispersed in acetone and centrifuged twice (7,000 rpm/30 min/0 °C, 7,000 rpm/15 min/0 °C). The pellet was dispersed in acetone (300 mL) and stirred over night at room temperature. After the centrifugation (7,000 rpm/15 min/0 °C), the pellet was washed with DMAc followed by centrifugation (7,000 rpm/15 min/0 °C). The pellet was dispersed in DMAc (250 mL) and stirred at r.t. After 3 h, LiCl (4.02 g, 94.8 mmol) was added to the mixture and kept stirring over-night. After adding a solution of acetic anhydride in pyridine (1/1 (v/v), 40 mL), the mixture was stirred 5 d. The reaction mixture was diluted with CH_2Cl_2 and washed with 1M HCl (100 mL) three times. The organic layer was dried over $MgSO_4$ and concentrated to give a white solid. The obtained solid and DMAP (139.6 mg, 1.14 mmol) was added to a solution of acetic anhydride in pyridine (1/2 (v/v), 120 mL) and stirred at r.t. for 3 d. After removing the solvent by evaporation, the residue was dissolved in ethyl acetate and washed with 1 M HCl and saturated $NaHCO_3$ solutions. After the organic layer was dried over Na_2SO_4 and concentrated by evaporation, the residue was dissolved with a little of CH_2Cl_2 and poured into the cold-MeOH. The precipitated product was dried under vacuo to give $AcCel_{3.0}$−C≡CH as a white solid (6.68 g). Yield: 55.7%.

$M_{\mathrm{n,NMR}}$ = 2,080 g mol^{-1}, $M_{\mathrm{n,MALDI}}$ = 2,360 g mol^{-1}, $M_{\mathrm{n,SEC}}$ = 2,560 g mol^{-1} (THF), $Đ$ = 1.06 (THF).

^{1}H NMR (400 MHz, DMSO-d_6): δ (ppm) 6.09 (d), 5.88−5.74 (m) (2x, rotamers, −C*H*N(Ac)−), 5.53−3.22 (m, *H*-1, -2, -3, -4, -5, -6$^{\mathrm{AcCel}n}$ of anhydro glucose repeating unit and non-reducing terminal end group, −N(Ac)CH_2−), 2.70−2.63 (m, −CC*H*), 2.34−1.64 (m, CH_3-Ac$^{\mathrm{AcCel}n}$, −N(C=O)CH_3).

Deacetylation of $\mathrm{AcCel_{3.0}}$–C≡CH

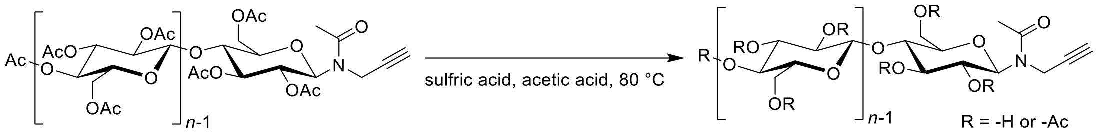

Synthesis of $\mathrm{AcCel_{2.6}}$–C≡CH

Typical deacetylation procedure is as follows (Method A): $\mathrm{AcCel_{3.0}}$–C≡CH (1.49 g, 645 μmol, $M_{\mathrm{n,MALDI}}$ = 2,310, $Đ$ = 1.07) was dissolved in acetic acid (25 mL) in a round-bottom flask. Concentrated sulfuric acid (410 μL) was added slowly to the solution followed by water (2.5 mL), and while the mixture was stirred at 80 °C. After 9.5 min, water was added to the mixture to precipitate the product. The precipitate was filtered and washed several times using water. After drying under reduced pressure, the cellulose acetate with degree of the substitution (DS) of 2.6 was obtained as a white powder (1.33 g). Note that the DS of cellulose acetate was labeled as subscript number, i.e., $\mathrm{AcCel_x}$–C≡CH (x means the DS).

Yield: 95.1%

See **Figure 4.8** for ^{1}H NMR spectrum.

Synthesis of AcCel$_{2.3}$–C≡CH

The method A was used for the deacetylation of AcCel$_{3.0}$–C≡CH (1.50 g, 649 μmol, $M_{\mathrm{n,MALDI}}$ = 2,310, $Đ$ = 1.07) with acetic acid (25 mL), concentrated sulfuric acid (410 μL), and water (2.5 mL) for 20 min to synthesize AcCel$_{2.3}$–C≡CH with the DS of 2.3 (1.01 g).

Yield: 75.1%

See **Figure 4.8** for ^{1}H NMR spectrum.

Synthesis of dihydroxyl-functionalized poly(δ-decanolactone) (HO–PDL–OH)

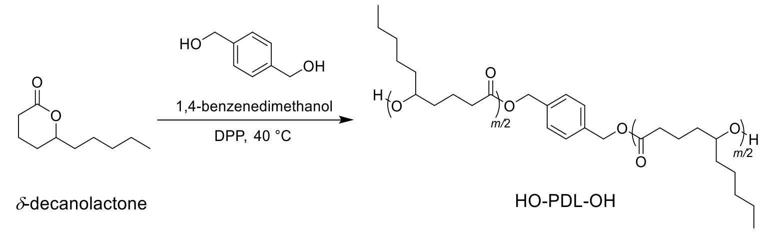

Synthesis of HO–PDL–OH

In an argon-filled glovebox, δ-DL (10.0 g, 58.7 mmol), 1,4-benzenedimethanol (40.6 mg, 0.294 mmol), and DPP (73.5 mg, 0.294 mmol) were placed in a Schlenk flask and it was then taken out from the glovebox. The whole mixture was stirred at 40 °C under an argon atmosphere in an oil bath. After stirring for 70.5 h, the monomer conversion reached 63% as revealed by ^{1}H NMR analysis of the aliquot of the mixture. The polymerization mixture was poured into MeOH, and the precipitated product was washed with MeOH several times to remove the unreacted monomer and catalyst. Finally, HO−PDL−OH was obtained as a colorless viscous liquid (5.49 g). Yield: 54.9%.

$M_{\mathrm{n,NMR}}$ = 17,500 g mol^{-1}, $M_{\mathrm{n,SEC}}$ = 21,900 g mol^{-1} (THF), $Đ$ = 1.05 (THF).

^{1}H-NMR (400 MHz, $CDCl_3$): δ (ppm) 7.34 (s, aromatic), 5.10 (s, $-\mathrm{Ph}-\mathrm{C}H_2\mathrm{O}-$), 4.93−4.81 (m, main chain $-\mathrm{CH_2C}H(\mathrm{C_5H_{11}})\mathrm{O}-$), 3.63−3.54 (br, ω-chain end $-\mathrm{CH_2C}H(\mathrm{C_5H_{11}})\mathrm{OH}$), 2.50−2.17 (m, $-(\mathrm{C{=}O})\mathrm{C}H_2\mathrm{CH_2}-$), 1.97−1.00 (m, $-(\mathrm{C{=}O})\mathrm{CH_2C}H_2\mathrm{C}H_2\mathrm{CH}(\mathrm{C}H_2(\mathrm{C}H_2)_3\mathrm{CH_3})\mathrm{O}-$), 0.99–0.75 (m, $-\mathrm{C}H_3$).

Synthesis of diazido-functionalized poly(δ-decanolactone) (N_3−PDL−N_3)

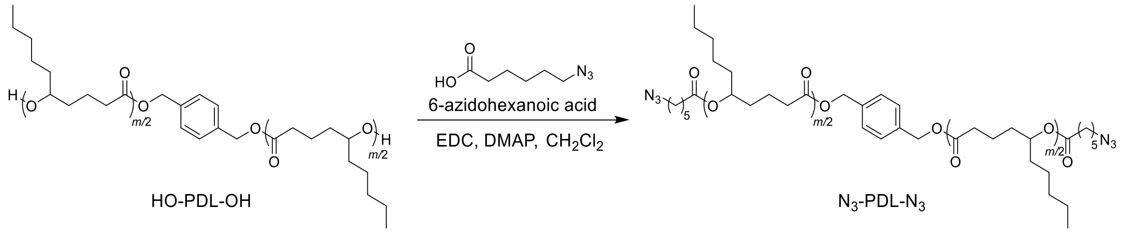

Synthesis of N_3−PDL−N_3

Prior to the reaction, a trace amount of MeOH in the HO−PDL−OH was removed completely by coevaporation with dry toluene. HO−PDL−OH (5.02 g, 0.287 mmol), 6-azidohexanoic acid (244.4 mg, 1.55 mmol), EDC·HCl (284.8 mg, 1.49 mmol), DMAP (187.8 mg, 1.53 mmol), and dry CH_2Cl_2 (20 mL) were mixed in round-bottomed flask. After stirring for 3 d at room temperature, the mixture was purified in the same way as described in Method A to give N_3−PDL−N_3 as a colorless viscous liquid (4.61 g). Yield: 90.3%.

$M_{\mathrm{n,NMR}}$ = 17,800 g mol^{-1}, $M_{\mathrm{n,SEC}}$ = 22,000 g mol^{-1} (THF), $Đ$ = 1.04 (THF).

^{1}H-NMR (400 MHz, $CDCl_3$): δ (ppm) 7.34 (s, aromatic), 5.10 (s, −Ph−CH_2O−), 4.94–4.79 (m, main chain −CH_2CH(C_5H_{11})O−), 3.28 (t, J = 7.2 Hz, −CH_2N_3), 2.39–2.20 (m, −(C=O)C$H_2$$CH_2$−), 1.84–1.00 (m, −(C=O)$CH_2CH_2CH_2$CH(C$H_2$(C$H_2$)$_3$$CH_3$)O−, −C$H_2CH_2CH_2$$CH_2$−$N_3$), 0.98–0.76 (m, −C$H_3$).

Synthesis of ABA-type BCP consisting of cellooligosaccharide acetate and PDL (AcCel$_x$-*b*-PDL-*b*-AcCel$_x$) via click reaction

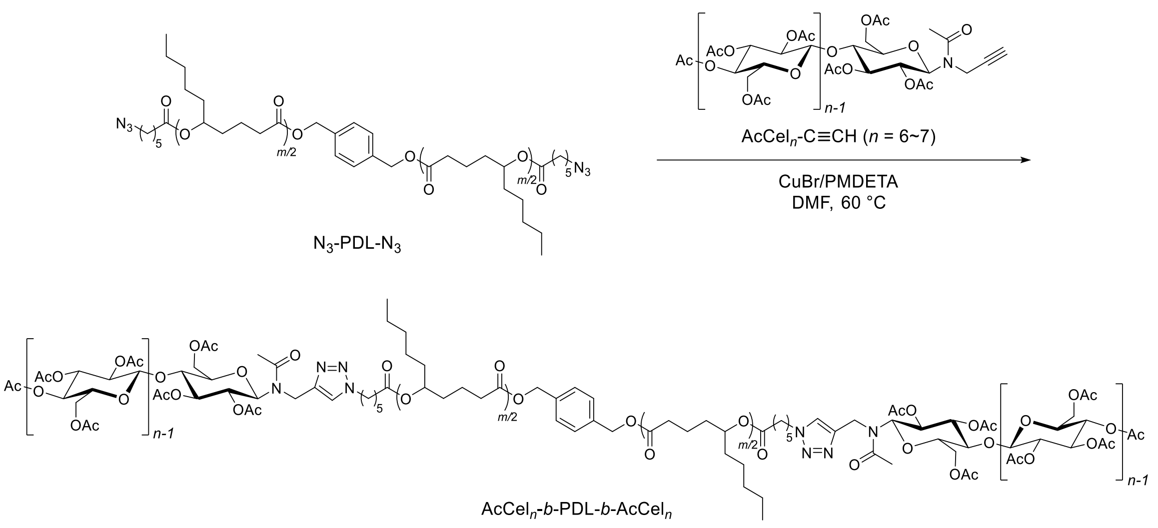

Synthesis of AcCel$_{3.0}$-*b*-PDL-*b*-AcCel$_{3.0}$

A typical click reaction procedure is as follows (Method B): A degassed solution of N_3–PDL–N_3 ($M_{n,NMR}$ = 17,800 g mol^{-1}, 1.43 g, 80.3 μmol) and PMDETA (37.8 μL, 181 μmol) in dry DMF (20 mL) was transferred to a Schlenk tube in which AcCel$_n$–C≡CH (425.1 mg, 184 μmol) and CuBr (27.7 mg, 193 μmol) were placed. The mixture was stirred for 43 h at 60 °C under an argon atmosphere. After cooling to room temperature, Dowex® 50WX2 and a few drops of water were added to remove Cu catalyst. The unreacted AcCel$_{3.0}$–C≡CH was removed by the preparative SEC in $CHCl_3$ to give AcCel$_{3.0}$-*b*-PDL-*b*-AcCel$_{3.0}$ as a pale-yellow elastic material (1.18 g). Yield: 65.6%.

$M_{n,SEC}$ = 27,700 g mol^{-1} (THF), $Đ$ = 1.03 (THF), $M_{n,total}$= 22,400 g mol^{-1}.

See **Figure 4.11** for ^{1}H NMR spectrum.

Synthesis of AcCel$_{2.6}$-*b*-PDL-*b*-AcCel$_{2.6}$

The Method B was used for the click reaction of N_3−PDL−N_3 ($M_{\mathrm{n,NMR}}$ = 17,800 g mol^{-1}, 1.60 g, 89.9 μmol) and AcCel$_n$−C≡CH (444.6 mg, 204 μmol) in dry DMF (20 mL) with CuBr (28.1 mg, 196 μmol) and PMDETA (41.3 μL, 198 μmmol) to synthesize AcCel$_{2.6}$-*b*-PDL-*b*-AcCel$_{2.6}$. After removing Cu catalyst using Dowex® 50WX2, the crude product was purified by reprecipitation to give AcCel$_{2.6}$-*b*-PDL-*b*-AcCel$_{2.6}$ as a white elastic material (1.19 g). Yield: 59.6%.

$M_{\mathrm{n,SEC}}$ = 30,200 g mol^{-1} (THF), $Đ$ = 1.04 (THF), $M_{\mathrm{n,total}}$= 22,200 g mol^{-1}.

See **Figure 4.12** for ^{1}H NMR spectrum.

Synthesis of AcCel$_{2.3}$-*b*-PDL-*b*-AcCel$_{2.3}$

The Method B was used for the click reaction of N_3−PDL−N_3 ($M_{\mathrm{n,NMR}}$ = 17,800 g mol^{-1}, 1.40 g, 78.7 μmol) and AcCel$_n$−C≡CH (372.5 mg, 178 μmol) in dry DMF (20 mL) with CuBr (27.0 mg, 188 μmol) and PMDETA (37.8 μL, 181 μmol). After removing Cu catalyst using Dowex® 50WX2, the crude product was purified by reprecipitation to give AcCel$_{2.3}$-*b*-PDL-*b*-AcCel$_{2.3}$ as a white elastic material (1.19 g). Yield: 68.8%.

$M_{\mathrm{n,SEC}}$ = 26,500 g mol^{-1} (THF), $Đ$ = 1.04 (THF), $M_{\mathrm{n,total}}$= 22,000 g mol^{-1}.

See **Figure 4.13** for ^{1}H NMR spectrum.

4.3. Results and Discussion

4.3.1. Synthesis of cellooligosaccharide

The author first investigated the improved synthesis of propargyl-functionalized cellooligosaccharide (Cel–C≡CH), a precursor of cellooligosaccharide triacetate, through enzymatic polymerization.[16,23,26–31] In Chapter 3, the author prepared Cel–C≡CH mainly consisting of 6–8-mers through the cellodextrin phosphorylase (CDP)-mediated oligomerization of *α*-D-glucose-1-phosphate (*α*G1P) in the presence of *N*-acetyl-propargyl D-(+)-cellobiose as a primer. Cellooligosaccharides with various functional groups at the reducing end and narrow dispersities (*Đ*) were easily obtained using CDP-mediated oligomerization. However, low product yields (~20%) were observed,[16] likely because phosphoric acid was also produced, which promoted the reverse reaction (i.e., phosphorolysis of the cellooligosaccharide). To improve the product yield, the author modified the enzyme polymerization system to avoid the accumulation of phosphoric acid. Sucrose and sucrose phosphorylase were added to the previous system[16] to simultaneously reuse the generated phosphoric acid and produce *α*G1P from sucrose. Consequently, the yield of Cel–C≡CH reached ~60%, which is three times greater than that achieved in Chapter 3 (~20%). The characterization data for the obtained Cel–C≡CH are shown in **Figure 4.2**. The ^{1}H NMR signals were assigned to the expected structure and a number-averaged degree of polymerization (DP) of 6.59 was calculated, which corresponds to a number-averaged molecular weight ($M_{\mathrm{n,NMR}}$) of 1,170 g mol^{-1}. Matrix-assisted laser desorption/ionization time-of-flight mass spectrometry (MALDI-TOF MS) analysis revealed two series of repeating peaks separated by 162 Da in the range of 900–1,500 Da. The major and minor series of peaks are consistent with the Na^{+} and K^{+} adducts, respectively, of Cel–C≡CH comprising 6–8-mers. The number-averaged molecular weight estimated from the MALDI-TOF MS analysis ($M_{\mathrm{n,MALDI}}$) was 1,210 g mol^{-1}, which is similar to the $M_{\mathrm{n,NMR}}$ value (1,170 g mol^{-1}).

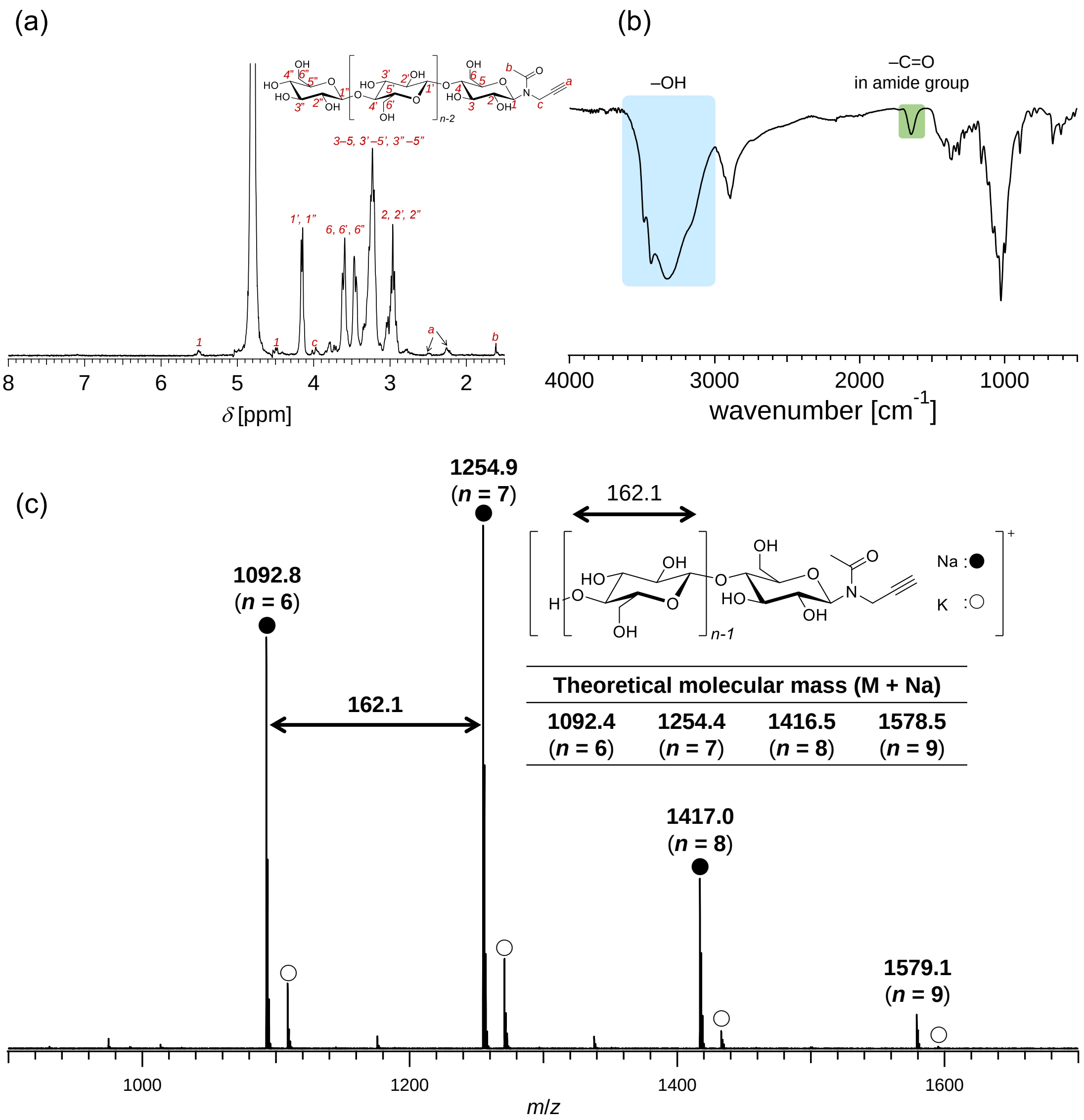

Theoretical molecular mass (M + Na)			
1092.4 (n = 6)	1254.4 (n = 7)	1416.5 (n = 8)	1578.5 (n = 9)

Figure 4.2. (a) ^{1}H NMR spectrum in D_2O containing 10% (w/w) NaOD, (b) FT-IR spectrum, and (b) MALDI-TOF MS spectrum and theoretical molecular mass of Cel–C≡CH.

The fully acetylated propargyl-functionalized cellooligosaccharide (i.e., celloologosaccharide triacetate (AcCel$_{3.0}$–C≡CH)) was prepared according to the established procedure.[16,32] The $M_{\mathrm{n,MALDI}}$ value of the synthesized AcCel$_{3.0}$–C≡CH (2,310 g mol^{-1}; **Figure 4.3**) was slightly larger than that of a AcCel$_{3.0}$–C≡CH synthesized in Chapter 3 ($M_{\mathrm{n,MALDI}}$ = 2,120 g mol^{-1}; **Figure 4.4**). As revealed by MALDI-TOF MS analysis, $AcCel_{3.0}$–C≡CH synthesized in this work exhibited repeating peaks corresponding to 6–11-mers, whereas the $AcCel_{3.0}$–C≡CH synthesized in Chapter 3 exhibited repeating peaks corresponding to 6–9-mers.[16] This result was further supported by size-exclusion chromatography (SEC) measurements, with the M_n determined by SEC ($M_{n,SEC}$) for $AcCel_{3.0}$–C≡CH ($M_{n,SEC}$ = 2,560 g mol^{-1}) synthesized in this study being larger than that of the previous sample ($M_{n,SEC}$ = 2,180 g mol^{-1}) (**Figure 4.5**).

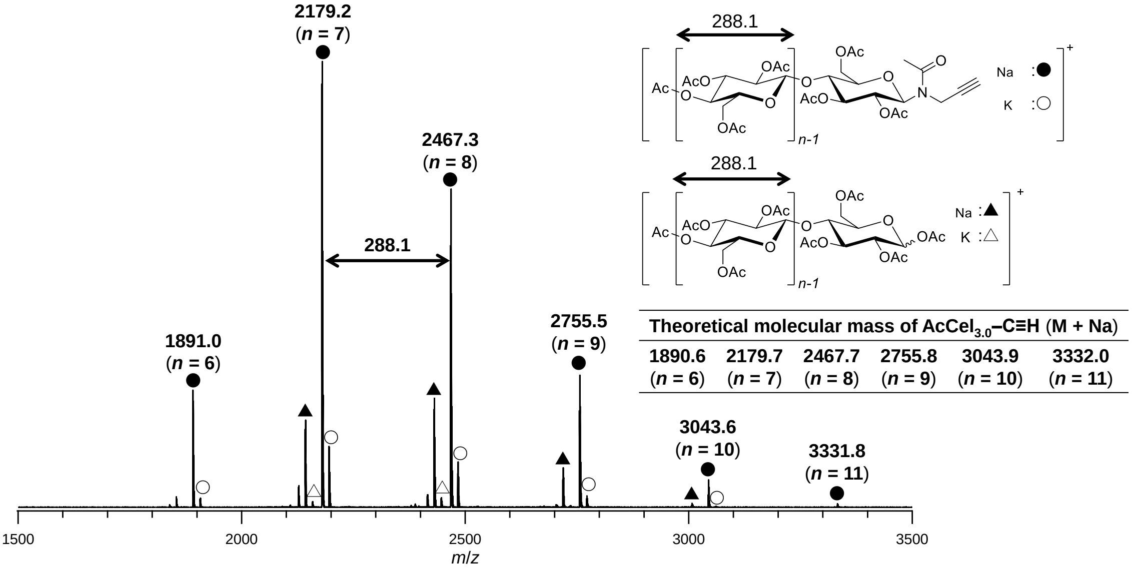

Theoretical molecular mass of $AcCel_{3.0}$–C≡H (M + Na)					
1890.6 (*n* = 6)	2179.7 (*n* = 7)	2467.7 (*n* = 8)	2755.8 (*n* = 9)	3043.9 (*n* = 10)	3332.0 (*n* = 11)

Figure 4.3. MALDI TOF MS spectrum and theoretical molecular mass of $AcCel_{3.0}$–C≡CH synthesized in Chapter 4.

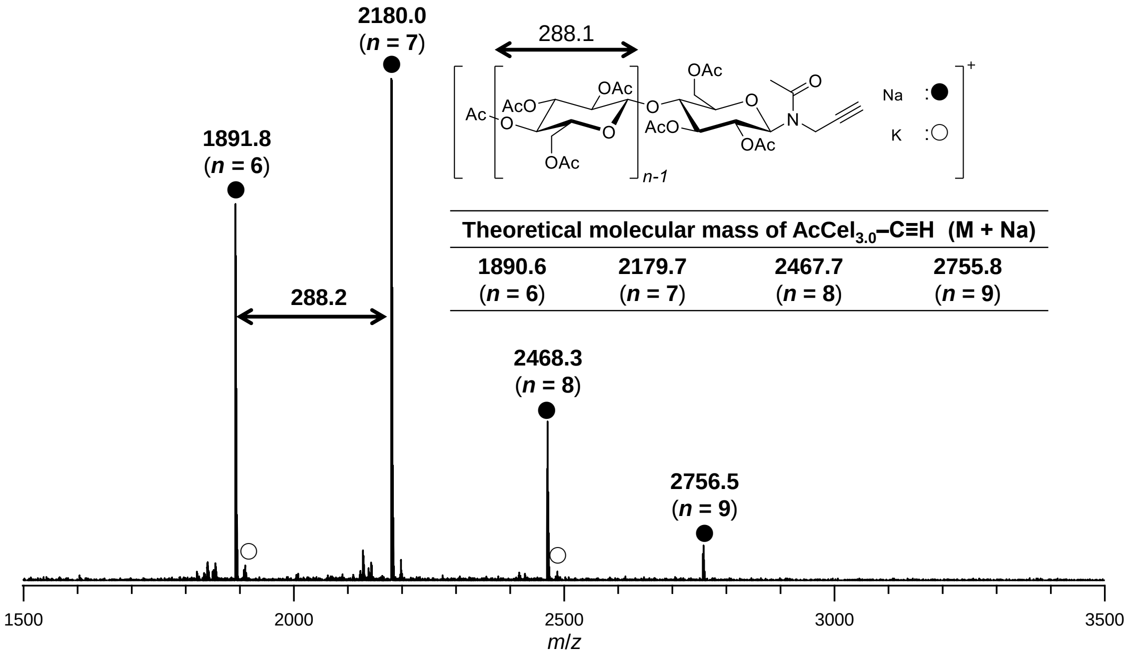

Theoretical molecular mass of $AcCel_{3.0}$–C≡H (M + Na)			
1890.6 (n = 6)	2179.7 (n = 7)	2467.7 (n = 8)	2755.8 (n = 9)

Figure 4.4. MALDI-TOF MS spectrum and theoretical molecular mass of $AcCel_{3.0}$–C≡CH reported in Chapter 3.

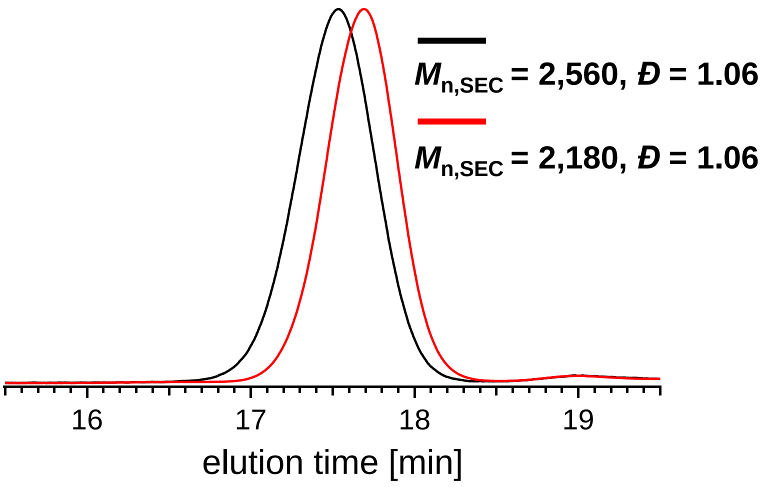

Figure 4.5. SEC traces of $AcCel_{3.0}$–C≡CH synthesized in Chapter 4 (black) and in Chapter 3 (red) (eluent, THF; flow rate, 1.0 mL min^{-1}).

Next, the partial deacetylation of $AcCel_{3.0}$–C≡CH was performed in the presence of sulfuric acid to obtain acetyl cellooligosaccharides with various DSs.[33–35] The author found that the DS could be easily controlled between 3.0 and 2.3 by varying the reaction time. $AcCel_{2.6}$–C≡CH and $AcCel_{2.3}$–C≡CH were obtained by hydrolyzing for 9.5 and 20 min, respectively (**Figures 4.6–4.8**). The DS of the product was determined by comparing the ^{1}H NMR signal intensities for the protons of the acetyl groups and glycosidic ring. Importantly, the propargyl group at the reducing end remained intact during deacetylation, as evidenced by the minor ^{1}H NMR signal of the methylidyne proton at ~2.88 ppm (**Figure 4.8** (a)). In addition, the intensity of the IR absorption band at ~3,500 cm^{-1} corresponding to hydroxy groups increased when the DS decreased (**Figure 4.8** (b)), which is consistent with the generation of more hydroxy groups as deacetylation proceeds. The MALDI-TOF MS spectra of $AcCel_{2.6}$–C≡CH and $AcCel_{2.3}$–C≡CH exhibited a series of repeated peaks that differed by ~42 Da from the signals of $AcCel_{3.0}$–C≡CH (**Figures 4.6** and **4.7**), which corresponds to the difference in molecular mass between the acetoxy group (OAc, 59.01 Da) and the hydroxy group (OH, 17.00 Da). These results indicate that the deacetylation of $AcCel_{3.0}$–C≡CH proceeded, while the ethynyl group was maintained. Thus, the author successfully synthesized three $AcCel_x$–C≡CH samples with different DSs but similar M_n and $Đ$ values (~2,000 g mol^{-1} and 1.07, respectively) (**Figure 4.8** (c)).

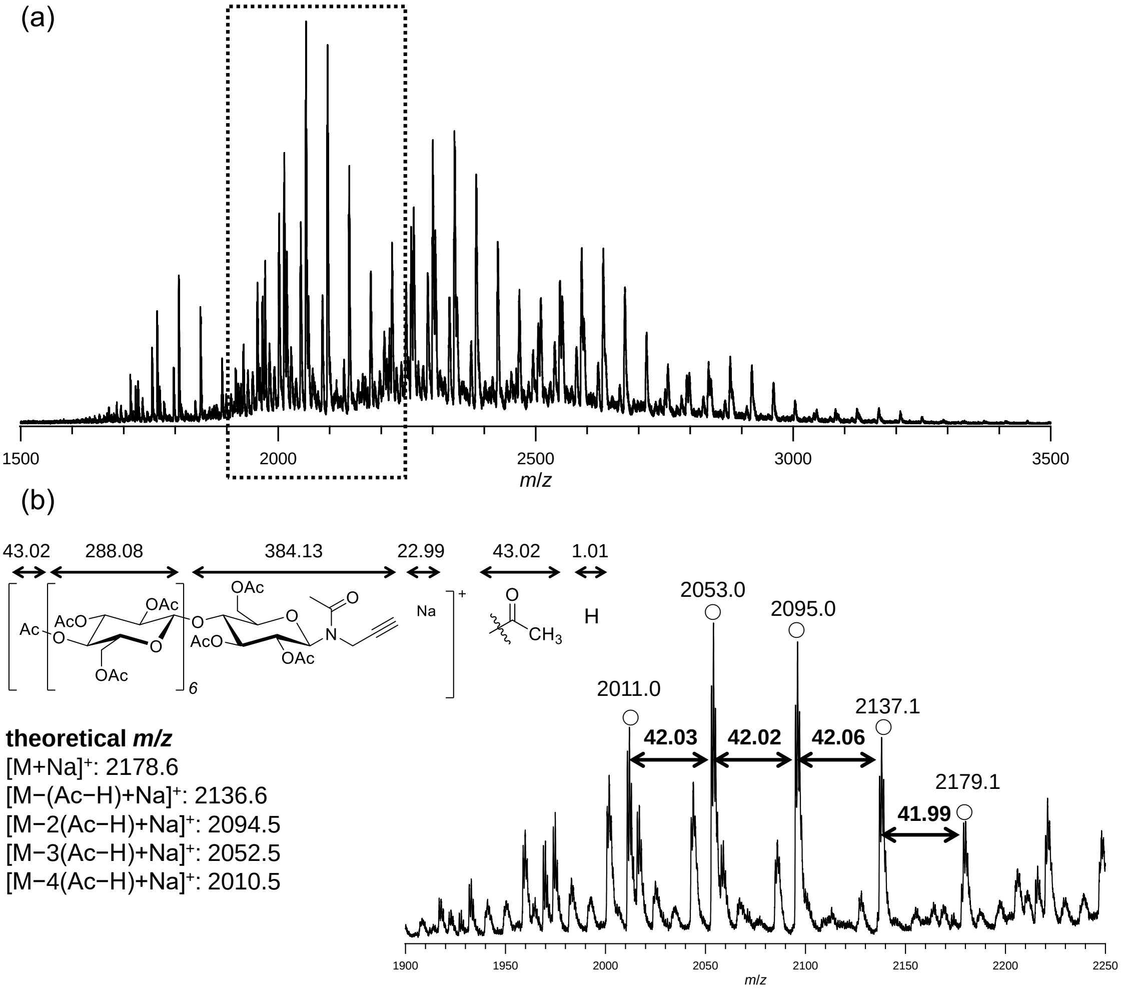

Figure 4.6. (a) MALDI TOF MS spectra and (b) expanded spectra from 1,900 Da to 2,250 Da of AcCel$_{2.6}$–C≡CH.

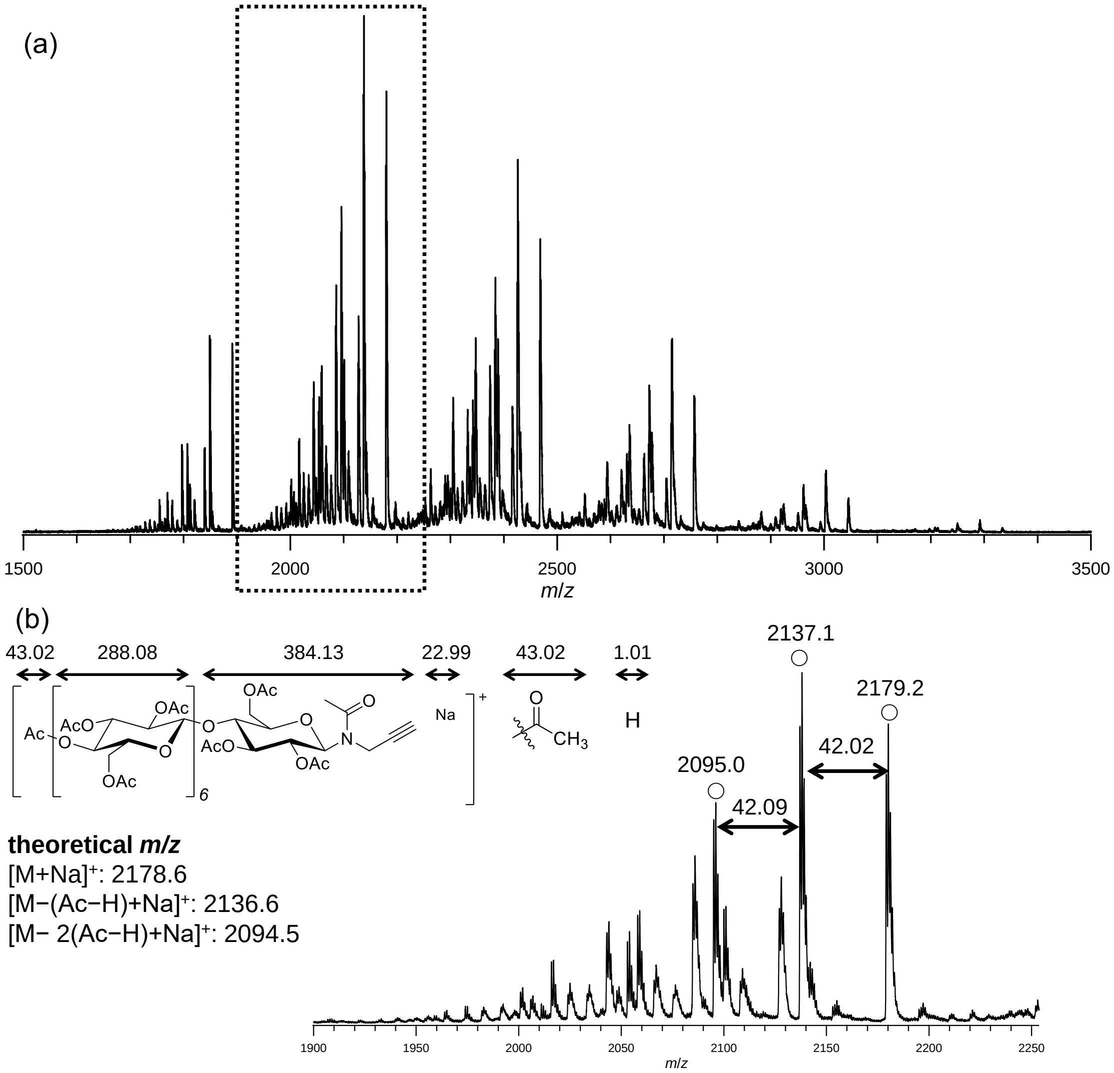

Figure 4.7. MALDI TOF MS spectra and expanded spectra from 1,900 Da to 2,250 Da of $AcCel_{2.3}$−C≡CH.

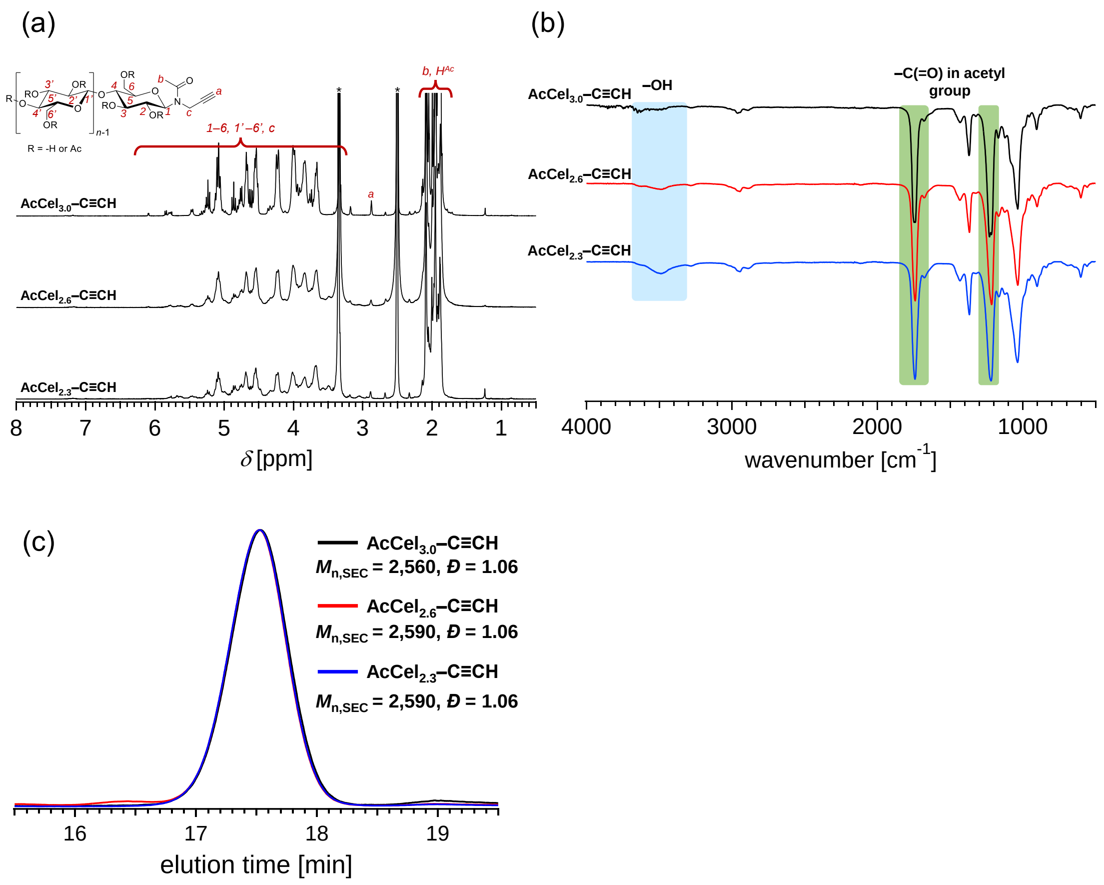

Figure 4.8. (a) ^{1}H NMR spectrum of AcCel$_{3.0}$–C≡CH (upper), AcCel$_{2.6}$–C≡CH (middle), and AcCel$_{2.3}$–C≡CH (lower) in DMSO-d_6 (400 MHz), (b) FT-IR spectrum of AcCel$_{3.0}$–C≡CH (upper), AcCel$_{2.6}$–C≡CH (middle), and AcCel$_{2.3}$–C≡CH, and (c) SEC traces of AcCel$_{3.0}$–C≡CH (black), AcCel$_{2.6}$–C≡CH (red), and AcCel$_{2.3}$–C≡CH (blue) (eluent, THF; flow rate, 1.0 mL min^{-1}).

4.3.2. BCP synthesis

To synthesize the target BCPs (AcCel$_{3.0}$-*b*-PDL-*b*-AcCel$_{3.0}$, AcCel$_{2.6}$-*b*-PDL-*b*-AcCel$_{2.6}$, and AcCel$_{2.3}$-*b*-PDL-*b*-AcCel$_{2.3}$), in which the DS of the acetyl cellooligosaccharide block varies, an *α*,*ω*-diazido-functionalized PDL (N$_3$–PDL–N$_3$; $M_{\mathrm{n,NMR}}$ = 17,800 g mol^{-1}, $Đ$ = 1.05) was synthesized according to the established procedure[15,16,36] (**Figures 4.9** and **4.10**). A copper-catalyzed azido-alkyne click reaction between N_3–PDL–N_3 and the $AcCel_x$–C≡CH samples produced the target BCPs in 60–70% isolated yield. After the click reaction, the reaction mixture was treated with a cation exchange resin and then reprecipitated in MeOH to afford the BCP. However, in the case of $AcCel_{3.0}$-*b*-PDL-*b*-$AcCel_{3.0}$, unreacted $AcCel_{3.0}$–C≡CH could not be removed by reprecipitation because of its poor solubility in MeOH. As the author was unable to find a solvent that selectively dissolved $AcCel_{3.0}$–C≡CH while precipitating BCP, unreacted $AcCel_{3.0}$–C≡CH was removed by preparative SEC, which afforded $AcCel_{3.0}$-*b*-PDL-*b*-$AcCel_{3.0}$ in 65.6% yield. In contrast, unreacted $AcCel_{2.6}$–C≡CH and $AcCel_{2.3}$–C≡CH were easily removed by simple reprecipitation in MeOH, giving $AcCel_{2.6}$-*b*-PDL-*b*-$AcCel_{2.6}$ and $AcCel_{2.3}$-*b*-PDL-*b*-$AcCel_{2.3}$ in 95.1% and 75.1% yield, respectively. This behavior suggests that the reduced DSs of $AcCel_{2.6}$–C≡CH and $AcCel_{2.3}$–C≡CH impart improved solubility in polar solvents such as MeOH.

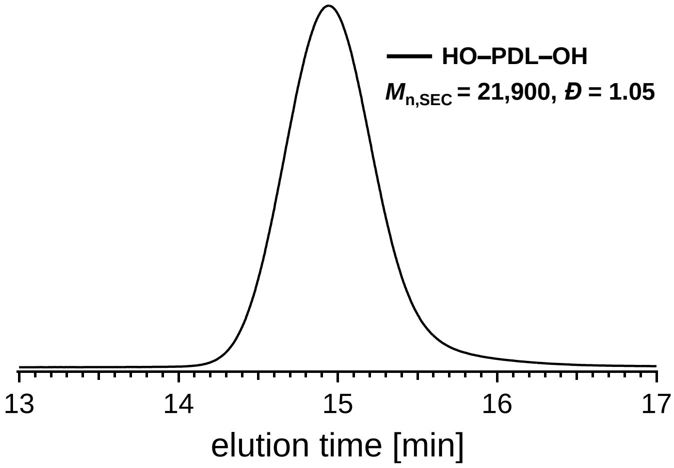

Figure 4.9. SEC trace of HO−PDL−OH (eluent, THF; flow rate, 1.0 mL min^{-1}).

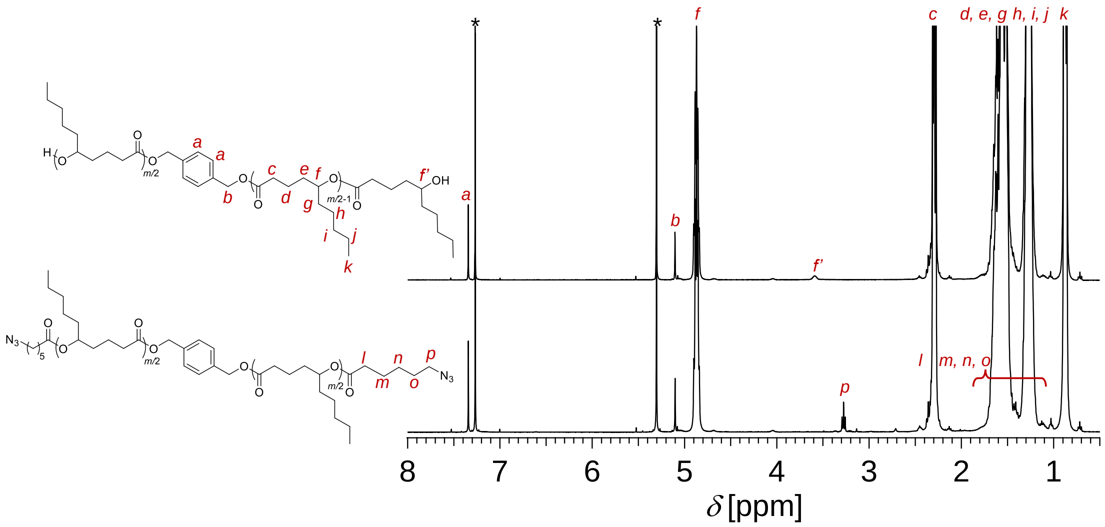

Figure 4.10. ^{1}H NMR spectra of HO–PDL–OH (upper) and N$_3$–PDL–N$_3$ (lower) (400 MHz, CDCl$_3$).

FT-IR spectroscopy confirmed that each click reaction proceeded quantitatively, as the absorption band at ~2,100 cm^{-1} derived from azido groups disappeared completely. The ^{1}H NMR spectra of the products exhibited proton signals corresponding to AcCel$_x$ (5.4–3.0 ppm) and PDL moieties (5.0–4.7, 2.6–0.7 ppm) as well as triazole rings (~7.4 and 7.3 ppm) (**Figures 4.11–4.13**). Moreover, SEC elution peaks appeared at higher molecular weights than for N$_3$–PDL–N$_3$ while maintaining a unimodal shape, and no elution peak corresponding to unreacted AcCel$_x$–C≡CH was observed (**Figure 4.14**). Collectively, these results support the successful synthesis of the target BCPs. The detailed characteristics (molecular weight, *Đ*, volume fraction of PDL segments (f_{PDL})) of AcCel$_{3.0}$-*b*-PDL-*b*-AcCel$_{3.0}$, AcCel$_{2.6}$-*b*-PDL-*b*-AcCel$_{2.6}$, and AcCel$_{2.3}$-*b*-PDL-*b*-AcCel$_{2.3}$ are summarized in **Table 4.1**.

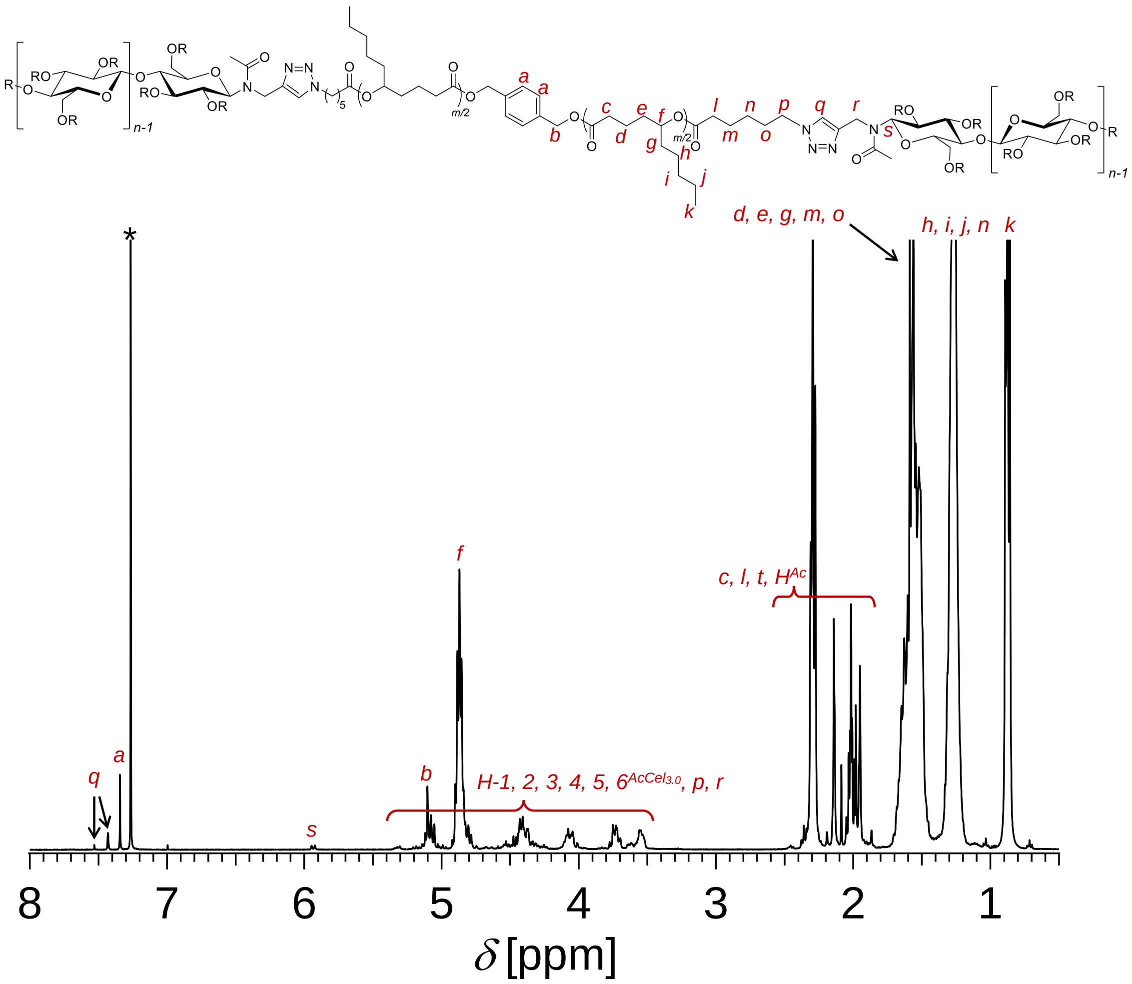

Figure 4.11. ^{1}H NMR spectrum of AcCel$_{3.0}$-*b*-PDL-*b*-AcCel$_{3.0}$ (400 MHz, CDCl$_3$).

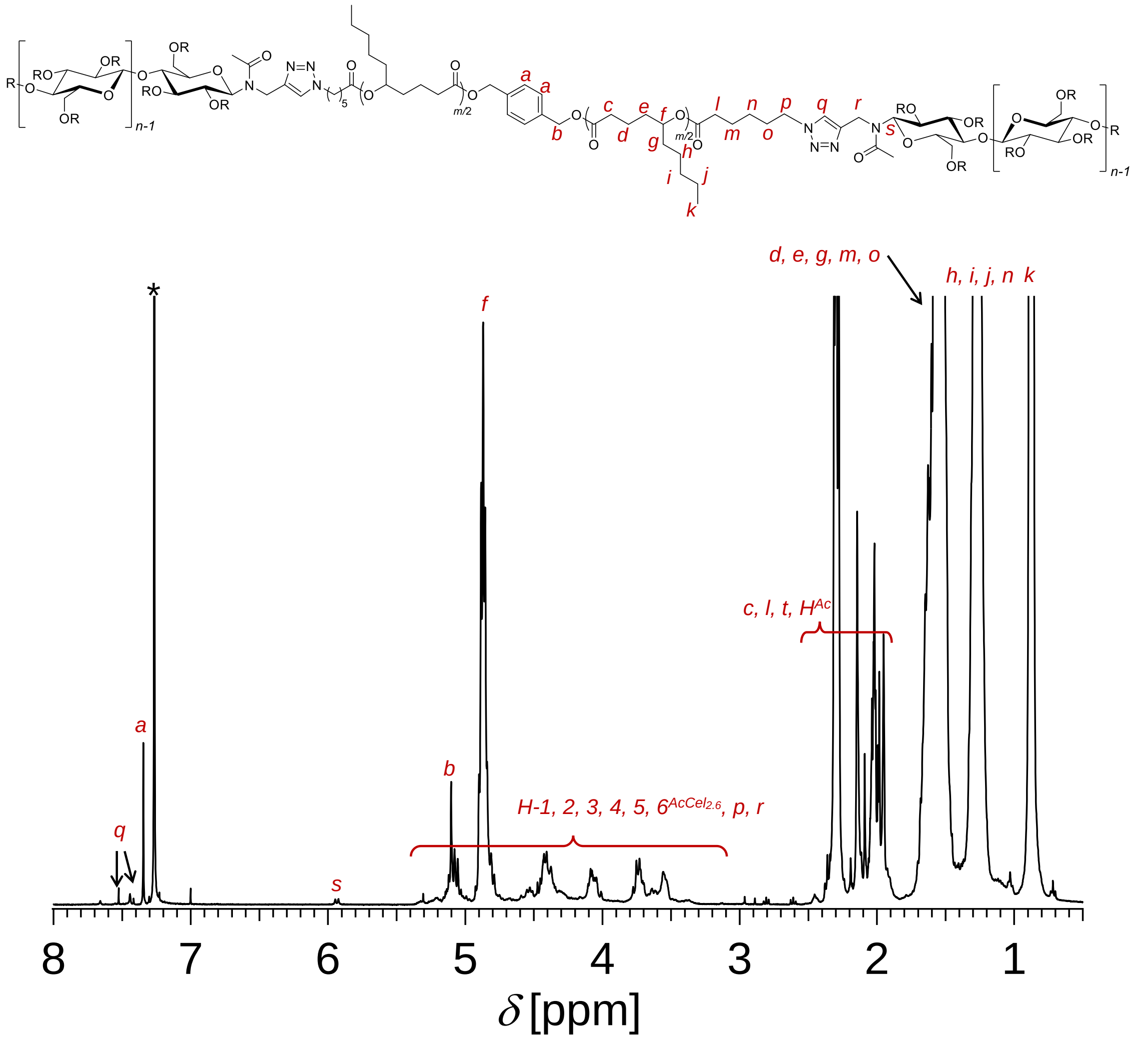

Figure 4.12. ^{1}H NMR spectrum of AcCel$_{2.6}$-*b*-PDL-*b*-AcCel$_{2.6}$ (400 MHz, CDCl$_3$).

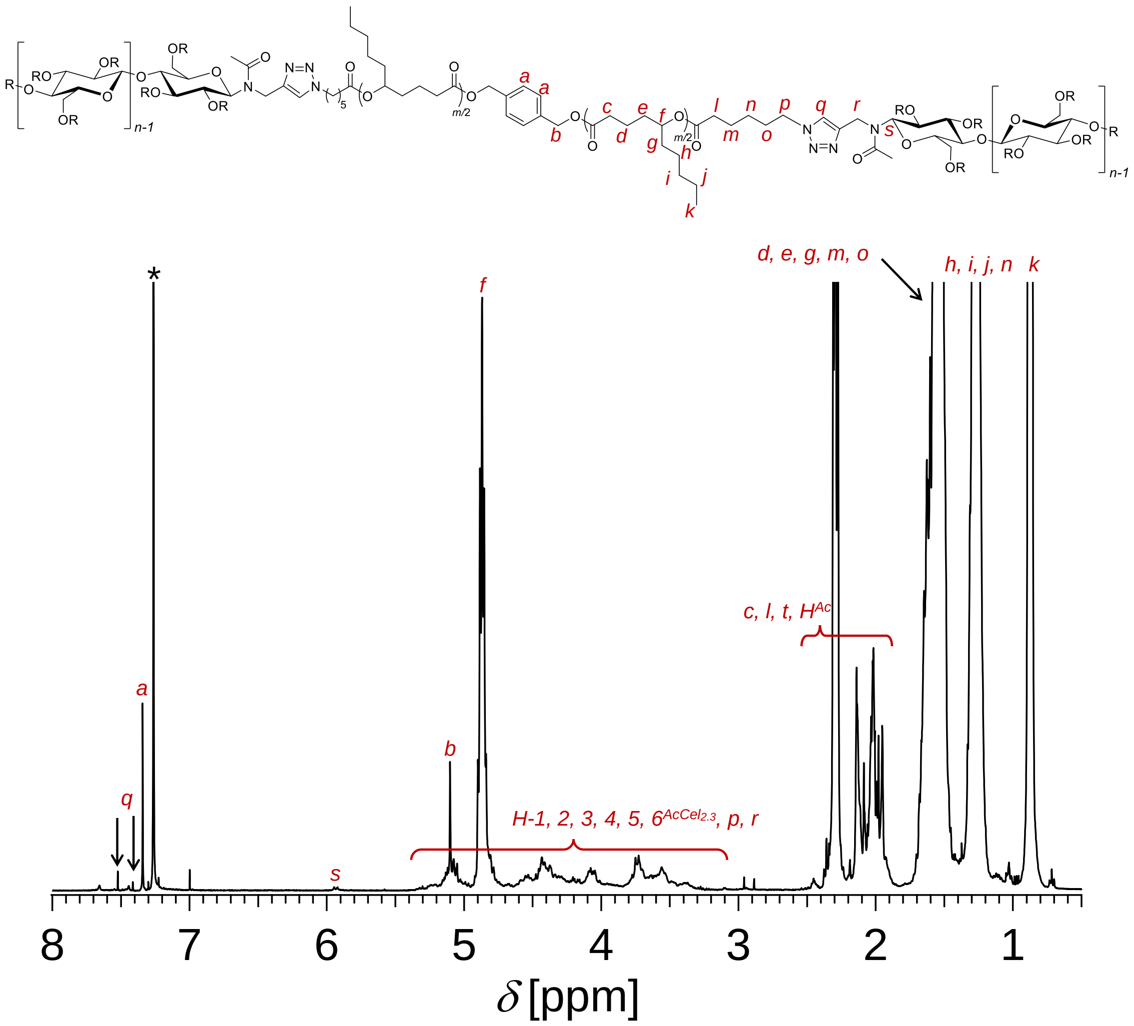

Figure 4.13. ^{1}H NMR spectrum of AcCel$_{2.3}$-*b*-PDL-*b*-AcCel$_{2.3}$ (400 MHz, CDCl$_3$).

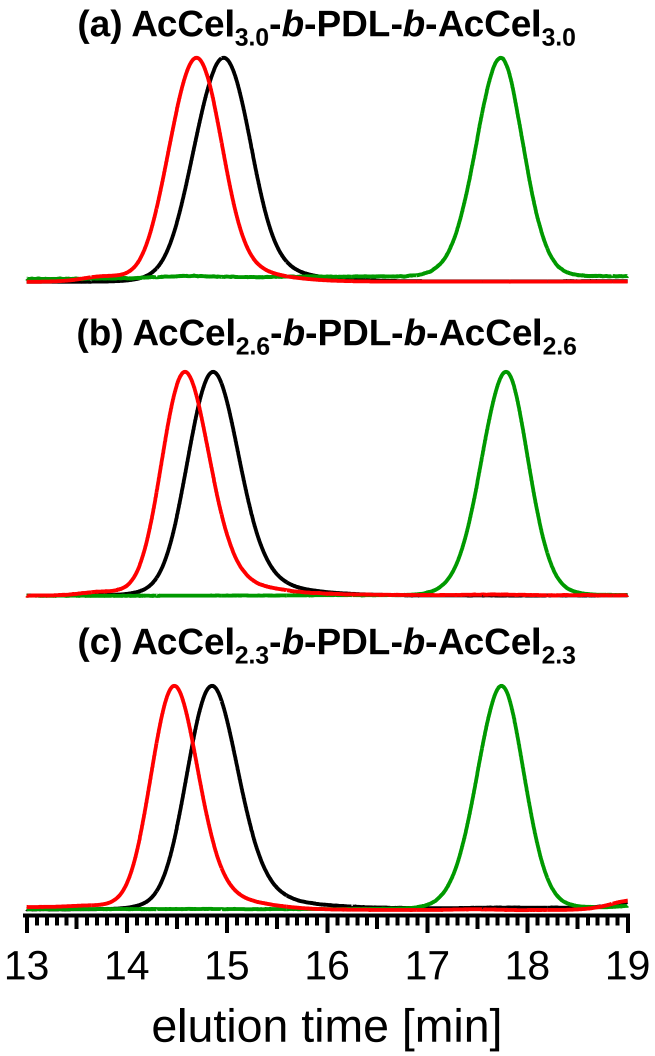

Figure 4.14. SEC traces of (a) $AcCel_{3.0}$-*b*-PDL-*b*-$AcCel_{3.0}$, (b) $AcCel_{2.6}$-*b*-PDL-*b*-$AcCel_{2.6}$, and (c) $AcCel_{2.3}$-*b*-PDL-*b*-$AcCel_{2.3}$ (eluent, THF; flow rate, 1.0 mL min^{-1}). The red, black, and green solid lines represent the BCPs, N_3–PDL–N_3, and the corresponding $AcCel_x$–C≡CH samples, respectively.

Table 4.1. Molecular characteristics of AcCel$_x$-*b*-PDL-*b*-AcCel$_x$

Polymer	M_n	$M_{n,SEC}$[e]	$Đ$[e]	$T_{g,PDL}$[f] [°C]	$T_{g,AcCel}$[f] [°C]	f_{PDL}[h]
AcCel$_{3.0}$–C≡CH	2,310[a]	2,560	1.06	-	110	-
AcCel$_{2.6}$–C≡CH	2,180[b]	2,590	1.06	-	116	-
AcCel$_{2.3}$–C≡CH	2,090[b]	2,590	1.06	-	121	-
N$_3$–PDL–N$_3$	17,800[c]	22,000	1.04	−58	-	-
AcCel$_{3.0}$-*b*-PDL-*b*-AcCel$_{3.0}$	22,400[d]	27,700	1.03	−55	n.d.[g]	0.79
AcCel$_{2.6}$-*b*-PDL-*b*-AcCel$_{2.6}$	22,200[d]	30,200	1.04	−56	n.d.[g]	0.80
AcCel$_{2.3}$-*b*-PDL-*b*-AcCel$_{2.3}$	22,000[d]	26,500	1.04	−57	n.d.[g]	0.81

[a]Determined by MALDI-TOF MS. [b]Calculated as M_n of AcCel$_{3.0}$–C≡CH − (3 − DS) × (M_n of an acetyl group (43.05) − atomic weight of H (1.01)) × DP. [c]Determined by ^{1}H NMR spectroscopy in CDCl$_3$. [d]Caluculated from the M_n values AcCel$_x$–C≡CH and N$_3$–PDL–N$_3$. [e]Determined by SEC in THF using PS standards. [f]Determined using DSC at a heating rate of 10 °C min^{-1}. [g]Not determined. [h]Calculated using the density of each block: 1.29 g cm^{-3} for AcCel$_x$–C≡CH and 0.97 g cm^{-3} for PDL.

4.3.3. Thermal properties

Thermal properties, such as the T_g and degradation temperature, are critical characteristics for elastomer applications. Thus, the author investigated the thermal properties of the AcCel$_x$-*b*-PDL-*b*-AcCel$_x$ samples and their constituent blocks using differential scanning calorimetry (DSC) and thermogravimetric analysis (TGA) under a N_2 atmosphere. DSC analysis of AcCel$_x$–C≡CH with different DSs revealed an increase in T_g ($T_{g,AcCel}$) with decreasing DS (110, 116, and 121 °C for DS = 3.0, 2.6, and 2.3; **Figure 4.15** (a)–(c)). This behavior is attributed to an increase in molecular interactions through hydrogen bonding as DS decreases, which results in decreased chain mobility.[37] The DSC curves of AcCel$_x$-*b*-PDL-*b*-AcCel$_x$ during the second heating process exhibited a baseline shift at approximately −55 °C corresponding to the T_g of the PDL segment ($T_{g,PDL}$; **Figure 4.15** (d)–(g)). The T_g of AcCel$_x$ ($T_{g,AcCel}$) was not clearly observed because of the small volume fraction of this segment in the BCPs ($f_{AcCelx} \approx 0.2$).

TGA analysis revealed a 5% weight-loss temperature ($T_{d5\%}$) of ~300 °C for the synthesized BCPs, AcCel$_x$–C≡CH, and N_3–PDL–N_3, which ensures sufficient thermal stability (**Figures 4.16** and **4.17**). Notably, during heating, the BCP films and AcCel$_x$–C≡CH powders underwent a solid–liquid transformation at 160–200 °C (**Figure 4.17**), indicating that the BCPs are thermoplastic in nature, which is favorable for potential TPE applications.

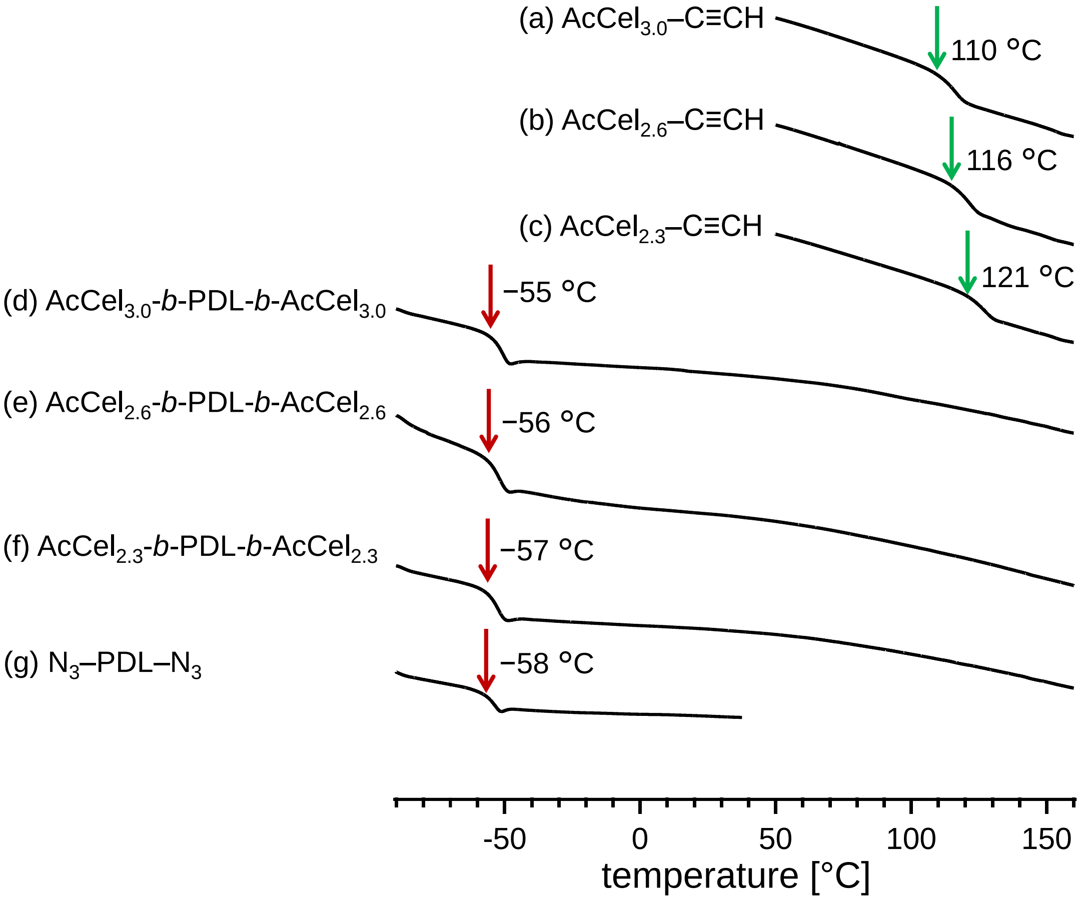

Figure 4.15. DSC curves of (a) $AcCel_{3.0}$–C≡CH, (b) $AcCel_{2.6}$–C≡CH, (c) $AcCel_{2.3}$–C≡CH, (d) $AcCel_{3.0}$-*b*-PDL-*b*-$AcCel_{3.0}$, (e) $AcCel_{2.6}$-*b*-PDL-*b*-$AcCel_{2.6}$, (f) $AcCel_{2.3}$-*b*-PDL-*b*-$AcCel_{2.3}$, and (g) N_3–PDL–N_3 during the second heating process.

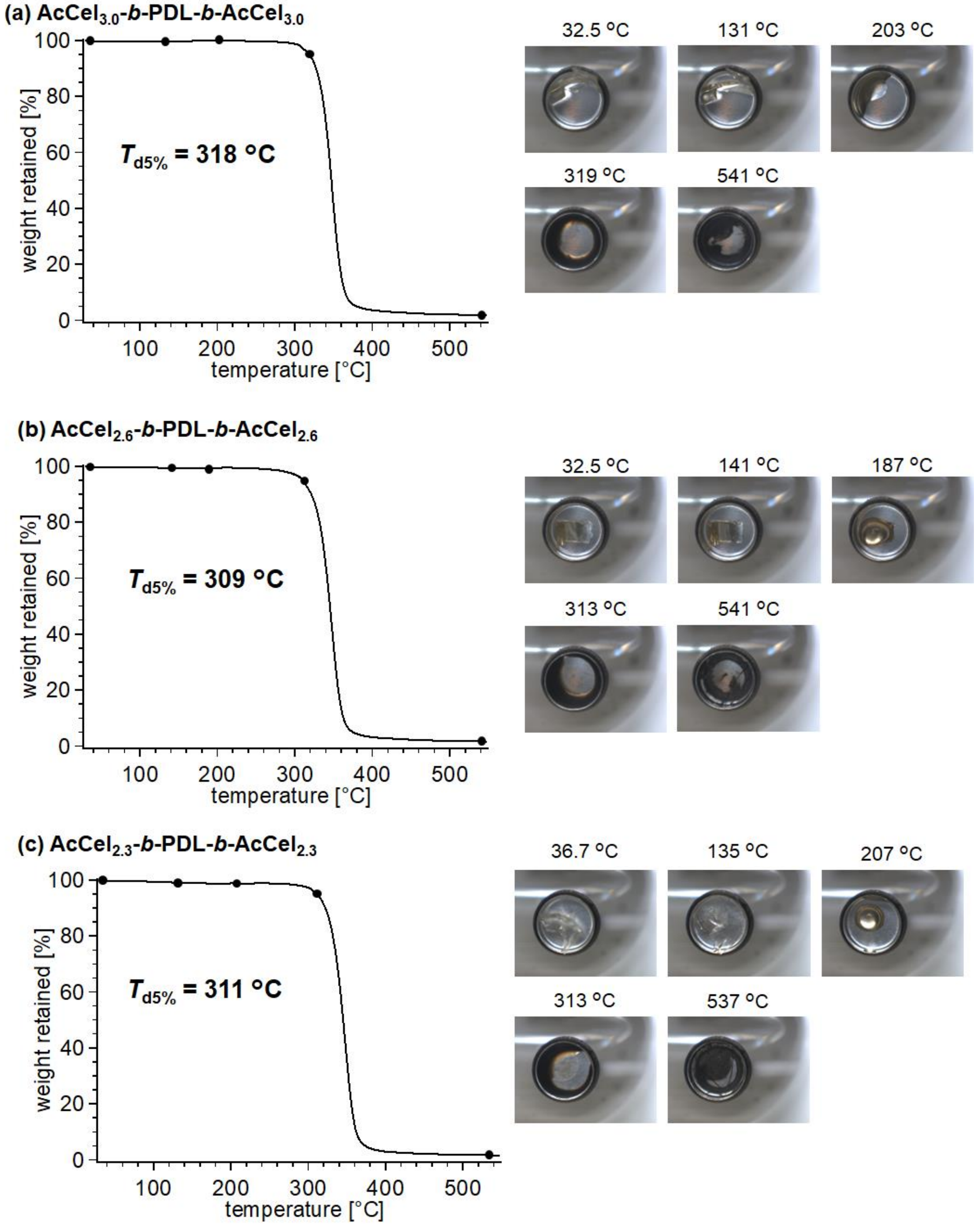

Figure 4.16. TGA curves of (a) $AcCel_{3.0}$-*b*-PDL-*b*-$AcCel_{3.0}$, (b) $AcCel_{2.6}$-*b*-PDL-*b*-$AcCel_{2.6}$, and (c) $AcCel_{2.3}$-*b*-PDL-*b*-$AcCel_{2.3}$ (under nitrogen atmosphere; heating rate, 10 °C min^{-1}). The inset photographs show the sample appearance at the temperature indicated by black circle. $T_{d5\%}$ represents the 5% weight loss temperature.

(a) AcCel$_{3.0}$–C≡CH

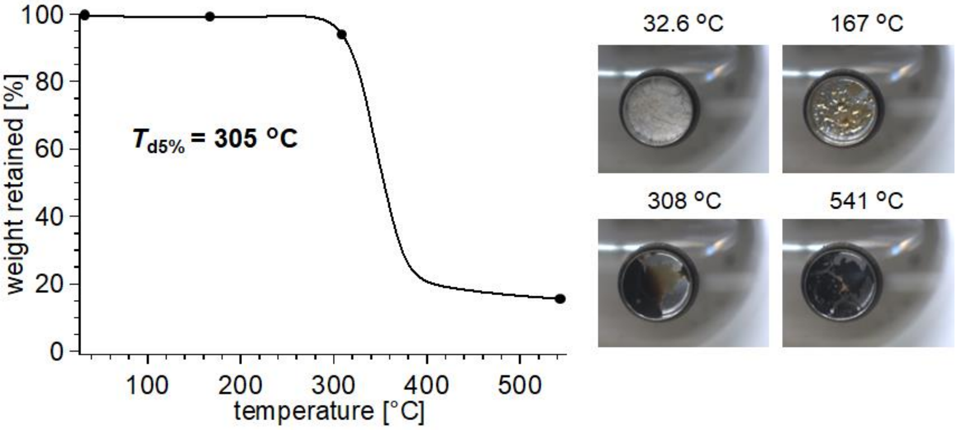

(b) AcCel$_{2.6}$–C≡CH

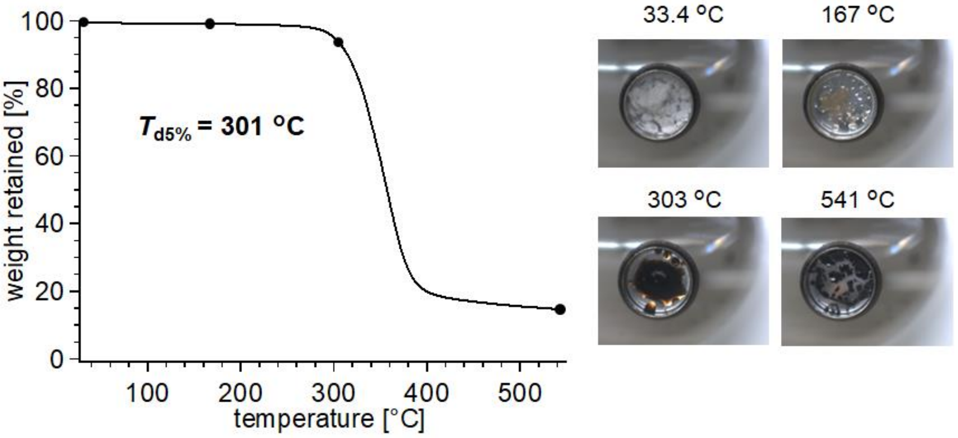

(c) $AcCel_{2.3}$–C≡CH

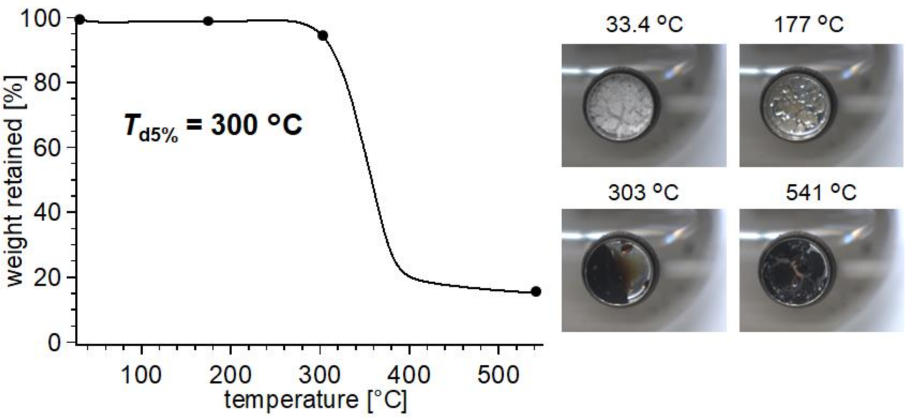

(d) N_3–PDL–N_3

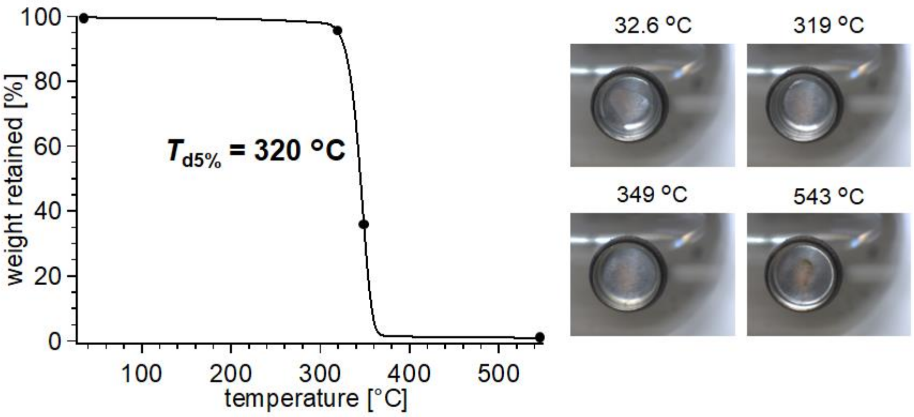

Figure 4.17. TGA curves of (a) $AcCel_{3.0}$–C≡CH, (b) $AcCel_{2.6}$–C≡CH, (c) $AcCel_{2.3}$–C≡CH, and (d) N_3–PDL–N_3 (under nitrogen atmosphere; heating rate, 10 °C min^{-1}). The inset photographs show the sample appearance at the temperature indicated by black circles. $T_{d5\%}$ represents 5% weight loss temperature.

4.3.4. Microphase-separated structures

Microphase-separated structures are known to affect the mechanical properties of TPEs. Therefore, SAXS measurements were performed to clarify the nanostructures of $AcCel_x$-*b*-PDL-*b*-$AcCel_x$ in the bulk state. Film samples were prepared by solvent casting from a $CHCl_3$ solution, drying at atmospheric pressure for 2 days, and then vacuum drying at room temperature for 2 days. Subsequently, the films were thermally annealed at 150 or 180 °C for 6 h under vacuum. The SAXS profiles of the AcCel_x-*b*-PDL-*b*-AcCel_x films without thermal annealing exhibited only a primary scattering peak, implying ill-defined nanostructures (**Figure 4.18**).

$\text{AcCel}_{3.0}$-*b*-PDL-*b*-$\text{AcCel}_{3.0}$ did not form ordered microphase-separated structures, even after thermal annealing, as indicated by the sole primary scattering peak in the SAXS profile. In contrast, the wide-angle X-ray diffraction (WAXD) profile of annealed $\text{AcCel}_{3.0}$-*b*-PDL-*b*-$\text{AcCel}_{3.0}$ showed sharp scattering peaks assignable to cellulose triacetate I crystals (**Figure 4.19** (a)). Initially, the author expected that $\text{AcCel}_{3.0}$-*b*-PDL-*b*-$\text{AcCel}_{3.0}$ would have an ordered body-centered cubic (BCC) spherical morphology, as observed for a BCP with a comparable composition and molecular weight in Chapter 3.[16] However, the M_n of the $\text{AcCel}_{3.0}$ segment in the present $\text{AcCel}_{3.0}$-*b*-PDL-*b*-$\text{AcCel}_{3.0}$ was slightly higher than that in the previous BCP, which greatly affected the crystallization ability, as evidenced by the WAXD analysis of $\text{AcCel}_{3.0}\text{–C≡CH}$ (**Figure 4.19** (d)). The nanostructures of semicrystalline BCPs are known to be influenced by the interplay between the driving forces for crystallization and microphase separation. The strong tendency of $\text{AcCel}_{3.0}\text{–C≡CH}$ to crystallize owing to its higher M_n could interfere with microphase separation, resulting in the ill-defined nanostructures observed for $\text{AcCel}_{3.0}$-*b*-PDL-*b*-$\text{AcCel}_{3.0}$. Considering the large effect of M_n on the crystallization ability of $\text{AcCel}_{3.0}$, this unique phenomenon requires further investigation in the future.

The SAXS profiles of the annealed AcCel$_{2.6}$-*b*-PDL-*b*-AcCel$_{2.6}$ and AcCel$_{2.3}$-*b*-PDL-*b*-AcCel$_{2.3}$ films exhibited multiple scattering peaks assignable to BCC spherical structures, whereas the WAXD profiles showed only amorphous halos. The intersphere distances ($d_{\text{S-S,SAXS}}$) of AcCel$_{2.6}$-*b*-PDL-*b*-AcCel$_{2.6}$ and AcCel$_{2.3}$-*b*-PDL-*b*-AcCel$_{2.3}$ were calculated to be 14.8 and 15.1 nm, respectively ($d_{\text{S-S,SAXS}} = (2\pi/q^*)(3/2^{1/2})$, where the q^* is the primary scattering peak position). Interestingly, AcCel$_{2.6}$-*b*-PDL-*b*-AcCel$_{2.6}$ and AcCel$_{2.3}$-*b*-PDL-*b*-AcCel$_{2.3}$ exhibited different d values despite their comparable molecular weights and volume fractions. The d value of a microphase-separated structure is known to reflect the Flory–Huggins interaction parameter (χ), as follows:[38]

$d = a\chi^{1/6}N^{2/3}$ (1)

where a is a constant related to the statistical chain length. Eq. (1) demonstrates that d increases with χ. Assuming that AcCel$_{2.6}$-*b*-PDL-*b*-AcCel$_{2.6}$ and AcCel$_{2.3}$-*b*-PDL-*b*-AcCel$_{2.3}$ have the same a and N values, a $\chi_{\text{AcCel2.3}}/\chi_{\text{AcCel2.6}}$ value of 1.13 can be determined based on eq. (1) and the $d_{\text{S-S,SAXS}}$ values of AcCel$_{2.3}$-*b*-PDL-*b*-AcCel$_{2.3}$ (15.1 nm) and AcCel$_{2.6}$-*b*-PDL-*b*-AcCel$_{2.6}$ (14.8 nm). This result indicates that reducing the DS of the AcCel$_x$ segments increases the χ value, leading to ordered microphase-separated structures.

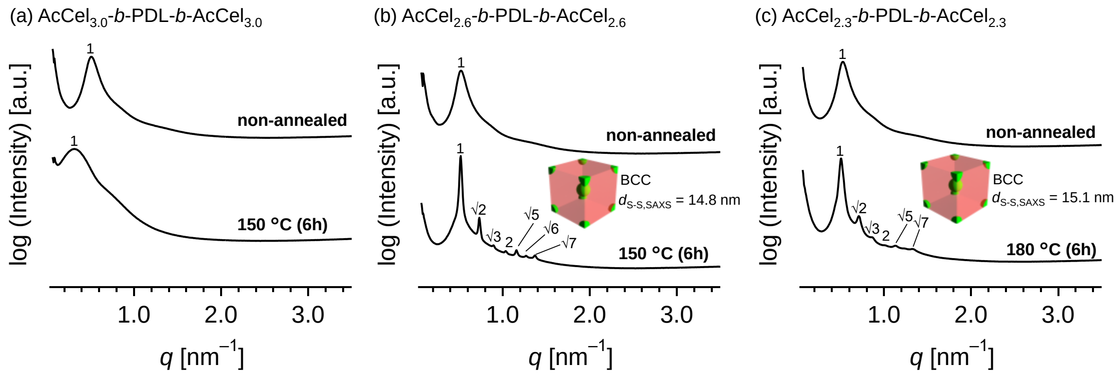

Figure 4.18. SAXS profiles of (a) AcCel$_{3.0}$-*b*-PDL-*b*-AcCel$_{3.0}$, (b) AcCel$_{2.6}$-*b*-PDL-*b*-AcCel$_{2.6}$, and (c) AcCel$_{2.3}$-*b*-PDL-*b*-AcCel$_{2.3}$ without thermal annealing (upper) and after thermal annealing at 150 or 180 °C for 6 h (lower).

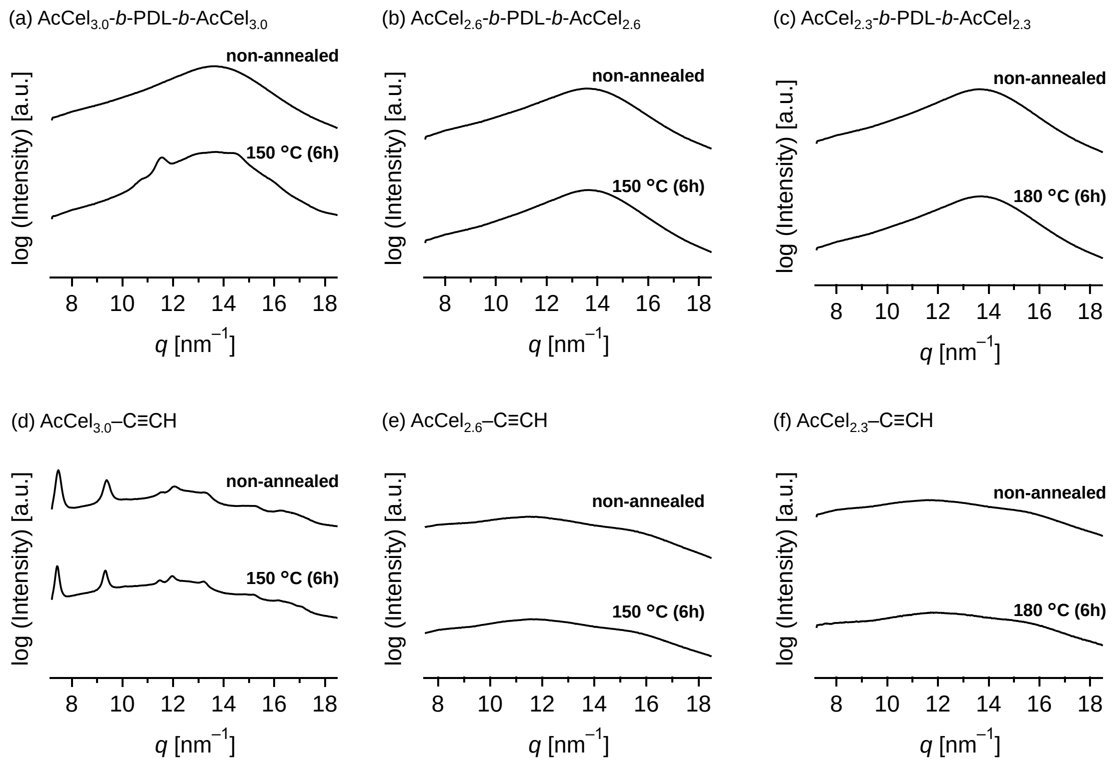

Figure 4.19. WAXD profiles of (a) AcCel$_{3.0}$-*b*-PDL-*b*-AcCel$_{3.0}$, (b) AcCel$_{2.6}$-*b*-PDL-*b*-AcCel$_{2.6}$, (c) AcCel$_{2.3}$-*b*-PDL-*b*-AcCel$_{2.3}$, (d) AcCel$_{3.0}$–C≡CH, (e) AcCel$_{2.6}$–C≡CH, and (f) AcCel$_{2.3}$–C≡CH without thermal annealing (upper) and after thermal annealing at 150 °C or 180 °C for 6 h (lower).

AFM was used to visualize the microphase-separated structures in the AcCel$_x$-*b*-PDL-*b*-AcCel$_x$ thin films (**Figure 4.20**). Thin films samples were prepared by spin-coating a $CHCl_3$ solution (1 wt%) of AcCel$_x$-*b*-PDL-*b*-AcCel$_x$ on bare Si substrates. The AFM phase images of AcCel$_x$-*b*-PDL-*b*-AcCel$_x$ before thermal annealing exhibited ill-ordered dotted patterns, consistent with the observation of a single primary scattering peak in the SAXS profiles of the non-annealed BCPs. Interestingly, the AFM image of the AcCel$_{3.0}$-*b*-PDL-*b*-AcCel$_{3.0}$ thin film showed fiber-like structures after thermal annealing, which could be related to the high crystallinity of the AcCel$_{3.0}$ segment. Few such fiber-like structures were observed in the synthesized AcCel$_{3.0}$-*b*-PDL-*b*-AcCel$_{3.0}$ with a comparable composition in Chapter 3.[16] This result indicates that the driving force for crystallization was stronger than that for microphase separation in the present AcCel$_{3.0}$–C≡CH sample with a higher M_n, resulting in the formation of an ill-ordered fiber-like pattern rather than an ordered microphase-separated structure. In contrast, the AFM phase images of the thermally annealed AcCel$_{2.6}$-*b*-PDL-*b*-AcCel$_{2.6}$ and AcCel$_{2.3}$-*b*-PDL-*b*-AcCel$_{2.3}$ thin films exhibited highly ordered dotted patterns, reflecting a BCC structure. The intersphere distances calculated from the fast Fourier transform (FFT) images ($d_{S\text{-}S,AFM}$) of the AcCel$_{2.6}$-*b*-PDL-*b*-AcCel$_{2.6}$ and AcCel$_{2.3}$-*b*-PDL-*b*-AcCel$_{2.3}$ films were 13.0 and 13.1 nm, respectively, which are similar to the $d_{S\text{-}S,SAXS}$ values.

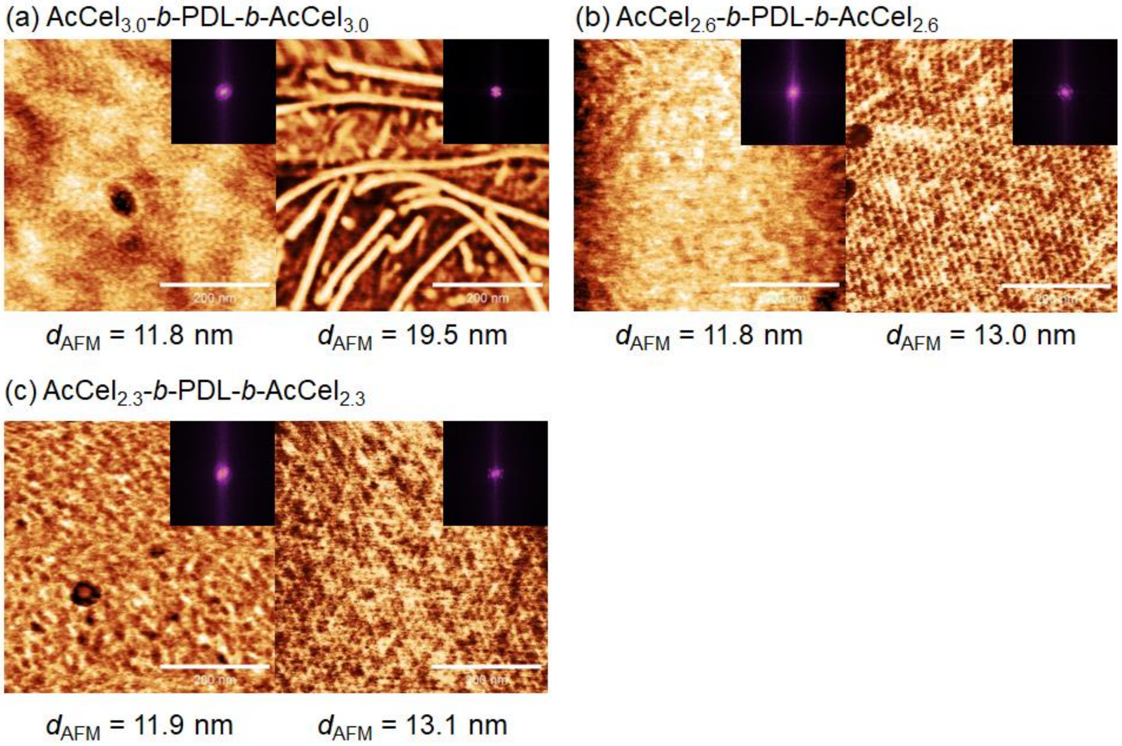

Figure 4.20. AFM phase images of (a) AcCel$_{3.0}$-*b*-PDL-*b*-AcCel$_{3.0}$, (b) AcCel$_{2.6}$-*b*-PDL-*b*-AcCel$_{2.6}$, and (c) AcCel$_{2.3}$-*b*-PDL-*b*-AcCel$_{2.3}$ thin films before (left) and after (right) thermal annealing at 150 °C (AcCel$_{3.0}$-*b*-PDL-*b*-AcCel$_{3.0}$ and AcCel$_{2.6}$-*b*-PDL-*b*-AcCel$_{2.6}$) or 180 °C (AcCel$_{2.3}$-*b*-PDL-*b*-AcCel$_{2.3}$) for 6 h. The insets show the corresponding FFT profiles. Scale bars are 200 nm.

In situ SAXS measurements were performed during heating to elucidate the order–disorder temperature (T_{ODT}) (**Figure 4.21**). The SAXS profiles were acquired at 10 °C steps upon heating from 30 to 280 °C. The primary scattering peak of each sample became sharper as the temperature increased to ~170 °C and then broadened at higher temperatures. Importantly, multiple scattering peaks attributed to BCC structures were observed at temperatures of 170–190 and 170–210 °C in the SAXS profiles of AcCel$_{2.6}$-*b*-PDL-*b*-AcCel$_{2.6}$ and AcCel$_{2.3}$-*b*-PDL-*b*-AcCel$_{2.3}$, respectively. This behavior suggested that the mobility of the polymer chains increased up to a certain temperature, which induced microphase separation. Notably, the SAXS profile of AcCel$_{3.0}$-*b*-PDL-*b*-AcCel$_{3.0}$ also exhibited multiple scattering peaks attributed to BCC structures at 150–160 °C. Thus, AcCel$_{3.0}$-*b*-PDL-*b*-AcCel$_{3.0}$ has sufficient potential for microphase separation in this temperature range, where the AcCel$_{3.0}$ segment does not crystallize; nevertheless, the driving force for crystallization overwhelms that for microphase separation as the temperature decreases, resulting in the formation an ill-ordered fiber structure. Consequently, an ordered microphase-separated structure was not observed in the SAXS profile of AcCel$_{3.0}$-*b*-PDL-*b*-AcCel$_{3.0}$ at room temperature.

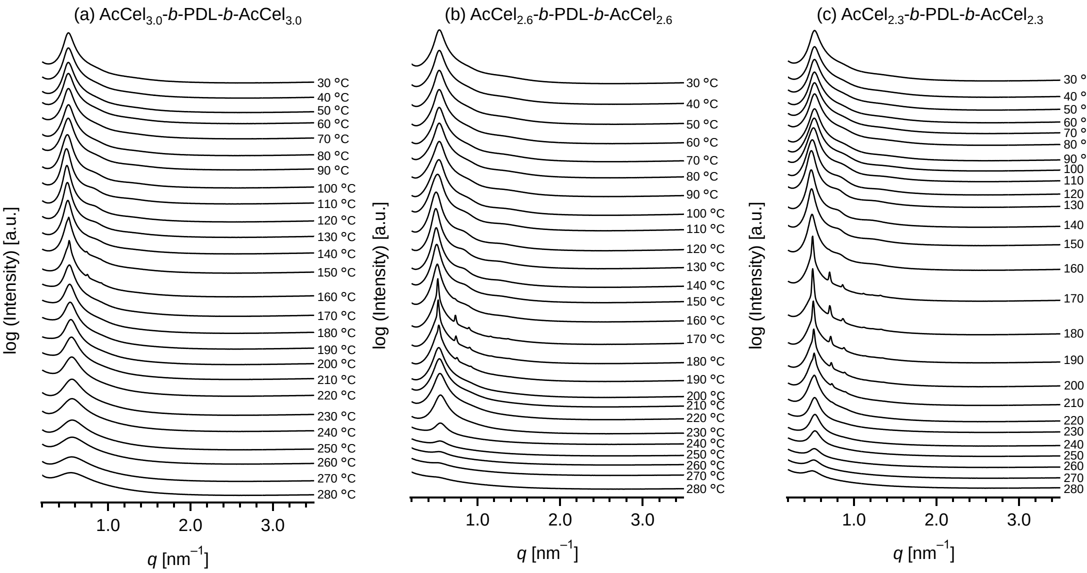

(a) AcCel$_{3.0}$-*b*-PDL-*b*-AcCel$_{3.0}$

(b) AcCel$_{2.6}$-*b*-PDL-*b*-AcCel$_{2.6}$

(c) AcCel$_{2.3}$-*b*-PDL-*b*-AcCel$_{2.3}$

Figure 4.21. SAXS profiles of (a) AcCel$_{3.0}$-*b*-PDL-*b*-AcCel$_{3.0}$, (b) AcCel$_{2.6}$-*b*-PDL-*b*-AcCel$_{2.6}$, and (c) AcCel$_{2.3}$-*b*-PDL-*b*-AcCel$_{2.3}$ acquired during the step-by-step heating from 30 °C to 280 °C by 10 °C steps.

The full width at half maximum (FWHM) of the primary scattering peak was plotted against the measurement temperature, and the T_{ODT} was determined as the temperature at which a change in the slope was observed (**Figure 4.22**). The T_{ODT} of $\mathrm{AcCel}_{3.0}$-*b*-PDL-*b*-$\mathrm{AcCel}_{3.0}$, $\mathrm{AcCel}_{2.6}$-*b*-PDL-*b*-$\mathrm{AcCel}_{2.6}$, and $\mathrm{AcCel}_{2.3}$-*b*-PDL-*b*-$\mathrm{AcCel}_{2.3}$ were estimated to be 181, 233, and 246 °C, respectively. Considering the comparable N and f_{PDL} values of the three BCPs, the increase in T_{ODT} as the DS of the $\mathrm{AcCel}_{\mathrm{x}}$ segment decreased indicates a corresponding increase in the χ value.[39] This hypothesis is supported by the observation that $\mathrm{AcCel}_{2.6}$-*b*-PDL-*b*-$\mathrm{AcCel}_{2.6}$ and $\mathrm{AcCel}_{2.3}$-*b*-PDL-*b*-$\mathrm{AcCel}_{2.3}$ are more likely to form microphase-separated structures than $\mathrm{AcCel}_{3.0}$-*b*-PDL-*b*-$\mathrm{AcCel}_{3.0}$. The increase in the χ value was attributed to the enhanced hydrophilicity of the cellulosic block, which increased the repulsion with the hydrophobic PDL block. Enhanced intrablock interactions via hydrogen bonding between the hydroxy groups on the cellulosic block could also contribute to an increase in χ with decreasing DS. Several previous studies have proposed that the χ value can be increased by enhancing intrablock interactions in typical AB-diblock BCPs.[38,40] Overall, the SAXS and AFM results indicate that the microphase separation behavior of cellulose acetate-based BCPs in both the bulk and thin film states can be controlled by adjusting the DS.

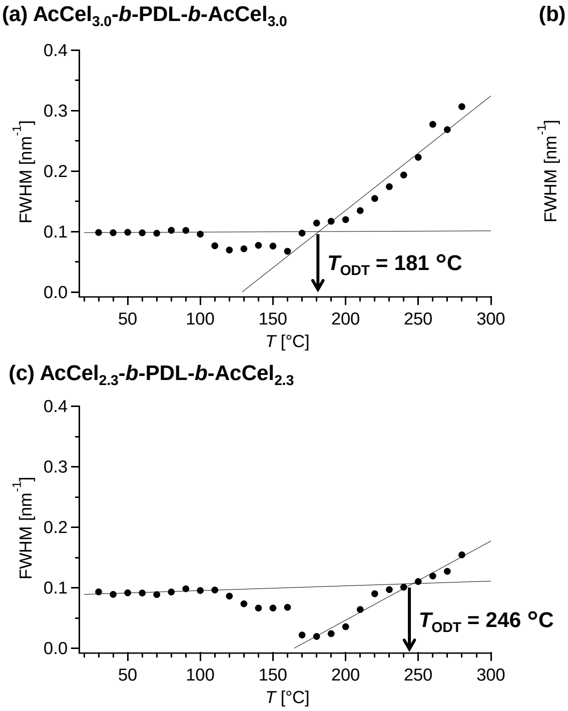

Figure 4.22. Dependence of the FWHM of the primary scattering peak on the measurement temperature for (a) AcCel$_{3.0}$-*b*-PDL-*b*-AcCel$_{3.0}$, (b) AcCel$_{2.6}$-*b*-PDL-*b*-AcCel$_{2.6}$, and (c) AcCel$_{2.3}$-*b*-PDL-*b*-AcCel$_{2.3}$.

4.3.5. Mechanical properties

Tensile tests were conducted to evaluate the potential of AcCel$_x$-*b*-PDL-*b*-AcCel$_x$ as elastomeric materials. The film samples for the tensile tests were prepared using the same procedure as for the SAXS measurements and then cut into dog-bone shapes. The stress–strain curves are shown in **Figure 4.23** and the key mechanical properties (Young's modulus (E), strain at break (ε_b), stress at break (σ_b), and toughness) are summarized in **Table 4.2**. The stress–strain curves of AcCel$_x$-*b*-PDL-*b*-AcCel$_x$ did not show a yield point, regardless of the annealing history, indicating that these samples have elastomeric properties (**Figure 4.23**). In addition, for tensile tests with 10 loading/unloading cycles, all the samples showed a small hysteresis loop, which further supported their sufficient elastic recovery (**Figure 4.24**).

The σ_b values of non-annealed AcCel$_{2.6}$-*b*-PDL-*b*-AcCel$_{2.6}$ (2.68 ± 0.08 MPa) and AcCel$_{2.3}$-*b*-PDL-*b*-AcCel$_{2.3}$ (2.14 ± 0.01 MPa) were slightly higher than that of AcCel$_{3.0}$-*b*-PDL-*b*-AcCel$_{3.0}$ (1.94 ± 0.13 MPa). Similarly, the ε_b values of non-annealed AcCel$_{2.6}$-*b*-PDL-*b*-AcCel$_{2.6}$ (420 ± 15%) and AcCel$_{2.3}$-*b*-PDL-*b*-AcCel$_{2.3}$ (378 ± 7%) were 1.2–1.3 times larger than that of AcCel$_{3.0}$-*b*-PDL-*b*-AcCel$_{3.0}$ (320 ± 5%). The same trend was observed for the annealed samples, with the ε_b values of 192 ± 5%, 310 ± 10%, and 317 ± 10% for AcCel$_{3.0}$-*b*-PDL-*b*-AcCel$_{3.0}$, AcCel$_{2.6}$-*b*-PDL-*b*-AcCel$_{2.6}$, and AcCel$_{2.3}$-*b*-PDL-*b*-AcCel$_{2.3}$, respectively. These results indicate that reducing the DS effectively improves the mechanical properties of AcCel$_x$-*b*-PDL-*b*-AcCel$_x$.

Interestingly, the E value of annealed AcCel$_{3.0}$-*b*-PDL-*b*-AcCel$_{3.0}$ (4.93 ± 0.07 MPa) was three times larger than that of non-annealed AcCel$_{3.0}$-*b*-PDL-*b*-AcCel$_{3.0}$ (1.64 ± 0.07 MPa), whereas the E values of AcCel$_{2.6}$-*b*-PDL-*b*-AcCel$_{2.6}$ (1.5–1.6 MPa) and AcCel$_{2.3}$-*b*-PDL-*b*-AcCel$_{2.3}$ (1.2–1.4 MPa) were not significantly affected by thermal annealing. This difference could be due to the high crystallinity of the annealed AcCel$_{3.0}$ segment. Indeed, for some BCP systems, it has been reported that enhanced crystallinity increases the modulus, although ε_b decreases.[3,41,42] Furthermore, the fiber-like structure observed in annealed AcCel$_{3.0}$-*b*-PDL-*b*-AcCel$_{3.0}$ could also be an important factor, as such a continuous hard domain would increase the *E* value. Satoh and Isono et al. previously found that a poly/oligosaccharide-based elastomer with a hexagonal cylinder (HEX) structure had a higher modulus than an elastomer with a BCC structure.[15] This difference originated from the continuous hard domain in the HEX structure, which could bear deformation under stretching.[43]

Table 4.2. Tensile properties of AcCel$_x$-*b*-PDL-*b*-AcCel$_x$

BCP	Annealing	E^a [MPa]	$\varepsilon_b a$ [%]	$\sigma_b{}^a$ [MPa]	Toughness^a[MPa]
AcCel3.0-*b*-PDL-*b*-AcCel3.0	none	1.64 ± 0.07	320 ± 5	1.94 ± 0.13	3.68 ± 0.27
	150 °C for 6 h	4.93 ± 0.07	192 ± 5	2.63 ± 0.06	3.28 ± 0.13
AcCel2.6-*b*-PDL-*b*-AcCel2.6	none	1.53 ± 0.03	420 ± 15	2.68 ± 0.08	5.89 ± 0.38
	150 °C for 6 h	1.56 ± 0.10	310 ± 10	2.15 ± 0.10	3.67 ± 0.24
AcCel2.3-*b*-PDL-*b*- AcCel2.3	none	1.38 ± 0.06	378 ± 7	2.14 ± 0.01	4.35 ± 0.13
	180 °C for 6 h	1.23 ± 0.04	317 ± 10	1.80 ± 0.10	3.11 ± 0.28

^{a}Tensile properties are shown as average values (with standard deviations).

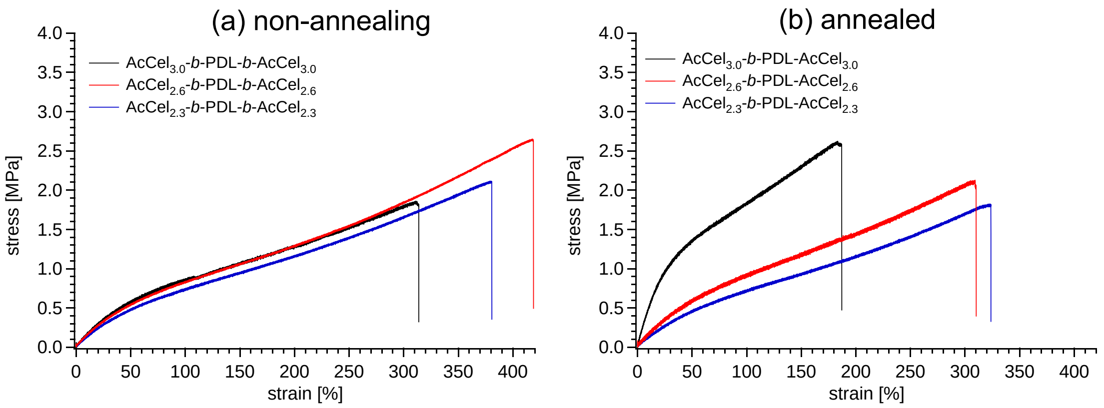

Figure 4.23. Typical stress–strain curves of $AcCel_{3.0}$-*b*-PDL-*b*-$AcCel_{3.0}$ (black), $AcCel_{2.6}$-*b*-PDL-*b*-$AcCel_{2.6}$ (red), and $AcCel_{2.3}$-*b*-PDL-*b*-$AcCel_{2.3}$ (blue) (a) before and (b) after thermal annealing.

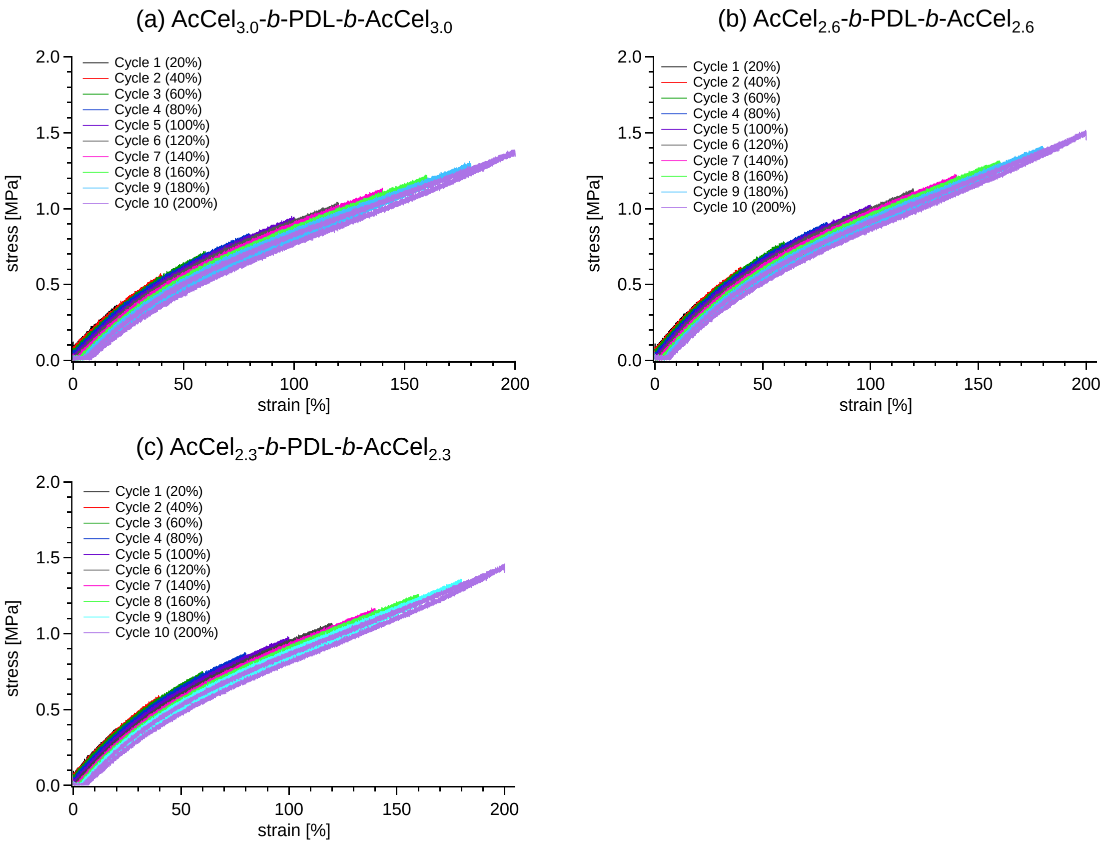

Figure 4.24. Cycle tensile testing with increasing strain by 20% (crosshead speed, 10 mm min^{-1}) for (a) $AcCel_{3.0}$-*b*-PDL-*b*-$AcCel_{3.0}$, (b) $AcCel_{2.6}$-*b*-PDL-*b*-$AcCel_{2.6}$, and (c) $AcCel_{2.3}$-*b*-PDL-*b*-$AcCel_{2.3}$.

Furthermore, the author investigated the stress relaxation behavior to evaluate the impact of DS on material deformation. Stress relaxation experiments were performed by monitoring the stress response of a sample under a constant applied strain of 70%. The average slope in the range of 30–300 s in the semi-log stress relaxation curve is smaller for AcCel$_{3.0}$-*b*-PDL-*b*-AcCel$_{3.0}$ (−11.5) than for AcCel$_{2.6}$-*b*-PDL-*b*-AcCel$_{2.6}$ (−9.04) and AcCel$_{2.3}$-*b*-PDL-*b*-AcCel$_{2.3}$ (−8.48), indicating that stress relaxation was suppressed as DS decreased (**Figure 4.25**). The stronger intermolecular forces derived from hydrogen bonding in the AcCel$_{2.6}$ and AcCel$_{2.3}$ segments likely prevented chain pullout and suppressed stress relaxation. Elastomers bearing hydrogen bonding motifs on their hard segments have been found to exhibit less stress relaxation than those without hydrogen bonds.[3] This stronger hydrogen bonding also improves the mechanical properties, such as σ_b and ε_b. In addition, the higher potential of AcCel$_{2.6}$-*b*-PDL-*b*-AcCel$_{2.6}$ and AcCel$_{2.3}$-*b*-PDL-*b*-AcCel$_{2.3}$ to form ordered microphase-separated structures could decrease stress relaxation by increasing the energy required for chain pullout.[3] Overall, the tensile and stress relaxation tests reveal that the DS is a highly important factor for controlling the mechanical properties of cellulose-based elastomers.

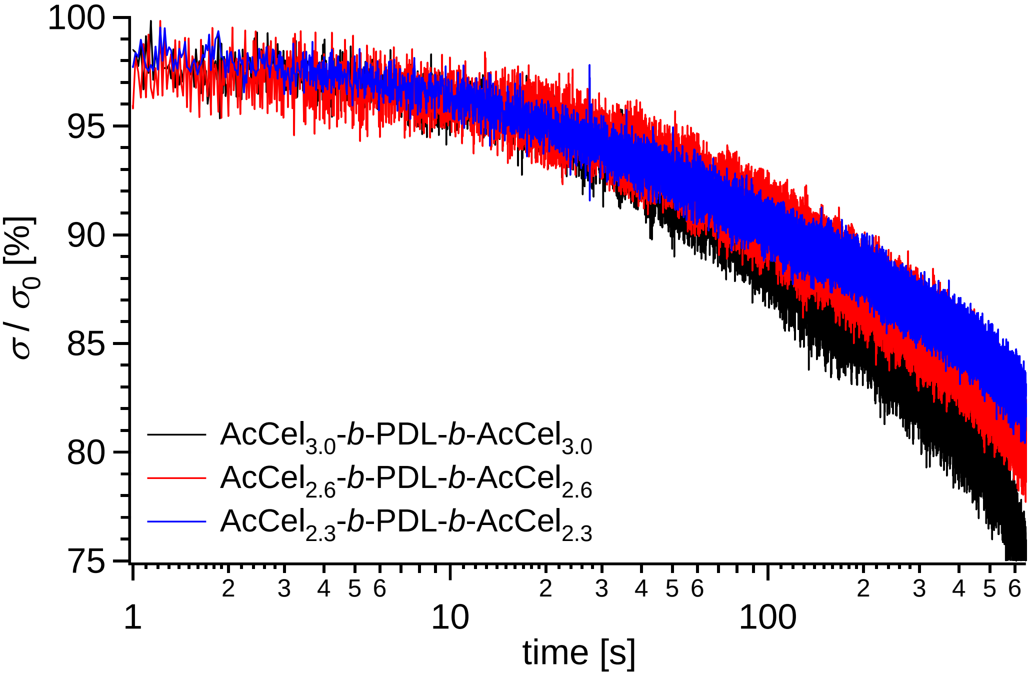

Figure 4.25. Stress relaxation curves of AcCel$_{3.0}$-*b*-PDL-*b*-AcCel$_{3.0}$ (black), AcCel$_{2.6}$-*b*-PDL-*b*-AcCel$_{2.6}$ (red), and AcCel$_{2.3}$-*b*-PDL-*b*-AcCel$_{2.3}$ (blue) at 70% strain.

4.3.6. Biodegradability potential

Cellulose acetate with a lower DS is more susceptible to biodegradation;[19–22] thus, the author investigated the effect of DS on the biodegradability of AcCel$_x$-*b*-PDL-*b*-AcCel$_x$. The author performed a preliminary biodegradability test with the non-annealed AcCel$_x$-*b*-PDL-*b*-AcCel$_x$ specimens in freshwater closed a recirculating aquaculture system (freshwater environment) rearing the Nile tilapia *Oreochromis niloticus* at 26 °C for 8 weeks. None of the specimens exhibited an obvious change in appearance, and NMR and SEC analyses revealed no significant changes before and after the biodegradation test (**Figures 4.26–4.30**). However, scanning electron microscopy (SEM) observations revealed that microorganisms were adhered to the AcCel$_x$-*b*-PDL-*b*-

$AcCel_x$ film surfaces after the biodegradation test (**Figure 4.31**). Interestingly, holes with diameters of <1 μm were observed in the $AcCel_{2.6}$-*b*-PDL-*b*-$AcCel_{2.6}$ and $AcCel_{2.3}$-*b*-PDL-*b*-$AcCel_{2.3}$ films but not in the $AcCel_{3.0}$-*b*-PDL-*b*-$AcCel_{3.0}$ film. These holes, which were likely formed by a microbial degradation process, indicate that the biodegradation potential increased as the DS decreased. Considering the NMR spectra and SEC results, biodegradation was assumed to proceed only on the surface of the $AcCel_x$-*b*-PDL-*b*-$AcCel_x$ films. Nevertheless, these results demonstrate that biodegradability of $AcCel_x$-*b*-PDL-*b*-$AcCel_x$ can be improved by simply tuning the DS of the hard segment. However, further long-term tests are required to obtain a comprehensive understanding of this process, and details of the biodegradation behavior in aqueous environments are currently being investigated.

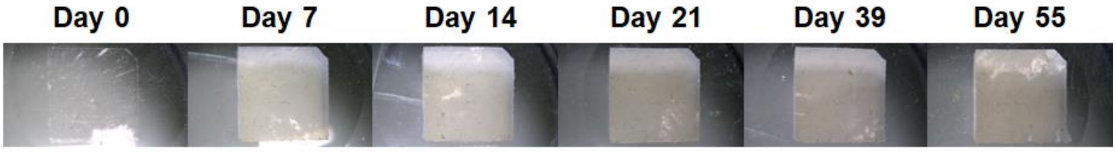

(a) $AcCel_{3.0}$-*b*-PDL-*b*-$AcCel_{3.0}$

(b) $AcCel_{2.6}$-*b*-PDL-*b*-$AcCel_{2.6}$

(c) $AcCel_{2.3}$-*b*-PDL-*b*-$AcCel_{2.3}$

Figure 4.26. The appearance images of (a) $AcCel_{3.0}$-*b*-PDL-*b*-$AcCel_{3.0}$, (b) $AcCel_{2.6}$-*b*-PDL-*b*-$AcCel_{2.6}$, and (c) $AcCel_{2.3}$-*b*-PDL-*b*-$AcCel_{2.3}$ after biodegradation test up to 55 days.

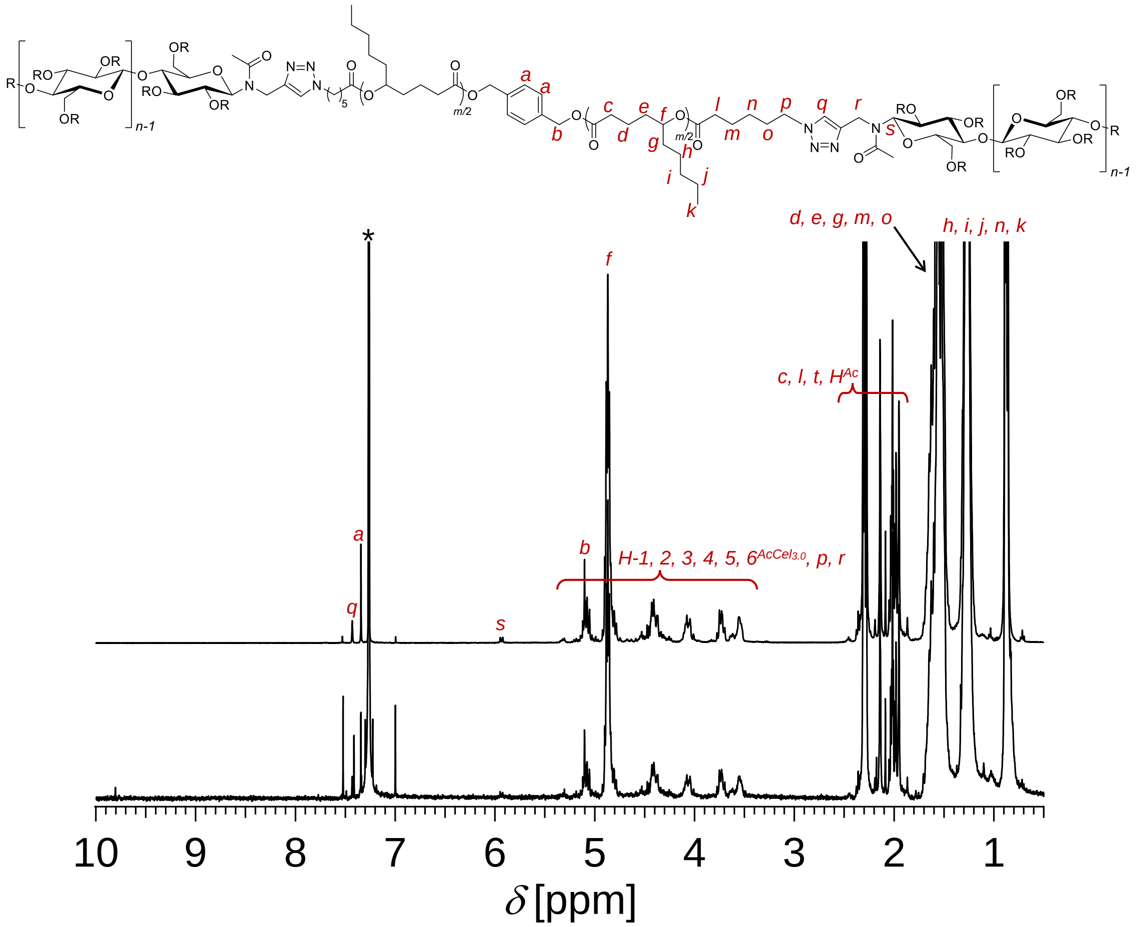

Figure 4.27. ^{1}H NMR spectrum of AcCel$_{3.0}$-*b*-PDL-*b*-AcCel$_{3.0}$ before (upper) and after (lower) biodegradation test (400 MHz, CDCl$_3$).

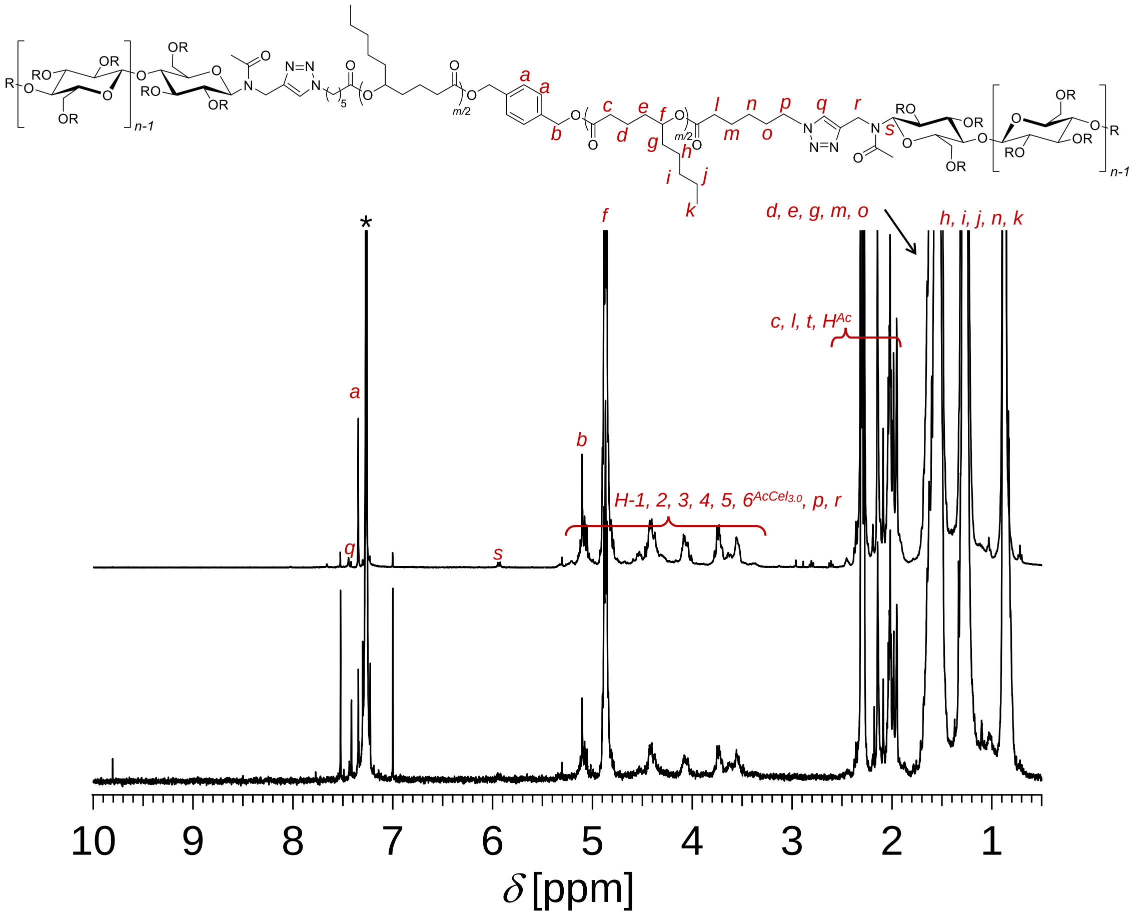

Figure 4.28. ^{1}H NMR spectrum of AcCel$_{2.6}$-*b*-PDL-*b*-AcCel$_{2.6}$ before (upper) and after (lower) biodegradation test (400 MHz, CDCl$_3$).

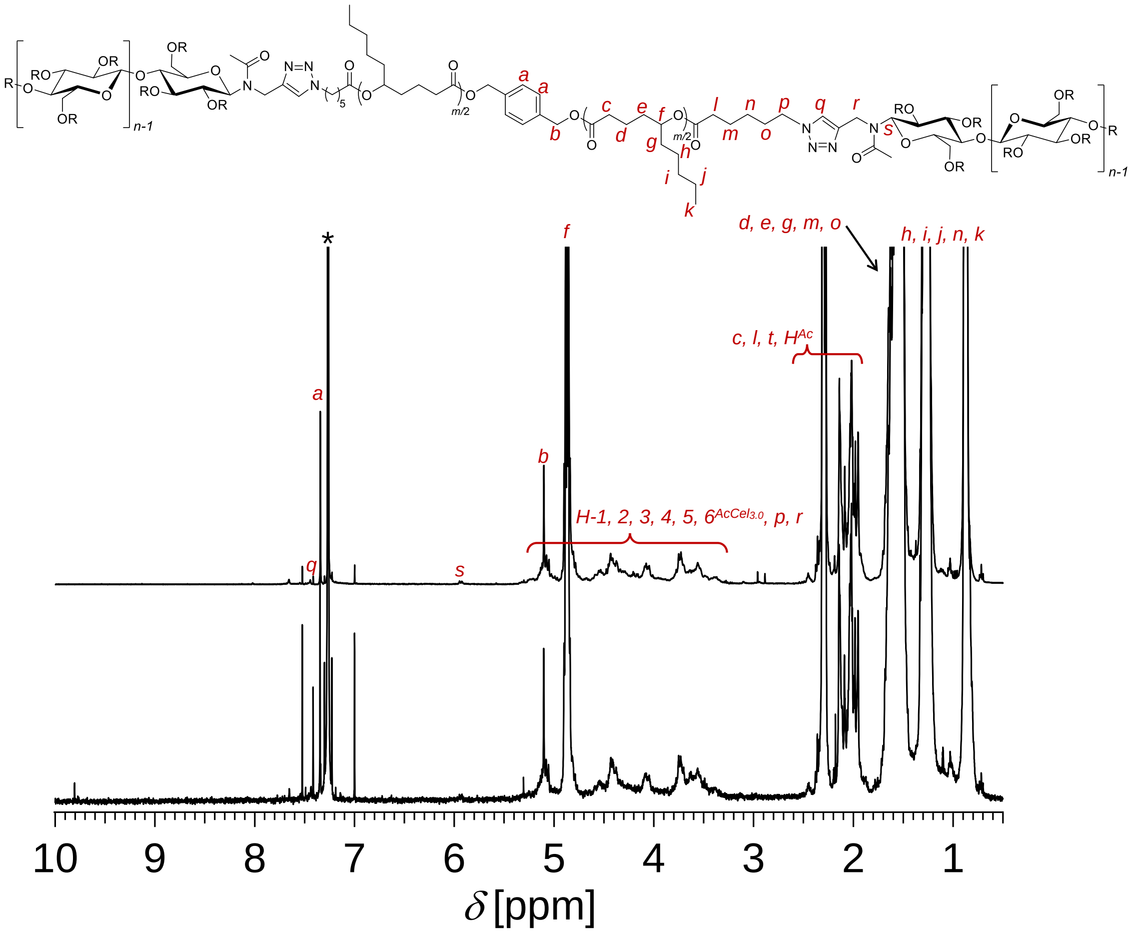

Figure 4.29. ^{1}H NMR spectrum of AcCel$_{2.3}$-*b*-PDL-*b*-AcCel$_{2.3}$ before (upper) and after (lower) biodegradation test (400 MHz, CDCl$_3$).

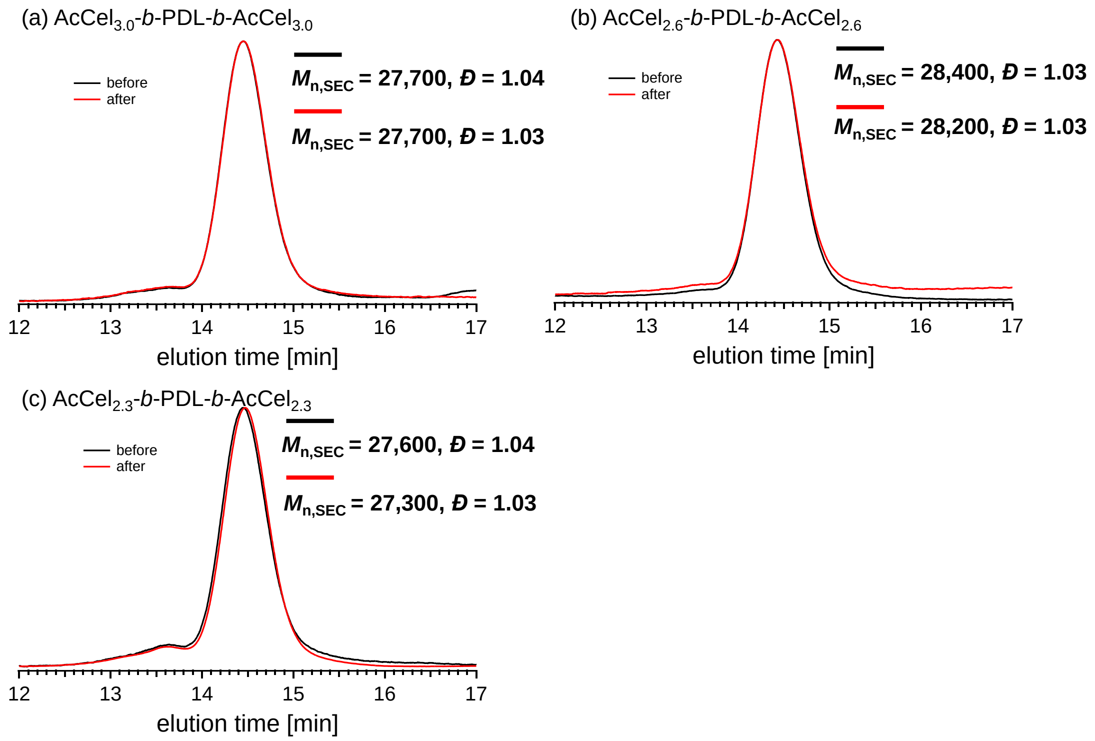

Figure 4.30. SEC traces of (a) $AcCel_{3.0}$-*b*-PDL-*b*-$AcCel_{3.0}$, (b) $AcCel_{2.6}$-*b*-PDL-*b*-$AcCel_{2.6}$, and (c) $AcCel_{2.3}$-*b*-PDL-*b*-$AcCel_{2.3}$ before (black) and after (red) biodegradation test (eluent, THF; flow rate, 1.0 mL min^{-1}).

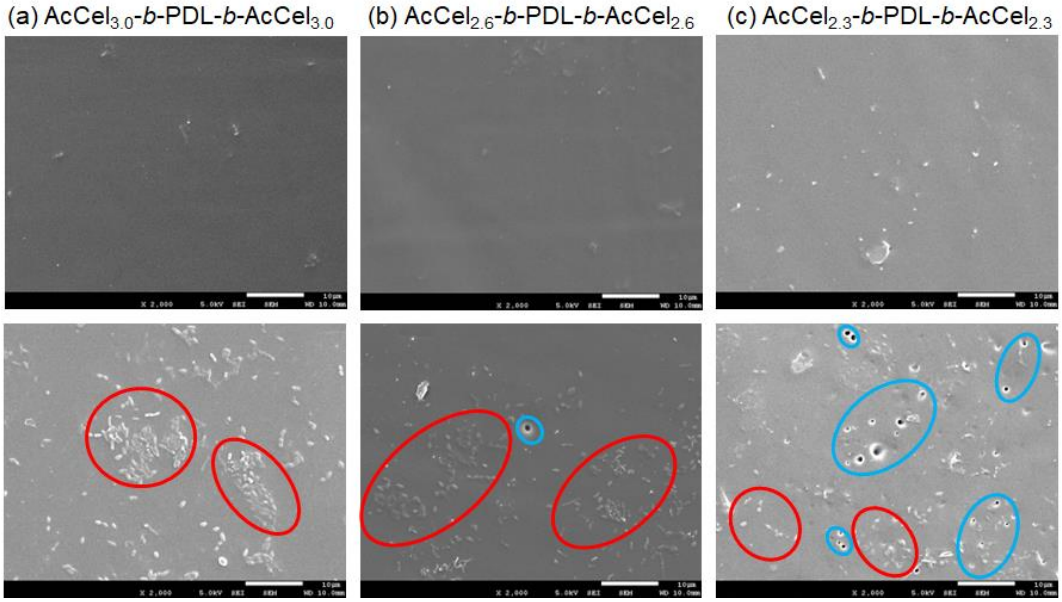

Figure 4.31. SEM images of (a) $AcCel_{3.0}$-*b*-PDL-*b*-$AcCel_{3.0}$, (b) $AcCel_{2.6}$-*b*-PDL-*b*-$AcCel_{2.6}$, and (c) $AcCel_{2.3}$-*b*-PDL-*b*-$AcCel_{2.3}$ films before (upper) and after (lower) degradation tests. The red and blue circles show microorganism and newly formed holes, respectively. Scale bars are 10 μm.

4.4. Conclusion

The author used a combination of CDP-mediated cellulose synthesis, ring-opening polymerization, and a click reaction to synthesize cellulose acetate-based BCPs, $AcCel_x$-*b*-PDL-*b*-$AcCel_x$, consisting of acetyl cellologiosaccharide ($AcCel_x$) hard segments with three different DSs and PDL soft segments. The microphase separation behavior and mechanical properties of $AcCel_x$-*b*-PDL-*b*-$AcCel_x$ were found to be highly dependent on the DS of the $AcCel_x$ segment. In particular, the stronger intermolecular interactions (i.e., hydrogen bonding) associated with decreasing DS positively affected these properties. The findings of this study clearly demonstrate that DS is a useful factor for improving and optimizing the physical properties of cellulose acetate-based TPEs. In addition, the author found that the biodegradability of $AcCel_x$-*b*-PDL-*b*-$AcCel_x$ in an aqueous environment increased as the DS decreased. Although further detailed biodegradation studies are necessary, this tendency is consistent with the fact that cellulose acetate itself is more susceptible to biodegradation when the DS is low.[19–22] Overall, DS was found to influence a range of material properties for not only cellulose acetate but also cellulose acetate-based BCPs. This approach can be expanded to the molecular design of a wide range of poly- or oligosaccharide-based BCP materials and will contribute to the development of next-generation environmentally benign polymeric materials that can replace conventional petroleum-based materials.

4.5. References

(1) Maji, P.; Naskar, K. Styrenic block copolymer-based thermoplastic elastomers in smart applications: Advances in synthesis, microstructure, and structure–property Relationships—A review. *J. Appl. Polym. Sci.* **2022**, *139*, e52942.

(2) Martello, M. T.; Schneiderman, D. K.; Hillmyer, M. A. Synthesis and Melt Processing of Sustainable Poly(*ε*-decalactone)-*block*-Poly(lactide) Multiblock Thermoplastic Elastomers. *ACS Sustain. Chem. Eng.* **2014**, *2*, 2519–2526.

(3) Watts, A.; Hillmyer, M. A. Aliphatic Polyester Thermoplastic Elastomers Containing Hydrogen-Bonding Ureidopyrimidinone Endgroups. *Biomacromolecules* **2019**, *20*, 2598–2609.

(4) Watts, A.; Kurokawa, N.; Hillmyer, M. A. Strong, Resilient, and Sustainable Aliphatic Polyester Thermoplastic Elastomers. *Biomacromolecules* **2017**, *18*, 1845–1854.

(5) Fournier, L.; Rivera Mirabal, D. M.; Hillmyer, M. A. Toward Sustainable Elastomers from the Grafting-Through Polymerization of Lactone-Containing Polyester Macromonomers. *Macromolecules* **2022**, *55*, 1003–1014.

(6) Liffland, S.; Hillmyer, M. A. Enhanced Mechanical Properties of Aliphatic Polyester Thermoplastic Elastomers through Star Block Architectures. *Macromolecules* **2021**, *54*, 9327–9340.

(7) Shin, J.; Martello, M. T.; Shrestha, M.; Wissinger, J. E.; Tolman, W. B.; Hillmyer, M. A. Pressure-Sensitive Adhesives from Renewable Triblock Copolymers. *Macromolecules* **2011**, *44*, 87–94.

(8) Isono, T.; Kawakami, N.; Watanabe, K.; Yoshida, K.; Otsuka, I.; Mamiya, H.; Ito, H.; Yamamoto, T.; Tajima, K.; Borsali, R.; Satoh, T. Microphase separation of carbohydrate-based star-block copolymers with sub-10 nm periodicity. *Polym. Chem.* **2019**, *10*, 1119–1129.

(9) Isono, T.; Otsuka, I.; Kondo, Y.; Halila, S.; Fort, S.; Rochas, C.; Satoh, T.; Borsali, R.; Kakuchi, T. Sub-10 nm Nano-Organization in AB_2- and AB_3-Type Miktoarm Star Copolymers Consisting of Maltoheptaose and Polycaprolactone. *Macromolecules* **2013**, *46*, 1461–1469.

(10) Mumtaz, M.; Takagi, Y.; Mamiya, H.; Tajima, K.; Bouilhac, C.; Isono, T.; Satoh, T.; Borsali, R. Sweet Pluronic poly(propylene oxide)-*b*-oligosaccharide block copolymer systems: Toward sub-4 nm thin-film nanopattern resolution. *Eur. Polym. J.* **2020**, *134*, 109831.

(11) Nishimura, T.; Katsuhara, S.; Lee, C.; Ree, B. J.; Borsali, R.; Yamamoto, T.; Tajima, K.; Satoh, T.; Isono, T. Fabrication of Ultrafine, Highly Ordered Nanostructures Using Carbohydrate-Inorganic Hybrid Block Copolymers. *Nanomaterials* **2022**, *12*, 1–14.

(12) Isono, T.; Komaki, R.; Lee, C.; Kawakami, N.; Ree, B. J.; Watanabe, K.; Yoshida, K.; Mamiya, H.; Yamamoto, T.; Borsali, R.; Tajima, K.; Satoh, T. Rapid access to discrete and monodisperse block co-oligomers from sugar and terpenoid toward ultrasmall periodic nanostructures. *Commun. Chem.* **2020**, *3*, 1–9.

(13) Isono, T.; Komaki, R.; Kawakami, N.; Chen, K.; Chen, H.-L.; Lee, C.; Suzuki, K.; Ree, B. J.; Mamiya, H.; Yamamoto, T.; Borsali, R.; Tajima, K.; Satoh, T. Tailored Solid-State Carbohydrate Nanostructures Based on Star-Shaped Discrete Block Co-Oligomers. *Biomacromolecules* **2022**, *23*, 3978–3989.

(14) Katsuhara, S.; Mamiya, H.; Yamamoto, T.; Tajima, K.; Isono, T.; Satoh, T. Metallopolymer-*block*-oligosaccharide for sub-10 nm microphase separation. *Polym. Chem.* **2020**, *11*, 2995–3002.

(15) Isono, T.; Nakahira, S.; Hsieh, H. -C.; Katsuhara, S.; Mamiya, H.; Yamamoto, T.; Chen, W. -C.; Borsali, R.; Tajima, K.; Satoh, T. Carbohydrates as Hard Segments for Sustainable Elastomers: Carbohydrates Direct the Self-Assembly and Mechanical Properties of Fully Bio-Based Block Copolymers. *Macromolecules* **2020**, *53*, 5408–5417.

(16) Katsuhara, S.; Takagi, Y.; Sunagawa, N.; Igarashi, K.; Yamamoto, T.; Tajima, K.; Isono, T.; Satoh, T. Enhanced Self-Assembly and Mechanical Properties of Cellulose-Based Triblock Copolymers: Comparisons with Amylose-Based Triblock Copolymers. *ACS Sustain. Chem. Eng.* **2021**, *9*, 9779–9788.

(17) de Freitas, R. R. M.; Senna, A. M.; Botaro, V. R. Influence of degree of substitution on thermal dynamic mechanical and physicochemical properties of cellulose acetate. *Ind. Crops Prod.* **2017**, *109*, 452–458.

(18) Hata, Y.; Serizawa, T. Self-assembly of cellulose for creating green materials with tailor-made nanostructures. *J. Mater. Chem. B* **2021**, *9*, 3944–3966.

(19) Kliem, S.; Kreutzbruck. M.; Bonten, C. Review on the Biologocal Degradation of Polymers in Various Environments. *Materials* **2020**, *13*, 4586.

(20) Erdal, N. B.; Hakkarainen, M. Degradation of Cellulose Derivatives in Laboratory , Man-Made , and Natural Environments. *Biomacromolecules* **2022**, *23*, 2713–2729.

(21) Puls, J.; Wilson, S. A.; Hölter, D. Degradation of Cellulose Acetate-Based Materials: A Review. *J. Polym. Environ.* **2011**, *19*, 152–165.

(22) Edgar, K. J.; Buchanan, C. M.; Debenham, J. S.; Rundquist, P. A.; Seiler, B. D.; Shelton, M. C.; Tindall, D. Advances in cellulose ester performance and applicaton. *Prog. Polym. Sci.* **2001**, *26*, 1605–1688.

(23) Hiraishi, M.; Igarashi, K.; Kimura, S.; Wada, M.; Kitaoka, M.; Samejima, M. Synthesis of highly ordered cellulose II in vitro using cellodextrin phosphorylase. *Carbohydr. Res.* **2009**, *344*, 2468–2473.

(24) Grandjean, C.; Boutonnier, A.; Guerreiro, C.; Fournier, J. M.; Mulard, L. A. On

the Preparation of Carbohydrate-Protein Conjugates Using the Traceless Staudinger Ligation. *J. Org. Chem.* **2005**, *70*, 7123–7132.

(25) Halila, S.; Manguian, M.; Fort, S.; Cottaz, S.; Hamaide, T.; Fleury, E.; Driguez, H. Syntheses of Well-Defined Glyco-Polyorganosiloxanes by “Click” Chemistry and Their Surfactant Properties. *Macromol. Chem. Phys.* **2008**, *209*, 1282–1290.

(26) Pylkkänen, R.; Mohammadi, P.; Arola, S.; De Ruijter, J. C.; Sunagawa, N.; Igarashi, K.; Penttilä, M. In Vitro Synthesis and Self-Assembly of Cellulose II Nanofibrils Catalyzed by the Reverse Reaction of Clostridium Thermocellum Cellodextrin Phosphorylase. *Biomacromolecules* **2020**, *21*, 4355–4364.

(27) Kuga, T.; Sunagawa, N.; Igarashi, K. Enzymatic synthesis of cellulose in space: gravity is a crucial factor for building cellulose II gel structure. *Cellulose* **2022**, *29*, 2999–3015.

(28) Sugiura, K.; Sawada, T.; Tanaka, H.; Serizawa, T. Enzyme-catalyzed propagation of cello-oligosaccharide chains from bifunctional oligomeric primers for the preparation of block co-oligomers and their crystalline assemblies. *Polym. J.* **2021**, *53*, 1133–1143.

(29) Sugiura, K.; Saito, M.; Sawada, T.; Tanaka, H.; Serizawa, T. Cellodextrin Phosphorylase-Catalyzed Single-Process Production and Superior Mechanical Properties of Organic−Inorganic Hybrid Hydrogels Composed of Surface-Carboxylated Synthetic Nanocelluloses and Hydroxyapatite. *ACS Sustinable Chem. Eng.* **2022**, *10*, 13484–13494.

(30) Petrović, D. M.; Kok, I.; Woortman, A. J. J.; Ćirić, J.; Loos, K. Characterization of Oligocellulose Synthesized by Reverse Phosphorolysis Using Different Cellodextrin Phosphorylases. *Anal. Chem.* **2015**, *87*, 9639–9646.

(31) Serizawa, T.; Kato, M.; Okura, H.; Sawada, T.; Wada, M. Hydrolytic activities of artificial nanocellulose synthesized via phosphorylase-catalyzed enzymatic reactions. *Polym. J.* **2016**, *48*, 539–544.

(32) Kamitakahara, H.; Enomoto, Y.; Hasegawa, C.; Nakatsubo, F. Synthesis of Diblock Copolymers with Cellulose Derivatives. 2. Characterization and Thermal Properties of Cellulose Triacetate-Block-Oligoamide-15. *Cellulose* **2005**, *12*, 527–541.

(33) Kono, H.; Hashimoto, H.; Shimizu, Y. NMR characterization of cellulose acetate: Chemical shift assignments, substituent effects, and chemical shift additivity. *Carbohydr. Polym.* **2015**, *118*, 91–100.

(34) Tezuka, Y.; Tsuchiya, Y. Determination of substituent distribution in cellulose acetate by means of a ^{13}C NMR study on its propanoated derivative. *Carbohydr. Res.* **1995**, *273*, 83–91.

(35) Cerqueira, D. A.; Valente, A. J. M.; Filho, G. R.; Burrows, H. D. Synthesis and

properties of polyaniline-cellulose acetate blends: The use of sugarcane bagasse waste and the effect of the substitution degree. *Carbohydr. Polym.* **2009**, *78*, 402–408.

(36) Isono, T.; Ree, B. J.; Tajima, K.; Borsali, R.; Satoh, T. Highly Ordered Cylinder Morphologies with 10 nm Scale Periodicity in Biomass-Based Block Copolymers. *Macromolecules* **2018**, *51*, 428–437.

(37) Kamide, K.; Saito, M. Thermal Analysis of Cellulose Acetate Solids with Total Degree of Substitution of 0.49, 1.75, 2.46, and 2.92. *Polym. J.* **1985**, *17*, 919–928.

(38) Zhou, S. X.; Janes, D. W.; Kim, C. Bin; Willson, C. G.; Ellison, C. J. Designing Intrablock Attractions to Increase the χ Parameter of a Symmetric Diblock Copolymer. *Macromolecules* **2016**, *49*, 8332–8340.

(39) Bates, F. S.; Fredrickson, G. H. BLOCK COPOLYMER THERMODYNAMICS: Theory and Experiment. *Annu. Rev. Phys. Chem.* **1990**, *41*, 525–557.

(40) Yoshida, K.; Tian, L.; Miyagi, K.; Yamazaki, A.; Mamiya, H.; Yamamoto, T.; Tajima, K.; Isono, T.; Satoh, T. Facile and Efficient Modification of Polystyrene-*block*-Poly(methyl methacrylate) for Achieving Sub-10 nm Feature Size. *Macromolecules* **2018**, *51*, 8064–8072.

(41) Jauzein, T.; Huneault, M. A.; Heuzey, M. C. Crystallinity and mechanical properties of polylactide/ether-amide copolymer blends. *J. Appl. Polym. Sci.* **2017**, *134*, 1–10.

(42) Sarasua, J. R.; Arraiza, A. L.; Balerdi, P.; Maiza, I. Crystallinity and Mechanical Properties of Optically Pure Polylactides and Their Blends. *Polym. Eng. Sci.* **2005**, *45*, 745–753.

(43) Crawford, K. E.; Sita, L. R. De Novo Design of a New Class of “Hard-Soft” Amorphous, Microphase-Separated, Polyolefin Block Copolymer Thermoplastic Elastomers. *ACS Macro Lett.* **2015**, *4*, 921–925.

Chapter 5

Development of Cellulose-Based Compatibilizers for Toughening Cellulose Acetate

5.1. Introduction

Plastics are one of the most ubiquitous materials in our daily life because they have attractive properties such as inexpensive, light, and durable etc. However, the existing plastics have the severe concern that they remain in the environment for long time due to their low biodegradability. Especially, marine plastic pollution has been recognized as the global environmental issue to be solved urgently.[1,2] It is reported that the plastic waste of several million tons leaks out into the ocean per a year.[2,3] To address the plastic pollution, some biodegradable polymers have been developed such as poly(lactic acid) (PLA) and poly(butylene succinate) (PBS), which are used for films, textile, garments, and biomedical materials etc.[4,5] However, most of biodegradable plastics have little biodegradability in the ocean because of the low bacterial density.[2,4,6] Thus, the outstanding methods to enhance the biodegradation in marine environment has been developed. For example, the approaches of incorporating the parts to be cleaved and hydrolyzed easily such as salicylate, RNA-like, and lactic acid moieties to the main chain have been reported.[7–9] However, the polymers possessing the marine biodegradability originally is more enticing because these synthetic methods are complicated.

Poly(3-hydroxyalkanoate) (PHA) and some polysaccharides such as cellulose and agarose, are be highly biodegradable in ocean even without any modification and have already been used industrially.[2,10,11] Above all, cellulose is one of the most attractive compared with the other marine degradable polymers because it is the most abundant on Earth. However, cellulose is insoluble in common organic solvents and incompatible with melt processing due to the strong intra- and intermolecular hydrogen bonding. This problem can be overcome through derivatization such as nitration, etherification, and esterification. Cellulose acetate, the common ester derivative of cellulose, has thermoplasticity, stiffness, and resistance for heat, grease, and impact and has been used industrially as an textiles, optical film, and cigarette filters etc. [12–15] Another attractive point is that cellulose acetate also has biodegradability in the ocean, depending on the degree of substitute (DS), which means the rate of biodegradability can be controlled easily as mentioned in the Chapter 4.[16–19] Therefore, plain cellulose acetate is highly attractive materials; however, the range of its application has been limited because of its brittleness. Thus, the mechanical properties of cellulose acetate should be improved for expanding its application.

The mechanical properties of polymers are often modified through polymer blending.[20,21] This technique has been used commercially for high-impact polystyrene and acrylonitrile-butadiene-styrene resin to enhance the impact and heat resistant. However, macrophase separation is occurred in general due to low entropy of mixing when two different polymers are mixed, resulting in decreasing the adhesion of the interface and declining in the mechanical properties.[20,21] In order to prompt the miscibility of two different polymers, a block copolymer (BCP) consisting of polymer units of each blend component is added as a compatibilizer.[20,21] The compatibilizer works like a surfactant, which reduces the interfacial tension to enhance the miscibility of the blended polymers and the adhesion of the polymer interface, resulting in improving mechanical properties.

Recently, Matson and co-workers have reported that cellulose acetate-*b*-polybutadiene (PB)-*b*-cellulose acetate was synthesized as a compatibilizer for cellulose acetate/PB blend.[22] Indeed, PB is known as a typical soft polymer and is a good candidate to modify the brittleness of cellulose acetate. However, PB has no biodegradability; thus, this method does not make full use of the strong point of cellulose acetate. Thus, the method of improving the mechanical properties of cellulose acetate has to be developed without decreasing the biodegradability. To this end, the author focuses on poly(*ε*-caprolactone) (PCL) as the soft blend partner which has high biodegradability even in the ocean in spite of petroleum-derived polymer.[4,6,11] In fact, some researchers have reported that the polymer physical properties can be modified by adding the PCL.[23,24] For example, Satoh et al. also succeeded in toughening PHA which is brittle like cellulose acetate by blending with PCL.[25] In this previous report, they synthesized the BCPs consisting of PHA and PCL as compatibilizers for the PHA/PCL blend and revealed that the compatibilization behavior state depended on the structures of the BCPs. Inspired by these studies, here, the author synthesized the three types of BCPs consisting of cellulose acetate (AcCel$_n$) and PCL as compatibilizers for toughening cellulose acetate as shown in **Scheme 5.1**. The synthesized BCPs worked as compatibilizers in cellulose triacetate (CTA)/PCL blend and improve the mechanical properties.

Scheme 5.1. Synthesis of three types of BCPs consisting of cellulose acetate (AcCel$_n$) and PCL

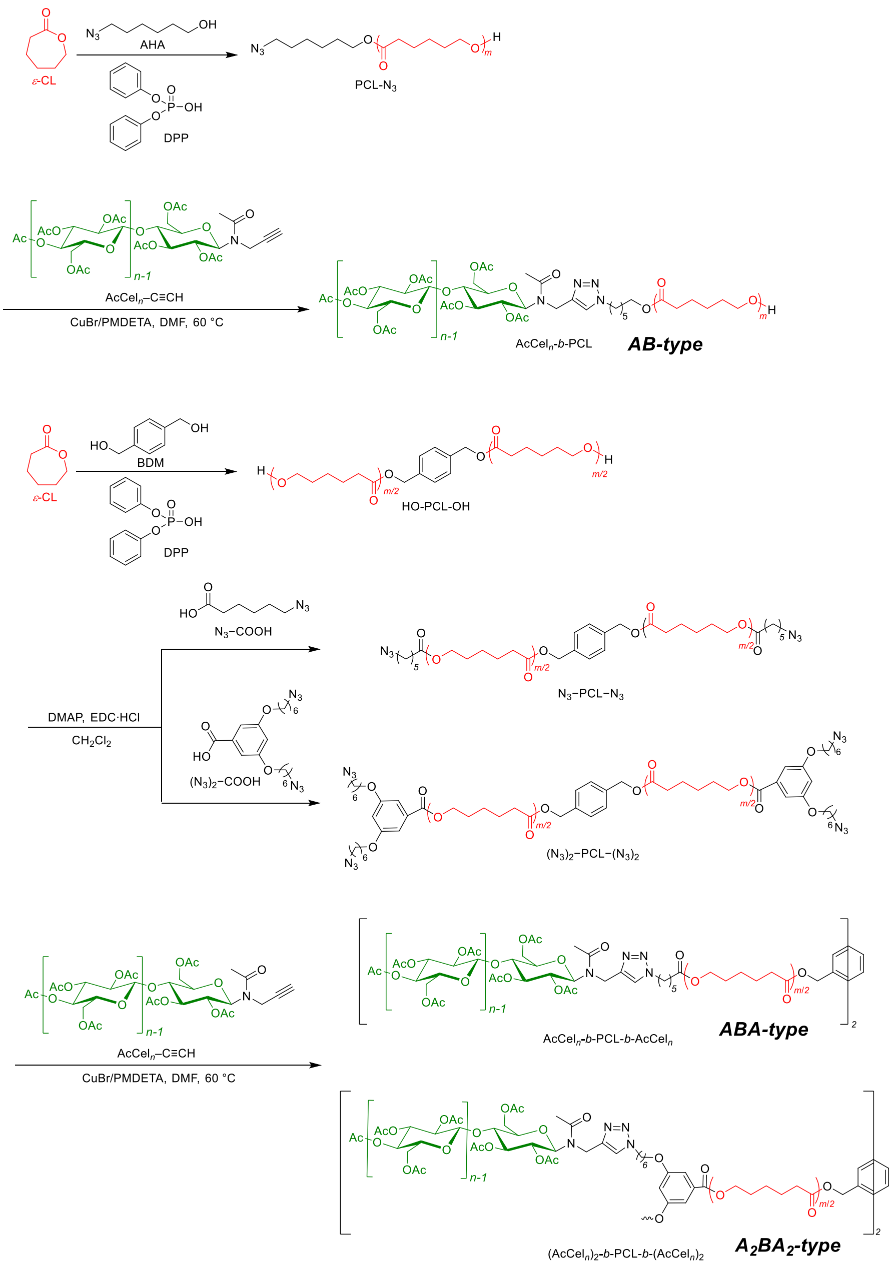

5.2. Experimental Section

5.2.1. Materials

α-D-Glucose 1-phosphate disodium salt hydrate (*α*G1P, ≥97%), 4-(2-hydroxyethyl)-1-piperazineethanesulfonic acid (HEPES, ≥99.5%, titration), aluminum oxide (activated, basic, Brockmann I), copper(I) bromide (CuBr, 99.999%), and poly(*ε*-caprolactone) (PCL; number-average molecular weight (M_n) = 80,000) were purchased from Sigma Aldrich and used as received. D(+)-cellobiose (CB), sodium sulfate (Na_2SO_4, >99.0%), anhydrous magnesium sulfate ($MgSO_4$, >95%), propargylamine (>95%), acetic anhydride (>97%), hydrochloric acid (HCl, 35–37%), ethyl acetate (AcOEt, >99.3%), acetone (>99.0%), *N*,*N*-dimethylformamide (DMF, >99.0%), *N*,*N*-dimethylethanamide (DMAc, >99.0%), lithium chloride (LiCl, >99.0%), and dry CH_2Cl_2 (>99.5%; water content, <0.001%) were purchased from Kanto Chemical Co., Inc. and used as received. Dichloromethane (CH_2Cl_2, >99.0%), chloroform ($CHCl_3$, >99.0%) and methanol (MeOH, 99.6%) were purchased from Junsei Chemical Co., Ltd., and used as received. *N*,*N*,*N′*,*N″*,*N″*-Pentamethyldiethlenetriamine (PMDETA, >98.0%), 1-(3-dimethylaminopropyl)-3-ethylcarbodiimide hydrochloride (EDC·HCl, >98.0%), and 4-dimethylaminopyridine (DMAP, >99.0%) were purchased from Tokyo Chemical Industry Co., Ltd. (TCI) and used as received. Cellulose triacetate (CTA) (degree of substitution (DS) ≈ 2.9, M_n = 130,000) was purchased from FUJIFILM Wako Pure

Chemical Corp. and used as received. Sucrose phosphorylase (SP) was purchased from Oriental Yeast Co., Ltd., and kept in a freezer after dissolving in Lysis buffer composed of 20 mM tris(hydroxymethyl)aminomethane-HCl and 10 mM imidazole. Diphenyl phosphate (DPP, >98.0%) and 1,4-benzenedimethanol (BDM, >99.0%) were purchased from Sigma Aldrich and TCI, respectively, and they were co-evaporated with dry toluene and dried under vacuum for a few days before use. *ε*-Caprolactone (*ε*-CL) was purchased from TCI and purified by distillation over CaH_2 under reduced pressure (80 Pa/80 °C). Cellodextrin phosphorylase (CDP)[26,27], 6-azidohexanoic acid[28], 6-azido-1-hexanol (AHA)[29], 3,5-bis(6-azidohexyloxy)benzoic acid[30], and *N*-acetyl-propargyl D-(+)-cellobiose (CB−C≡CH)[31] were prepared according to previous reported methods.

5.2.2. Instruments

^{1}H NMR measurement

^{1}H NMR (400 MHz) spectra were obtained using a JEOL JNM-ECS 400 instrument at 25 °C.

Size exclusion chromatography (SEC)

SEC measurements were performed at 40 °C in THF (flow rate, 1.0 mL min^{-1}) using a Jasco high-performance liquid chromatography system (PU-980 Intelligent HPLC Pump, CO-2065 Plus Intelligent Column Oven, RI-2031 Plus Intelligent RI

Detector, and PU-4180 pump as a degasser) equipped with a Shodex KF-G guard column (4.6 mm × 10 mm; particle size, 8 μm) and two Shodex KF-804L columns (linear; particle size 7 μm; 8.0 mm × 300 mm; exclusion limit, 4×10^4). The number-average molecular weight ($M_{\mathrm{n,SEC}}$) and dispersity ($Đ$) were calculated based on polystyrene standards.

Preparative SEC

The preparative SEC purification was performed in $CHCl_3$ (10 mL min^{-1}) at room temperature (r.t.) using LC-9201 liquid chromatography system (Japan Analytical Industry Co. Ltd. (JAI)) equipped with a JAI JAIGEL-2HR column (20 mm × 600 mm; exclusion limit, 5×10^3), JAIGEL-3HR column (20 mm × 600 mm; exclusion limit, 7×10^4), and a JAI RI-50s refractive index detector.

Fourie transform infrared spectroscopy (FT-IR)

The FT-IR spectra were obtained using a PerkinElmer Frontier MIR spectrometer equipped with a single reflection diamond universal attenuated total reflection (ATR) accessory.

Differential scanning calorimetry (DSC)

The DSC measurement was performed using a Hitachi DSC 7000X under nitrogen atmosphere. All BCP samples were heated to 240 °C, cooled to −90 °C, and heated again to 240 °C at the heating and cooling rate of 10 °C min^{-1}. The CTA/PCL- and CTA/PCL/BCP-blend films were heated from 30 °C to 335 °C at the heating rate of

10 °C min^{-1}.

Thermogravimetric analysis (TGA)

The TGA measurement was performed using Hitachi STA200RV under nitrogen atmosphere. All polymer samples were heated up to 550 °C at the heating rate of 10 °C min^{-1}.

Matrix-assisted laser desorption ionization time-of-flight mass (MALDI-TOF MS) spectrometry

The MALDI-TOF MS measurement of the obtained cellooligosaccharide was performed using an AB Sciex TOF/TOF 5800 system equipped with a 349-nm Nd:YAG laser. Five hundred shots were accumulated for the spectra and an acceleration voltage was adjusted between 10 and 30 kV depending on both the molecular weight and the nature of each analyzed compounds in the reflector mode. For the ethynyl-functionalized cellooligosaccharide, the sample was prepared by mixing an ultrapure water dispersion of the compound (1.0 mg mL^{-1}, 200 μL), acetonitrile solution of a matrix (2,5-dihydroxybenzoic acid, 10 mg mL^{-1}, 100 μL), and trifluoroacetic acid (0.2% (v/v), 300 μL). A 1 μL aliquot of this mixture was loaded on a sample plate. For ethynyl-functionalized cellooligosaccharide acetate, the sample was prepared by mixing a THF solution of the compound (5 mg mL^{-1}, 100 μL) and a matrix (2,5-dihydroxybenzoic acid, 10 mg mL^{-1}, 500 μL). A 1 μL aliquot of this mixture was loaded on a sample plate, which was coated by an acetone solution of NaI (1 μL, 1 mmol L^{-1}) as the cationic agent.

Tensile testing

The tensile tests were performed with an INSTRON 34SC-1 tensile tester at the temperature of 19 °C and the humidity of 40%. The film samples for the tensile tests were prepared by casting the polymer solutions in $CHCl_3$ (20 mL) with the weight ratio of CTA/PCL/block copolymer = 67/23/10 or CTA/PCL = 75/25 (total 900 mg) ratio onto a Teflon dish (diameter = 100 mm) and drying at r.t. overnight followed by vacuum drying at r.t. for 24 h. The obtained films were hot-pressed at 200 °C under 3 MPa for 3 min and aged for 72 h, and then cut into a dog bone shape of 12 × 2 × 0.105–0.188 mm (Japanese Industrial Standards (JIS) K6251). For each film, five samples were tested and the average values of the elastic modulus, strain at break, stress at break, and toughness were calculated. The crosshead speed applied during the measurements was 10 mm min^{-1}. The strain at break was taken as the engineering strain where the stress drops suddenly.

5.2.3. Synthetic details

Synthesis of ethynyl-functionalized cellooligosaccharide (Cel$_n$−C≡CH) using CDP and SP

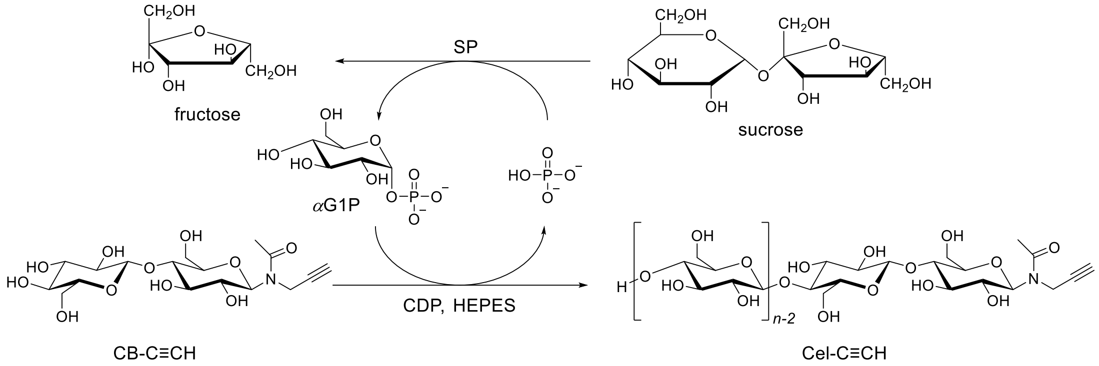

10 mM αG1P, 50 mM CB−C≡CH, and 500 mM sucrose were incubated with 50 μg mL^{-1} CDP and 5 U mL^{-1} SP in 50 mM HEPES buffer solutions (pH 7.5, 70 mL, divided into seven centrifuge tubes) at 40 °C. After incubating for 7 days, the reaction mixtures were centrifuged to isolate the insoluble product and the resulting pellet was washed with water followed by centrifugation at 14,000 rpm for 20 min at 4 °C several times to give wet Cel$_n$−C≡CH. The aliquot of the obtained product was freeze-dried in vacuo for 2 days to give a white powder (4.72 g). Yield: 61.4%.

$M_{\mathrm{n,NMR}}$ = 1,220 g mol^{-1} (DP = 6.95), $M_{\mathrm{n,MALDI}}$ = 1,190 g mol^{-1} (DP = 6.69)

^{1}H NMR (400 MHz, 10% (w/w) NaOD-D$_2$O): δ (ppm) 5.61–5.43, 4.54–4.36 (m, rotamers, −CHN(Ac)−), 4.15 (d, J = 8.0 Hz, H-1$^{\mathrm{Cel}n}$), 4.06–2.66 (m, H-2, -3, -4, -5, -6$^{\mathrm{Cel}n}$, O$H^{\mathrm{Cel}n}$, −N(Ac)CH_2−), 2.54−2.45 (m, −CCH), 2.36−2.17 (m, −N(C=O)CH_3).

Synthesis of ethynyl-functionalized cellooligosaccharide acetate (AcCel$_n$−C≡CH)

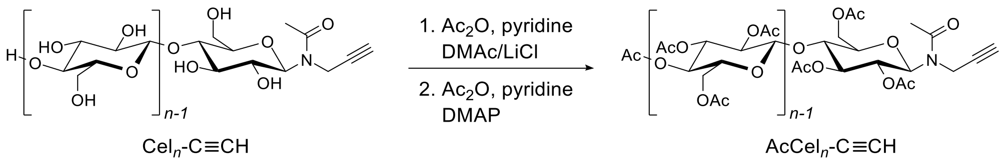

Wet Cel$_n$−C≡CH (4.58 g, by dry weight) was dispersed in acetone and centrifuged twice (13,000 rpm/20 min/0 °C, 14,000 rpm/20 min/0 °C). The pellet was dispersed in acetone (100 mL) and stirred over night at r.t. After the centrifugation (10,000 rpm/20 min/0 °C), the pellet was washed with DMAc (100 mL) followed by centrifugation (12,000 rpm/20 min/0 °C). The pellet was dispersed in DMAc (150 mL). After stirring for 3 h at r.t., the mixture was added LiCl (3.61 g, 85.2 mmol) and kept stirring overnight. After adding a solution of acetic anhydride in pyridine (1/1 (v/v), 30 mL), the mixture was stirred for 6 days at r.t. The reaction mixture was diluted with CH_2Cl_2 and washed with dilute HCl (100 mL) three times. The organic layer was dried over $MgSO_4$ and concentrated to give a white solid. The obtained solid (9.16 g) and DMAP (118.6 mg, 0.97 mmol) were then dissolved in a solution of acetic anhydride in pyridine (1/2 (v/v), 90 mL) and stirred at r.t. After stirring for 6 days, the reacting mixture was added another portion of DMAP (23.5 mg, 0.192 mmol) and acetic anhydride/pyridine (1/2 (v/v), 30 mL) and stirred for 1 day. After removing the solvent by evaporation, the residue was dissolved in ethyl acetate and washed with 1 M HCl (100 mL) and saturated $NaHCO_3$ (100 mL) solutions. The organic layer was dried over Na_2SO_4

and concentrated to give AcCel$_n$−C≡CH as an orange solid (4.12 g). Yield: 45.7 %.

$M_{\mathrm{n,NMR}}$ = 2,020 g mol^{-1}, $M_{\mathrm{n,MALDI}}$ = 2,340 g mol^{-1}, $M_{\mathrm{n,SEC}}$ = 2,420 g mol^{-1} (THF), $Đ$ = 1.07 (THF).

^{1}H NMR (400 MHz, DMSO-d_6): δ (ppm) 6.10 (d), 5.91−5.72 (m) (2x, rotamers, −CHN(Ac)−), 5.56−3.53 (m, H-1, -2, -3, -4, -5, -6$^{\mathrm{AcCel}n}$ of anhydro glucose repeating unit and non-reducing terminal end group, −N(Ac)CH_2−), 2.35−1.65 (m, −CCH), 2.47−1.76 (m, CH_3-Ac$^{\mathrm{AcCel}n}$, −N(C=O)CH_3).

Synthesis of monoazido-functionalized PCL (PCL–N_3)

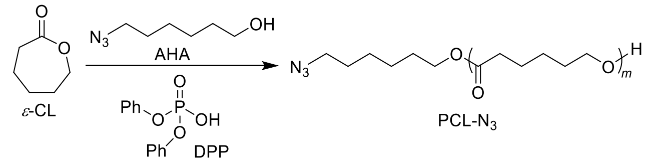

Synthesis of PCL$_{7k}$–N_3

Typical polymerization procedure is as follows (Method A). In an argon-filled glovebox, ε-CL (5.50 mL, 52.0 mmol), AHA (52.5 μL, 0.370 mmol), and DPP (4.7 mg, 0.019 mmol) were placed in a sealed reaction vessel. After the reaction vessel was taken out from the glovebox, the mixture was stirred at 80 °C under an argon atmosphere in an aluminum bath. After stirring for 23 h, the monomer conversion reached 42% as revealed by ^{1}H NMR analysis of the aliquot of the mixture. The polymerization mixture was poured into the cold MeOH/*n*-hexane (9/1 (v/v)), and the precipitated product was washed with MeOH several times to remove the unreacted monomer and catalyst. Finally, PCL$_{7k}$–N_3 was obtained as a white powder (2.15 g). Yield: 35.9%

$M_{n,NMR}$ = 7,110 g mol^{-1}, $M_{n,SEC}$ = 11,300 (THF), $Đ$ = 1.06 (THF).

^{1}H NMR (400 MHz, $CDCl_3$): δ (ppm) 4.06 (t, J = 6.6 Hz, $-C(=O)-(CH_2)_4-C\mathit{H}_2-O-$, $N_3-(CH_2)_5-C\mathit{H}_2-$), 3.65 (q, J = 5.5 Hz, $-C(=O)-(CH_2)_4-C\mathit{H}_2-OH$), 3.28 (t, J = 7.0 Hz, 2H, $N_3-C\mathit{H}_2-(CH_2)_5-O-$), 2.73−2.18 (m, $-C(=O)-C\mathit{H}_2-(CH_2)_4-O-$), 2.11−1.17 (m, 6 $N_3-CH_2-C\mathit{H}_2-C\mathit{H}_2-C\mathit{H}_2-C\mathit{H}_2-CH_2-O-$, $-C(=O)-CH_2-C\mathit{H}_2-C\mathit{H}_2-C\mathit{H}_2-CH_2-O-$).

Synthesis of PCL_{13k}–N_3

The method A was used for the polymerization of ε-CL (9.10 mL, 86.1 mmol) with AHA (73.8 µL, 0.521 mmol), and DPP (6.7 mg, 0.027 mmol) for 40 h to give PDL_{13k}–N_3 as a white powder (6.34 g). Yield: 64.0%

$M_{n,NMR}$ = 13,000 g mol^{-1}, $M_{n,SEC}$ = 22,400 g mol^{-1} (THF), $Đ$ = 1.05 (THF).

^{1}H NMR (400 MHz, $CDCl_3$): δ (ppm) 4.06 (t, J = 6.6 Hz, $-C(=O)-(CH_2)_4-CH_2-O-$, $N_3-(CH_2)_5-CH_2-$), 3.65 (q, J = 6.0 Hz, $-C(=O)-(CH_2)_4-CH_2-OH$), 3.27 (t, J = 6.6 Hz, $N_3-CH_2-(CH_2)_5-O-$), 2.70−2.20 (m, $-C(=O)-CH_2-(CH_2)_4-O-$), 1.99–1.11 (m, $N_3-CH_2-CH_2-CH_2-CH_2-CH_2-CH_2-O-$, $-C(=O)-CH_2-CH_2-CH_2-CH_2-CH_2-O-$).

Synthesis of dihydroxy-functionalized PCL (HO–PCL–OH)

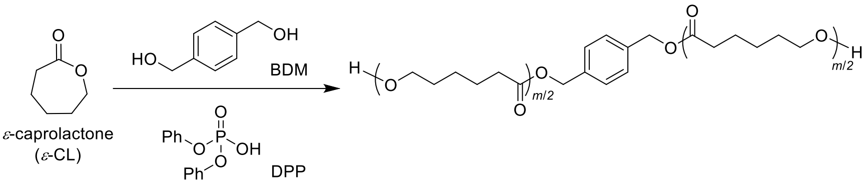

Synthesis of HO–PCL$_{14k}$–OH

The method A was used for the polymerization of ε-CL (9.26 mL, 87.6 mmol) with BDM (96.8 mg, 0.701 mmol), and DPP (8.8 mg, 0.35 mmol) for 24 h to give HO–PCL$_{14k}$–OH as a white powder (8.47 g). Yield: 83.9%

$M_{n,NMR}$ = 13,600 g mol^{-1}, $M_{n,SEC}$ = 22,600 g mol^{-1} (THF), $Đ$ = 1.05 (THF).

^{1}H NMR (400 MHz, CDCl$_3$): δ (ppm) 7.35 (s, *aromatic* C$_2$-*H*, C$_3$-*H*, C$_5$-*H*, C$_6$-*H*), 5.11 (s, −C*H*$_2$−Ph−C*H*$_2$−), 4.21−3.90 (m, −C(=O)−(CH$_2$)$_4$−C*H*$_2$−O−), 3.65 (t, *J* = 6.6 Hz, −C(=O)−(CH$_2$)$_4$−C*H*$_2$−OH), 2.40−2.24 (m, −C(=O)−C*H*$_2$−(CH$_2$)$_4$−O−), 1.99–1.17 (m, −C(=O)−CH$_2$−C*H*$_2$−C*H*$_2$−C*H*$_2$−CH$_2$−O−).

Synthesis of HO–PCL$_{15k}$–OH

The method A was used for the polymerization of ε-CL (6.51 mL, 61.6 mmol) with BDM (51.4 mg, 0.372 mmol), and DPP (4.7 mg, 0.019 mmol) for 36 h to give HO–PCL$_{15k}$–OH as a white powder (4.12 g). Yield: 58.2%

$M_{\mathrm{n,NMR}}$ = 15,400 g mol^{-1}, $M_{\mathrm{n,SEC}}$ = 24,600 g mol^{-1} (THF), $Đ$ = 1.06 (THF).

^{1}H NMR (400 MHz, $CDCl_3$): δ (ppm) 7.35 (s, *aromatic* C_2-*H*, C_3-*H*, C_5-*H*, C_6-*H*), 5.11 (s, $-CH_2-Ph-CH_2-$), 4.19−3.92 (m, $-C(=O)-(CH_2)_4-CH_2-O-$), 3.64 (q, J = 8.4 Hz, $-C(=O)-(CH_2)_4-CH_2-OH$), 2.44−2.20 (m, $-C(=O)-CH_2-(CH_2)_4-O-$), 1.98–1.15 (m, $-C(=O)-CH_2-CH_2-CH_2-CH_2-CH_2-O-$).

Synthesis of diazido-functionalized PCL (N_3–PCL–N_3)

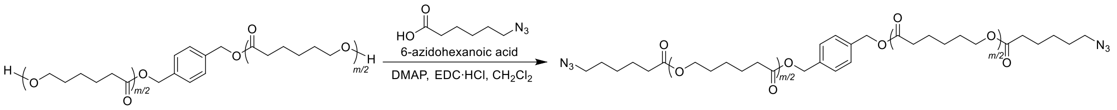

Synthesis of N_3*–PCL*$_{15k}$*–*N_3

A typical end azido-functionalization procedure is as follows (Method B). Prior to the reaction, a trace amount of MeOH in the HO–PCL$_{14k}$–OH was removed completely by co-evaporation with dry toluene. HO–PCL$_{14k}$–OH (3.54 g, 0.260 mmol), 6-azidohexanoic acid (0.294 g, 1.87 mmol), EDC·HCl (0.355 g, 1.85 mmol), DMAP (0.166 g, 1.36 mmol), and dry CH_2Cl_2 (20 mL) were placed in a round-bottom flask. After stirring for 2 days at r.t., the mixture was poured into cold MeOH, and the precipitated product was washed with MeOH several times. Finally, N_3–PCL$_{15k}$–N_3 was obtained as a white powder (3.43 g). Yield: 90.2%

$M_{n,NMR}$ = 14,600 g mol^{-1}, $M_{n,SEC}$ = 23,500 g mol^{-1} (THF), $Đ$ = 1.05 (THF).

^{1}H NMR (400 MHz, $CDCl_3$): δ (ppm) 7.35 (s, *aromatic* C_2-*H*, C_3-*H*, C_5-*H*, C_6-*H*), 5.10 (s, $-CH_2-Ph-CH_2-$), 4.17−3.90 (m, $-C(=O)-(CH_2)_4-CH_2-O-$), 3.28 (t, J = 7.0 Hz, $-C(=O)-(CH_2)_4-CH_2-N_3$), 2.45–2.19 (m, $-C(=O)-CH_2-(CH_2)_4-O-$, $-C(=O)-CH_2-CH_2-CH_2-CH_2-CH_2-N_3$), 1.87–1.10 (m, $-C(=O)-CH_2-CH_2-CH_2-CH_2-CH_2-O-$, $-C(=O)-CH_2-CH_2-CH_2-CH_2-CH_2-N_3$).

Synthesis of tetraazido-functionalized PCL ((N3)2–PCL–(N3)2)

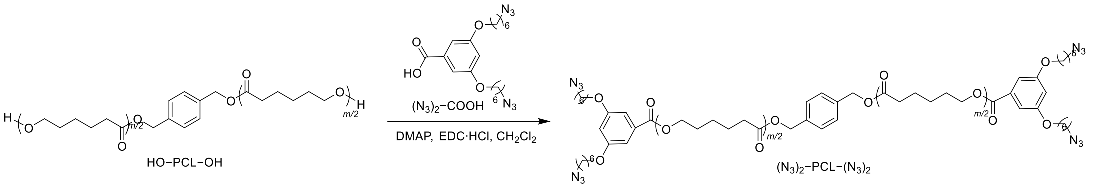

Synthesis of (N3)2–PCL16k–(N3)2

The method B was used for the reaction of HO–PCL$_{15k}$–OH (1.96 g, 0.127 mmol) with 3,5-bis((6-azidohexyl)oxy)benzoic acid (0.362 g, 0.895 mmol) in the presence of EDC·HCl (0.176 g, 0.918 mmol) and DMAP (0.078 g, 0.064 mmol) in dry CH_2Cl_2 (15 mL) to give $(N_3)_2$–PCL$_{16k}$–$(N_3)_2$ as a white powder (1.98 g). Yield: 95.8%

$M_{n,NMR}$ = 16,300 g mol^{-1}, $M_{n,SEC}$ = 24,800 g mol^{-1} (THF), $Đ$ = 1.06 (THF).

See **Figure 5.8** for ^{1}H NMR spectrum.

Synthesis of AcCel$_n$-*b*-PCL

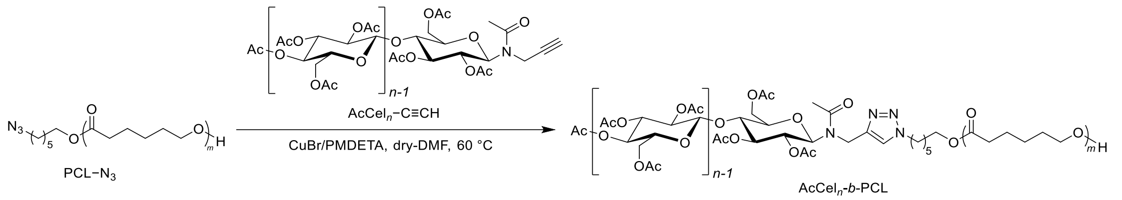

Synthesis of AcCel$_n$-b-PCL$_{7k}$

A typical click reaction procedure is as follows (Method C). A degassed solution of PMDETA (67.7 μL, 0.324 mmol) in DMF (20 mL) was transferred to a Schlenk tube in which PCL$_{7k}$–N$_3$ ($M_{n,NMR}$ = 7,110 g mol^{-1}, 2.01 g, 0.283 mmol), AcCel$_n$–C≡CH (823 mg, 0.352 mmol), and CuBr (47.3 mg, 0.330 mmol) were placed. The whole mixture was stirred for 28 h at 60 °C under an argon atmosphere. After cooling to room temperature, the mixture was passed through a short pad of aluminum oxide and eluted with THF to remove Cu catalyst, and the crude product was reprecipitated in MeOH to remove the residual PMDETA. Finally, the crude product was purified by the preparative SEC in CHCl$_3$ to remove unreacted AcCel$_n$–C≡CH to give AcCel$_n$-*b*-PCL$_{7k}$ as a brown solid (2.03 g). Yield: 74.0%

M_n = 9,450 g mol^{-1}, $M_{n,SEC}$ = 15,700 g mol^{-1} (THF), $Đ$ = 1.03 (THF).

See **Figure 5.11** for ^{1}H NMR spectrum.

Synthesis of AcCel$_n$-b-PCL$_{13k}$

The method C was used for the click reaction of PCL$_{13k}$–N$_3$ ($M_{n,NMR}$ = 13,000 g mol^{-1}, 2.50 g, 0.192 mmol) and AcCel$_n$–C≡CH (504 mg, 0.216 mmol) in DMF (20 mL) with CuBr (29.4 mg, 0.205 mmol) and PMDETA (41.5 µL, 199 µmol) to give AcCel$_n$-*b*-PCL$_{13k}$ as a brown solid (2.14 g). Yield: 72.3%

M_n = 15,300 g mol^{-1}, $M_{n,SEC}$ = 24,200 g mol^{-1} (THF), $Đ$ = 1.03 (THF).

See **Figure 5.12** for ^{1}H NMR spectrum.

Synthesis of AcCel$_n$-*b*-PCL-*b*-AcCel$_n$

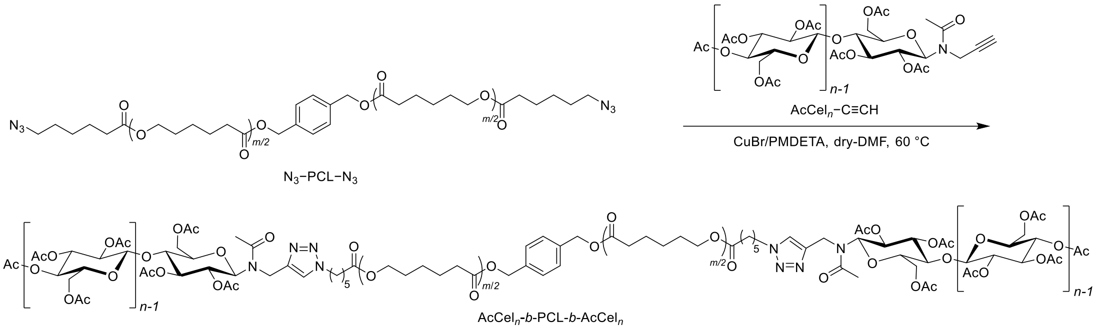

Synthesis of AcCel$_n$-b-PCL$_{15k}$-b-AcCel$_n$

The method C was used for the click reaction of N$_3$–PCL$_{15k}$–N$_3$ ($M_{n,NMR}$ = 14,600 g mol^{-1}, 1.50 g, 0.103 mmol) and AcCel$_n$–C≡CH (641 mg, 0.274 mmol) in DMF (20 mL) with CuBr (36.0 mg, 0.251 mmol) and PMDETA (50.0 µL, 239 µmol) to give AcCel$_n$-*b*-PCL$_{15k}$-*b*-AcCel$_n$ as a brown solid (1.40 g). Yield: 72.1%

$M_{n,\text{total}}$ = 19,300 g mol^{-1}, $M_{n,SEC}$ = 27,300 g mol^{-1} (THF), $Đ$ = 1.04 (THF).

See **Figure 5.10** for ^{1}H NMR spectrum.

Synthesis of (AcCel$_n$)$_2$-*b*-PCL-*b*-(AcCel$_n$)$_2$

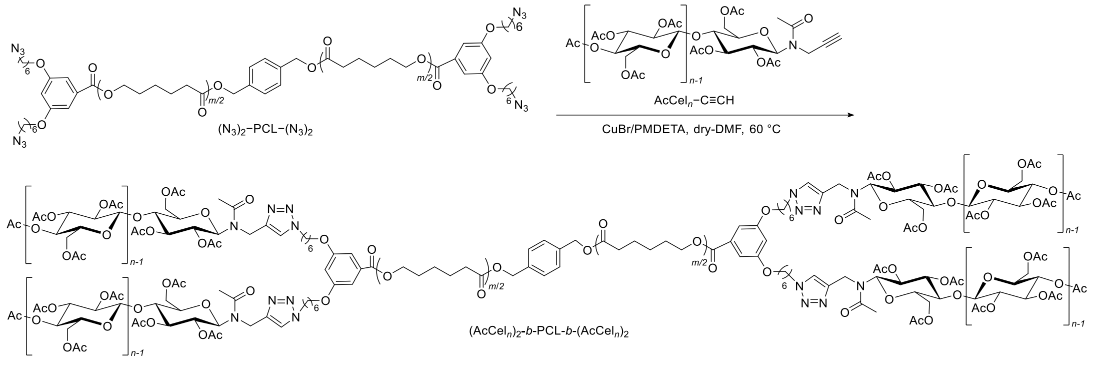

Synthesis of (AcCel$_n$)$_2$-b-PCL$_{16k}$-b-(AcCel$_n$)$_2$

The method C was used for the click reaction of (N$_3$)$_2$–PCL$_{16k}$–(N$_3$)$_2$ ($M_{\text{n,NMR}}$ = 16,300 g mol^{-1}, 1.50 g, 0.110 mmol) and AcCel$_n$–C≡CH (1.16 g, 0.496 mmol) in DMF (20 mL) with CuBr (63.6 mg, 0.443 mmol) and PMDETA (94.4 µL, 452 µmol) to give AcCel$_n$-*b*-PCL$_{13k}$ as a brown solid (1.21 g). Yield: 51.2%

$M_{\text{n,total}}$ = 25,700 g mol^{-1}, $M_{\text{n,SEC}}$ = 28,300 g mol^{-1} (THF), $Đ$ = 1.06 (THF).

See **Figure 5.13** for ^{1}H NMR spectrum.

5.3. Results and Discussion

5.3.1. Synthesis of propargyl-functionalized cellooligosaccharide triacetate

The author first synthesized propargyl-functionalized cellooligosaccharide (Cel$_n$–C≡CH), a precursor of the cellooligosaccharide triacetate, through the enzymatic polymerization. In the Chapter 4, the author has demonstrated the preparation of Cel$_n$–C≡CH mainly consisted of 6–8-mers through oligomerization of α-D-glucose-1-phophate (αG1P) in the presence of *N*-acetyl-propargyl D-(+)-cellobiose as a primer using cellodextrin phosphorylase (CDP) and sucrose phosphorylase (SP) in high product yield. The author synthesized Cel$_n$–C≡CH according to this method again. The characterization data of the obtained Cel$_n$–C≡CH is shown in **Figure 5.1**. The signals in the ^{1}H NMR spectrum are justifiably assigned to the expected structure and gives the number-averaged degree of polymerization (DP) was calculated to be 6.95 that corresponds to a number-averaged molecular weight ($M_{\mathrm{n,NMR}}$) of 1,220. The matrix-assisted laser desorption/ionization time-of-flight mass (MALDI-TOF MS) spectrum shows two series of repeating peaks separated by 162 Da in 900–1,500 Da range; the major series of peaks are consistent with the Na adducts and the minor series of peaks are consistent with the K adducts of Cel$_n$–C≡CH comprised 6- to 8-mers. The number-averaged molecular weight based on the MALDI-TOF MS analysis ($M_{\mathrm{n,MALDI}}$) was estimated to be 1,190, which is close to the $M_{\mathrm{n,NMR}}$ value.

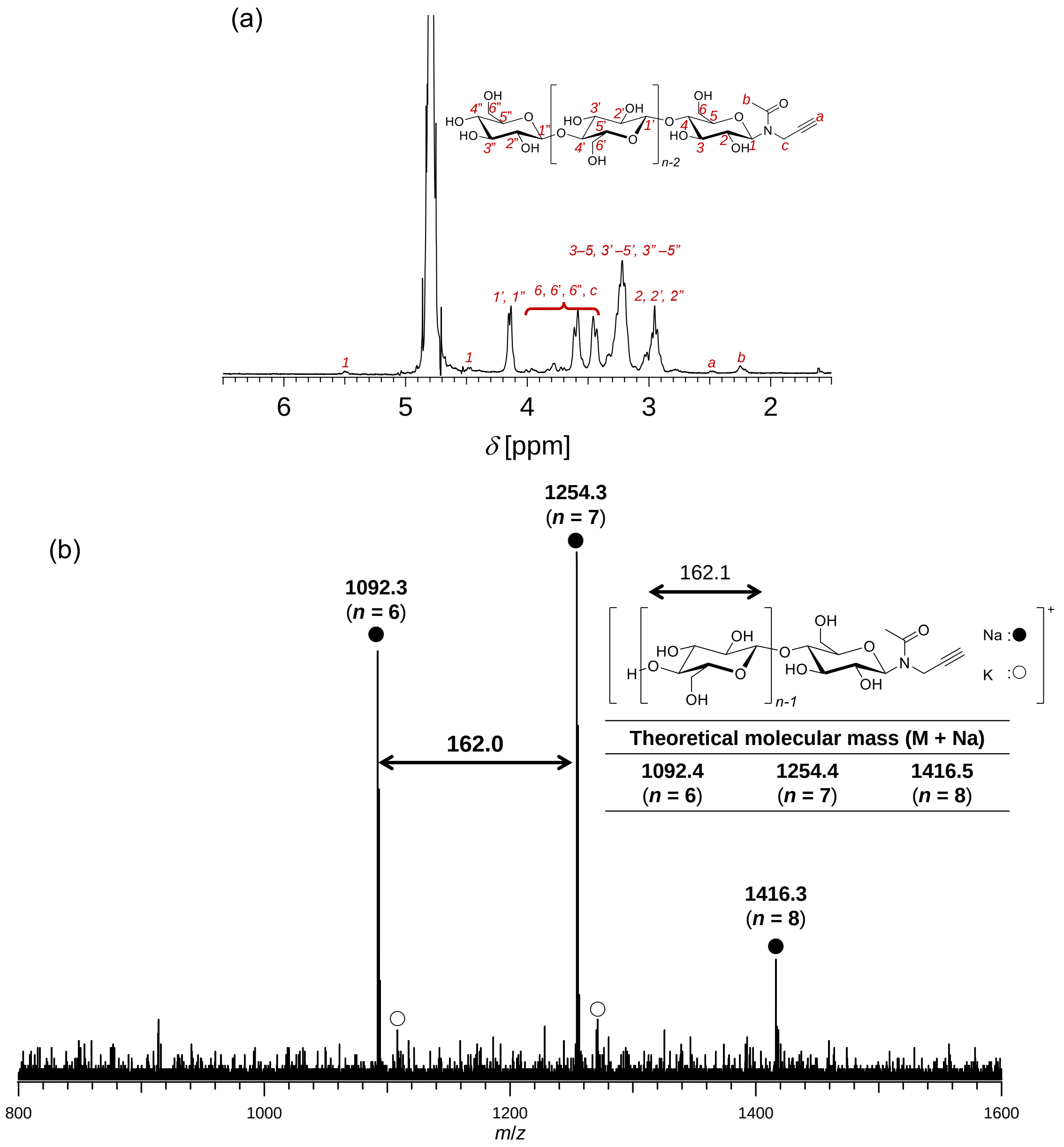

Figure 5.1. (a) ^{1}H NMR spectrum in D_2O containing sodium trimethylsilylpropanesulfonate (DSS) and 10% (w/w) NaOD and (b) MALDI-TOF MS spectrum and theoretical molecular mass of Cel$_n$–C≡CH.

Next, the obtained Cel$_n$–C≡CH was completely acetylated following the procedure reported previously in the Chapters 3 and 4. The complete acetylation was confirmed by ^{1}H NMR, FT-IR, and MLADI-TOF MS analyses. The obtained AcCel$_n$–C≡CH showed a monomodal elution peak with a narrow dispersity (*Đ* = 1.07) in the size exclusion chromatography (SEC) trace, and the $M_{\mathrm{n,NMR}}$ and $M_{\mathrm{n,MALDI}}$ values were calculated to be 2,020 and 2,340, respectively (See **Figure 5.2** for other characterization data).

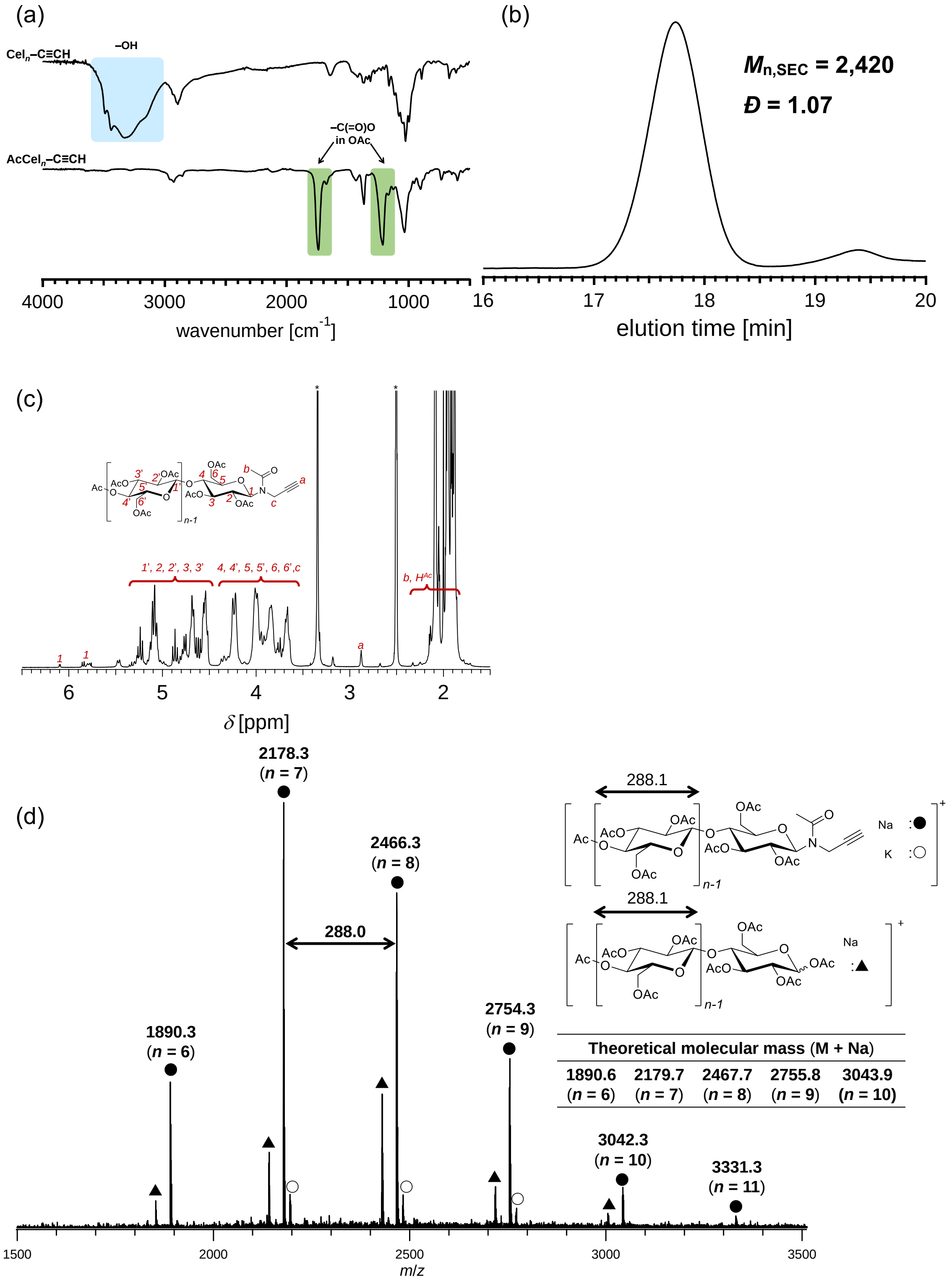

Theoretical molecular mass (M + Na)				
1890.6 (n = 6)	2179.7 (n = 7)	2467.7 (n = 8)	2755.8 (n = 9)	3043.9 (n = 10)

Figure 5.2. (a) FT-IR spectra of Cel$_n$–C≡CH (upper) and AcCel$_n$–C≡CH (lower), (b) SEC trace of AcCel$_n$–C≡CH (eluent, THF; flow rate, 1.0 mL min^{-1}), (c) ^{1}H NMR spectrum of AcCel$_n$–C≡CH in DMSO-d_6 (400 MHz), and (c) MALDI-TOF MS spectrum and theoretical molecular mass of AcCel$_n$–C≡CH.

5.3.2. BCP synthesis

The BCPs consisting of AcCel$_n$ and PCL were synthesized by copper-catalyzed azido-alkyne cycloaddition (CuAAC) reaction of AcCel$_n$–C≡CH and azido-functionalized PCL. To prepare the azido-functionalized PCLs, the diphenyl phosphate (DPP)-catalyzed ROP of *ε*-caprolactone (*ε*-CL) was performed at 80 °C using the appropriate initiators following the previous report.[25] As an example, *α*-azido-functionalized PCL (PCL$_{7k}$–N$_3$; the subscript means the molecular weight) was prepared via DPP-catalyzed ROP using 6-azido-1-hexanol (N$_3$–OH) as the initiator. The polymerization was carried out at the $[\varepsilon\text{-CL}]_0/[\text{N}_3\text{–OH}]_0/[\text{DPP}]_0$ ratio of 142/1/0.05 for 23 h in the bulk, and N$_3$–PCL$_{7k}$ ($M_{\text{n,NMR}}$ = 7,110; $Đ$ = 1.06) was obtained in 35.9% yield (**Figure 5.3**). Similarly, PCL$_{13k}$–N$_3$ ($M_{\text{n,NMR}}$ = 13,000; $Đ$ = 1.06; 64.0% yield) was also synthesized with the $[\varepsilon\text{-CL}]_0/[\text{N}_3\text{–OH}]_0/[\text{DPP}]_0$ ratio of 165/1/0.05 (**Figure 5.4**).

The *α,ω*-diazido-functionalized PCL (N$_3$–PCL$_{15k}$–N$_3$) and *α,α,ω,ω*-tetraazido-functionalized PCL ((N$_3$)$_2$–PCL$_{17k}$–(N$_3$)$_2$) were prepared by condensation reaction of *α,ω*-diol-functionalized PCL (HO–PCL–OH), which had been synthesized by DPP-catalyzed ROP using 1,4-benzenedimethanol as an initiator (SEC traces are shown in **Figures 5.5** and **5.6**), with 6-azidohexanoic acid (N$_3$–COOH) and 3,5-bis(6-azidohexyloxy)benzoic acid ((N$_3$)$_2$–COOH), respectively. The ^{1}H NMR and FT-IR analyses revealed the successful synthesis of N$_3$–PCL$_{15k}$–N$_3$ and (N$_3$)$_2$–PCL$_{17k}$–(N$_3$)$_2$, and the SEC analysis confirmed the narrow *Đ* of 1.05–1.06. The $M_{\mathrm{n,NMR}}$ values were determined to be 14,600 and 16,700 for $\mathrm{N_3}$–PCL$_{15\mathrm{k}}$–$\mathrm{N_3}$ and $\mathrm{(N_3)_2}$–PCL$_{17\mathrm{k}}$–$\mathrm{(N_3)_2}$, respectively (**Figures 5.7–5.9**).

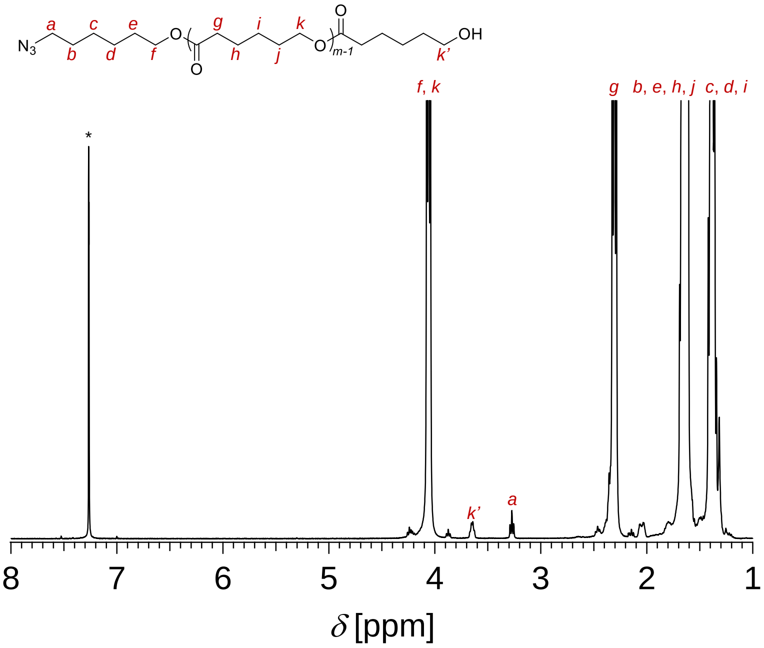

Figure 5.3. ^{1}H NMR spectrum of PCL$_{7\mathrm{k}}$–$\mathrm{N_3}$ in $\mathrm{CDCl_3}$ (400 MHz). The asterisk denotes the solvent peak.

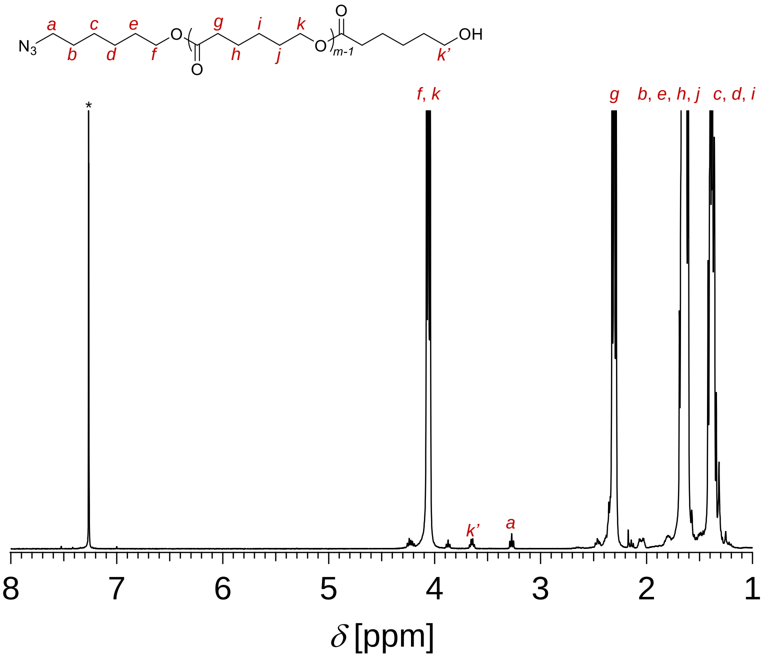

Figure 5.4. ^{1}H NMR spectrum of PCL$_{13k}$–N$_3$ in CDCl$_3$ (400 MHz). The asterisk denotes the solvent peak.

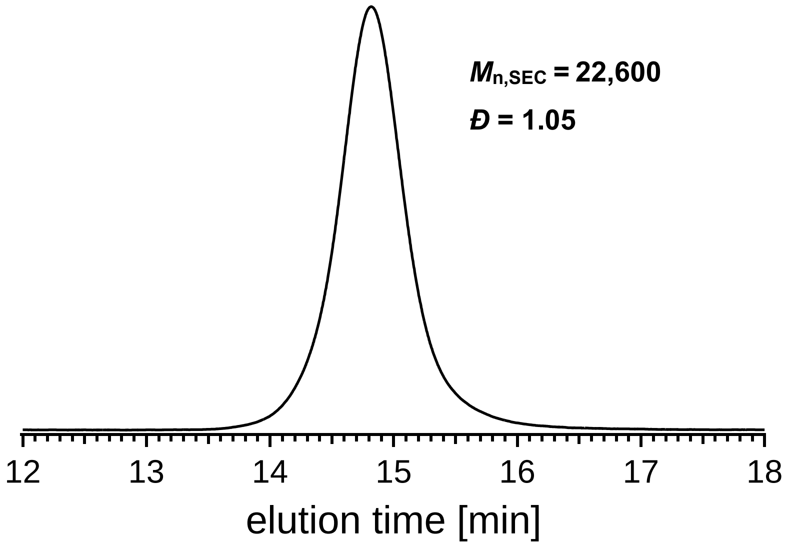

Figure 5.5. SEC trace of HO–PCL$_{14k}$–OH (eluent, THF; flow rate, 1.0 mL min^{-1}).

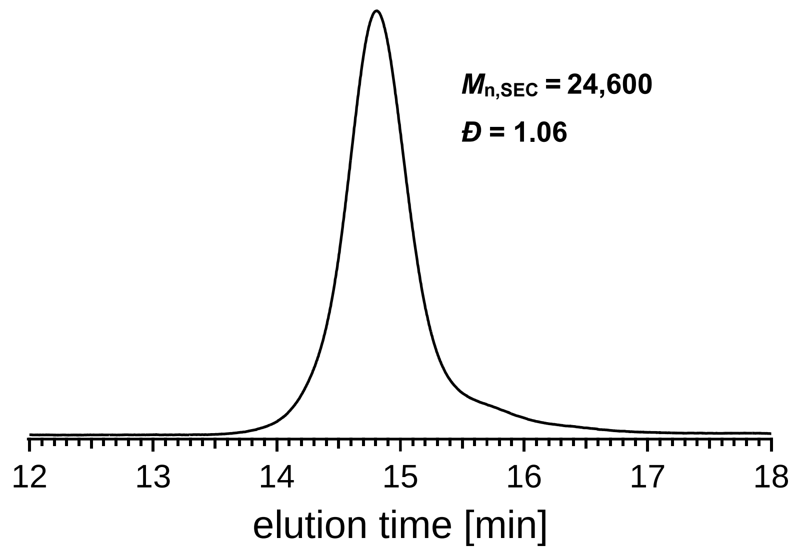

Figure 5.6. SEC trace of HO–PCL$_{15k}$–OH (eluent, THF; flow rate, 1.0 mL min^{-1}).

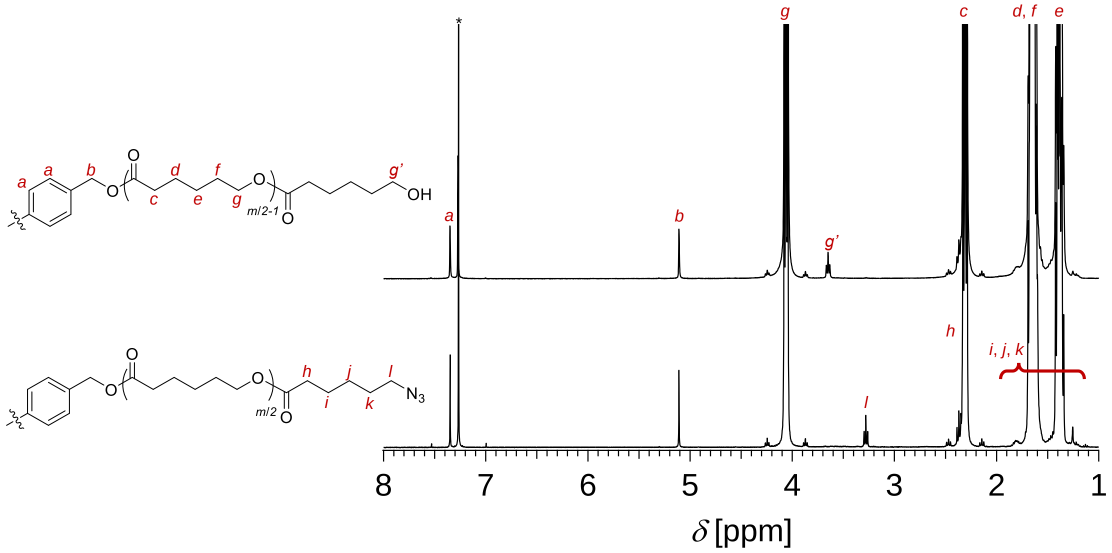

Figure 5.7. ^{1}H NMR spectrum of HO–PCL$_{14k}$–OH (upper) and N$_3$–PCL$_{15k}$–N$_3$ (lower) in CDCl$_3$ (400 MHz). The asterisk denotes the solvent peak.

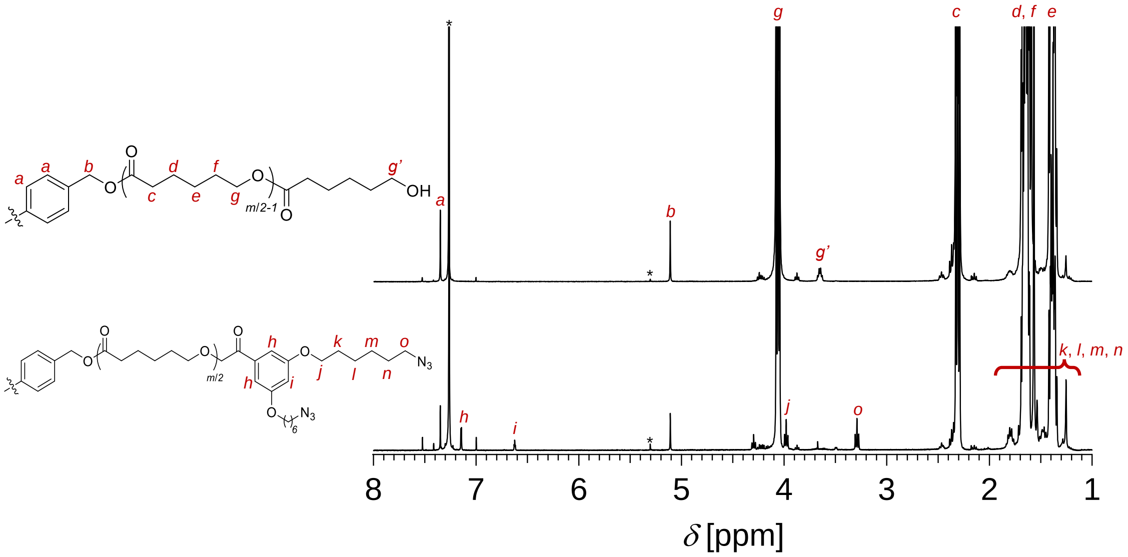

Figure 5.8. ^{1}H NMR spectrum of HO–PCL$_{15k}$–OH (upper) and (N$_3$)$_2$–PCL$_{16k}$–(N$_3$)$_2$ (lower) in CDCl$_3$ (400 MHz). The asterisk denotes the solvent peak.

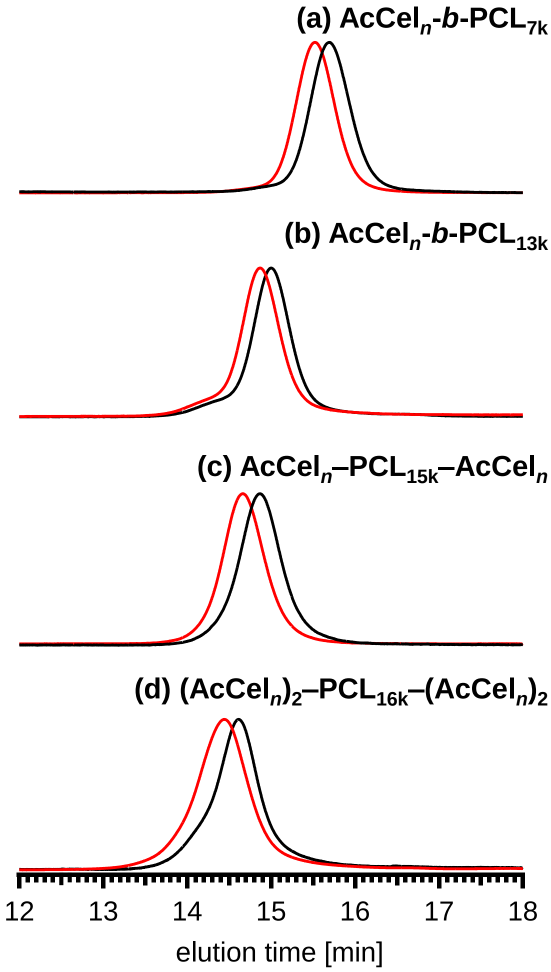

Figure 5.9. SEC traces of (a) AcCel$_n$-*b*-PCL$_{7k}$, (b) AcCel$_n$-*b*-PCL$_{13k}$, (c) AcCel$_n$-*b*-PCL$_{15k}$-*b*-AcCel$_n$, and (d) (AcCel$_n$)$_2$-*b*-PCL$_{16k}$-*b*-(AcCel$_n$)$_2$ (eluent, THF; flow rate, 1.0 mL min^{-1}). The red and black line represent the BCPs and their corresponding azido-functionalized PCL precursors, respectively.

The obtained azido-functionalized PCLs were applied to the CuAAC reaction with AcCel$_n$–C≡CH to give the desired BCPs. The CuAAC reaction of N$_3$–PCL$_{15k}$–N$_3$ and AcCel$_n$–C≡CH was performed in *N*,*N*-dimethylformamide (DMF) at 60 °C in the presence of CuBr/PMDETA as the catalyst system with a slight excess of AcCel$_n$–C≡CH with respect to the azido group. The crude product was purified by filtering over a pad of aluminum oxide and reprecipitation to remove the Cu catalyst and PMDETA ligand, respectively. Finally, the unreacted AcCel$_n$–C≡CH was removed using preparative SEC in $CHCl_3$ and the product was obtained in 72.1% yield. The ^{1}H NMR spectrum of the product was reasonably assigned to the expected structure of the BCP (**Figure 5.10** (a)). The SEC elusion peak of the synthesized product was monomodal and observed at the higher molecular weight region than that of N_3–PCL$_{15k}$–N_3 (**Figure 5.9**). The Fourier transformed infrared (FT-IR) spectral analysis revealed the disappearance of the absorption band at ca. 2,100 cm^{-1} corresponding to the azido group upon the reaction. (**Figure 5.10** (b)) These results suggested the CuAAC reaction of N_3–PCL$_{15k}$–N_3 and AcCel$_n$–C≡CH was completely proceeded to give the ABA-type BCP, i.e., AcCel$_n$-*b*-PCL$_{15k}$-*b*-AcCel$_n$. In a similar manner, the author has successfully synthesized the other three BCPs, i.e., AcCel$_n$-*b*-PCL$_{7k}$, AcCel$_n$-*b*-PCL$_{13k}$, and (AcCel$_n$)$_2$-*b*-PCL$_{17k}$-*b*-(AcCel$_n$)$_2$, from N_3–PCL$_{7k}$, N_3–PCL$_{13k}$, and $(N_3)_2$-*b*-PCL$_{17k}$-*b*-$(N_3)_2$, respectively in 43–80% yields (**Figures 5.9** and **5.11–5.13**). The detail characterization data, such as the molecular weight of BCPs ($M_{n,total}$), PCL ($M_{n,PCL}$), and the volume fraction of the AcCel$_n$ segments (f_{AcCeln}), are summarized in **Table 5.1**.

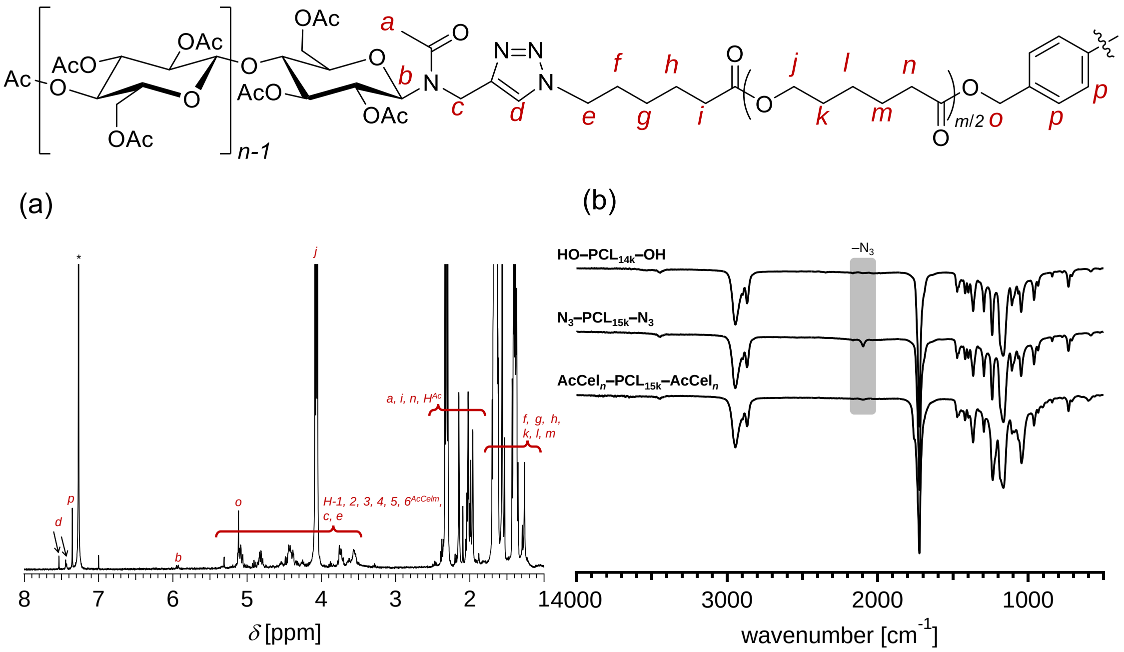

Figure 5.10. (a) ^{1}H NMR spectrum of AcCel$_n$-*b*-PCL$_{15k}$-*b*-AcCel$_n$ in CDCl$_3$ (400 MHz). The asterisk denotes the solvent peak, (b) FT-IR spectra HO–PCL$_{14k}$–OH (upper), N$_3$–PCL$_{15k}$–N$_3$ (middle), and AcCel$_n$-*b*-PCL$_{15k}$-*b*-AcCel$_n$ (lower).

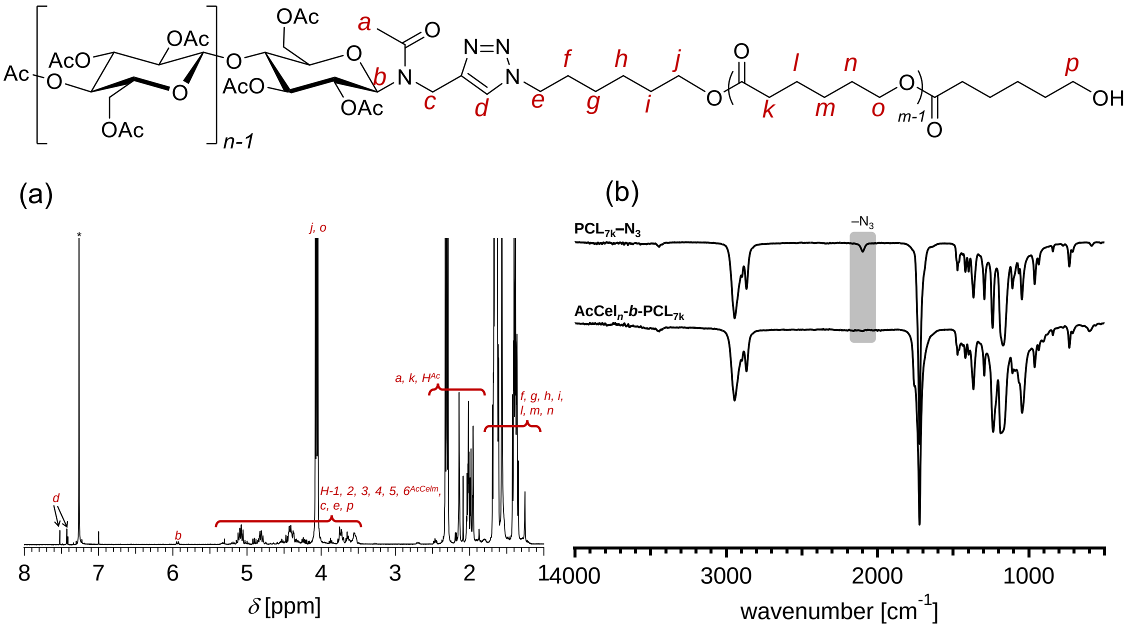

Figure 5.11. (a) ^{1}H NMR spectrum of AcCel$_n$-*b*-PCL$_{7k}$ in CDCl$_3$ (400 MHz). The asterisk denotes the solvent peak, (b) FT-IR spectra PCL$_{7k}$–N$_3$ (upper) and AcCel$_n$-*b*-PCL$_{7k}$ (lower).

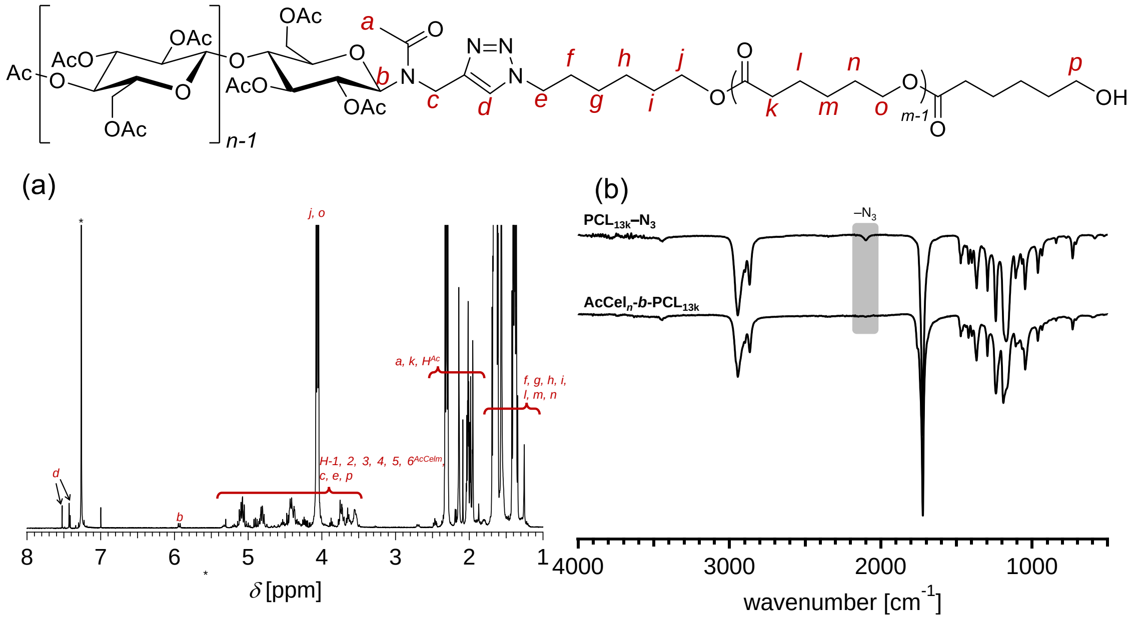

Figure 5.12. (a) ^{1}H NMR spectrum of AcCel$_n$-b-PCL$_{13k}$ in CDCl$_3$ (400 MHz). The asterisk denotes the solvent peak, (b) FT-IR spectra PCL$_{13k}$–N$_3$ (upper) and AcCel$_n$-b-PCL$_{13k}$ (lower).

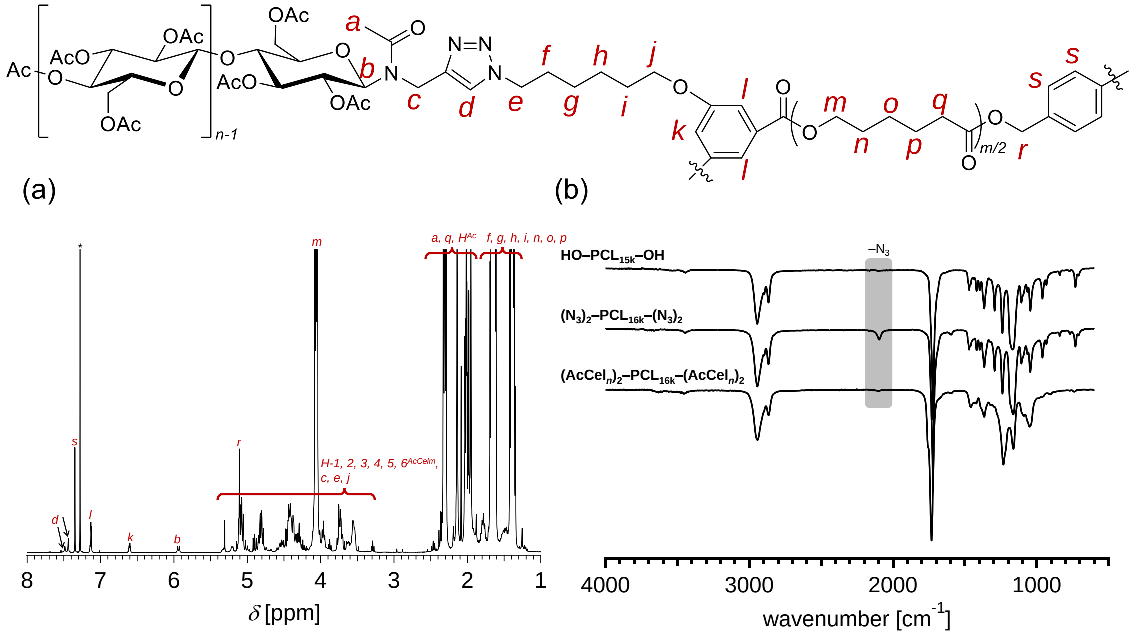

Figure 5.13. (a) ^{1}H NMR spectrum of AcCel$_n$-b-PCL$_{16k}$-b-AcCel$_n$ in CDCl$_3$ (400 MHz). The asterisk denotes the solvent peak, (b) FT-IR spectra HO–PCL$_{14k}$–OH (upper), (N$_3$)$_2$–PCL$_{16k}$–(N$_3$)$_2$ (middle), and (AcCel$_n$)$_2$-b-PCL$_{16k}$-b-(AcCel$_n$)$_2$ (lower).

Table 5.1. Molecular characteristics of the synthesized BCPs composed of AcCel$_n$ and PCL segments

BCP	$M_{\text{n,total}}{}^{a}$	$M_{\text{n,PCL}}{}^{b}$	$f_{\text{AcCeln}}{}^{c}$	$M_{\text{n,SEC}}{}^{d}$	$Đ^{d}$
AcCel$_n$-*b*-PCL$_{7\text{k}}$	9,700	7,110	0.23	15,700	1.03
AcCel$_n$-*b*-PCL$_{13\text{k}}$	15,400	13,000	0.14	24,200	1.03
AcCel$_n$-*b*-PCL$_{15\text{k}}$-*b*-AcCel$_n$	18,900	14,600	0.22	27,300	1.04
(AcCel$_n$)$_2$-*b*-PCL$_{16\text{k}}$-*b*-(AcCel$_n$)$_2$	25,700	16,300	0.34	28,300	1.06

^{a}Calculated from the molecular weight of AcCel$_n$–C≡CH determined by MALDI TOF MS spectrum and and $M_{\text{n,PCL}}$. ^{b}Determined by ^{1}H NMR spectroscopy in $CDCl_3$. ^{c}Calculated using the density of each block: 1.29 g cm^{-3} for AcCel$_n$–C≡CH and 1.15 g cm^{-3} for PCL. ^{d}Determined by SEC in THF using polystyrene standards.

5.3.3. Investigation of physical properties of CTA/PCL/BCP-blend film

The author conducted tensile tests of the films blended with CTA (M_{n} = 130,000), PCL (M_{n} = 80,000), and BCPs (CTA/PCL/BCP) and CTA and PCL (CTA/PCL) to investigate whether the synthesized BCPs functionalized as compatibilizers. The solvent-cast films from $CHCl_3$ were heat-pressed at 3 MPa and 200 °C for 3 min and aged for 3 days at room temperature before cutting into the dog-bone-shaped specimens for the tensile test. Here, each film was named as follows: BCP-free for the binary CTA/PCL blend film; AB$_{7\text{k}}$-blend, AB$_{13\text{k}}$-blend, AB$_{15\text{k}}$A-blend, and A$_2$B$_{16\text{k}}$A$_2$-blend for CTA/PCL/AcCel$_n$-*b*-PCL$_{7\text{k}}$, AcCel$_n$-*b*-PCL$_{13\text{k}}$, AcCel$_n$-*b*-PCL$_{15\text{k}}$-*b*-AcCel$_n$, and (AcCel$_n$)$_2$-*b*-PCL$_{16\text{k}}$-*b*-(AcCel$_n$)$_2$, respectively.

The stress-strain curves and mechanical properties (Young's modulus (E), strain at break (ε_{b}), stress at break (σ_{b}), and toughness) of the CTA/PCL/BCP-blend films, BCP-free, neat-PCL and -CTA films are summarized in **Figures 5.14** and **5.15** and **Table 5.2** and **5.3**) respectively. As a result of the tensile test, the neat-CTA film was fractured when only 2.2% strain was applied, demonstrating highly brittle nature. Compared to the neat-CTA (ε_b: 12.2 MPa and σ_b: 2.2%), the ε_b and σ_b of the BCP-free film, the binary blend film of CTA and PCL, are slightly increased (ε_b: 26.9 MPa and σ_b: 3.8 %). However, importantly, the σ_bs of AB_{7k}- (4.6%), AB_{13k}- (4.8%), $AB_{15k}A$- (8.2%), and $A_2B_{16k}A_2$-blend (8.8%) are more improved compared to the BCP-free film. Also, the ε_b values of AB_{7k}- (40.3 MPa), AB_{13k}- (44.2 MPa), $AB_{15k}A$- (44.3 MPa), and $A_2B_{16k}A_2$-blend (43.5 MPa) are larger than that of BCP-free film. That is why the toughness of the BCP-blend films are much higher than that of BCP-free film. In particular, the toughness of $A_2B_{16k}A_2$-blend (2.67 MPa) is 4.0 times larger than that of BCP-free (0.67 MPa). These results strongly implied that all the synthesized BCPs functionalized as compatibilizers and toughened CTA effectively. Notably, each E of the BCP-blend films (ca. 1.2–1.4 MPa) is slightly higher than that of BCP-free (ca. 1.1 MPa). This is attributed to the increase of crystallinity resulting from co-crystallization of BCP and homopolymer.[20] Indeed, differential scanning calorimetry (DSC) measurement revealed that each enthalpies of fusion corresponding to PCL segment (ΔH_{PCL}) and CTA matrix (ΔH_{CTA}) in the BCP-blend films were higher compared with those in the BCP-free film (**Figure 5.16** and **Table 5.4**). The calculated crystallinity of CTA matrix (X_{CTA}) and PCL (X_{PCL}) domain in the BCP-blended films are also ca. 1.1–1.3 and 1.6–2.0 times larger than those of the

BCP-free film.

Interestingly, the stress-strain curves of $AB_{15k}A$- and $A_2B_{16k}A_2$-blend films exhibited a similar behavior and the mechanical properties of $AB_{15k}A$- and $A_2B_{16k}A_2$-blend films are remarkably improved. This is due to the polymer structure of the added BCPs, i.e., $AcCel_n$-*b*-PCL_{15k}-*b*-$AcCel_n$ and $(AcCel_n)_2$-*b*-PCL_{16k}-*b*-$(AcCel_n)_2$, which were added to the $AB_{15k}A$- and $A_2B_{16k}A_2$-film, respectively. The PCL middle segments were assumed to form the loop structure in the PCL domain, which enhanced the entanglement with PCL chain. As a result, these BCPs exist stably at the CTA/PCL-interfaces. improving the ε_b. A similar result was reported in previous study, where the PCL/poly(3-hydroxybutyrate-*co*-3-hydroxyhexanoate) films blended with ABA- and A_2BA_2-type BCPs as compatibilizers showed superior ε_b to that with AB-type compatibilizers.[25] Therefore, the A_nBA_n-type, i.e., triblock architecture is suitable for the design of compatibilizer regardless of the kind of polymer.

Next, to investigate the effect of the synthesized BCPs on blend morphology, atomic force microscopy (AFM) observation was performed. The samples for AFM observation were prepared by spin-coating 0.5 wt% $CHCl_3$ solution of CTA/PCL/BCP (67/23/10 wt%) and CTA/PCL (75/25 wt%) onto Si substrate at 3,000 rpm for 60 s followed by annealed at 200 °C for 30 min. Each sample for AFM observation was named in the same way as the sample for tensile test. The phase images of the samples are shown in **Figure 5.17** where white area is corresponding to PCL domain. The average radius of PCL domain (R_{PCL}) of BCP-free, AB_{7k}-, AB_{13k}-, $AB_{15k}A$-, and $A_2B_{16k}A_2$-blend was 37.1 ± 0.8, 33.2 ± 1.6, 36.1 ± 0.7, 36.8 ± 0.9 and 36.3 ± 0.4 nm, respectively. This result indicates that the synthesized BCPs did not contribute to induce the dispersion of PCL domain. Therefore, the improving of the mechanical properties of the CTA/PCL/BCP-blend films attributed to enhance adhesion of the interface between CTA/PCL. The AFM observation results also supported the usefulness of the synthesized BCP as compatibilizers.

Table 5.2. Mechanical properties of the CTA/PCL/BCP blended films[a]

Film[b]	E / GPa	ε_b / %	σ_b / MPa	Toughness / MPa
(a) neat CTA	0.74 ± 0.09	2.2 ± 0.7	12.2 ± 4.4	0.17 ± 0.10
(b) BCP-free	1.07 ± 0.05	3.8 ± 1.3	26.9 ± 6.4	0.67 ± 0.42
(c) AB_{7k}-blend	1.34 ± 0.12	4.6 ± 1.2	40.3 ± 8.7	1.18 ± 0.55
(d) AB_{13k}-blend	1.37 ± 0.08	4.8 ± 0.6	44.2 ± 2.3	1.29 ± 0.24
(e) $AB_{15k}A$-blend	1.18 ± 0.03	8.2 ± 0.6	44.3 ± 0.9	2.49 ± 0.25
(f) $A_2B_{16k}A_2$-blend	1.16 ± 0.06	8.8 ± 0.4	43.5 ± 1.3	2.67 ± 0.23

[a] Tensile properties are shown as average values (with standard deviations) for five specimens. [b] Prepared by heat-pressing at 200 °C and 3 MPa for 3 min and subsequent aging for 72 h. (a) CTA/PCL (75/25 wt%), (b) CTA/PCL/AcCel$_n$-*b*-PCL$_{7k}$ (67/23/10 wt%), (c) CTA/PCL/AcCel$_n$-*b*-PCL$_{13k}$ (67/23/10 wt%), (d) CTA/PCL/AcCel$_n$-*b*-PCL$_{15k}$-*b*-AcCel$_n$ (67/23/10 wt%), and (e) CTA/PCL/(AcCel$_n$)$_2$-*b*-PCL$_{16k}$-*b*-(AcCel$_n$)$_2$ (67/23/10 wt%).

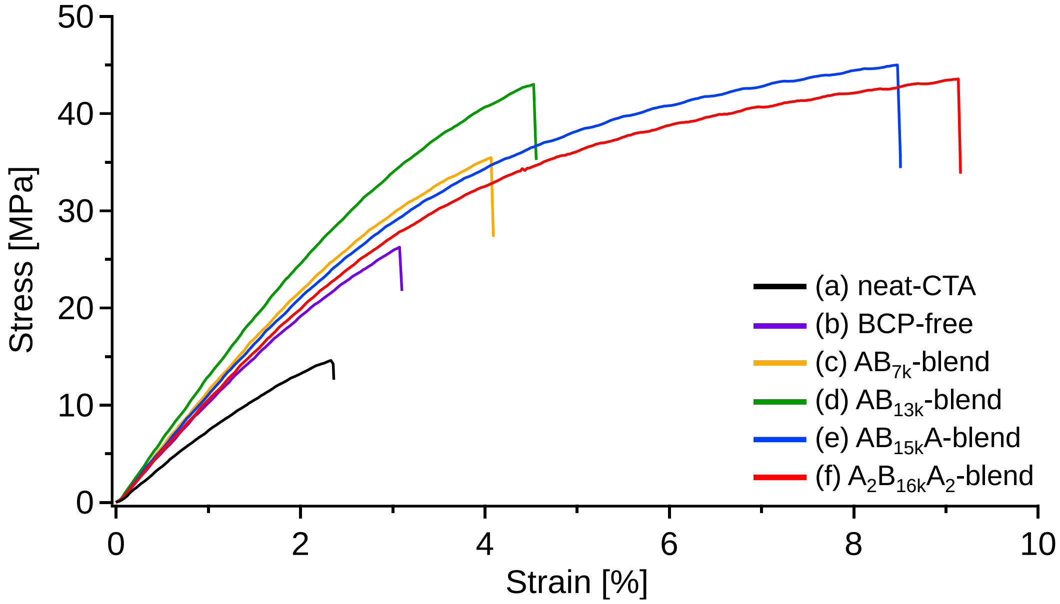

Figure 5.14. Typical stress-strain curves of (a) neat-CTA (100 wt%), (b) BCP-free, (c) AB_{7k}-blend, (d) AB_{13k}-blend, (e) $AB_{15k}A$-blend, and (f) $A_2B_{16k}A_2$-blend.

Table 5.3. Mechanical properties of the PCL film[a]

Film	*E* / GPa	ε_b / %	σ_b / MPa	Toughness / MPa
PCL	0.075 ± 0.015	804 ± 114	12.4 ± 4.2	68.6 ± 25.4

[a]Tensile properties are shown as average values (with standard deviations) for five specimens.

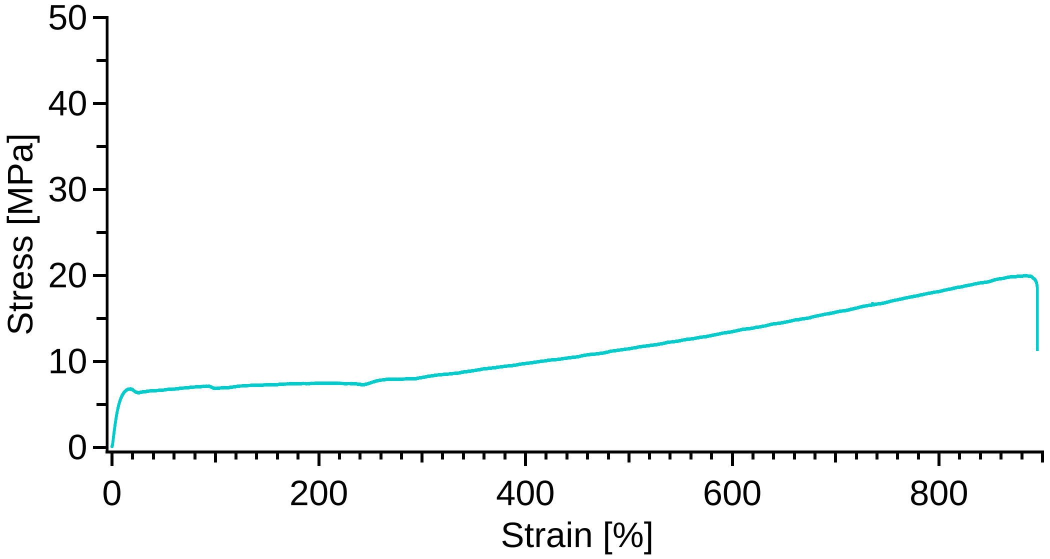

Figure 5.15. Typical stress-strain curve of PCL film.

Table 5.4. Thermal properties of CTA/PCL/BCP blended films

sample	$\Delta H_{\mathrm{CTA}}{}^{a}$ / J g^{-1}	X_{CTA} / %	$\Delta H_{\mathrm{PCL}}{}^{a}$ / J g^{-1}	X_{PCL} / %
BCP-free	11.6	33.2	13.2	29.9
AB_{7k}-blend	21.6	50.6	15.3	37.5
AB_{13k}-blend	21.0	47.8	12.2	30.3
$AB_{15k}A$-blend	19.0	44.9	14.9	36.4
$A_2B_{16k}A_2$-blend	17.6	43.4	14.0	33.7

[a]Determined by DSC during the 1st heating at a rate of 10 °C min^{-1}.

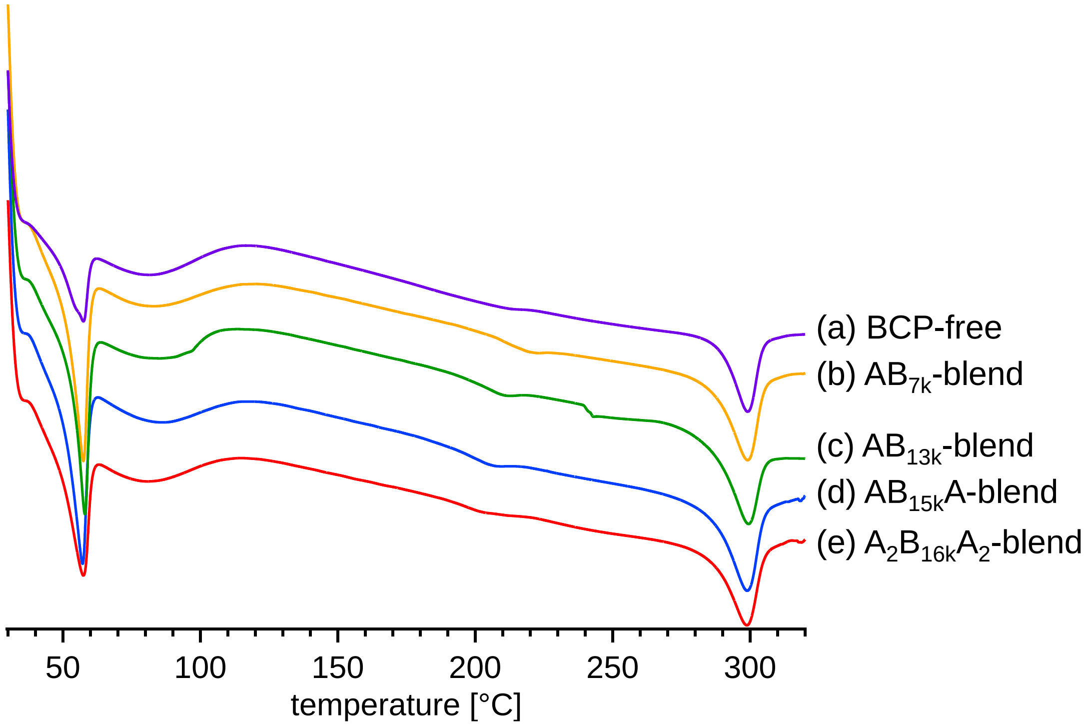

Figure 5.16. DSC curves of (a) BCP-free, (b) AB_{7k}-blend, (c) AB_{13k}-blend, (d) $AB_{15k}A$-blend, and (e) $A_2B_{16k}A_2$-blend films during 1st heating run (heating rate: 10 °C, min^{-1}).

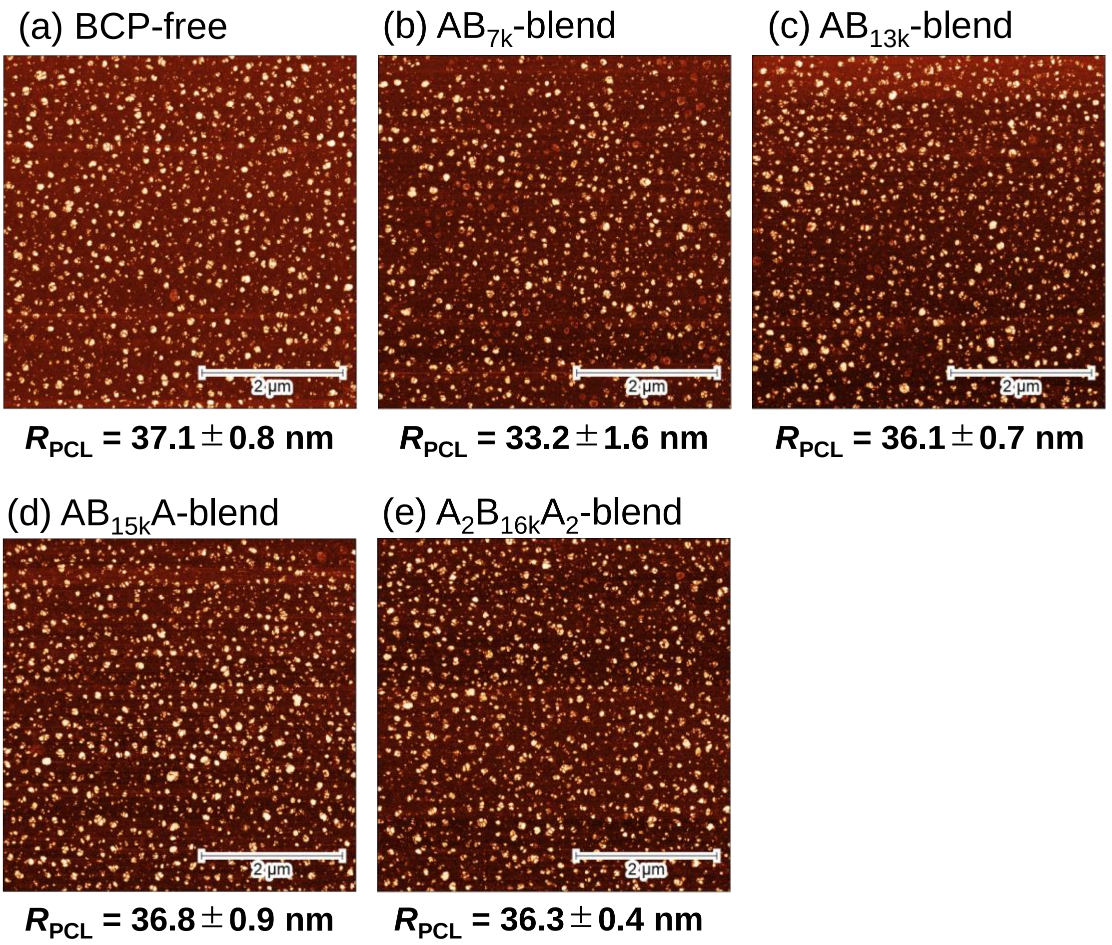

Figure 5.17. AFM phase images of (a) BCP-free, (b) AB_{7k}-blend, (c) AB_{13k}-blend, (d) $AB_{15k}A$-blend, and (e) $A_2B_{16k}A_2$-blend after thermal annealing at 200 °C for 30 min. $R_{PCL} = R_i^3 / R_i^2$ ($R_i = (a_i/\pi)^{1/2}$, a_i is the area of each domain). R_{PCL} is shown as average values (with standard deviations) for three samples. Scale bars are 2 μm.

5.4. Conclusion

The author successfully synthesized the BCPs consisting of AcCel$_n$ and PCL with various architectures (AB-, ABA-, and A$_2$BA$_2$-type) using CDP-mediated oligomerization, ring-opening polymerization, and click reaction. These BCPs acted as a compatibilizer and toughened the CTA/PCL blend films. In addition, the crystallinity was slightly increased by adding the BCPs, which also influenced on the mechanical properties. Interestingly, the mechanical properties of CTA/PCL/BCP-blend films depended on the architecture of compatibilizer. The A$_n$BA$_n$ triblock sequence is effective structure due to the improved stability at the interface, which will be useful guideline for designing the new compatibilizer. On the other hand, the dispersion state of PCL domain in CTA matrix was not changed dramatically before and after adding BCPs from the AFM observation. However, this result indicates that the adhesion of interface between CTA and PCL was strengthened by the added BCPs as compatibilizer.

This study is significant foundation for expanding the application of cellulose acetate-based materials which is attracting attention as environmentally benign materials to solve the plastic pollution problem and contributes to the development in industrial area.

5.5. References

(1) Millican, J. M.; Agarwal, S. Plastic Pollution: A Material Problem? *Macromolecules* **2021**, *54*, 4455–4469.

(2) Wang, G. -X.; Huang, D.; Ji, J. -H.; Völker, C.; Wurm, F. R. Seawater-Degradable Polymers—Fighting the Marine Plastic Pollution. *Adv. Sci.* **2021**, *8*, 1–26.

(3) MacLeod, M.; Arp, H. P. H.; Tekman, M. B.; Jahnke, A. The global threat from plastic pollution. *Science* **2021**, *373*, 61–65.

(4) Haider, T. P.; Völker, C.; Kramm, J.; Landfester, K.; Wurm, F. R. Plastics of the Future? The Impact of Biodegradable Polymers on the Environment and on Society. *Angew. Chem. Int. Ed.* **2019**, *58*, 50–62.

(5) Rafiqah, S. A.; Khalina, A.; Harmaen, A. S.; Tawakkal, I. A.; Zaman, K.; Asim, M.; Nurrazi, M. N.; Lee, C. H. A Review on Properties and Application of Bio-based Poly(Butylene Succinate). *Polymers* **2021**, *13*, 1–28.

(6) Suzuki, M.; Tachibana, Y.; Kasuya, K. ichi. Biodegradability of poly(3-hydroxyalkanoate) and poly(*ε*-caprolactone) via biological carbon cycles in marine environments. *Polym. J.* **2021**, *53*, 47–66.

(7) Kim, H. J.; Hillmyer, M. A.; Ellison, C. J. Enhanced Polyester Degradation through Transesterification with Salicylates. *J. Am. Chem. Soc.* **2021**, *143*, 15784–15790.

(8) Rheinberger, T.; Wolfs, J.; Paneth, A.; Gojzewski, H.; Paneth, P.; Wurm, F. R. RNA-Inspired and Accelerated Degradation of Polylactide in Seawater. *J. Am. Chem. Soc.* **2021**, *143*, 16673–16681.

(9) Liu, T. -Y.; Huang, D.; Xu, P. -Y.; Lu, B.; Wang, G. X.; Zhen, Z. -C.; Ji, J. Biobased Seawater-Degradable Poly(butylene succinate-L-lactide) Copolyesters: Exploration of Degradation Performance and Degradation Mechanism in Natural Seawater. *ACS Sustain. Chem. Eng.* **2022**, *10*, 3191–3202.

(10) Zhong, Y.; Godwin, P.; Jin, Y.; Xiao, H. Biodegradable polymers and green-based antimicrobial packaging materials: A mini-review. *Adv. Ind. Eng. Polym. Res.* **2020**, *3*, 27–35.

(11) Kliem, S.; Kreutzbruck. M.; Bonten, C. Review on the Biologocal Degradation of Polymers in Various Environments. *Materials* **2020**, *13*, 4586.

(12) Mekonnen, T.; Mussone, P.; Khalil, H.; Bressler, D. Progress in bio-based plastics and plasticizing modifications. *J. Mater. Chem. A* **2013**, *1*, 13379–13398.

(13) Yamaguchi, M.; Manaf, M. E. A.; Songsurang, K.; Nobukawa, S. Material design of retardation films with extraordinary wavelength dispersion of orientation birefringence: a review. *Cellulose* **2012**, *19*, 601–613.

(14) Puls, J.; Wilson, S. A.; Hölter, D. Degradation of Cellulose Acetate-Based Materials: A Review. *J. Polym. Environ.* **2011**, *19*, 152–165.

(15) Xu, R.; Yin, C.; Zhang, J.; Zhou, Y.; Mi, Q.; Zhang, J. Triggering the Biodegradability and Green-Reuse of Cigarette Filters by a Facile and Home-Operating Treatment. *ACS Sustain. Chem. Eng.* **2022**, *10*, 2822–2829.

(16) Mazzotta, M. G.; Reddy, C. M.; Ward, C. P. Rapid Degradation of Cellulose Diacetate by Marine Microbes. *Environ. Sci. Technol. Lett.* **2022**, *9*, 37–41.

(17) Quintana, R.; Persenaire, O.; Bonnaud, L.; Dubois, P. Recent advances in (reactive) melt processing of cellulose acetate and related biodegradable bio-compositions. *Polym. Chem.* **2012**, *3*, 591–595.

(18) Erdal, N. B.; Hakkarainen, M. Degradation of Cellulose Derivatives in Laboratory , Man-Made , and Natural Environments. *Biomacromolecules* **2022**, *23*, 2713–2729.

(19) Tateiwa, J.; Kimura, S.; Kasuya, K. ichi; Iwata, T. Multilayer biodegradable films with a degradation initiation function triggered by weakly alkaline seawater. *Polym. Degrad. Stab.* **2022**, *200*, 109942.

(20) Self, J. L.; Zervoudakis, A. J.; Peng, X.; Lenart, W. R.; Macosko, C. W.; Ellison, C. J. Linear, Graft, and Beyond: Multiblock Copolymers as Next-Generation Compatibilizers. *JACS Au* **2022**, *2*, 310–321.

(21) Koning, C.; Van Duin, M.; Pagnoulle, C.; Jerome, R. STRATEGIES FOR COMPATIBILIZATION OF POLYMER BLENDS. *Prog. Polym. Sci.* **1998**, *23*, 707–757.

(22) Arrington, K. J.; Haag, J. V.; French, E. V.; Murayama, M.; Edgar, K. J.; Matson, J. B. Toughening Cellulose: Compatibilizing Polybutadiene and Cellulose Triacetate Blends. *ACS Macro Lett.* **2019**, *8*, 447–453.

(23) Bragança, F. C.; Rosa, D. S. Thermal, Mechanical and Morphological Analysis of Poly (ε-caprolactone), Cellulose Acetate and Their Blends. *Polym. Adv. Technol.* **2003**, *14*, 669–675.

(24) Rosa, D. S.; Guedes, C. G. F.; Casarin, F.; Bragança, F. C. The effect of the M_w of PEG in PCL/CA Blends. *Polym. Test.* **2005**, *24*, 542–548.

(25) Oyama, T.; Kobayashi, S.; Okura, T.; Sato, S.; Tajima, K.; Isono, T.; Satoh, T. Biodegradable Compatibilizers for Poly(hydroxyalkanoate)/Poly(ε-caprolactone) Blends through Click Reactions with End-Functionalized Microbial Poly(hydroxyalkanoate)s. *ACS Sustain. Chem. Eng.* **2019**, *7*, 7969–7978.

(26) Krishnareddy, M.; Kim, Y.-K.; Kitaoka, M.; Mori, Y.; Hayashi, K. Cellodextrin Phosphorylase from *Clostridium thermocellum* YM4 Strain Expressed in Escherichia Coli. *J. Appl. Glycosci.* **2002**, *49*, 1–8.

(27) Hiraishi, M.; Igarashi, K.; Kimura, S.; Wada, M.; Kitaoka, M.; Samejima, M. Synthesis of highly ordered cellulose II in vitro using cellodextrin phosphorylase. *Carbohydr. Res.* **2009**, *344*, 2468–2473.

(28) Grandjean, C.; Boutonnier, A.; Guerreiro, C.; Fournier, J. M.; Mulard, L. A. On

the Preparation of Carbohydrate-Protein Conjugates Using the Traceless Staudinger Ligation. *J. Org. Chem.* **2005**, *70*, 7123–7132.

(29) Malkoch, M.; Schleicher, K.; Drockenmuller, E.; Hawker, C. J.; Russell, T. P.; Wu, P.; Fokin, V. V. Structurally Diverse Dendritic Libraries: A Highly Efficient Functionalization Approach Using Click Chemistry. *Macromolecules* **2005**, *38*, 3663–3678.

(30) Isono, T.; Nakahira, S.; Hsieh, H. -C.; Katsuhara, S.; Mamiya, H.; Yamamoto, T.; Chen, W. -C.; Borsali, R.; Tajima, K.; Satoh, T. Carbohydrates as Hard Segments for Sustainable Elastomers: Carbohydrates Direct the Self-Assembly and Mechanical Properties of Fully Bio-Based Block Copolymers. *Macromolecules* **2020**, *53*, 5408–5417.

(31) Halila, S.; Manguian, M.; Fort, S.; Cottaz, S.; Hamaide, T.; Fleury, E.; Driguez, H. Syntheses of Well-Defined Glyco-Polyorganosiloxanes by “Click” Chemistry and Their Surfactant Properties. *Macromol. Chem. Phys.* **2008**, *209*, 1282–1290.

Chapter 6

Conclusion

In this dissertation, the author achieved designing and synthesizing various oligosaccharide-based block copolymers (BCPs) as functional materials, such as practical lithographic materials, thermoplastic elastomers (TPE), and compatibilizer, by combining oligosaccharides, e.g., maltooligosaccharide and cellooligosaccharide, with proper synthetic polymers. A summary of the important achievements and findings in the present study is as follows:

Chapter 2. Fabrication of Sub-10 nm Microphase-Separated Structures Using Metallopolymer-block-Oligosaccharide

In Chapter 2, the author successfully synthesized the novel oligosaccharide-based BCPs consisting of maltooligosaccharide (maltotoriose (MT) and maltohexaose (MH)) and metallopolymer (poly(vinyl ferrocene) (PVFc)) through the combination of living anionic polymerization and the click reaction. In this study, three types of the oligosaccharide-based BCPs, PVFc-*b*-MT, PVFc-*b*-MH, and PVFc-*b*-$(MT)_2$, were synthesized. Among them, PVFc-*b*-MT did not form the ordered microphase-separated structure due to its small molecular weight; on the other hand, PVFc-*b*-MH and PVFc-*b*-$(MT)_2$ formed hexagonally close-packed cylinder (HEX) microphase-separated structures with sub-10 nm domain-spacing (*d*). This is the first example of demonstrating microphase-separated structures with a *d* of < 10 nm from metal-containing BCPs.

Furthermore, lamellar (LAM) morphology was obtained by blending PVFc-*b*-$(MT)_2$ and glucose. Such LAM and HEX morphologies are useful for BCP lithography process. Importantly, the author demonstrated the sufficient etching contrast between the oligosaccharide and PVFc, supporting the nanolithographic applications of those BCPs. To summarize, the author has developed a novel functional material by combining oligosaccharide and metallopolymer to simultaneously achieve small *d* value, sufficient thermal stability, and high etching selectivity, which could be one of the candidates for next generation lithographic materials.

Chapter 3. Synthesis of Cellulose-based Triblock Copolymers for Investigating Microphase Separation Behavior and Mechanical Properties: Comparisons with Amylose-based Triblock Copolymers

In Chapter 3, the author designed the novel bio-based elastomers ($AcCel_n$-*b*-PDL-*b*-$AcCel_n$s) consisting cellulose triacetate ($AcCel_n$) as the hard segment and poly(δ-decanolactone) (PDL) as the soft segment. $AcCel_n$-*b*-PDL-*b*-$AcCel_n$s were precisely synthesized by combining living ring-opening polymerization (ROP), cellodextrin-phosphorylase (CDP)-mediated oligomerization, and click reaction. Furthermore, their amylose counterparts consisting of amylose triacetate and PDL ($AcMal_n$-*b*-PDL-*b*-$AcMal_n$s) were also synthesized in a similar manner. Interestingly, the $AcCel_n$-*b*-PDL-*b*-

AcCel*ₙ*s exhibited more ordered microphase-separated structures than AcMal*ₙ*-*b*-PDL-*b*-AcMal*ₙ*s. This is due to the differences in the types of glycosidic bond (i.e., *β*-1,4 or *α*-1,4 linkages) in their oligosaccharide segments. In addition, AcCel*ₙ*-*b*-PDL-*b*-AcCel*ₙ*s were tougher than the corresponding AcMal*ₙ*-*b*-PDL-*b*-AcMal*ₙ*, which indicates that stronger physical crosslinking of the AcCel*ₙ* segments. This is the first example showing that the small differences in the primary structures of the oligosaccharide segments (i.e., *α*-1,4 or *β*-1,4 linkages) affect the microphase separation behaviors and mechanical properties of oligosaccharide-based BCPs. Through this study, the author demonstrated the usefulness of cellulose-based BCPs in developing new bio-based and sustainable polymeric materials.

Chapter 4. Design of Cellulose-Based Block Copolymers: DS effects on Microphase Separation Behaviors and Mechanical Properties

In Chapter 4, the author designed cellulose-based BCPs (AcCel$_x$-*b*-PDL-*b*-AcCel$_x$) consisting of acetyl celloloogiosaccharide (AcCel$_x$: x represents degree of substitution (DS)) with three different DSs and PDL to toughen the cellulose-based thermoplastic elastomer. AcCel$_x$-*b*-PDL-*b*-AcCel$_x$ was synthesized by combining CDP-mediated cellulose synthesis, ROP, and a click reaction in a similar manner as mentioned in Chapter 3. Importantly, the DS of the AcCel$_x$ segment highly influenced on the microphase separation behaviors and mechanical properties of AcCel$_x$-*b*-PDL-*b*-AcCel$_x$ because of the stronger intermolecular interactions (i.e., hydrogen bonding) associated with decreasing DS. The author clearly demonstrated that the DS was a significant factor for improving and optimizing the physical properties of cellulose-based TPEs in terms of self-assemble behavior, mechanical properties, and biodegradation behaviors. Such DS optimization approach can be a useful molecular design applicable to a wide range of poly/oligosaccharide-based materials, which will contribute to the development next-generation environmentally benign polymeric materials that can replace conventional petroleum-based materials.

Chapter 5. Development of Cellulose-Based Compatibilizers for Toughening Cellulose Acetate

In Chapter 5, the author synthesized the BCPs consisting of AcCel$_n$ and poly(ε-caprolactone) (PCL) with various architectures (AB-, ABA-, and A$_2$BA$_2$-type) as compatibilizer for a blend system of commercially available cellulose triacetate (CTA) and PCL. The synthesis of these BCPs was performed by following the method described in Chapters 3 and 4. The synthesized BCPs acted as effective compatibilizer for CTA/PCL-blend film. Importantly, the author revealed that molecular weight and architecture of the compatibilizer affected the mechanical properties of the blends, so that these factors are the important variable for designing useful compatibilizers. This work expands the application of cellulose acetate-based materials, which are recently attracting much attention as environmentally benign materials, and will pave the way to settle the plastic pollution problem.

In conclusion, the author has established the outstanding molecular design and synthesis method for versatile functional oligosaccharide-based materials utilizing the strong point of poly/oligosaccharide. To synthesize the desired oligosaccharide-based BCPs, the author adopted the synthetic pathway based on not only organic chemistry approach, such as living polymerization and click reaction but also biochemical approach such as enzyme-mediated oligomerization. Moreover, the author found that the judicious choice of the oligosaccharide and synthetic polymer blocks is the key to realize desirable functions. The author believes that the findings in this dissertation will be important foundations to develop next generation materials to lead the advancement of both the microelectronics industry and sustainable polymer industry.